



FLUIDS ENGINEERING DIVISION

Editor

J. KATZ (2009)

Assistant to the Editor

L. MURPHY (2009)

Associate Editors

M. J. ANDREWS (2009)

S. BALACHANDAR (2008)

A. BESKOK (2008)

S. L. CECCIO (2009)

D. DRIKAKIS (2008)

P. DUPONT (2010)

I. EAMES (2010)

C. HAH (2009)

T. J. HEINDEL (2010)

J. KOMPENHANS (2009)

J. A. LIBURDY (2010)

P. LIGRANI (2008)

R. MITTAL (2009)

T. J. O'HERN (2008)

U. PIOMELLI (2010)

Z. RUSAK (2010)

D. SIGNER (2008)

Y. ZHOU (2008)

PUBLICATIONS COMMITTEE

Chair, B. RAVANI

OFFICERS OF THE ASME

President, THOMAS M. BARLOW

Executive Director, THOMAS G. LOUGHLIN

Treasurer, T. D. PESTORIUS

PUBLISHING STAFF

Managing Director, Publishing

P. DI VIETRO

Manager, Journals

C. MCATEER

Production Coordinator

A. HEWITT

Transactions of the ASME, Journal of Fluids Engineering (ISSN 0098-2202) is published monthly by The American Society of Mechanical Engineers, Three Park Avenue, New York, NY 10016. Periodicals postage paid at New York, NY and additional mailing offices.

POSTMASTER: Send address changes to Transactions of the ASME, Journal of Fluids Engineering, c/o THE AMERICAN SOCIETY OF MECHANICAL ENGINEERS, 22 Law Drive, Box 2300, Fairfield, NJ 07007-2300.

CHANGES OF ADDRESS must be received at Society headquarters seven weeks before they are to be effective.

Please send old label and new address.

STATEMENT from By-Laws. The Society shall not be responsible for statements or opinions advanced in papers or ... printed in its publications (B7.1, Par. 3).

COPYRIGHT © 2008 by the American Society of Mechanical Engineers. Authorization to photocopy material for internal or personal use under those circumstances not falling within the fair use provisions of the Copyright Act, contact the Copyright Clearance Center (CCC), 222 Rosewood Drive, Danvers, MA 01923, tel: 978-750-8400, www.copyright.com. Request for special permission or bulk copying should be addressed to Reprints/Permission Department. Canadian Goods & Services Tax Registration #126148048.

Journal of Fluids Engineering

Published Monthly by ASME

VOLUME 130 • NUMBER 11 • NOVEMBER 2008

RESEARCH PAPERS

Flows in Complex Systems

- 111101 Vortex Breakdown in an Enclosed Cylinder With a Partially Rotating Bottom-Wall
P. Yu, T. S. Lee, Y. Zeng, and H. T. Low
- 111102 The Effect of Impeller Cutback on the Fluid-Dynamic Pulsations and Load at the Blade-Passing Frequency in a Centrifugal Pump
Raúl Barrio, Eduardo Blanco, Jorge Parrondo, José González, and Joaquín Fernández
- 111103 Design Principles and Measured Performance of Multistage Radial Flow Microturbomachinery at Low Reynolds Numbers
Changgu Lee, Selin Arslan, and Luc G. Fréchette
- 111104 A Parametric Study of Passive Flow Control for a Short, High Area Ratio 90 deg Curved Diffuser
T. P. Chong, P. F. Joseph, and P. O. A. L. Davies
- 111105 Strategies for Simulating Flow Through Low-Pressure Turbine Cascade
Andreas Gross and Hermann F. Fasel

Fundamental Issues and Canonical Flows

- 111201 Laminar Non-Newtonian Fluid Flow in Noncircular Ducts and Microchannels
Y. S. Muzychka and J. Edge

Multiphase Flows

- 111301 Head Drop of a Spatial Turbopump Inducer
Nellyana Gonzalo Flores, Eric Goncalvès, Regiane Fortes Patella, Julien Rolland, and Claude Rebattet
- 111302 Thermodynamic Effect on Cavitation Performances and Cavitation Instabilities in an Inducer
Kengo Kikuta, Yoshiki Yoshida, Mitsuo Watanabe, Tomoyuki Hashimoto, Katsuji Nagaura, and Katsuhide Ohira
- 111303 On the Preliminary Design and Noncavitating Performance Prediction of Tapered Axial Inducers
Luca d'Agostino, Lucio Torre, Angelo Pasini, and Angelo Cervone
- 111304 Turbulence Structure Modification and Drag Reduction by Microbubble Injections in a Boundary Layer Channel Flow
C. C. Gutiérrez-Torres, Y. A. Hassan, and J. A. Jimenez-Bernal
- 111305 PIV Study of Adverse and Favorable Pressure Gradient Turbulent Flows Over Transverse Ribs
M. Agelinchaab and M. F. Tachie

(Contents continued on inside back cover)

This journal is printed on acid-free paper, which exceeds the ANSI Z39.48-1992 specification for permanence of paper and library materials. ©™

♻️ 85% recycled content, including 10% post-consumer fibers.

Techniques and Procedures

- 111401 **Optical Diffusometry Techniques and Applications in Biological Agent Detection**
Aloke Kumar, Venu M. Gorti, Hao Shang, Gil U. Lee,
Nung Kwan Yip, and Steve T. Wereley

The ASME Journal of Fluids Engineering is abstracted and indexed in the following:

Applied Science & Technology Index, Chemical Abstracts, Chemical Engineering and Biotechnology Abstracts (Electronic equivalent of Process and Chemical Engineering), Civil Engineering Abstracts, Computer & Information Systems Abstracts, Corrosion Abstracts, Current Contents, Ei EncompassLit, Electronics & Communications Abstracts, Engineered Materials Abstracts, Engineering Index, Environmental Engineering Abstracts, Environmental Science and Pollution Management, Excerpta Medica, Fluidex, Index to Scientific Reviews, INSPEC, International Building Services Abstracts, Mechanical & Transportation Engineering Abstracts, Mechanical Engineering Abstracts, METADEX (The electronic equivalent of Metals Abstracts and Alloys Index), Petroleum Abstracts, Process and Chemical Engineering, Referativnyi Zhurnal, Science Citation Index, SciSearch (The electronic equivalent of Science Citation Index), Shock and Vibration Digest, Solid State and Superconductivity Abstracts, Theoretical Chemical Engineering

Vortex Breakdown in an Enclosed Cylinder With a Partially Rotating Bottom-Wall

P. Yu
T. S. Lee
Y. Zeng

Department of Mechanical Engineering,
National University of Singapore,
9 Engineering Drive 1,
Singapore 117576, Singapore

H. T. Low

Department of Mechanical Engineering,
and Division of Bioengineering,
National University of Singapore,
9 Engineering Drive 1,
Singapore 117576, Singapore
e-mail: mpelowht@nus.edu.sg

A numerical study of the axisymmetric flow in a cylindrical chamber of height H is presented, which is driven by a bottom disk rotating at angular velocity Ω . However, unlike most previous studies, the present rotating disk is of smaller radius than the bottom-wall. The boundary curves for the onset of vortex breakdown are presented using different definitions of the nondimensional parameters, depending on whether the cylinder radius R or the disk radius r_d is used as the length scale. The study shows that the boundary curves are best correlated when presented in terms of the Reynolds number $\Omega r_d^2/\nu$, aspect ratio H/R , and cylinder-to-disk ratio R/r_d . The cylinder-to-disk ratio R/r_d up to 1.6 is found to have noticeable effect on vortex breakdown; this is attributed to the change of effective aspect ratio. The contours of streamline, angular momentum, and azimuthal vorticity are presented and compared with those of whole bottom-wall rotation. [DOI: 10.1115/1.2969427]

Keywords: vortex breakdown, swirling flow, recirculation flow

Introduction

Swirling flow inside a cylindrical chamber, of a radius R and a height H , with a bottom-wall rotating at angular velocity Ω has attracted much attention. This flow problem, having simple configuration and well defined boundary conditions, is particularly suitable for the detailed investigation of the vortex-breakdown phenomena. Only two dimensionless parameters are needed to characterize the flow structure: the aspect ratio H/R and the Reynolds number $Re = \Omega R^2/\nu$, where ν is the kinematic viscosity.

A detailed experimental investigation for vortex breakdown has been done by Escudier [1]. The stability boundaries with one, two, or even three successive vortex-breakdown bubbles, as well as a transition toward unsteady flows, were mapped in a plot of the Reynolds number and aspect ratio. These experimental visualizations have been confirmed by the numerical model of Lopez [2], who solved the unsteady axisymmetric Navier–Stokes equations. Brown and Lopez [3] explained that the physical mechanism of vortex breakdown is due to the negative azimuthal vorticity induced by an excess centrifugal force in the axial region near the stationary top end-wall.

Recently, some interesting variants of the above flow problem have also been investigated. Spohn et al. [4,5] considered the case in which the stationary end-wall at the top was replaced by a free surface. The experimental results showed that the vortex-breakdown bubbles may attach to the free surface at certain Reynolds numbers. The numerical works of Valentine and Jahnke [6] and Lopez [7] indicated that the free surface effect may be approximately modeled by having a middle plane in a cylinder of twice the height, in which both end-walls rotate at the same speed. Another recent variant is the effect of introducing a rotating central rod, which has been reported by Mullin et al. [8], Mullin et al. [9], and Husain et al. [10]; their results indicated that the presence of the rotating-rod can either intensify or suppress vortex-breakdown bubbles. The effects of the lid shape on vortex breakdown have been investigated numerically by Yu et al. [11]. Their

results show that the concave-cone lid delays or even completely suppresses vortex breakdown while the convex-cone lid precipitates the onset of vortex breakdown.

Another interesting configuration is that of a partially rotating bottom-wall, in which the central part consists of a rotating disk of a smaller radius r_d . Such a configuration was considered by Piva and Meiburg [12] who numerically studied the case with a free surface. The stationary bottom-wall significantly alters the flow structure. The sidewall does not have a significant effect on the flow structure near the disk if it is far away, as in the cases of the cylinder-to-disk ratio above 2.3. Most of their results are for the cylinder-to-disk ratio above 2 although there are streamline contours for lower ratios down to 1. The flow in such a chamber with a rigid lid was investigated numerically by Yu et al. [13]. Three regions, namely, the quasiwhole bottom-wall rotating region, the vortex-breakdown boundary invariance region, and the mixed region, were defined to characterize the occurrence of vortex breakdown.

A related application of the swirling flow with a partially rotating bottom-wall may be found in a bioreactor chamber filled with a medium rotated by a rod at the base [14]. A prototype designed by Kostov et al. [15] has a working volume of 2 ml, with agitation generated by a small magnetic stir bar placed at the bottom, which was rotated at 300 rpm. Another novel bioreactor model designed by Thouas et al. [16] consisted of a cylindrical vessel with a working volume of 50 ml, in which the culture medium is stirred by a surface disk of diameter smaller than the vessel diameter.

In the above bioreactors, the swirling flow and its vortex breakdown may affect the cell culture in terms of local shear stress and mixing. Dusting et al. [17] found that the shear stress is lower in the vortex-breakdown region than that in the main recirculating flow. Yu et al. [18] found that the oxygen concentration is higher in the vortex-breakdown region than that in the main recirculating center. In a recent study by Mununga [19], there is a partially rotating disk at the top with the whole wall rotating at the bottom. The top rotating disk was proposed to control vortex breakdown in bioreactors.

The objective of the present study was to numerically investigate vortex breakdown in an enclosed cylinder with a rotating disk whose radius is smaller than that of the chamber. Such a flow situation is of interest in relation to the flow pattern in a micro-bioreactor stirred by a rotating magnetic-rod at the bottom [15].

Contributed by the Fluids Engineering Division of ASME for publication in the JOURNAL OF FLUIDS ENGINEERING. Manuscript received June 6, 2007; final manuscript received July 3, 2008; published online September 19, 2008. Assoc. Editor: Rajat Mittal.

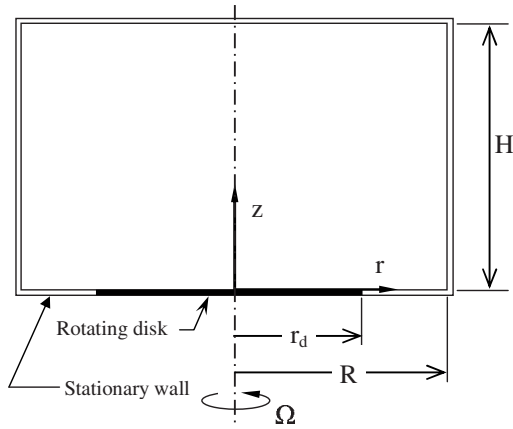


Fig. 1 Cylindrical chamber with a partially rotating bottom-wall

Also presented are the contours of the streamline Ψ , angular momentum ($\Gamma = rv_\theta$), azimuthal vorticity ω , the centrifugal force, the radial pressure-gradient force, and the resultant of the two forces, at different Reynolds number, aspect ratio, and cylinder-to-disk ratio.

Numerical Method

Figure 1 schematically shows the flow model, which is a cylindrical chamber of radius R filled with fluid and driven by a disk of radius r_d rotating at angular velocity Ω . The present study was motivated by a prototype microbio-reactor as described in Kostov et al. [15]. The diameter of the microbio-reactor is around 10 mm with a working volume of 2 ml. In contrast, laboratory and industrial bioreactors are of volume ranging from 0.5 l to 1000 l. Bioreactors may be classified based on their volumes; mini for volume below 100 ml [20], and micro for volume of a few microliter [15]. In cell-culture applications, the kinematic viscosity of the culture medium is around $10^{-6} \text{ m}^2 \text{ s}^{-1}$ and the rotation is around 300 rpm. In the prototype microbio-reactor, these typical parameters give a Reynolds number of around 1000, which is in the range of the present computation.

Both steady [8,9] and unsteady [7,12] flow equations have been used for numerical modeling of the onset of vortex-breakdown phenomena in earlier works. The present study is based on the primitive-variable formulation of the steady axisymmetric Navier–Stokes equations, expressed as follows:

$$\frac{1}{r} \frac{\partial(rv_r)}{\partial r} + \frac{\partial v_z}{\partial z} = 0 \quad (1)$$

$$\frac{1}{r} \frac{\partial(rv_r v_r)}{\partial r} + \frac{\partial(v_z v_r)}{\partial z} = -\frac{1}{\rho} \frac{\partial p}{\partial r} + \nu \left[\frac{\partial}{\partial r} \left(\frac{1}{r} \frac{\partial}{\partial r} (rv_r) \right) + \frac{\partial^2 v_r}{\partial z^2} \right] + \frac{v_\theta^2}{r} \quad (2)$$

$$\frac{1}{r} \frac{\partial(rv_r v_z)}{\partial r} + \frac{\partial(v_z v_z)}{\partial z} = -\frac{1}{\rho} \frac{\partial p}{\partial z} + \nu \left[\frac{1}{r} \frac{\partial}{\partial r} \left(r \frac{\partial v_z}{\partial r} \right) + \frac{\partial^2 v_z}{\partial z^2} \right] \quad (3)$$

$$\frac{1}{r} \frac{\partial(rv_r v_\theta)}{\partial r} + \frac{\partial(v_z v_\theta)}{\partial z} = \nu \left[\frac{\partial}{\partial r} \left(\frac{1}{r} \frac{\partial}{\partial r} (rv_\theta) \right) + \frac{\partial^2 v_\theta}{\partial z^2} \right] - \frac{v_r v_\theta}{r} \quad (4)$$

where v_r , v_z , and v_θ are the radial, axial, and azimuthal velocities, respectively; r and z are the radial and axial coordinates, respectively.

The boundary conditions can be expressed as

$$v_r = 0, \quad v_z = 0, \quad v_\theta = 0 \quad \text{on stationary wall} \quad (5)$$

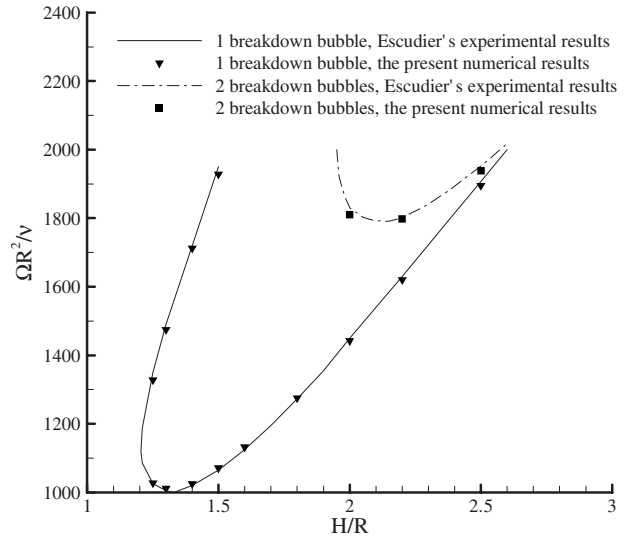


Fig. 2 Boundary curves for the onset of vortex breakdown for whole bottom-wall rotating

$$v_r = 0, \quad v_z = 0, \quad v_\theta = \Omega r \quad \text{on rotational wall} \quad (6)$$

The equations were discretized by the second-order central difference scheme and to solve them, a computer code was developed based on finite volume method.

To ensure grid-independent solution and accurate resolution in space, a sufficiently fine grid should be used. For Re less than 2000, a grid size of $1/60$ was found to be sufficient for the flow in a cylindrical enclosure with the rotating bottom-wall [2]. Valentine and Jahnke [6] also reported that there were no significant differences between the results using grid sizes of $1/60$ and $1/120$ for Re up to 3000 for the flow in a cylinder with both end-walls rotating. The above studies indicated that for Re less than 2000, a uniform grid size of $1/60$ associated with second-order difference scheme is fine enough for these types of flow problems. However, to precisely capture the first onset of the vortex-breakdown bubble, which is small, a uniform grid size of $1/200$ was used to perform the present simulations. It was found that the errors in detecting the Reynolds numbers at which the bubble appeared and disappeared are within 0.5% if the uniform grid sizes are varied between $1/100$ and $1/200$ for Re less than 2000.

Note that there is a discontinuity in the boundary conditions at the outer edge of the rotating disk. In the present study, as the grid size was chosen as $1/100$ or $1/200$, there is a grid line located just at the outer edge of the rotating disk. Thus, the singularity problem was avoided as properties were evaluated at the control volume center. The comparison of the testing simulations between the grid sizes $1/100$ and $1/200$ also confirmed that the solutions are not affected by the discontinuity.

For further validation, the present code was used to capture the vortex-breakdown phenomena in the case of the whole bottom-wall rotation. The occurrence of the vortex-breakdown bubble is a continuous process with an increase in Re . The procedure of Mullin et al. [9] was used to distinguish between the parameter regions where the vortex-breakdown bubble appears and disappears. Keeping the aspect ratio fixed and gradually increasing the Reynolds number in steps of 10, the streamline was calculated and the vortex breakdown was deemed to occur when a region was first visibly noted to be enclosed by the zero streamline.

The onsets of vortex breakdown are estimated in a wide range of parameter space, as shown in Fig. 2 and compared with the experimental results [1]. There are two boundaries for the curve of first vortex breakdown (solid line): As the Reynolds number increases, the right boundary shows the onset of vortex breakdown and the left boundary shows its disappearance. There is also an

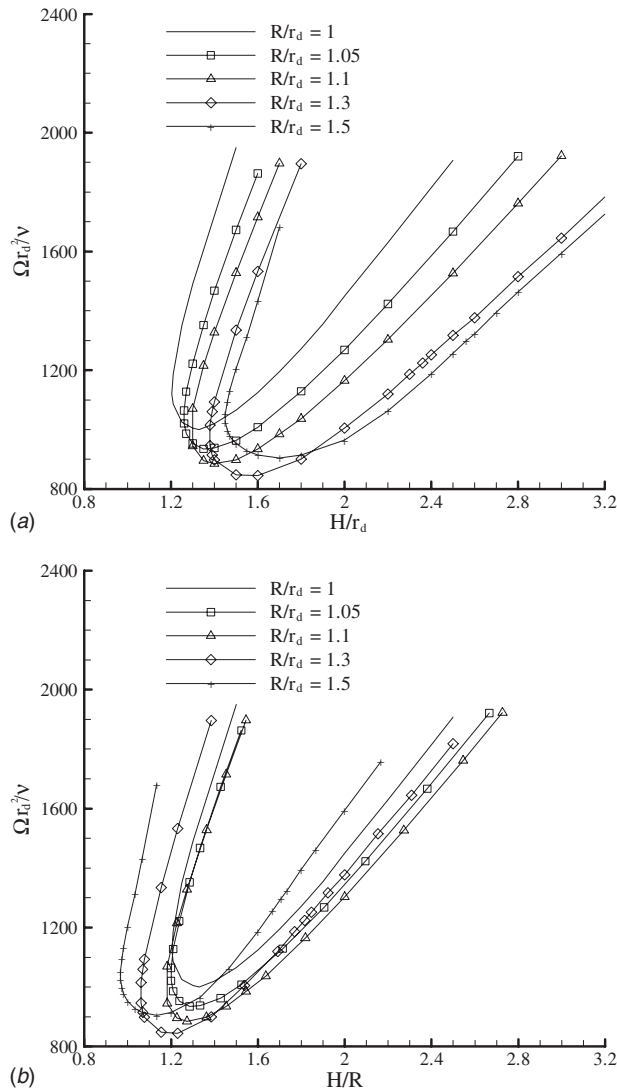


Fig. 3 Boundary curves for the onset of vortex breakdown for a partially rotating bottom-wall; different parameters effect: (a) ($\Omega r_d^2/\nu, H/r_d$); (b) ($\Omega r_d^2/\nu, H/R$)

upper curve (dash line), which shows the boundary between one and two vortex-breakdown bubbles as the Reynolds number increases. The good agreement with the experimental results [1] indicates that the present code is satisfactory for detecting the appearance and the disappearance of the vortex-breakdown bubbles.

Results and Discussion

Boundary Curves for Vortex Breakdown. The boundaries for the onset of vortex breakdown are mapped in a plot of the Reynolds number and the aspect ratio (see Figs. 3(a) and 3(b)), with different curves for different R/r_d . The Reynolds number is defined as $Re = \Omega r_d^2/\nu$ [12]. However, there are two possible definitions for the aspect ratio ($H/R, H/r_d$), as either the cylinder radius R or the disk radius r_d may be chosen as the length scale. Thus two plots are presented to cover the combinations of dimensionless parameters.

It is interesting that Fig. 3(a) seems to indicate that vortex breakdown will occur at a smaller Re if R/r_d is larger, for the same H/r_d , since the boundary curves shift downward. In other words, a smaller rotating disk seems to be more effective in causing vortex breakdown, but this effect has arisen because H/R has

become smaller. Thus using H/r_d may not be able to show the effect of R/r_d at a constant aspect ratio H/R and the real influence of R/r_d has not been isolated.

In a previous study on a partially rotating bottom-wall by Piva and Meiburg [12], the results are presented in terms of parameters $\Omega r_d^2/\nu$ and H/r_d . However, their main results are for larger R/r_d from 2.3 to 3.3. Their results showed that for $R/r_d \geq 2.3$ the influence of the sidewall becomes insignificant. This is different from the present study with the cylinder-to-disk ratio $R/r_d \leq 1.6$ in which case the sidewall has more influence and the aspect ratio H/R is important. Thus it is more meaningful to use the aspect ratio H/R if the sidewall is not distant. Only by considering a constant aspect ratio H/R can the effect of a varying R/r_d be isolated.

In Fig. 3(b), the boundary curves for vortex breakdown are presented in terms of the Reynolds number $\Omega r_d^2/\nu$, the aspect ratio H/R , and the cylinder-to-disk ratio R/r_d . The curves of different R/r_d are now closer to that of the whole bottom-wall rotation ($R/r_d=1$). It shows the real effect of the partial rotation.

The critical aspect ratio to have vortex breakdown is reduced to $H/R \approx 1.0$ as compared to the whole bottom-wall rotation in which the critical aspect ratio is 1.2. The minimum Re for vortex breakdown is reduced to 850 as compared to 1000 for the whole bottom-wall rotation.

The shape of the boundary curves is rather similar to that of the whole bottom-wall rotation. With an increase in Re , the right boundary-curve shows transition from no bubble to single bubble, and the left boundary-curve shows transition from single bubble to no bubble. The right boundary curve does not seem to show any consistent trend with R/r_d ; the Reynolds number for the onset of vortex breakdown reduces when R/r_d is increased from 1.0 to 1.1, after which the onset Re increases with R/r_d . As for the left boundary curve, there is no much effect for R/r_d from 1.0 to 1.1, after which the Reynolds number increases with R/r_d .

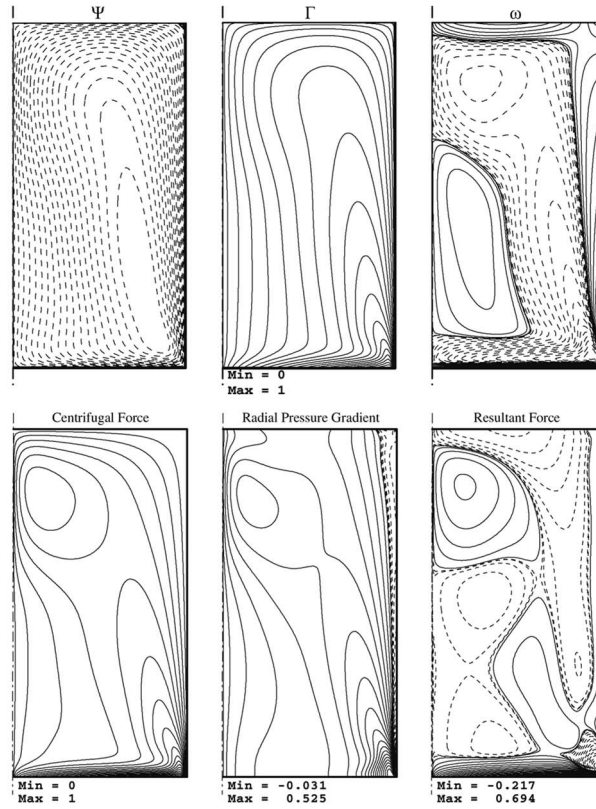
Description of Flow Behavior. A typical flow field in the meridional plane is shown by the streamline plot labeled by Ψ in Figs. 4(a)(i) and 4(a)(ii) which are for $R/r_d=1$, the case of the whole bottom-wall rotation. The flow pattern (left diagram labeled by Ψ) indicates an Ekman boundary layer at the bottom-wall generated by the rotation. The Ekman boundary layer imparts angular momentum ($\Gamma = rv_\theta$) to the fluid and centrifuges it toward the sidewall. The fluid then spirals up the sidewall followed by the top wall, forming boundary layers at these two walls. The angular momentum is nearly conserved [5] during the radial inward flow near the upper region. Finally, the fluid on the top wall spirals down along the center axis to be sucked back into the Ekman layer.

In Fig. 4(a)(i) $Re=1200, H/R=2$, there is no vortex-breakdown bubble because this corresponds to the no-breakdown region (Fig. 3(b)) of the boundary plot. However, for the condition of $Re=1500$ and $H/R=2$, the boundary plot indicates one vortex-breakdown bubble (Fig. 3(b)); it is consistent that the flow pattern in Fig. 4(a)(ii) shows a vortex breakdown bubble. The location, size, and shape of the bubble agree well with the experimental flow visualization reported by Escudier [1].

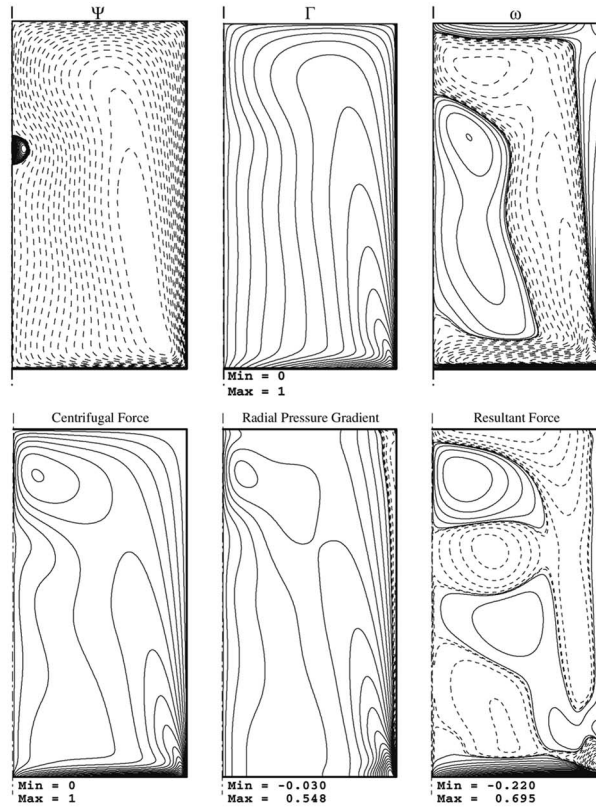
In Figs. 4(a)(i) and 4(a)(ii) the diagrams of the angular momentum labeled by Γ and azimuthal vorticity labeled by ω are also shown. It is noted that the vortex-breakdown bubble is located near the regions where the angular momentum is wavy (see Fig. 4(a)(ii) under label Γ) and where the azimuthal vorticity is positive (see Fig. 4(a)(ii) under label ω). This is consistent with the observations of Lopez [2] (negative in Brown and Lopez [3]).

There have been several previous studies on three-dimensional vortex breakdown in this type of geometry recently. A brief discussion is provided here giving an idea of where in parameter space the flow becomes three-dimensional and unsteady and what form these flows take. The flow is steady and axisymmetric for Reynolds number up to 2000. However, with an increase in Re ,

i) $Re=1200$



ii) $Re = 1500$



(a) $R/r_d = 1$

Fig. 4 Contours of streamline Ψ , angular momentum Γ , azimuthal vorticity ω in meridional plane for aspect ratio $H/R=2$; (i) $Re=1200$, (ii) $Re=1500$; (a) $R/r_d=1.0$, (b) $R/r_d=1.1$, (c) $R/r_d=1.3$, (d) $R/r_d=1.5$; contour levels C_i are nonuniformly spaced, with 20 positive levels $C_i = \text{Max}(\text{variable}) \times (i/20)^3$ and 20 negative levels $C_i = \text{Min}(\text{variable}) \times (i/20)^3$

the swirling flow in the enclosed chamber may become unsteady and/or nonaxisymmetric. For low aspect ratios, $1 < H/R < 1.63$, a symmetry-breaking Hopf bifurcation occurs at Reynolds number around 2500 [21,22]. The direct numerical simulation of Marques et al. [21] showed that the flows evolve to three-dimensional states characterized by rotating waves with an azimuthal wave number of 2. For intermediate aspect ratios, $1.63 < H/R < 2.76$, the flow becomes unsteady prior to a transition to three-dimensional flow [22–24]. The detailed numerical simulation [23,24] showed that for $H/R=2.5$, the flow bifurcates to a time-periodic axisymmetric state at $Re \approx 2707$ and becomes three-dimensional for Re greater than approximately 3580. For higher aspect ratios, $H/R > 2.76$, the flow bifurcates from the basic state to three-dimensional state characterized by rotating waves with an azimuthal wave number of 4 [25]. Besides the above bifurcations, a double Hopf bifurcation, which involved the simultaneous bifurcation of an axisymmetric limit cycle and a rotating wave, has been found at $Re \approx 2627$ and $H/R \approx 1.583$ [21]. Also, at $H/R = 1.72$, there is competition between two axisymmetric limit cycles, at about $Re=2660$ [26].

Mechanism of Vortex Breakdown. The mechanism of vortex breakdown has been explained in terms of pressure-gradient and centrifugal forces by Brown and Lopez [3], Coriolis and centrifugal forces [27], and adverse axial pressure gradient [10]. In Figs. 4 and 5 the contours of the centrifugal force, the radial pressure-gradient force, and the resultant of the two forces are also presented. These force and pressure-gradient contours will be used in later sections to explain the effects of Reynolds number, aspect ratio, and cylinder-to-disk ratio on vortex breakdown.

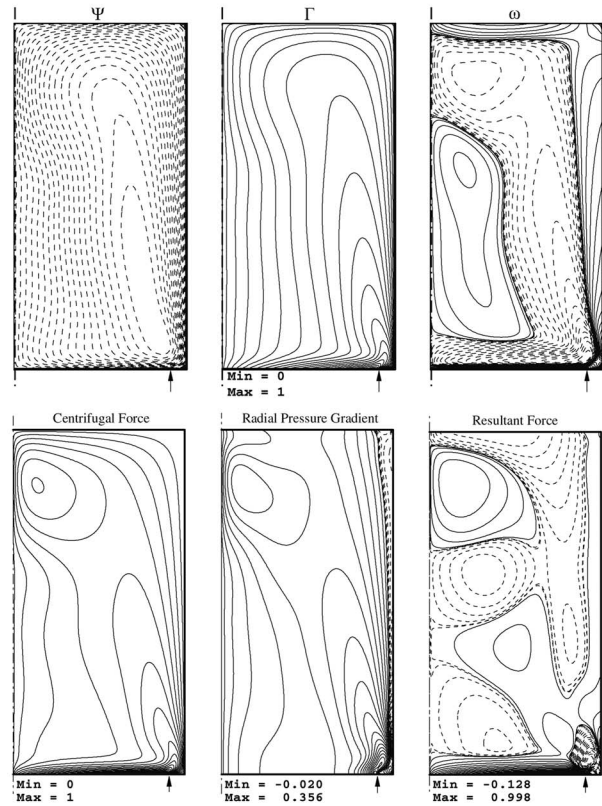
Ideally, to show the sequence of events leading to vortex breakdown, the force and pressure-gradient contours should be presented before the onset of vortex breakdown. This sequence of events has been explained by Lopez [2] in terms of angular momentum. In the present study, the sequence of events has been computed in terms of force and pressure-gradient contours before and after vortex breakdown occurred, which shows more clearly the differences in the contours.

The angular momentum is nearly constant along a streamline [2] (also see present Fig. 4 under the label Γ). Thus the azimuthal velocity grows with the decrease in r when the swirling flow converges toward the axis along the top wall. Physically, because of the negative value of radial velocity (from the sidewall toward the axis), the Coriolis force acts in the direction of rotation so as to increase the azimuthal velocity [27]. This increases the centrifugal force and the resultant force has a positive region near the top axial region (see Fig. 4 under the label “Resultant Force”), which makes the angular momentum contours and streamlines deviate away from the axis there [3,27] (also see present Fig. 4 under the label Γ).

Subsequent to the divergence, the flow turning toward the axis has been explained by Brown and Lopez [3]. On the diverging stream surface, the centrifugal force v^2/r is decreased due to the conservation of angular momentum. Also the axial and azimuthal velocity components are reduced due to the divergence, leading to an increase in pressure and reduction in radial pressure gradient. However, the centrifugal force reduces more than the radial pressure gradient. Thus the flow has a turn toward the axis. This explains the waviness in the stream surface. When the amplitude of the wave increases and the wavelength decreases, the associated axial deceleration causes the flow to stagnate below the crest of the wave. A near spherical region of recirculating fluid is formed, termed a vortex-breakdown bubble.

The role of axial pressure gradient has been discussed by Husain et al. [10]. The flow is azimuthal velocity dominant and the pressure distribution is governed by the cyclostrophic balance. On the diverging stream surface, the azimuthal velocity is decreased and thus the pressure along the axis increases. This creates an

i) $Re=1200$



ii) $Re = 1500$

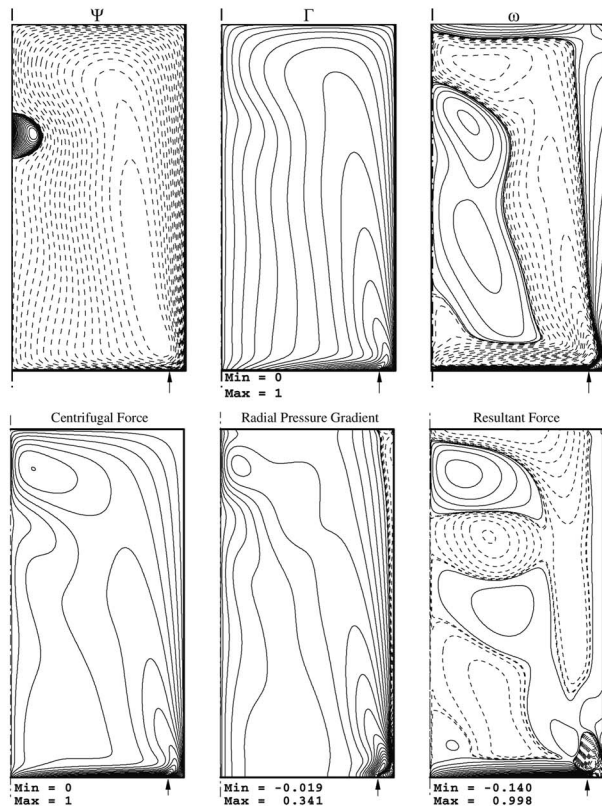
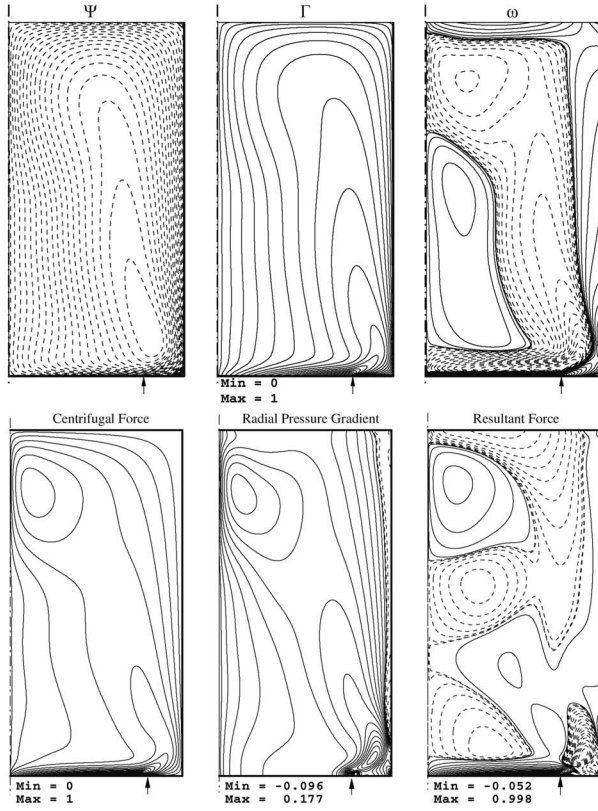
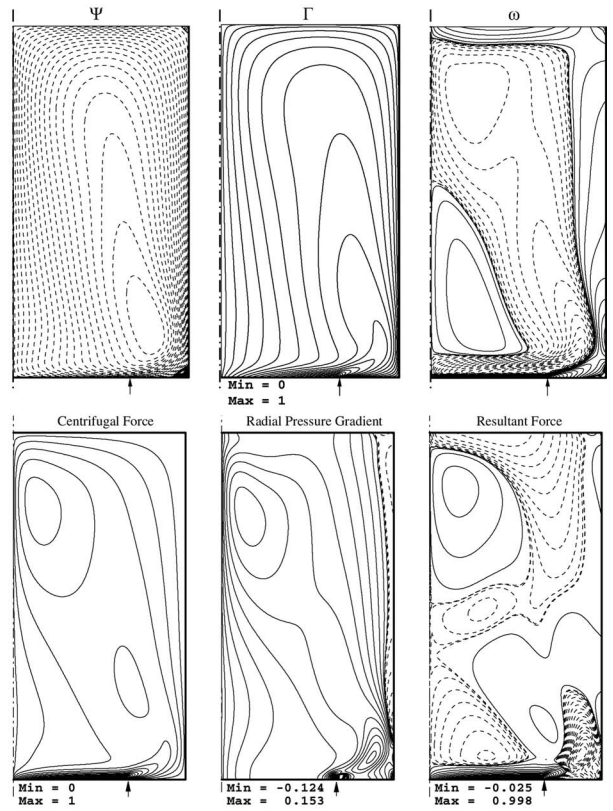


Fig. 4 (Continued).

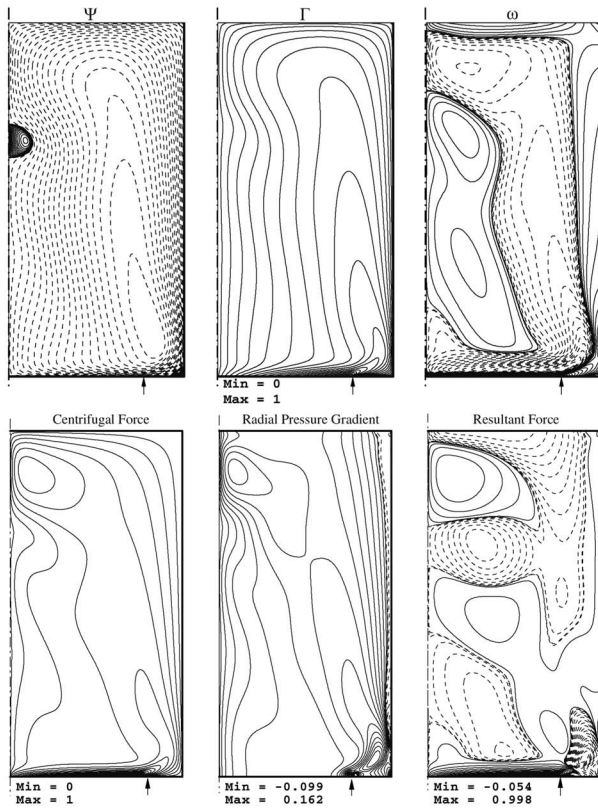
i) $Re=1200$



i) $Re=1200$



ii) $Re = 1500$



ii) $Re = 1500$

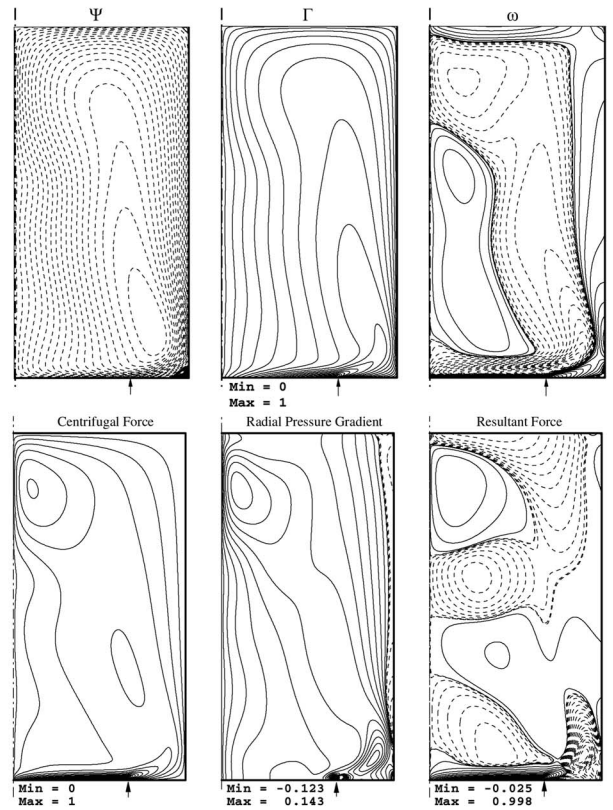
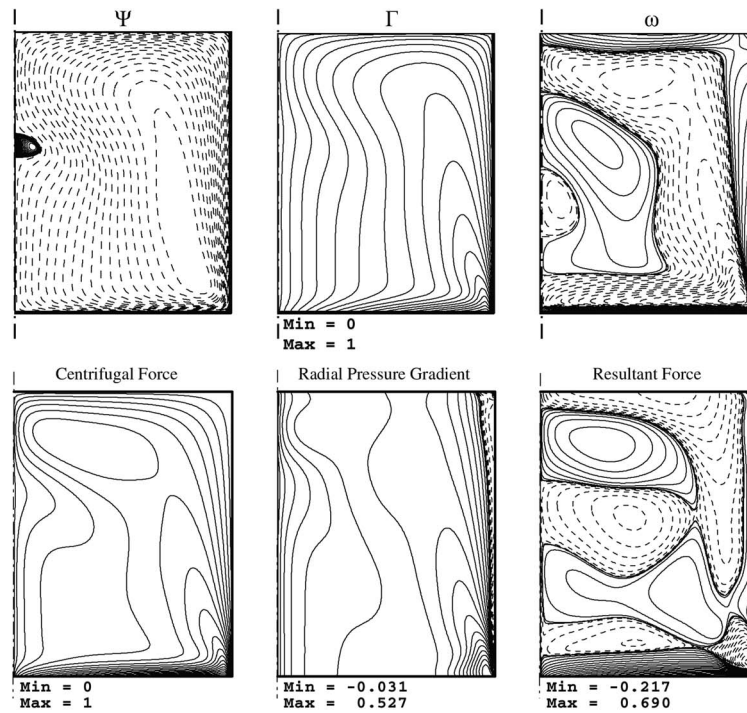


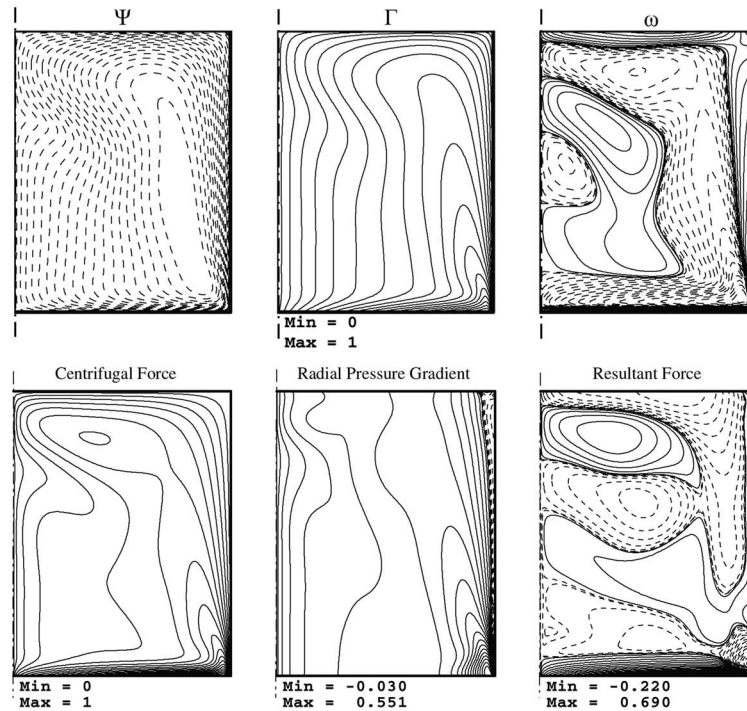
Fig. 4 (Continued).

Fig. 4 (Continued).

i) $Re=1200$



ii) $Re = 1500$



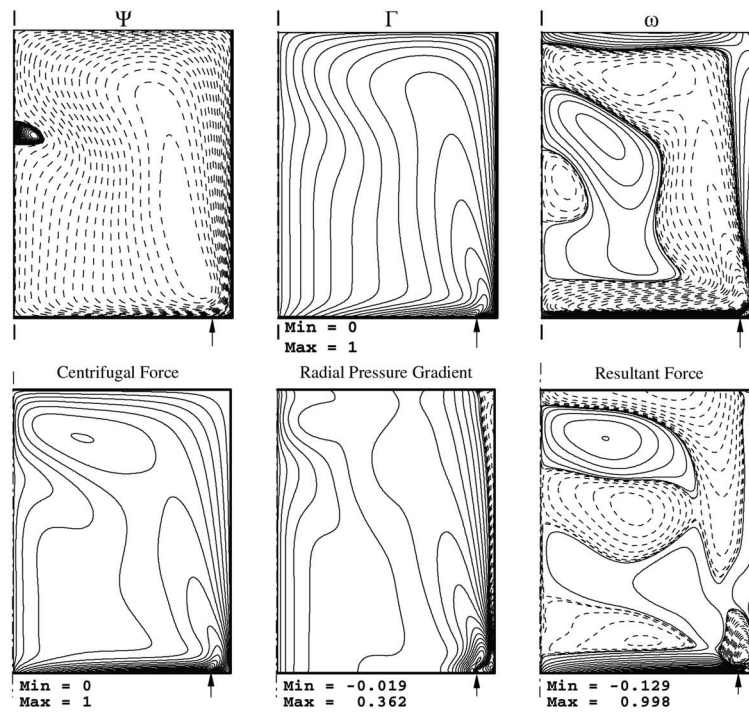
(a) $R/r_d = 1$

Fig. 5 Contours of streamline Ψ , angular momentum Γ , and azimuthal vorticity ω in the meridional plane for the aspect ratio $H/R=1.3$; (i) $Re=1200$ and (ii) $Re=1500$; (a) $R/r_d=1.0$, (b) $R/r_d=1.1$, (c) $R/r_d=1.3$, and (d) $R/r_d=1.5$; contour levels C_i are nonuniformly spaced, with 20 positive levels $C_i = \text{Max}(\text{variable}) \times (i/20)^3$ and 20 negative levels $C_i = \text{Min}(\text{variable}) \times (i/20)^3$

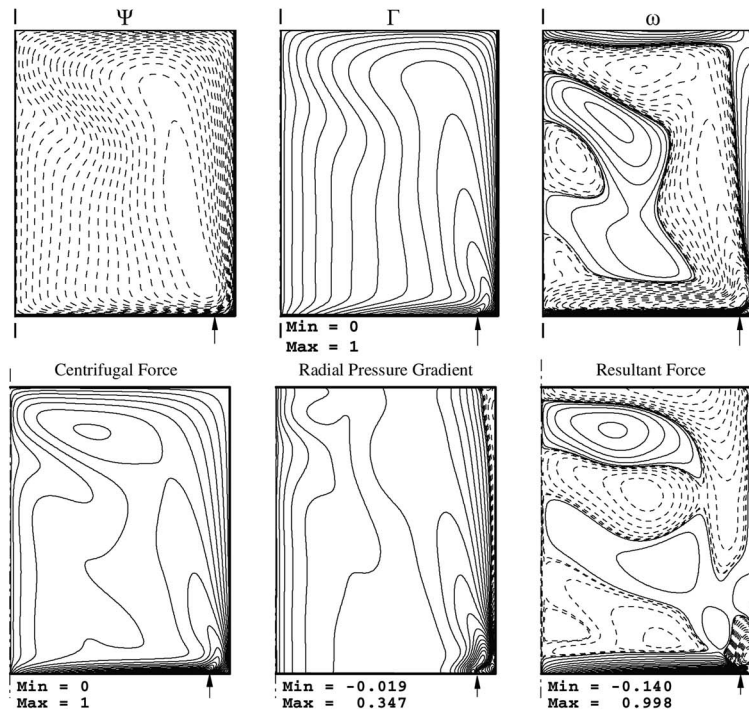
adverse pressure gradient along the axis that acts to obstruct the meridional motion of the flow along the axis. When the adverse pressure gradient becomes sufficiently large, it causes vortex breakdown.

Effect of Reynolds Number. The effect of Re on the boundary of vortex breakdown is summarized in Fig. 3(b). For the whole bottom-wall rotation at an aspect ratio greater than 1.2, there is no vortex-breakdown bubble at a Re lower than 1000. As the Rey-

i) $Re=1200$



ii) $Re = 1500$



(b)

$R/r_d = 1.1$

Fig. 5 (Continued).

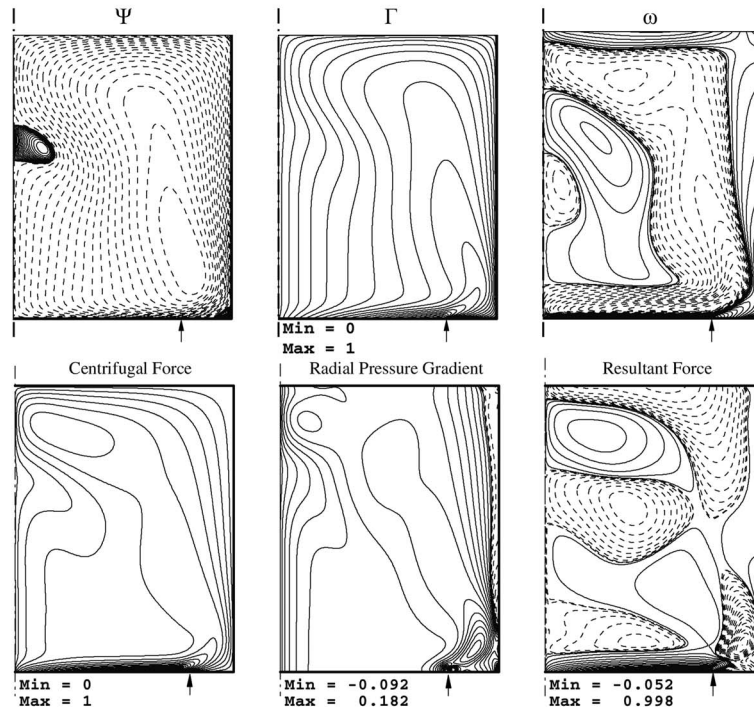
nolds number increases, there is a transition to vortex-breakdown bubble (at the right boundary curve). The vortex-breakdown bubble grows larger with Re . With a further increase in Re , the vortex-breakdown bubble becomes smaller and then disappears (at the left boundary curves).

The contours of streamlines, angular momentum, and vorticity are shown in Figs. 4(a)(i) $Re=1200$ and 4(a)(ii) $Re=1500$ for the

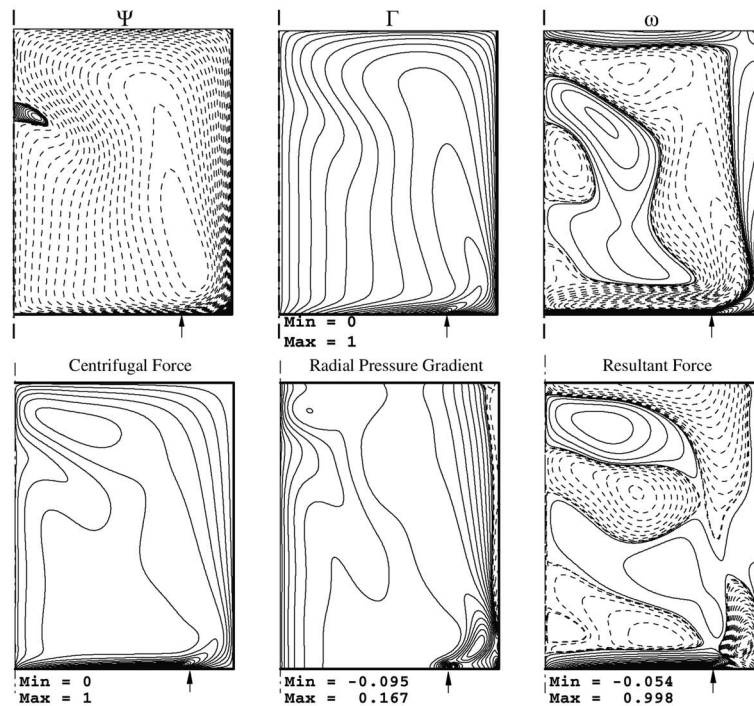
case of the whole bottom-wall rotation $R/r_d=1$. It shows the change to vortex breakdown as Re is increased to 1500, in accordance with the vortex boundary plot of Fig. 3(b), for an aspect ratio of 2.

At higher Re , a greater proportion of the fluid's angular momentum is advected to the upper core region (near the top wall at the axial region), which may be seen by comparing Figs. 4(a)(ii)

i) $Re=1200$



ii) $Re = 1500$



(c)

$R/r_d = 1.3$

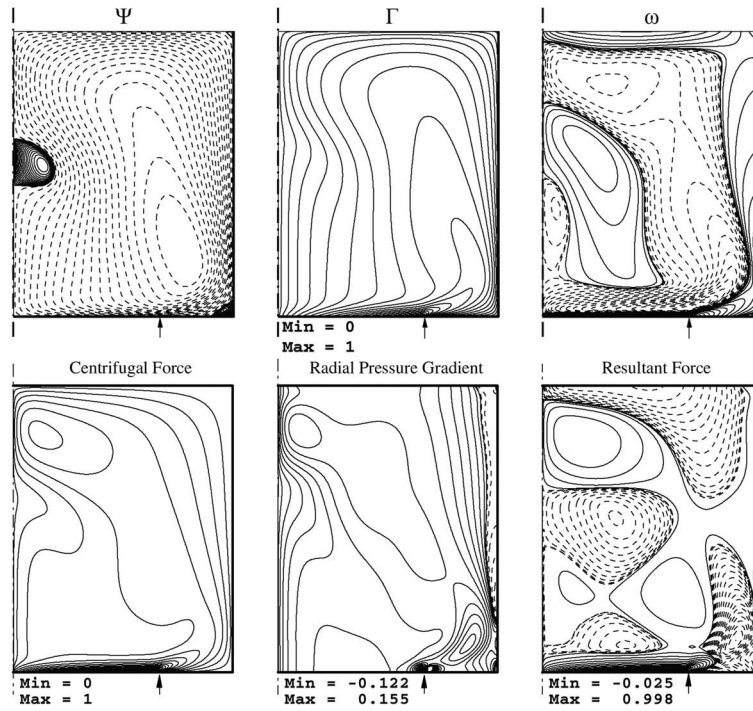
Fig. 5 (Continued).

with 4(a)(i); this gives a higher centrifugal force due to the convection of azimuthal velocity and action of the Coriolis force [27]. The imbalance of centrifugal force and radial pressure gradient (see the resultant force contour in Fig. 4(a)(i) and 4(a)(ii)) generates a weak centrifugal wave in the fluid as it moves downward away from the top wall near the axial region. Thus the contours of angular momentum near the upper axial region show waviness as

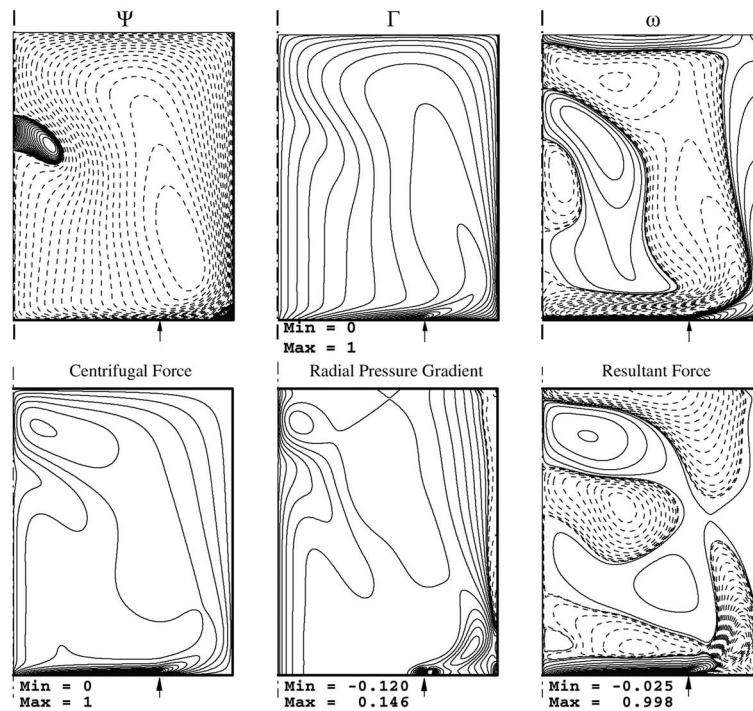
explained by Lopez [2] (see Fig. 4(a)(ii) under the label Γ). As explained by Husain et al. [10], this wavy motion generates an adverse pressure gradient along the axis to cause vortex breakdown. This mechanism explains the transition to vortex breakdown and the growth in bubble size.

However, at a smaller aspect ratio of 1.3, the opposite trend occurs. With an increase in Re from 1200 to 1500, vortex break-

i) $Re=1200$



ii) $Re = 1500$



(d)

$R/r_d = 1.5$

Fig. 5 (Continued).

down disappears (Figs. 5(a)(i) and 5(a)(ii)). Although this phenomenon is known, there has been little explanation for it. At a higher Re , similar to the case of the high aspect ratio of 2, a greater proportion of the fluid's angular momentum is advected to the upper core region (near the top wall at the axial region). The higher angular momentum gives steeper gradient in its contours near the top surface, due to the small aspect ratio. Thus there is

greater loss of angular momentum, due to viscous losses at the top surface, hence smaller centrifugal force near the upper core region. The resultant force is thus less at a higher Re (see resultant force contours in Figs. 5(a)(i) and 5(a)(ii)). The centrifugal wave is not strong enough to generate vortex breakdown.

The region of positive azimuthal vorticity near the axial region, coinciding roughly with the wavy streamlines, is extended notice-

ably at higher Re, as seen by comparing ω plots of Figs. 4(a)(i) and 4(a)(ii). The development of a recirculation bubble is a result of the positive azimuthal vorticity, as explained by Brown and Lopez [3] (negative vorticity in their paper) through the stretching and tilting of vortex lines.

Effect of Aspect Ratio. The effect of the aspect ratio on the boundary of vortex breakdown is shown in Fig. 3(b). For higher aspect ratio, the vortex-breakdown bubble disappears as the aspect ratio increases beyond the right boundary curve; for example, there is no vortex-breakdown bubble at $H/R=2$ for $Re=1200$. To examine the aspect ratio effects, the streamlines, angular momentum, and azimuthal vorticity are shown in Figs. 5(a)(i) and 4(a)(i) for $H/R=1.3$ and $H/R=2$, respectively, at $Re=1200$. The streamline contours show that there is a change to no vortex breakdown as the aspect ratio is increased from $H/R=1.3$ to 2.0. At $H/R=2$, the angular momentum is lower at the upper core region (near the top wall at the axial region).

The angular momentum of the fluid is decreased by viscous dissipation along the cylinder sidewall [5]. Hence, for a chamber with a bigger aspect ratio, the angular momentum near the top axial region is less than that for a smaller aspect ratio. Thus, the centrifugal force is smaller, which leads to the resultant force being smaller, and the centrifugal wave is not big enough to generate vortex breakdown (compare resultant force contours in Figs. 4(a)(i) and 5(a)(i)).

However, for a smaller aspect ratio, the vortex-breakdown bubble disappears as the aspect ratio decreases to values before the left boundary curve; for example, there is no vortex-breakdown bubble at $H/R=1.3$ for $Re=1500$. The effects of the aspect ratio on the streamlines, angular momentum, and azimuthal vorticity are shown in Figs. 5(a)(ii) and 4(a)(ii) for $H/R=1.3$ and $H/R=2$, respectively, at $Re=1500$. The streamline contours show that there is a change to no vortex breakdown as the aspect ratio is reduced to 1.3, as seen in Fig. 4(a)(ii). At $H/R=1.3$, the angular momentum is lower at the upper core region (near the top wall at the axial region).

At a smaller aspect ratio, there is a high viscous loss near the top lid region, as the angular momentum gradients are steeper due to the chamber being more confined. Reducing the aspect ratio further will increase the viscous effect of the top lid, which leads to a decrease in the angular momentum, hence decreases in the centrifugal force and the resultant force (see centrifugal force and resultant force contours in Figs. 4(a)(ii) and 5(a)(ii)). Thus, vortex breakdown disappears with the reduction in the aspect ratio (compare Figs. 4(a)(ii) and 5(a)(ii)).

To summarize, there are two main mechanisms that explain the effect of aspect ratio. When the aspect ratio is high, the losses are mainly from the sidewall and increasing the aspect ratio leads to the disappearance of vortex breakdown. However, when the aspect ratio is small, the losses are mainly from the top lid and reducing the aspect ratio will lead to the disappearance of vortex breakdown.

Effect of Cylinder-to-Disk Ratio. In Figs. 4(b)–4(d) and Figs. 5(b)–5(d) the diagrams of streamline Ψ , angular momentum Γ , and azimuthal vorticity ω for the case of the partial bottom-wall rotation are shown. The arrow below the bottom-wall indicates the radius of the rotating wall. As compared with the whole bottom-wall rotation, the partial bottom-wall rotation has some effects on the onset and size of the vortex-breakdown bubble, which are consistent with those of the boundary curves in Fig. 3(b).

The contours of streamlines show that the corner vortex becomes obvious for the smaller rotating disk (see Figs. 4(d) and 5(d)) as the fluid is unable to turn a sharp corner. In a previous study by Piva and Meiburg [12], the corner vortex extends to the top surface at a large R/r_d greater than 2.3.

The distribution of the angular momentum is of particular interest in the present study. The fluid obtains its angular momentum in the Ekman layer on the rotating disk and loses angular momen-

tum as it moves along the stationary bottom- and sidewalls. The momentum contours clearly show that angular momentum is being dissipated when the fluid leaves the rotating disk (see Fig. 4(d) below label Γ) and moves along the stationary bottom-wall.

The azimuthal vorticity contours show some differences as compared with those of the whole bottom-wall rotation. The positive azimuthal vorticity near the sidewall starts from the edge of the rotating disk (Fig. 4(d) for partial bottom-wall rotation) instead of from the corner (Fig. 4(a) for whole bottom-wall rotation), which is consistent with the development of an additional boundary layer along the stationary bottom-wall.

Note that when there is a vortex-breakdown bubble, the angular momentum shows waviness (for example, compare Γ plots of Figs. 4(b)(i) and 4(b)(ii)). Also, the positive azimuthal vorticity has a larger region (compare ω plots of Figs. 4(b)(i) and 4(b)(ii)). These two features are consistent with the results of Lopez [2].

For the right boundary curve in Fig. 3(b), it shifts rightward when R/r_d is increased from 1.0 to 1.1. Then it shifts leftward when R/r_d is further increased from 1.1 to 1.5. There seems to be two opposing influences of R/r_d ; thus its resultant effect depends on which one is dominant.

The opposing influences of R/r_d may be interpreted by using the physical mechanism of vortex breakdown for swirling flow, as explained by Brown and Lopez [3], Gelfgat et al. [27], and Husain et al. [10]. The central core flow diverges if the centrifugal force exceeds the radial pressure gradient. The initial increase in R/r_d from 1.0 to 1.1 has the effect of increasing the centrifugal force near the upper core region (see centrifugal force contours in Figs. 4(a) and 4(b)) because the fluid is rotated through a smaller rotating wall, which gives more swirling motion away from the sidewall where there is viscous loss of angular momentum. The increased centrifugal force causes an imbalance with the pressure gradient (see resultant force contours in Figs. 4(a) and 4(b)), which leads to bigger vortex-breakdown bubble. Thus the physical aspect ratio has to be larger for vortex breakdown to cease; that is, the effective aspect ratio has become smaller.

The increase in R/r_d from 1.1 to 1.5 has the effect of causing loss of angular momentum because the stationary part of the bottom-wall is bigger. The centrifugal force at the axial region near the top wall is reduced (see centrifugal force contours in Figs. 4(c) and 4(d)), which leads to cessation of vortex breakdown. As compared with the whole bottom-wall rotation, the cylinder-to-disk ratio of 1.5 has no vortex breakdown at a smaller aspect ratio. That is, the effective aspect ratio seems to be larger; thus the physical aspect ratio can be smaller for vortex breakdown to cease.

Figure 3(b) (left boundary curve) shows that with a smaller rotating disk, the boundary-curve shifts rightward when the cylinder-to-disk ratio is increased from 1.0 to 1.1. Then it shifts leftward when the cylinder-to-disk ratio is further increased from 1.1 to 1.5. Again, there seems to be two opposing influences of R/r_d ; thus its resultant effect depends on which one is dominant.

The initial increase in R/r_d from 1.0 to 1.1 has the effect of reducing the centrifugal force at the axial core region near the top (see centrifugal force contours in Figs. 5(a) and 5(b)), because the fluid is rotated through a smaller rotating wall, which gives more swirling motion at the top region. The viscous loss of angular momentum there is more due to the steeper gradient. The reduced centrifugal force leads to no vortex-breakdown bubble.

The increase in R/r_d from 1.1 to 1.5 has the effect of reducing viscous loss of angular momentum from the top surface as the main swirling motion is nearer to the axis. The centrifugal force at the axial region near the top wall is higher, which leads to vortex breakdown (see centrifugal force contours in Figs. 5(c) and 5(d)). As compared with the whole bottom-wall rotation, the cylinder-to-disk ratio R/r_d of 1.5 has vortex breakdown at a smaller aspect ratio.

There is a critical aspect ratio H/R below which vortex breakdown never occurs at any Re (see left boundary curves in Fig.

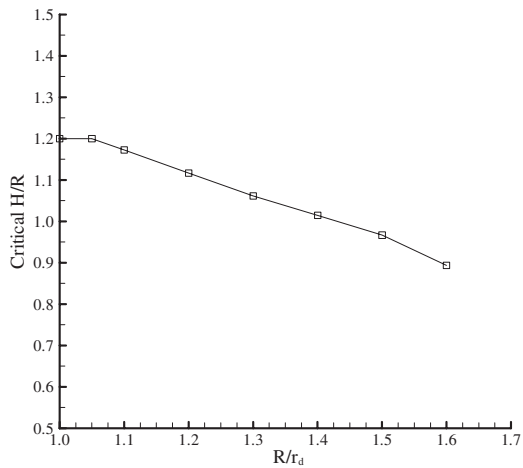


Fig. 6 Critical aspect ratio for onset of vortex breakdown at various cylinder-to-disk ratio

3(b)). It is seen that the critical aspect ratio for the partially rotating bottom-wall is less than that for the whole bottom-wall rotation; the critical value is 0.97 for $R/r_d=1.5$. The critical value for different R/r_d is summarized in Fig. 6, which decreases approximately linearly with an increase in R/r_d . The additional stationary bottom-wall acts like a sidewall, which seems to increase the aspect ratio; thus vortex breakdown may occur at a smaller aspect ratio.

Concluding Remarks

The flow in an enclosed cylinder with a partially rotating bottom-wall may be of interest to a cell-culture bioreactor stirred by a magnetic rotating-rod at the bottom, in which the mixing parameter and shear stress may be influenced by the vortex-breakdown phenomena. This study presents nondimensional results of the boundary curves for the first onset of vortex breakdown. It is concluded that the aspect ratio should be based on the cylinder radius. An additional parameter is the cylinder-to-disk ratio. The present definition of Re is similar to that of Piva and Meiburg [12], whose flow chamber also has a partially rotating bottom-wall but with a free surface. However, their aspect ratio is differently defined as H/r_d because their cylinder-to-disk ratio R/r_d is varied to a value much larger than that of the present study. It is shown that correlating the results in terms of these parameters is more meaningful.

The critical aspect ratio to have vortex breakdown is found to be reduced to about 1, as compared with the whole bottom-wall rotation in which the critical aspect ratio is 1.2. The minimum Re for vortex breakdown is reduced to 850 as compared with 1000 for the whole bottom-wall rotation. At the same Re , R/r_d influences the vortex-breakdown boundary curve by either increasing or reducing the effective aspect ratio. Thus, the physical aspect ratio for onset or cessation of vortex breakdown is changed as compared with that of whole bottom-wall rotation. The influence may be interpreted from the action of the Coriolis force [27], the balance between the radial pressure-gradient and the centrifugal force [3], and the formation of adverse axial pressure gradient [10]. The results of the contours of the streamlines, angular momentum, and azimuthal vorticity are presented; these detailed contours are consistent with the findings of Lopez [2] that vortex

breakdown occurs when, near the axial region, the angular momentum contours are wavy and the extent of positive azimuthal vorticity is larger.

Acknowledgment

The authors would like to thank Professor M. P. Escudier for his kind help in providing the experimental data on the stability boundaries for vortex breakdown.

References

- [1] Escudier, M. P., 1984, "Observations of the Flow Produced in a Cylindrical Container by a Rotating Endwall," *Exp. Fluids*, **2**, pp. 189–194.
- [2] Lopez, J. M., 1990, "Axisymmetric Vortex Breakdown, Part 1: Confined Swirling Flow," *J. Fluid Mech.*, **221**, pp. 533–552.
- [3] Brown, G. L., and Lopez, J. M., 1990, "Axisymmetric Vortex Breakdown, Part 2: Physical Mechanisms," *J. Fluid Mech.*, **221**, pp. 553–576.
- [4] Spohn, A., Mory, M., and Hopfinger, E. J., 1989, "Observations of Vortex Breakdown in an Open Cylindrical Container by a Rotating Bottom," *Exp. Fluids*, **14**, pp. 70–77.
- [5] Spohn, A., Mory, M., and Hopfinger, E. J., 1998, "Experiments on Vortex Breakdown in a Confined Flow Generated by a Rotating Disc," *J. Fluid Mech.*, **370**, pp. 73–99.
- [6] Valentine, D. T., and Jahnke, C. C., 1994, "Flows Induced in a Cylinder With Both End Walls Rotating," *Phys. Fluids*, **6**, pp. 2702–2710.
- [7] Lopez, J. M., 1995, "Unsteady Swirling Flow in an Enclosed Cylinder With Reflectional Symmetry," *Phys. Fluids*, **7**, pp. 2700–2714.
- [8] Mullin, T., Tavener, S. J., and Cliffe, K. A., 1998, "On the Creation of Stagnation Points in a Rotating Flow," *ASME J. Fluids Eng.*, **120**, pp. 685–689.
- [9] Mullin, T., Kobine, J. J., Tavener, S. J., and Cliffe, K. A., 2000, "On the Creation of Stagnation Points Near Straight and Sloped Walls," *Phys. Fluids*, **12**, pp. 425–431.
- [10] Husain, H. S., Shtern, V., and Hussain, F., 2003, "Control of Vortex Breakdown by Addition of Near-Axial Swirl," *Phys. Fluids*, **15**, pp. 271–279.
- [11] Yu, P., Lee, T. S., Zeng, Y., and Low, H. T., 2006, "Effects of Conical Lids on Vortex Breakdown in an Enclosed Cylindrical Chamber," *Phys. Fluids*, **18**, p. 117101.
- [12] Piva, M., and Meiburg, E., 2005, "Steady Axisymmetric Flow in an Open Cylindrical With a Partially Rotating Bottom Wall," *Phys. Fluids*, **17**, p. 063603.
- [13] Yu, P., Lee, T. S., Zeng, Y., and Low, H. T., 2007, "Characterization of Flow Behavior in an Enclosed Cylinder With a Partially Rotating End-Wall," *Phys. Fluids*, **19**, p. 057104.
- [14] Yu, P., Lee, T. S., Zeng, Y., and Low, H. T., 2005, "Fluid Dynamics of a Micro-Bioreactor for Tissue Engineering," *Fluid Dyn. Mater. Process.*, **1**, pp. 235–246.
- [15] Kostov, Y., Harms, P., Randers-Eichhorn, L., and Rao, G., 2001, "Low-Cost Micro-Bioreactor for High-Throughput Bioprocessing," *Biotechnol. Bioeng.*, **72**, pp. 346–352.
- [16] Thouas, G. A., Sheridan, J., and Hourigan, K., 2007, "A Bioreactor Model of Mouse Tumor Progression," *J. Biomed. Biotechnol.*, **2007**, p. 32754.
- [17] Dusting, J., Sheridan, J., and Hourigan, K., 2006, "A Fluid Dynamic Approach to Bioreactor Design for Cell and Tissue Culture," *Biotechnol. Bioeng.*, **94**, pp. 1197–1208.
- [18] Yu, P., Lee, T. S., Zeng, Y., and Low, H. T., 2005, "Effect of Vortex Breakdown on Mass Transfer in a Cell Culture Bioreactor," *Mod. Phys. Lett. B*, **19**, pp. 1543–1546.
- [19] Mununga, L., Hourigan, K., Thompson, M. C., and Leweke, T., 2004, "Confined Flow Vortex Breakdown Control Using a Small Rotating Disk," *Phys. Fluids*, **16**, pp. 4750–4753.
- [20] Kumar, S., Wittmann, C., and Heinzle, E., 2004, "Minibioreactors," *Biotechnol. Lett.*, **26**, pp. 1–10.
- [21] Marques, F., Lopez, J. M., and Shen, J., 2002, "Mode Interactions in an Enclosed Swirling Flow: A Double Hopf Bifurcation Between Azimuthal Wave-numbers 0 and 2," *J. Fluid Mech.*, **455**, pp. 263–281.
- [22] Gelfgat, A. Yu., Bar-Yoseph, P. Z., and Solan, A., 2001, "Three-Dimensional Instability of Axisymmetric Flow in a Rotating Lid-Cylinder Enclosure," *J. Fluid Mech.*, **438**, pp. 363–377.
- [23] Blackburn, H. M., and Lopez, J. M., 2000, "Symmetry Breaking of the Flow in a Cylinder Driven by a Rotating Endwall," *Phys. Fluids*, **12**, pp. 2698–2701.
- [24] Blackburn, H. M., and Lopez, J. M., 2002, "Modulated Rotating Waves in an Enclosed Swirling Flow," *J. Fluid Mech.*, **465**, pp. 33–58.
- [25] Marques, F., and Lopez, J. M., 2001, "Precessing Vortex Breakdown Mode in an Enclosed Cylinder Flow," *Phys. Fluids*, **13**, pp. 1679–1682.
- [26] Lopez, J. M., 2006, "Rotating and Modulated Rotating Waves in Transitions of an Enclosed Swirling Flow," *J. Fluid Mech.*, **553**, pp. 323–346.
- [27] Gelfgat, A. Yu., Bar-Yoseph, P. Z., and Solan, A., 1996, "Stability of Confined Swirling Flow With and Without Vortex Breakdown," *J. Fluid Mech.*, **311**, pp. 1–36.

The Effect of Impeller Cutback on the Fluid-Dynamic Pulsations and Load at the Blade-Passing Frequency in a Centrifugal Pump

Raúl Barrio
Eduardo Blanco

Jorge Parrondo
e-mail: parrondo@uniovi.es

José González

Área de Mecánica de Fluidos,
Universidad de Oviedo,
Campus de Viesques,
33271 Gijón, Spain

Joaquín Fernández
Escuela de Ingenierías Industriales,
Universidad de Extremadura,
Avenida de Elvas s/n,
06071 Badajoz, Spain

A study is presented on the fluid-dynamic pulsations and the corresponding dynamic forces generated in a centrifugal pump with single suction and vaneless volute due to blade-volute interaction. Four impellers with different outlet diameters, obtained from progressive cutbacks (trimmings) of the greatest one, were successively considered in the test pump, so that the radial gap between the impeller and the volute ranged from 8.8% to 23.2% of the impeller radius. The study was based on the numerical computation of the unsteady flow through the machine for a number of flow rates by means of the FLUENT code, solving the 3D unsteady Reynolds-averaged Navier–Stokes equations. Additionally, an experimental series of tests was conducted for the pump with one of the impellers, in order to obtain pressure fluctuation data along the volute front wall that allowed contrasting the numerical predictions. The data collected from the numerical computations were used to estimate the dynamic radial forces and torque at the blade-passing frequency, as a function of flow rate and blade-tongue radial gap. As expected, for a given impeller diameter, the dynamic load increases for off-design conditions, especially for the low range of flow rates, whereas the progressive reduction of the impeller-tongue gap brings about corresponding increments in dynamic load. In particular, varying the blade-tongue gap within the limits of this study resulted in multiplying the maximum magnitude of the blade-passing frequency radial force by a factor of about 4 for low flow rates (i.e., below the nominal flow rate) and 3 for high flow rates. [DOI: 10.1115/1.2969273]

Keywords: centrifugal pump, volute casing, blade-tongue interaction, unsteady flow simulation, pressure fluctuation measurements, blade-passing frequency load, effect of impeller-tongue radial gap

Introduction

The flow through fluid machinery is exposed to several mechanisms that create unsteadiness and are responsible for dynamic load on the machine and for noise generation. In the case of conventional centrifugal pumps with volute casing operating under normal conditions, a relevant unsteady phenomenon is the fluid-dynamic rotor-stator interaction and, in particular, the periodic interaction between the impeller blades and the volute tongue [1,2]. This excitation arises from the nonuniform profile of the relative flow exiting the impeller, with jet-wake patterns, which is perceived as a fluctuating flow at the volute [3]. The excitation is especially intense where the distance between the impeller and the volute is small, that is, at the tongue region of the volute. The corresponding unsteady load is associated with the blade-passage frequency and its harmonics.

Very frequently, the radial gap between the impeller and the tongue is altered in commercial pumps because manufacturers commonly use the cutting back of the impellers (trimming) to be mounted in a specific volute as a means to augment the range of performance characteristics while precluding excessive production costs. This brings about the modification of the flow velocity and pressure distribution along the volute, together with a change in efficiency for moderate impeller cutbacks [4,5].

For a given pump, the fluid-dynamic excitation at the blade-

passing frequency is very dependent on the point of operation: The perturbations are minima for flow rates around the best efficiency point and increase for both low and high flow rates [6–8]. Besides, the magnitude of the excitation is dependent on the geometry of the machine at the tongue region, including the tongue shape, the number of impeller blades, the orientation of the trailing edge of the blades, and, certainly, the radial gap between the impeller and the volute tongue [3].

Particularly during the past two decades, several studies have been conducted on the blade-tongue interaction in centrifugal pumps. Hasegawa et al. [6] studied the dynamic forces on the impeller blades of a centrifugal pump with vaneless volute for several flow rates, by means of a numerous set of pressure sensors mounted inside the impeller and a slip ring to extract the pressure signals. They concluded that the resultant force exerted on the blades was affected strongly by the passing of the trailing edge in front of the volute tongue, especially for off-design conditions. They also studied the effect of reducing the number of impeller blades from 7 to 3 [9] and concluded that, though there was a little difference in the fluctuating force exerted on each separate blade, their summation on the whole impeller was larger for the three blade impeller. Kaupert and Staubli [7] conducted a similar study on a high specific speed centrifugal pump with double volute. They analyzed the transmission of the disturbances induced by the two tongues through the instrumented channel of the impeller, observing an increasing perturbation magnitude when progressively deviating from the nominal flow rate.

Dong et al. [10] tested a centrifugal pump operating 35% above the design flow rate, which could be equipped with several volutes having tongue gaps ranging from 7% to 28% of the impeller ra-

Contributed by the Fluids Engineering Division of ASME for publication in the JOURNAL OF FLUIDS ENGINEERING. Manuscript received May 8, 2007; final manuscript received June 11, 2008; published online September 22, 2008. Assoc. Editor: Yu-Tai Lee. Paper presented at the 2005 ASME Fluids Engineering Division Summer Meeting and Exhibition (FEDSM2005), Houston, TX, June 19–23, 2005.

dius. The analysis of detailed particle image velocimetry (PIV) measurements [11], combined with pressure and noise data for each case, shown a progressive reduction in excitation levels when increasing the blade-to-tongue gap up to 20% of the impeller radius.

Morgenroth and Weaver [12] investigated the transmission to the ducting system of the blade-passing frequency pressure fluctuations from a pump with different tongue tips, so that the radius of the tip could be varied while maintaining a constant blade-to-tongue gap of 5.8% of the impeller radius. They found that rounding the tongue tip resulted in a reduction of the emitted noise.

Parrondo et al. [8] measured the pressure fluctuations at the blade-passing frequency along the volute of a pump with a specific speed of 0.48 for a wide range of flow rates (from 0% to 160% of the nominal flow rate) and two impellers with different diameters. They observed that reducing the blade-to-tongue gap from 15.8% to 10% of the impeller radius led to an increase in the maximum pressure amplitude at off-design conditions of about 50%.

The dynamic blade-tongue load may lead to excessive vibration and noise levels under certain conditions and, therefore, there is interest in the estimation of this fluctuating load at the design stage of the machines. This purpose can be achieved by means of the numerical calculation of the unsteady flow through the pumps, with an adequate computational fluid dynamics (CFD) code. Such unsteady numerical calculations have been the subject of several studies on different types of pumps and with different methodologies, ranging from inviscid models [13,14] to large eddy simulation (LES) flow simulations [15] and including both 2D [16] and 3D models [17–21]. González et al. [22] used a CFD code to solve the 3D unsteady Reynolds-averaged Navier–Stokes (URANS) flow equations and compute the pressure fluctuations at f_{BP} in a centrifugal pump with two different impellers. Then they used the predictions of pressure fluctuations along the front side of the volute to estimate the dynamic radial forces on the impeller and obtained a satisfactory agreement when comparing them with the forces resulting from the pressure fluctuation measurements.

This paper presents a systematic extension of the methodology outlined in Ref. [22] to estimate the total fluid-dynamic load induced in a centrifugal pump with a single vaneless volute, equipped with four impellers of different outlet diameters: 0.190, 0.200, 0.210, and 0.215 m. These four impellers, obtained from progressive trimmings from a primary impeller, permitted to vary the impeller-tongue gap from 23.2% to 8.8% of the impeller radius. The unsteady 3D Reynolds-averaged Navier–Stokes equations were solved by means of the commercial code FLUENT for each of the four impellers operating with a number of flow rates. Additionally, experiments were conducted in laboratory for the same pump, equipped with the 0.210 m impeller, to measure the pressure fluctuations along the volute for different flow rates, in order to contrast the predictions from computations. The numerical results were used to quantify the dynamic radial forces on the impellers at the blade-passing frequency, as well as the fluctuating torque, showing the effects of varying the impeller diameter.

Experimental Measurements

The pump available for this study was a single suction and single volute casing centrifugal pump, with an impeller of 0.210 m in diameter and seven blades with logarithmic profile and a nondimensional specific speed $\omega_s=0.47$. The main features of the pump are summarized in Table 1. Figure 1 shows a scheme of the pump, with a detail of the tongue region and the location along the volute of the orifices used to capture dynamic pressure signals.

The pump was tested at a constant speed of 1620 ± 1 rpm in the laboratory facility described in Ref. [8], complemented with a magnetic flow meter to measure the flow rate and piezoresistive transducers for pressure measurement at the pump inlet and outlet. Additionally, for the dynamic measurements, the pump was instrumented with Kistler 701A piezoelectric pressure transducers

Table 1 Main characteristics of the experimental test pump

| | |
|---|--------|
| Impeller outlet diameter, d_2 (m) | 0.210 |
| Impeller outlet width, b_2 (m) | 0.016 |
| Radius at tongue tip, r_3 (m) | 0.117 |
| Impeller-tongue radial gap, G | 0.114 |
| Number of blades, z | 7 |
| Outlet blade angle relative to tangential direction (deg) | 29 |
| Blade lean at trailing edge (pressure side) (deg) | 10 |
| Blade lean at trailing edge (suction side) (deg) | 29 |
| Mean blade thickness at trailing edge (m) | 0.007 |
| Rotating speed, ω (rad s ⁻¹) | 169.65 |
| Blade-passing frequency, f_{BP} (Hz) | 189.0 |
| Specific speed, ω_s | 0.47 |

mounted on the front side of the volute at 36 measurement positions. These transducers were located every 10 deg around the impeller at a radial distance of 2.5 mm from the impeller outlet (Figs. 1 and 2). Pressure signals from the transducers were amplified, digitized, and fast Fourier transform (FFT) processed to obtain the spectral distributions of the pressure (amplitude and

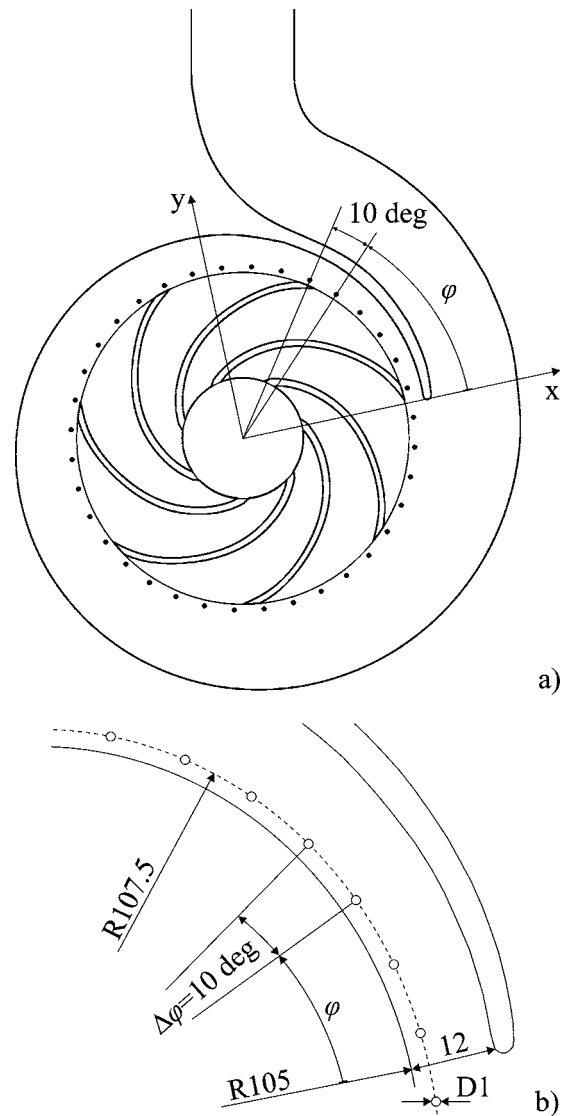


Fig. 1 (a) Scheme of the test pump with location of measurement points. (b) Detail of the tongue region (dimensions in mm).

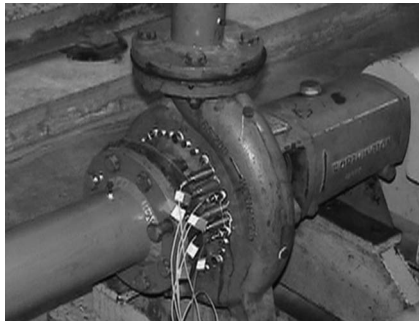


Fig. 2 Test pump with pressure transducers installed on the volute

phase) for flow rates ranging from 0% to 160% of nominal flow rate. Further details about the instrumentation and test procedures can be found in Ref. [8]. Measurement uncertainty was estimated to be less than $\pm 0.8\%$ for the flow rate and $\pm 1\%$ for the pump head. The sensitivity of the piezoelectric transducers was checked by comparing their dynamic response to the one from a reference piezoresistive transducer, when located simultaneously at an especially designed device that underwent transient processes. The measurement uncertainty estimated for the pressure fluctuations at f_{BP} was $\pm 1.5\%$.

As an example of the experimental results, Fig. 3 shows the spectra of the pressure signals obtained for each flow rate at the position $\varphi = 25$ deg, which corresponds to the narrow region of the volute (see angle definition in Fig. 1). As expected, the dominant spikes in these spectra are associated with the impeller rotation frequency (27 Hz) and, over all, to the blade-passing frequency f_{BP} (189 Hz). In agreement with previous studies [8], the maximum pressure amplitudes at f_{BP} correspond to the lowest range of flow rate; the high flow rates exhibit large amplitudes, too, whereas at nominal flow rate, the perturbations are very small. Indeed, the dynamic excitation at f_{BP} is very much dependent on the pump operating point, i.e., on the characteristics of the matching between the flow coming out from the impeller channels and the flow in the volute, particularly in the surroundings of the tongue [6,11].

A complementary series of tests was conducted to measure the flow rate that recirculates from the volute toward the pump inlet, through the clearance between the wear ring and the impeller shroud (see Fig. 4). This radial clearance was 0.1 mm, with an axial extent of 16 mm. For these tests, the channels of the impeller were blocked completely with a sealing paste. An auxiliary pump created a pressure difference through the test pump and the subsequent leakage flow was then measured volumetrically. It was determined that with the pump running at 1620 rpm and operating at the best efficiency flow rate, the leakage flow was less than 4%.

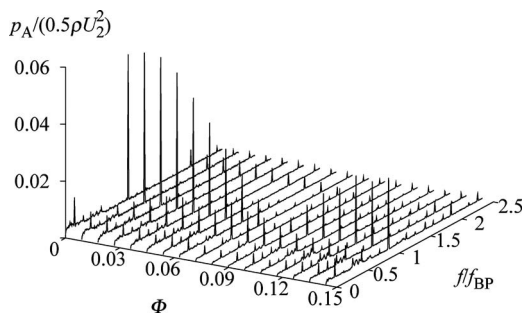


Fig. 3 Experimental pressure spectra at angular position $\varphi = 25$ deg, as a function of frequency and flow rate ($d_2 = 0.210$ m)

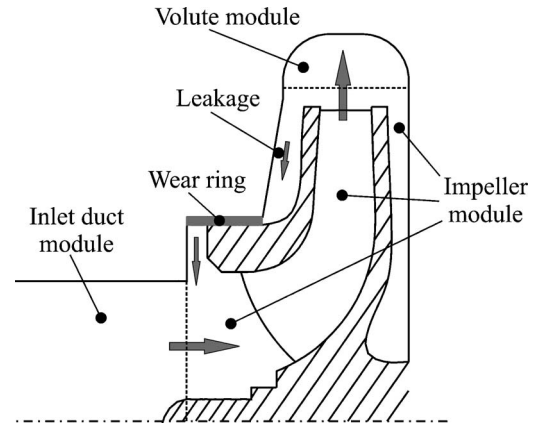


Fig. 4 Flow through pump and leakage from volute to impeller eye

Numerical Model

For the computations of the flow through the pump, the domain was separated into four modularized zones: inlet duct, impeller, volute, and diffuser plus outlet duct. Each of the modules was built and meshed independently, so that only the portion corresponding to the impeller module had to be replaced when changing the impeller diameter, unlike in previous studies by the authors [22]. This prevented any mesh distortion in the rest of the modules that could affect the results of the simulations. The inlet and outlet ducts included in the domain were 0.45 m and 0.30 m long, respectively, in order to take apart the sections at which boundary conditions are imposed. The impeller module extends further than the physical impeller toward both the pump inlet and the volute (see dot lines in Fig. 4), for convenience of grid matching between adjacent modules with relative motion. Besides, the impeller module contains the two lateral spaces between the casing and each side of the impeller, i.e., shroud and hub; the former extends from the volute until the wear ring round the eye of the impeller and the second one from the volute until the driving shaft (Fig. 4). Since the leakage flow measured for the test pump was rather small, it was neglected in the numerical model, in order to keep a reasonable degree of simplicity for the computations. Figure 5 gives some views of the geometry of the modeled pump, including the inlet and outlet portions, the impeller seen from the inlet side, and a comparison of the relative impeller-tongue gaps considered in this study.

Different unstructured mesh types were created for each zone depending on the geometrical characteristics, with special mesh refinement at strategic locations, such as the leading edge of the blades and the tongue region. Prismatic cells were used for the inlet and outlet pipe portions, and tetrahedral cells were used for the rest of the domain, including the impeller and the volute modules. Figure 6 shows some details of the surface meshes at different regions of the domain, such as the tongue separating the volute and the diffuser, the hub of the impeller with its blades, and the suction pipe with the inlet guide vane.

Two grid surfaces, one between the inlet duct and the impeller modules and another between the impeller and the volute modules (dot lines in Fig. 4), are subject to relative motion of the meshes at each side, due to the rotation of the impeller. This relative motion of the impeller grid with respect to the inlet and the volute modules during simulation is supported in FLUENT by means of a sliding mesh technique, which uses an interpolation routine to confront data of the cells at both sides.

Turbulence was simulated by means of a standard $k-\epsilon$ model, and standard wall functions were used to calculate boundary layer variables. The time dependent term scheme was a second order implicit. The pressure-velocity coupling was established by means

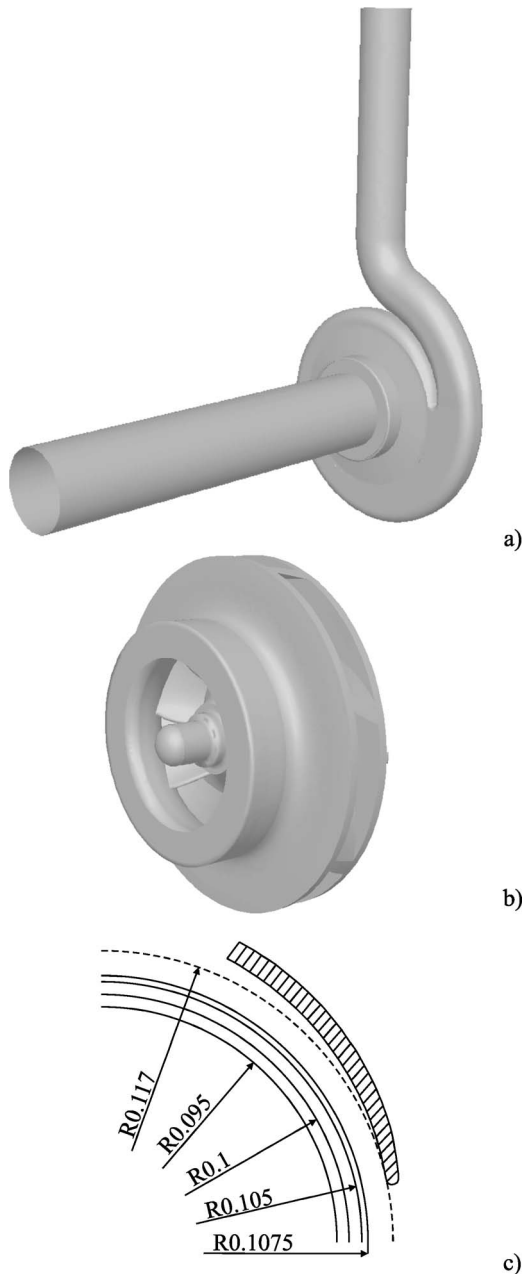


Fig. 5 Pump numerical model. (a) Pump with inlet and outlet ducts. (b) Impeller surface. (c) Impeller-tongue gap for the impeller cutbacks tested.

of the SIMPLEC algorithm. Second order upwind discretizations were used for the convection terms and central difference schemes for the diffusion terms. As boundary conditions, a constant total pressure was considered at the inlet and a uniform static pressure at the outlet dependent on the flow rate. The latter was introduced by means of an added loss proportional to the exit dynamic pressure, which simulates the effect of a regulation valve. With these types of boundary conditions imposed at some distance from the machine, the pulsating flow results to be less distorted and more realistic than when defining a fixed flow rate [18,22].

Mesh independence tests were carried out for the 0.210 m impeller and the highest flow rate (about 160% of nominal flow rate), by using mesh sizes ranging approximately between 4×10^5 and 2×10^6 cells. In each case, the mesh was especially refined at the tongue region. Table 2 summarizes the size of the mesh (for each of the modules) finally selected for the bulk of the

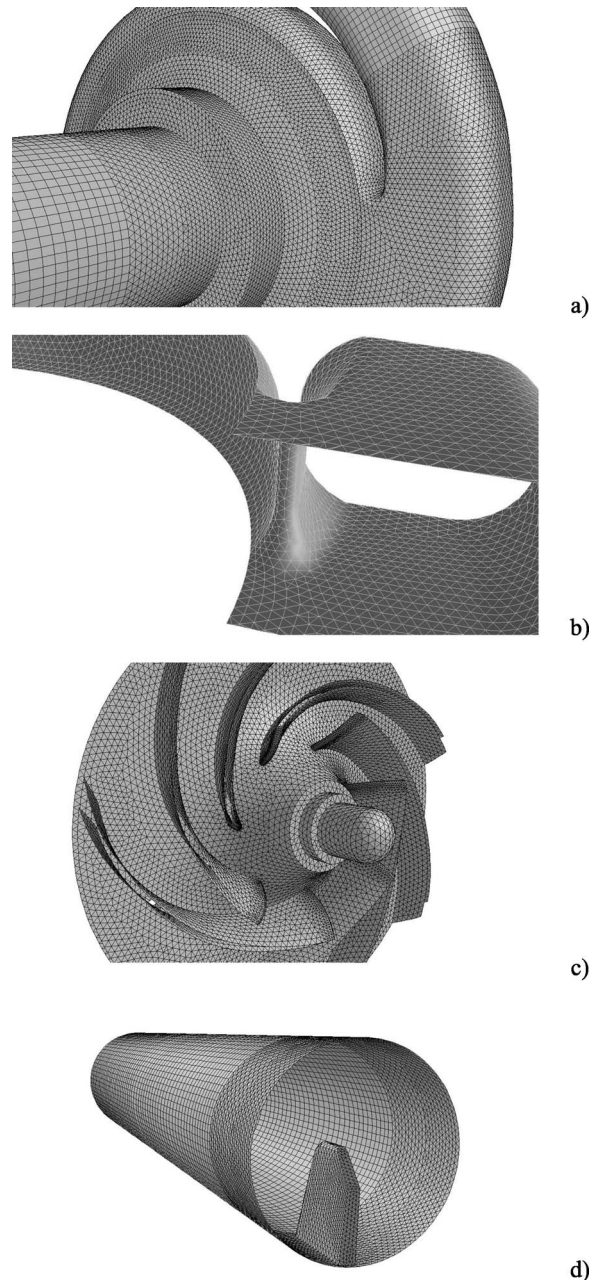


Fig. 6 Details of the surface mesh. (a) Inlet duct, volute and diffuser. (b) Tongue separating volute and diffuser. (c) Impeller with shroud removed. (d) Suction duct with inlet guide vane.

simulations, with approximately 765,000 cells in total. With this final mesh, the variation observed in flow rate with respect to the 2×10^6 cell mesh was less than 1% and less than 1.5% for the

Table 2 Mesh size of the modules of the pump numerical model

| Module | Total cell number |
|--------------------------|-------------------|
| Inlet duct | 128,271 |
| Impeller | 347,933 |
| Volute | 191,079 |
| Outlet diffuser and duct | 98,137 |
| Total | 765,420 |

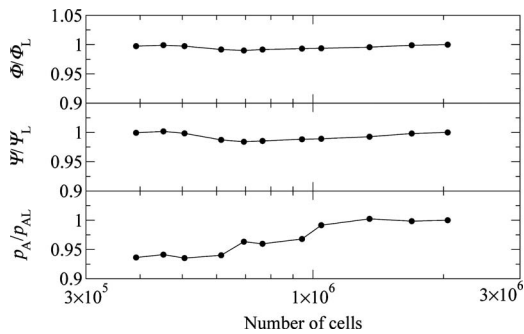


Fig. 7 Effect of mesh refinement (total number of cells) on the numerical predictions for the $d^*=1$ impeller operating at 160% of the nominal flow rate. From top to bottom: flow coefficient, head coefficient, and amplitude of f_{BP} pressure fluctuation at angular position $\varphi=25$ deg, all of them normalized by the values corresponding to the upper limit of number of cells.

head (Fig. 7). The variation for the amplitude of pressure fluctuations at a given reference position ($\varphi=25$ deg, front side of volute) was less than 4% (Fig. 7). This grid size is still not adequate enough to investigate the local boundary layer variables, but global variables and dynamic flow patterns are well captured, according to previous experience [18]. Additionally, the effect of the inlet and outlet duct lengths on the pressure fluctuations was explored by means of simulations with both ducts halved and doubled with respect to the chosen values of 0.45 m (inlet) and 0.3 m (outlet). The predictions obtained for the pressure fluctuation at the reference position differed in less than 2.4%.

For each of the configurations tested (impeller diameters and flow rates), first, a steady flow calculation was carried out for a given relative position of the impeller (frozen). After achieving convergence, the resulting velocity and pressure fields were taken as the initial conditions for the proper unsteady flow computations. Each blade passage was computed in a time sequence of 32 steps, i.e., 224 time steps per impeller revolution. At a rotation speed of $169.95 \text{ rad s}^{-1}$, the corresponding time interval was $1.65 \times 10^{-4} \text{ s}$. At least ten impeller revolutions were imposed in the simulation process to ensure the achievement of a stabilized periodic solution in the numerical sense, that is, the flow variables become periodic when considering one full revolution, with predominant fluctuations at the blade-passing frequency. Then the evolution of the flow during one single blade passage was recorded, analyzed, and postprocessed to derive both global (head, flow rate, and forces) and local variables (pressure fluctuations).

Numerical and Experimental Results

For each of the impellers, numerical simulations were performed for five flow rates, with flow coefficients Φ ranging from approximately 0.02 to 0.14. These five flow rates correspond to flow ratios of about 20%, 60%, 100%, 120%, and 160% of the nominal flow rate for each impeller. The nondimensional head-flow rate diagram of Fig. 8 shows the operating points obtained for each impeller in the simulations as well as the experimental performance curve for the 0.210 m impeller ($d^*=1$). For each relative flow rate, the operating points corresponding to the four impellers nearly superpose each other. As expected for this kind of machines, comparison of the numerical and the experimental data for the 0.210 m impeller gives good qualitative and quantitative agreement. The difference between the head predicted and measured for this impeller remains below 6% for all flow rates but the highest one; for the latter, for which the head curve drops fast when further increasing the flow rate, the difference between the flow rate predicted and measured (for the same measured head)

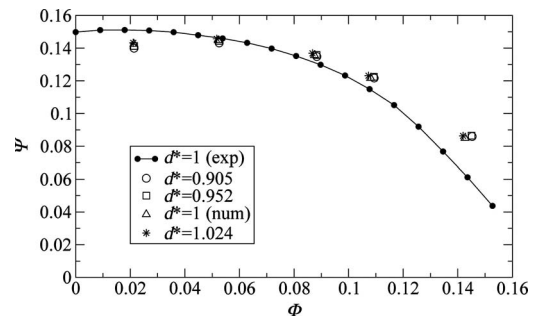


Fig. 8 Experimental head-flow rate curve ($d^*=1$) and numerical predictions for four impeller diameters

was about 11%. Part of these differences can be attributed to the leakage flow between the volute and the impeller inlet, which was not considered in the numerical model.

Figure 9 presents an example of the instantaneous absolute velocity vectors calculated with the 0.210 m impeller operating at three different flow rates (about 20%, 100%, and 160% of the nominal flow rate). The three diagrams, which correspond to the same relative position of the impeller blades, highlight the distribution of the flow in the tongue region (at midspan of the impeller outlet in the axial direction). At the nominal flow rate, there is a

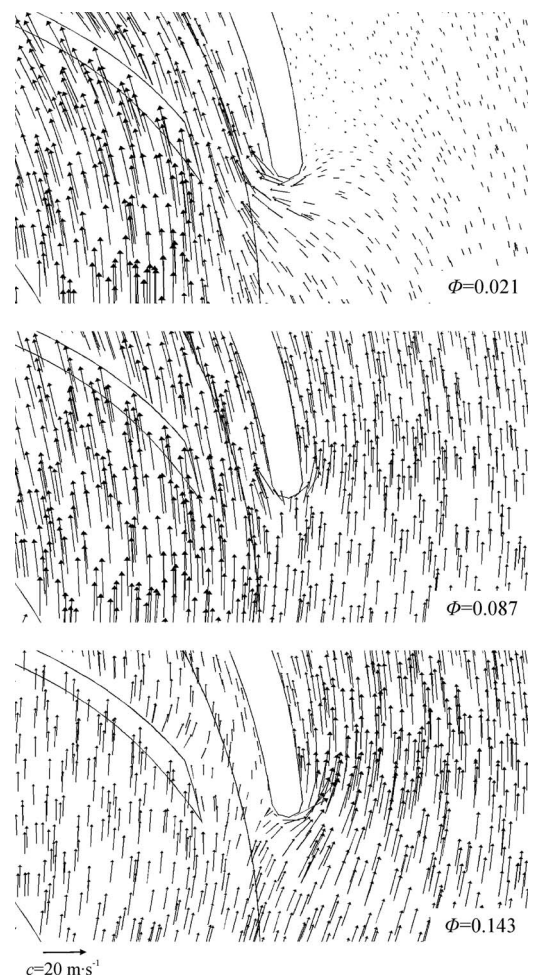


Fig. 9 Velocity vectors in the near-tongue region for the $d^*=1$ impeller at midspan of impeller outlet width and three flow coefficients (equivalent to 20%, 100%, and 160% of the nominal flow rate)

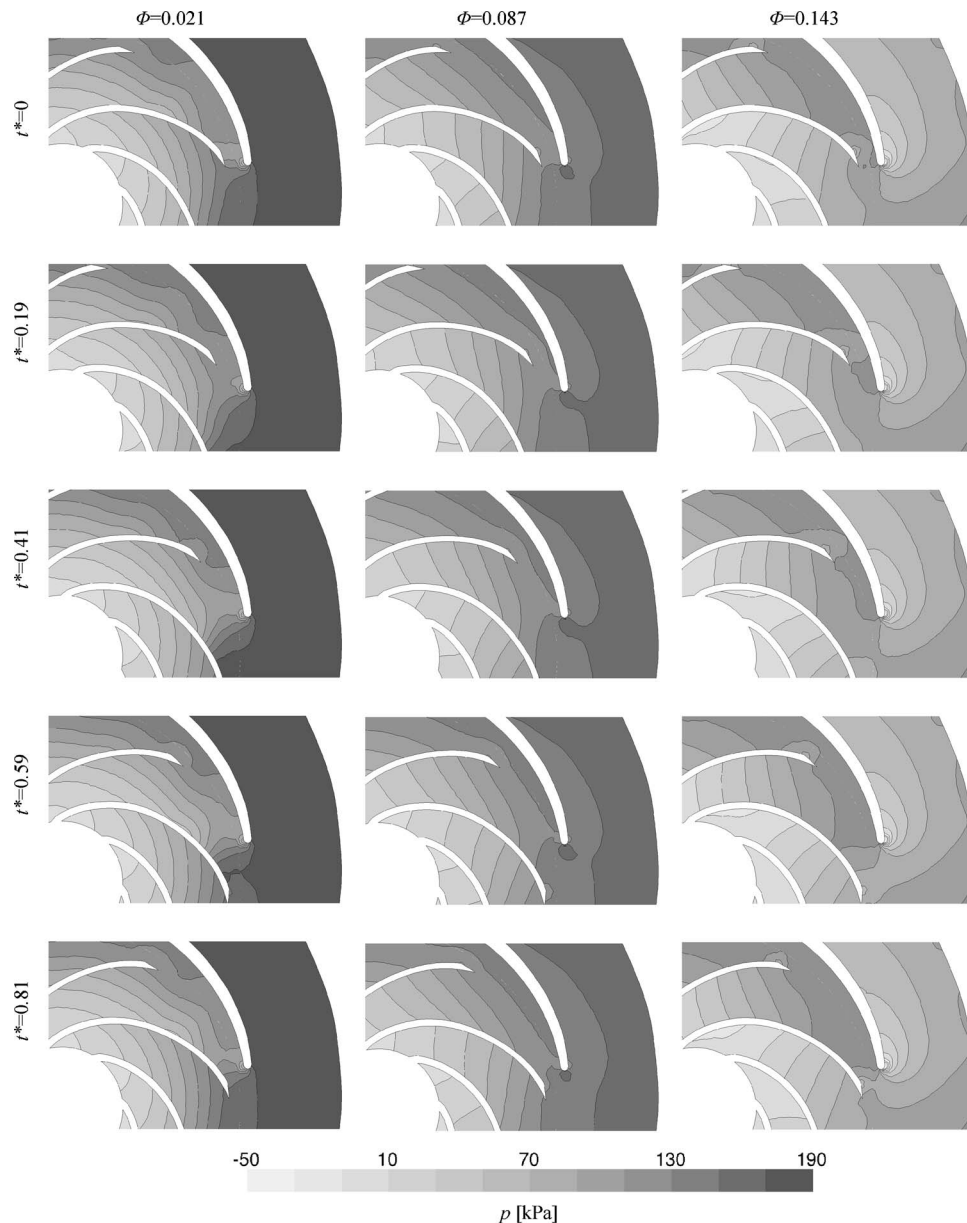


Fig. 10 Time evolution of the static pressure in the near-tongue region for the $d^*=1$ impeller (at midspan of impeller outlet width) during one blade-passage period. Results for three flow coefficients, equivalent to 20%, 100%, and 160% of the nominal flow rate.

good matching of the flow coming out from the impeller and the volute, since the flow aligns with the tongue. On the contrary, at off-design conditions, the absolute velocity of the flow approaching the tongue forms a large incidence angle with it. At high flow rate, most of the flow is directed toward the outlet duct, so that the stagnation point on the tongue shifts toward the impeller side and a wake is formed on the diffuser side of the tongue. At low flow rate, a significant portion of the flow close to the exit section of the volute recirculates through the impeller-tongue gap toward the narrow region of the volute. In this case, the stagnation point on the tongue shifts toward the diffuser side, inducing a wake on the impeller side of the tongue. These results are similar to the ones presented in other references [1,23].

The different positions of the stagnation and wake regions around the tongue tip when varying the flow rate can be also appreciated in Fig. 10. This figure represents the evolution of the static pressure in the impeller and in the surroundings of the tongue (midspan of impeller outlet) for five time steps distributed

during a single blade passage, for the 0.210 m impeller ($d^*=1$) and for three different flow rates (the same ones of Fig. 9).

For $\Phi=0.143$, Fig. 10 shows that, as expected for centrifugal fluid machines with high flow rates, the pressure difference across the wall of the blades is always large, whereas the average pressure achieved in the diffuser is rather low. In fact, the minimum pressure in the pump for this highest flow rate happens to be located at the wake from the tip of the tongue, on the diffuser side, which suggests the possibility of cavitation at the tongue of centrifugal pumps operating at very large flow rates, in accordance with the experimental study by Bachert et al. [24]. Regarding the pressure fluctuations during one blade-passage period, the relative peak-to-peak variations in the region of the impeller-tongue gap are above 40% of the average pressure. At any position along the volute, the minimum pressure value during the fluctuation cycle coincides with the passing by of an impeller blade.

For $\Phi=0.087$ (nominal flow rate), Fig. 10 shows a lesser pres-

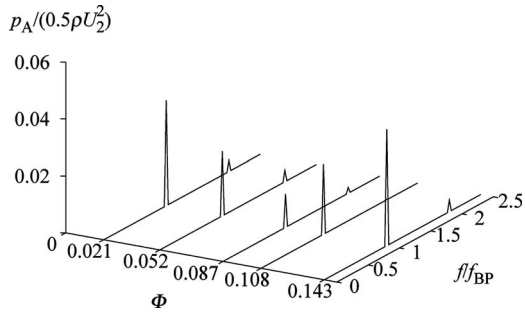


Fig. 11 Spectra of the numerical pressure fluctuations at angular position $\varphi=25$ deg, as a function of frequency and flow coefficient ($d^*=1$)

sure difference across the wall of the blades than in the previous case, as well as a bigger pressure value (and a more uniform distribution) in the diffuser. The amplitude of the pressure fluctuations in the volute is now very small, but the minimum value during the fluctuation cycle still coincides with the blade passage, like for the high flow rate.

As expected, the maximum pressure in the diffuser in Fig. 10 corresponds to $\Phi=0.021$, i.e., the lowest flow rate tested. The temporal sequence of pressure diagrams shows a particular feature: the pressure difference across the wall of the blades (between the pressure and the suction sides), which in average is small if compared to the other two flow rates, turns to be negative in a significant part of the impeller channels when they pass by the tongue. This behavior, already observed experimentally by Hasegawa et al. [6], is associated with the flow recirculating from the broad part of the volute through the impeller-tongue gap side (see Fig. 9), which imposes a transient partial blockage of the flow approaching the exit of the impeller and brings about recirculation inside the impeller channel. The resulting effect on the pressure fluctuations observed in the region of the impeller-tongue gap is a remarkable pressure fluctuation magnitude, with peak-to-peak variations of about 60% of the average pressure. In addition, there is an important shift in the phase of the pressure fluctuations with respect to the other two flow rates of Fig. 10 ($\Phi=0.087$ and $\Phi=0.143$): now the alignment of the blades with the tongue corresponds approximately to the maximum value of the pressure during the fluctuation cycle.

In order to contrast the predictions of the numerical model regarding the flow fluctuations, the pressure values computed at 36 positions distributed along the front wall of the volute (equivalent to the locations used in the experiments) were recorded during one blade passage (32 time instants) and FFT processed to obtain pressure amplitudes and phases at f_{BP} . In analogy with Fig. 3, Fig. 11 presents the spectra of the numerical pressure signals for the 0.210 m impeller ($d^*=1$) at position $\varphi=25$ deg (see Fig. 1) for each of the simulated flow rates. Due to the characteristics of the numerical model, these pressure spectra only exhibit nonzero values at the blade-passing frequency and its harmonics. As expected, the amplitude of the spikes at f_{BP} , which are the predominant ones, increases at off-design conditions, in good agreement with the experimental spectra of Fig. 3.

Figure 12 compares the distribution along the volute of the pressure amplitude calculated at f_{BP} , for the four impellers and the five flow rates tested (a column for each impeller and a row for each flow rate). The pressure amplitude has been normalized with respect to density and the external tangential velocity, which is different for each impeller. In the case of the reference impeller ($d^*=1$), the pressure fluctuations obtained from experiments are shown as well. Comparison between the numerical and the experimental pressure fluctuation data for this impeller gives a satisfactory concordance, even quantitatively, which is in agreement with previous results by the authors [18]. The most remarkable difference with respect to measurements corresponds to the two low flow rates in the near-tongue region of the volute ($0 < \varphi < 30$ deg), i.e., the zone with maximum pressure fluctuations: predictions underestimate these maximum amplitudes in about 40%. At least in part, this difference can be attributed to the flow separation that is expected from the tip of the tongue toward the volute side for such low flow rates (see Fig. 9), because it represents a notorious difficulty for a precise numerical simulation of the flow in that region, due to the lack of sufficient spatial resolution.

All the curves in Fig. 12 show some degree of modulation, with up to seven hills along the φ axis (angular position). This modulation is the result of the combination of the hydraulic disturbances that follow the passage of each blade along the volute (jet-flow pattern) and, on the other hand, the perturbations induced when the blades pass by in front of the volute tongue [8]. Whereas the former only has a localized influence, the latter can affect significantly a large part of the pump. Along the volute, both disturbances combine with a relative phase that is dependent on the angular position, so that the resulting fluctuations can be either

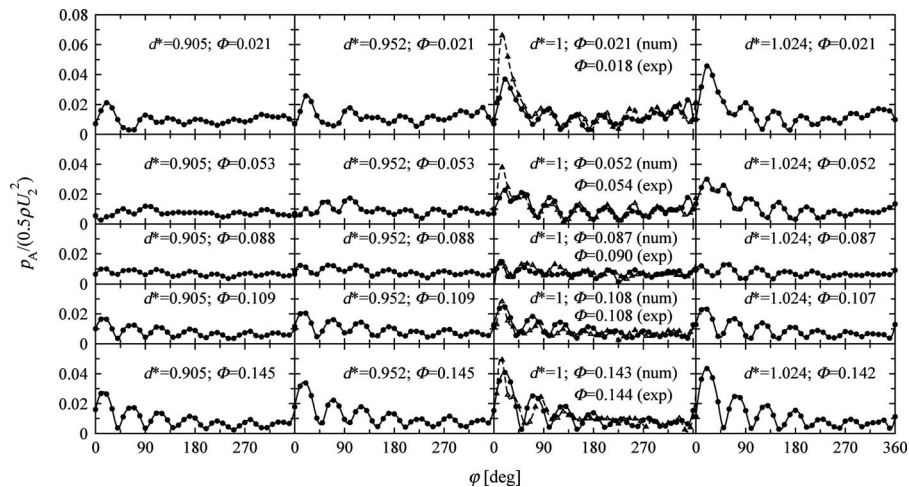


Fig. 12 Amplitude of pressure fluctuations predicted at f_{BP} along the front wall of the volute, for four impeller diameters (one at each column) and five flow coefficients (one at each row). For impeller $d^*=1$, the experimental data are also shown (Δ , experimental data; \bullet , numerical results).

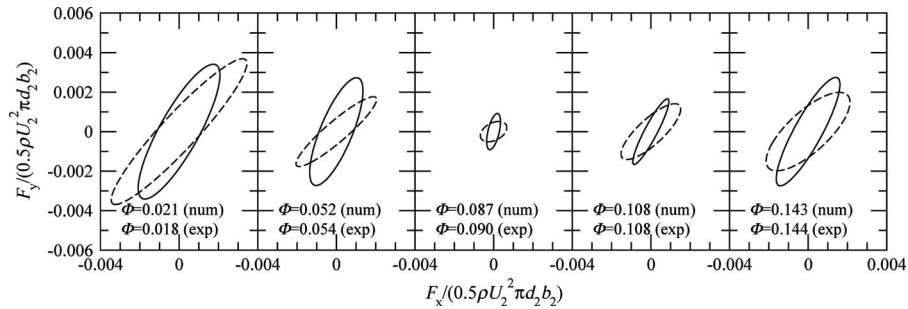


Fig. 13 Orbit of the unsteady partial radial forces on the impeller obtained from integration of pressure fluctuations at f_{BP} along the front wall of the volute for the $d^*=1$ impeller and five flow coefficients (... , experimental data; —, numerical predictions)

reinforced or canceled. In Fig. 12, the four impellers present a similar dependence between the distribution of pressure amplitude and the flow rate. When operating close to the nominal flow rate, the amplitude of the pressure fluctuations is small and rather uniform along the volute, but for both small and high flow rates the pressure fluctuation amplitude increases, particularly in the narrow zone of the volute (in agreement with the conclusions of Fig. 10).

These results indicate a progressive reinforcement of the blade-tongue interaction when deviating from nominal operating conditions. For a given flow coefficient, the maximum amplitudes of the pressure fluctuations increase with the impeller diameter, i.e., they increase when reducing the blade-to-tongue gap. This is an expectable result since a smaller rotor-stator distance implies less space for the flow to adapt to the geometry changes, that is, it implies greater velocity gradients and greater stresses. In terms of the normalized pressure values, when changing from a gap ratio of 23.2% to 17.0% (the normalized impeller diameter d^* varies from 0.905 to 0.952), the predicted increment in maximum pressure fluctuation amplitude results to be about 18% for the smallest flow rate and 26% for the biggest one. These variations increase to about 73% and 52%, respectively, when reducing the gap ratio from 23.2% to 11.4% (from $d^*=0.905$ to $d^*=1$). Finally, reducing the gap ratio from 23.2% to 8.8% (from $d^*=0.905$ to $d^*=1.024$) gives increments in maximum pressure fluctuation of about 110% and 60%, respectively, for the smallest and biggest flow rates. These results are in agreement with the trends reported in Ref. [22].

Radial Forces and Torque at the Blade-Passing Frequency

After completing and storing the unsteady flow computations corresponding to at least one blade passage period for each impeller and flow rate, the evolution of global magnitudes such as the unsteady radial forces and torque could be calculated.

In order to check the procedure, first of all, the partial radial forces at the blade-passing frequency attributed to the outlet pressure distribution were estimated for the $d^*=1$ impeller from the experimental pressure fluctuations captured along the front side of the volute (amplitude and phase at f_{BP}). These forces were obtained by assuming instantaneous pressure uniformity in the axial direction, so that each measurement location was assigned to an angular portion of the cylindrical periphery of the impeller and the modulus and argument of the radial force at each time instant resulted from proper integration of the pressure data. The same calculations (i.e., assuming axial uniformity in pressure) were performed for that impeller ($d^*=1$) from the numerical predictions of pressure fluctuation at the 36 positions along the volute wall. The partial radial forces so obtained for the five flow rates tested numerically are presented in Fig. 13 by means of orbit diagrams

(x -component versus y -component), where the x -axis (null force argument) is aligned with the tongue tip (equivalent to $\varphi=0$ deg in Fig. 1).

As shown in Fig. 13, the blade-passing frequency forces for a given flow rate complete one elliptical trace during the blade-passing period. Although there are some differences in the orientation of the numerical and experimental ellipses and in the maximum force values, the trend of the force can be considered well captured by the model, with a very small magnitude for the nominal flow rate and increasing values for off-design conditions, as expected. For the two biggest flow rates (about 120% and 160% of the nominal flow rate), the difference in maximum force magnitude between the numerical and the experimental data keeps below 10% and the same occurs for the case of 60% of nominal flow rate. Only for the lowest flow rate tested that difference increases to about 25%. Nevertheless, these differences are sensibly smaller than the ones observed in the maximum amplitude of pressure fluctuation for the two lowest flow rates (Fig. 12), due to the attenuating effect of the pressure integration around the impeller outlet. Regarding the argument of the maximum force, the difference between the numerical and experimental values results to be lesser than 30 deg. These results are similar to those reported in Ref. [22].

In consequence, the numerical simulations performed were considered adequate for a reasonable estimation of the total unsteady radial forces on the impeller, i.e., not only the ones derived from the pressure fluctuations at the wall of the volute. Hence, total radial forces were computed at each time step by means of a full integration of the instantaneous pressure and shear stress distribution determined numerically on the impeller surfaces (blades, shroud, and hub), only excluding the surface of the shroud wear ring. The time signals of the force components in the x and y directions (meridian plane) were FFT processed to give the amplitude and relative phase corresponding to the blade-passing frequency and its harmonics. The resulting unsteady radial forces for each impeller and flow rate are plotted in the orbit diagrams of Fig. 14. The values of these radial forces for the $d^*=1$ impeller are significantly greater than those obtained from the pressure fluctuation data at the volute front side (Fig. 13). This is due to the simplifying assumptions implicit in those calculations, such as the noninclusion of momentum flux distribution on the impeller surfaces and, especially, the consideration of pressure uniformity in the axial direction, since pressure fluctuations are largest at mid-span of the impeller exit (see, for instance, Ref. [22]). Besides, Fig. 14 contains the total unsteady radial forces, including the contribution from the f_{BP} harmonics; therefore, the shape of the resulting force traces is not elliptical but irregular, sometimes with two lobes. In spite of the irregularities, most of the orbits are very strained in the vertical direction, i.e., the magnitude of the x -component of the radial fluctuating force is very small compared to the y -component.

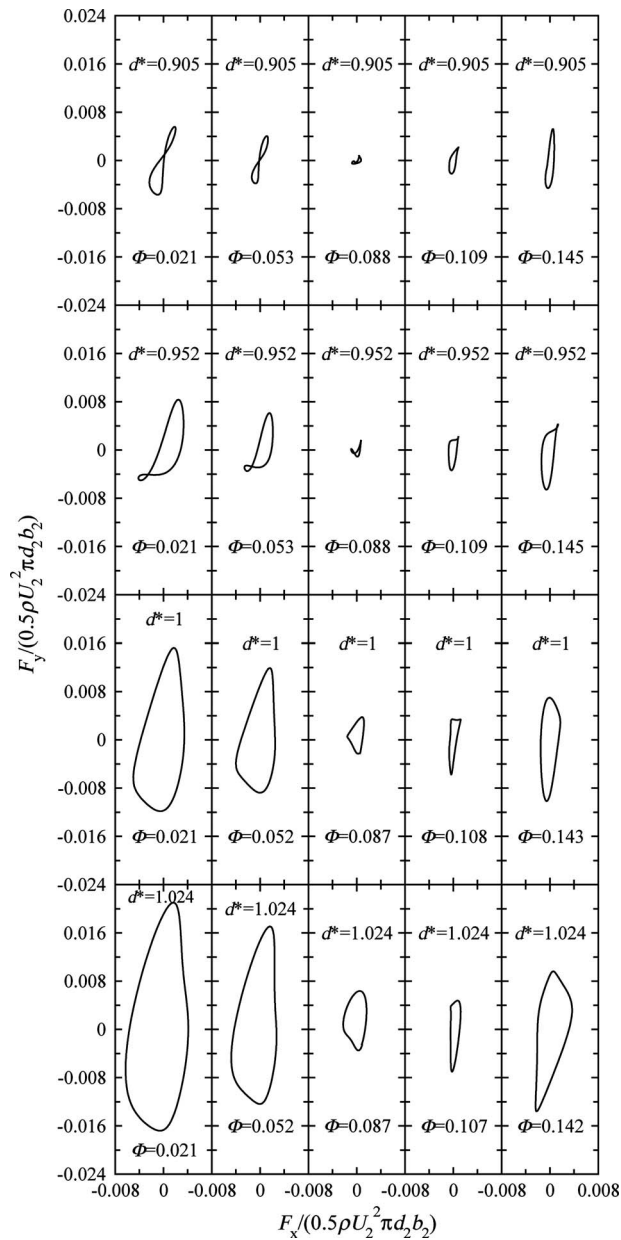


Fig. 14 Orbit of the total unsteady radial force on the impeller predicted for four impeller diameters (one at each row) and five flow coefficients (one at each column)

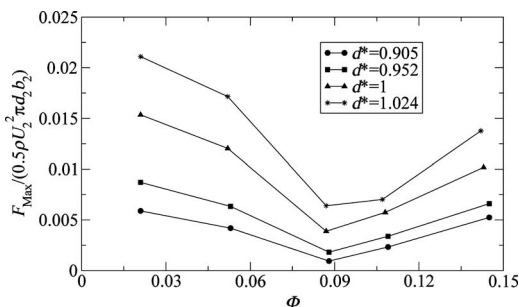


Fig. 15 Prediction of the maximum magnitude of the total unsteady radial force as a function of the flow coefficient for the four impellers tested

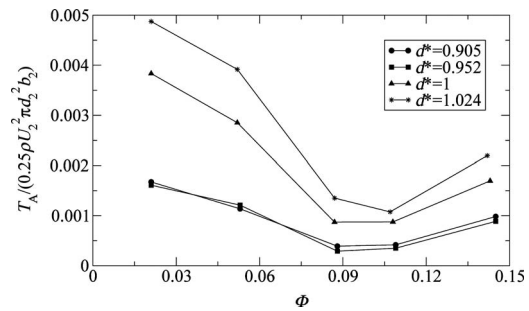


Fig. 16 Prediction of the f_{BP} unsteady torque as a function of flow coefficient for the four impellers tested

Figure 15 compares the values of the maximum unsteady total radial force for each impeller, and flow rate. As expected, for a given impeller, the maximum force value is lowest at nominal flow rate and increases at off-design conditions. Quantitatively, this trend depends on the gap value: in the case of the two smallest impellers, the magnitude of the maximum force is similar for both low and high flow rates, whereas the two biggest impellers present force magnitudes that are particularly high for the low flow rates.

On the other hand, for any given flow coefficient, the maximum value of the normalized unsteady radial force increases when diminishing the impeller-tongue gap, with more accused variations for the smallest gaps. For example, reducing the gap ratio from 11.4% to 8.8% (i.e., increasing d^* from 1.0 to 1.024) leads to an increment in the maximum unsteady force of about 40% for the two small flow rates and close to 30% for the biggest flow rate. A total variation of impeller diameter between the smallest and biggest values used in this study, which corresponds to a gap reduction from 23.2% to 8.8%, results in multiplying the maximum unsteady force by a factor of 3.8 for small flow rates and about 2.8 for the big flow rates. This trend matches well with a relationship of proportionality between the maximum force amplitude and G^{-n} (with $n > 0$) as proposed by Guelich and Bolleter [3] to correlate pressure pulsations. After collecting data from tests under a variety of conditions, they suggested values for the exponent n between 0.6 and 0.9. However, the present predictions of the maximum unsteady force indicate greater values: 1.4 for the small flow rates and 1.1 for the big flow rates, with regression coefficients R^2 well above 0.99 for all the flow rates tested.

Additionally, the instantaneous total torque on the pump shaft was determined from the numerical simulations and then filtered at the blade-passing frequency. Figure 16 shows the resulting torque amplitude at f_{BP} as a function of the flow rate, for each impeller diameter. The general trend of the curves resembles that of Fig. 15, with minimum values of the fluctuating torque for flow rates close to the nominal one. The most remarkable difference is that the curves of the fluctuating torque for the two small impellers ($d^* = 0.905$ and $d^* = 0.952$) nearly overlap. Varying the impeller diameter from $d^* = 0.952$ to $d^* = 1.024$ (reduction of the impeller-tongue gap from 17.0% to 8.8%) makes the fluctuating torque amplitude multiply by factors of about 3.2 for the small flow rates and 2.4 for the big ones. A fit of the torque data with a potential function of the type G^{-n} gives exponents of n similar to the ones obtained by fitting the force data, but in this case the regression coefficients R^2 are poor (usually below 0.9). The torque fluctuation amplitude showed in Fig. 16 is particularly high for the small flow rates, for which the steady driving torque is low (typical of centrifugal fluid machines). This results in high values for the relative torque fluctuations with respect to the mean torque, especially for the smallest tongue gaps. For the present case and a flow coefficient of $\Phi = 0.052$ (60% of nominal flow rate), the relative torque amplitudes (zero-to-peak) are 3.1% and 4.4% of the steady torque predicted for the impellers with $d^* = 1$ and d^*

=1.024, respectively. The same relative torques reach values of 5.7% and 7.6% when considering a flow coefficient of $\Phi=0.021$ (20% of nominal flow rate).

The trends observed when varying the impeller-tongue gap in this study are expected to be qualitatively similar for higher performance pumps, though the quantitative extrapolation of these results is not straightforward. The absolute values of the fluctuating radial forces and torque estimated at f_{BP} for the pump tested can be considered low for many applications, provided the pumps have sufficient structural robustness. Hence, small blade-tongue gaps are to be preferred since they usually give higher efficiencies [4]. In fact, in the present case, the pump efficiency (including viscous hydraulic losses and disk friction losses) estimated from the numerical simulations varied almost linearly from 71.2% to 74.7% when increasing the tongue gap from the maximum to the minimum value tested. These results suggest that still better efficiencies can be achieved for further reductions of the impeller-tongue gap below 8.8% but that can also bring about strong increments in the magnitude of the fluctuations so that eventually they might represent an unacceptable dynamic excitation for the pump.

On the other hand, augmenting the impeller-tongue gap from 17.0% to 23.2% gives no significant reduction in the torque fluctuation amplitude, though it still makes the magnitude of the radial force decrease in around 30%. Hence, further increments of the impeller-tongue gap above those limits are not expected to affect significantly the f_{BP} fluid-dynamic forces and torque, in agreement with Dong et al. [10] with respect to noise production.

Conclusions

The blade-volute interaction in centrifugal pumps can be estimated by means of the unsteady numerical simulation of the flow with an appropriate CFD code provided with a sliding mesh technique. For this investigation, the software package FLUENT was used to study the dynamic characteristics of the flow in a vaneless volute centrifugal pump with different impellers, obtained from successive cutbacks of the outlet diameter. The goal of the study was analyzing the effect of varying the tongue radial gap on the pressure fluctuations and radial forces and torque at the blade-passing frequency for a variety of flow rates.

The comparison between the numerical and experimental data for one of the impellers ($d^*=1$) shows head differences below 6% for all flow rates but the highest one. The predictions of pressure fluctuations along the front side of the volute show, too, a good agreement with the measurements, with maximum fluctuation amplitudes for off-design conditions in the near-tongue region of the volute. Only for the lowest flow rates, the prediction of maximum pressure amplitude results to be excessively low which is attributable to the difficulty to simulate properly the flow separation from the tongue tip. According to the numerical predictions, the progressive reduction of the impeller-tongue gap from 23.2% to 8.8% of the impeller radius results in subsequent increments of the maximum pressure amplitude up to about 110% for the low flow rate and 60% for the high flow rates. Hence, greater pressure increments are to be expected for further gap reductions.

Unsteady partial forces in the radial direction were calculated for the $d^*=1$ impeller from integration round the volute of both the numerical and experimental pressure fluctuation data at f_{BP} . The comparison of these calculations corroborates that the methodology used for flow simulation can provide a reasonable estimation of the blade-tongue interaction forces from an engineering point of view. Thus, total unsteady radial forces were computed numerically for all the impellers and flow rates by means of a full integration of the instantaneous pressure and shear stress distribution on the impeller surfaces (only excluding the shroud wear ring). The data obtained show that the unsteady forces are minima in the range of the nominal flow rate, and that, for off-design conditions, reducing the radial gap from 23.2% to 8.8% of the

impeller radius results in multiplying the magnitude of the radial forces by factors of about 2.8 and 3.8 for high and low flow rates, respectively. The predictions of torque fluctuation at the blade-passing frequency follow a very similar trend.

The minimum radial gap of this study, 8.8% of the impeller radius, lies within the range 5–10%, which is the usual design recommendation for volute pumps [25]. According to the present results, further reduction of the radial gap below those limits can produce a strong amplification of the dynamic load amplitude, thus increasing the potential for pump damage. On the other hand, the augmentation of the radial gap above about 20% of the impeller radius will have little effect on the f_{BP} load. The effects of smaller blade-tongue gaps or other geometry modifications, such as different blade or tongue shapes, on the dynamic load due to blade-tongue interaction can be also explored with the methodology of this study, i.e., by means of an appropriate numerical simulation of the unsteady flow through the pumps.

Acknowledgment

The authors gratefully acknowledge the financial support of the Ministerio de Educación y Ciencia (Spain) under Project Nos. MEC06-DPI15034 and TRA2007-62708, and of the Gobierno del Principado de Asturias (Plan de Ciencia, Tecnología e Innovación 2006–2009). The authors also express their appreciation to the reviewers, whose comments were very helpful in guiding the preparation of the final version of the article.

Nomenclature

- b_2 = impeller width at outlet (m)
- c = velocity modulus (m s^{-1})
- c_{2r} = radial component of the velocity at impeller outlet (m s^{-1})
- d^* = $d_2/0.210$, normalized outlet diameter of impeller
- d_2 = impeller outlet diameter (m)
- f = frequency (Hz)
- F = magnitude of unsteady pressure force (zero-to-peak) (N)
- f_{BP} = $z\omega/(2\pi)$, blade-passing frequency (Hz)
- g = gravity (m s^{-2}).
- G = impeller-to-tongue radial gap
- H_N = nominal head (m)
- k = turbulent kinetic energy ($\text{m}^2 \cdot \text{s}^{-2}$)
- p_A = pressure fluctuation amplitude (zero-to-peak) (Pa)
- Q_N = nominal flow rate ($\text{m}^3 \cdot \text{s}^{-1}$)
- r_3 = tongue-tip radius (m)
- t^* = t/t_{BP} , normalized time
- t_{BP} = $1/f_{BP}$, period of blade passage (s)
- t = time (s).
- T_A = torque fluctuation amplitude (zero-to-peak) (N m).
- U_2 = $\omega d_2/2$, tangential velocity at impeller outlet (m s^{-1})
- z = number of blades
- φ = angular position from tongue tip, measured in the rotating direction (deg)
- Φ = c_{2r}/U_2 , flow coefficient
- ε = turbulent dissipation ($\text{m}^2 \text{s}^{-3}$)
- ρ = fluid density (water) (kg m^{-3})
- Ψ = $gH/(U_2^2/2)$, head coefficient
- ω = rotating speed (rad s^{-1})
- ω_S = $\omega Q_N^{1/2}/(gH_N)^{3/4}$, specific speed

Subscripts

- L = value for computations with 2×10^6 cells
- Max = maximum value

x, y = Components in x -, y -directions

References

- [1] Brennen, C. E., 1994, *Hydrodynamics of Pumps*, Oxford University Press and CETI Inc., New York.
- [2] Japikse, D., Marscher, W. D., and Furst, R. B., 1997, *Centrifugal Pump Design and Performance*, Concepts ETI Inc., Wilder, VT.
- [3] Guelich, J. F., and Bolleter, U., 1992, "Pressure Pulsations in Centrifugal Pumps," *ASME J. Vib. Acoust.*, **114**, pp. 272–279.
- [4] Kittredge, C. P., 1985, "Centrifugal Pumps: General Performance Characteristics," *Pump Handbook*, 2nd ed., I. G. Karassik, W. C. Krutzsch, W. H. Fraser, and J. P. Messina, eds., McGraw-Hill, New York.
- [5] Neumann, B., 1991, *The Interaction Between Geometry and Performance of a Centrifugal Pump*, Mechanical Engineering, London.
- [6] Hasegawa, Y., Kikuyama, K., Maeda, T., and Murakami, M., 1990, "Unsteady Pressure Distributions and Forces on the Impeller Blades of a Centrifugal Pump," *Proceedings of XV IAHR Symposium 1990*, Belgrade, Yugoslavia, Sep. 11–14.
- [7] Kaupert, K. A., and Staubli, T., 1999, "The Unsteady Pressure Field in a High Specific Speed Centrifugal Pump Impeller. Part I: Influence of the Volute," *ASME J. Fluids Eng.*, **121**, pp. 621–626.
- [8] Parrondo, J. L., González, J., and Fernández, J., 2002, "The Effect of the Operating Point on the Pressure Fluctuations at the Blade Passage Frequency in the Volute of a Centrifugal Pump," *ASME J. Fluids Eng.*, **124**, pp. 784–790.
- [9] Hasegawa, Y., Kikuyama, K., and Maeda, T., 1990, "Effects of Blade Number on Hydraulic Force Perturbation on Impeller of Volute-Type Centrifugal Pump," *JSME Int. J., Ser. II*, **33**(4), pp. 736–742.
- [10] Dong, R., Chu, S., and Katz, J., 1997, "Effect of Modification to Tongue and Impeller Geometry on Unsteady Flow, Pressure Fluctuations and Noise in a Centrifugal Pump," *ASME J. Turbomach.*, **119**, pp. 506–515.
- [11] Chu, S., Dong, R., and Katz, J., 1995, "Relationship Between Unsteady Flow, Pressure Fluctuations and Noise in a Centrifugal Pump—Part B: Effects of Blade-Tongue Interactions," *ASME J. Fluids Eng.*, **117**, pp. 30–35.
- [12] Morgenroth, M., and Weaver, D. S., 1998, "Sound Generation by a Centrifugal Pump at Blade Passing Frequency," *ASME J. Turbomach.*, **120**, pp. 736–743.
- [13] Fatsis, A., Pierret, S., and Van den Braembussche, R., 1997, "Three-Dimensional Unsteady Flow and Forces in Centrifugal Impellers With Circumferential Distortion of the Outlet Static Pressure," *ASME J. Turbomach.*, **119**, pp. 94–102.
- [14] Van Esch, B. P. M., and Kruyt, N. P., 2001, "Hydraulic Performance of a Mixed-Flow Pump: Unsteady Inviscid Computations and Loss Models," *ASME J. Fluids Eng.*, **123**, pp. 256–264.
- [15] Byskov, R. K., Jacobsen, C. B., and Pedersen, N., 2003, "Flow in a Centrifugal Pump Impeller at Design and Off-Design Conditions—Part II: Large Eddy Simulations," *ASME J. Fluids Eng.*, **125**, pp. 73–83.
- [16] Wang, H., and Tsukamoto, H., 2001, "Fundamental Analysis on Rotor-Stator Interaction in a Diffuser Pump by Vortex Method," *ASME J. Fluids Eng.*, **123**, pp. 737–747.
- [17] Shi, F., and Tsukamoto, H., 2001, "Numerical Study of Pressure Fluctuations Caused by Impeller-Diffuser Interaction in a Diffuser Pump Stage," *ASME J. Fluids Eng.*, **123**, pp. 466–474.
- [18] González, J., Fernández, J., Blanco, E., and Santolaria, C., 2002, "Numerical Simulation of the Dynamic Effects Due to Impeller-Volute Interaction in a Centrifugal Pump," *ASME J. Fluids Eng.*, **124**, pp. 348–355.
- [19] Majidi, K., 2005, "Numerical Study of Unsteady Flow in a Centrifugal Pump," *ASME J. Turbomach.*, **127**, pp. 363–371.
- [20] Zhang, M., and Tsukamoto, H., 2005, "Unsteady Hydrodynamic Forces due to Rotor-Stator Interaction on a Diffuser Pump With Identical Number of Vanes on the Impeller and Diffuser," *ASME J. Fluids Eng.*, **127**, pp. 743–751.
- [21] González, J., and Santolaria, C., 2006, "Unsteady Flow Structures and Global Variables in a Centrifugal Pump," *ASME J. Fluids Eng.*, **128**, pp. 937–946.
- [22] González, J., Parrondo, J., Santolaria, C., and Blanco, E., 2006, "Steady and Unsteady Radial Forces for a Centrifugal Pump With Impeller to Tongue Gap Variation," *ASME J. Fluids Eng.*, **128**, pp. 454–462.
- [23] Miner, S. M., Flack, R. D., and Allaire, P. E., 1992, "Two Dimensional Flow Analysis of a Laboratory Centrifugal Pump," *ASME J. Fluids Eng.*, **114**, pp. 333–339.
- [24] Bachert, R., Ludwig, G., and Stoffel, B., 2005, "Three Dimensional, Impressed Cavitation Effects at the Tongue of the Volute in a Radial Pump," *Proceedings of FEDSM, 05*, Houston, TX, Jun. 19–23, ASME, New York, ASME Paper No. FEDSM2005-77373.
- [25] Jekat, W. K., 1985, "Centrifugal Pump Theory," *Pump Handbook*, 2nd ed., I. G. Karassik, W. C. Krutzsch, W. H. Fraser, and J. P. Messina, eds., McGraw-Hill, New York.

Design Principles and Measured Performance of Multistage Radial Flow Microturbomachinery at Low Reynolds Numbers

Changgu Lee
Selin Arslan

Department of Mechanical Engineering,
Columbia University,
New York, NY 10027

Luc G. Fr chet te

Department of Mechanical Engineering,
Columbia University,
New York, NY 10027;
Department of Mechanical Engineering,
Universit  de Sherbrooke,
Sherbrooke, QC, J1K 2R1, Canada

This paper introduces and experimentally demonstrates the design concept of multistage microturbomachinery, which is fabricated using silicon microfabrication technology. The design process for multistage microscale turbomachinery based on meanline analysis is presented, along with computational fluid dynamics predictions of the key aerodynamic performance parameters required in this design process. This modeling was compared with a microturbine device with a 4 mm diameter rotor and 100 μm chord blades, based on microelectromechanical system technology, which was spun to 330,000 rpm and produced 0.38 W of mechanical power. Modeling suggests a turbine adiabatic efficiency of 35% and $Re = 266$ at the maximum speed. The pressure distribution across the blade rows was measured and showed close agreement with the calculation results. Using the model, the microturbine is predicted to produce 3.2 W with an adiabatic efficiency of 63% at a rotor speed of 1.1×10^6 rpm. [DOI: 10.1115/1.2979010]

1 Introduction

Recently, silicon turbomachines have been developed for various applications, such as power generation, propulsion, compression, and pumping [1,2]. Although there are limitations in the choice of structural shapes due to the 2D characteristic of the microfabrication process, the potential benefits of high power per unit volume and low production cost due to batch processing are attractive [3,4]. To date, the development efforts of microscale turbomachines have mostly focused on those with just one pair of stator and rotor blade rows. However, a single stage configuration can only provide a limited pressure ratio, consequently restricting the thermal efficiency of miniature thermodynamic machines. Thus the need for multiple blade rows has arisen from theoretical and practical aspects during the development of gas turbines [1] and steam turbines [5]. High pressure ratios are especially beneficial to achieve a reasonable efficiency in a Rankine cycle, which produces power by expanding high pressure superheated steam through a turbine. The working fluid is pressurized in liquid state by a pump, allowing high pressure ratios, which compensate for the typically lower operating temperatures than in gas phase Brayton power cycles.

In this context, the concept of the multistage turbine was suggested for the micro-Rankine cycle power generation [5]. The whole system consists of microfabricated heat exchangers, a pump, a generator, bearings, and the turbine. The system was designed to generate a few watts of electrical power from a source of heat with an overall energy conversion efficiency between 1% and 12% depending on the thermal conditions. As a core power conversion component, the efficiency and power output of the turbine proved to be critical for the performance of the whole system.

This paper will present the design principles of multistage microturbomachinery, and characterization of a demo turbine device to demonstrate the concept of microscale radial flow multistage turbomachinery and to provide design basis for development of

the related technology. In the first part of this paper, the design approach for the microturbine with a planar geometry will be explained followed by aerodynamic analysis of blade rows at low Reynolds number using computational fluid dynamics (CFD). The configuration and fabrication of the demo device and the working principle of the components will be shown briefly for completeness. Finally, the characterization and test results of the rotating system and the microturbine performance will be presented.

2 Design Principles of Multistage Microturbines

2.1 Design Space for Microturbomachinery. Typically, large scale turbomachines operate at high Reynolds numbers (on the order of 10^6) and exhibit turbulent flow. Microscale configurations considered to date are mostly in the low Reynolds number range ($100 < Re < 10,000$), suggesting mainly laminar flow and higher viscous losses [1,2]. Unfortunately, the body of literature on blade passage aerodynamics (such as design correlations) is limited to high Reynolds numbers; hence new investigations are required at smaller scales.

Furthermore, the microfabrication approach constrains the designer to nontraditional configurations. Lithography allows precise patterning of the aerodynamic profiles on the surface of a silicon wafer, and these airfoil shapes are then transferred into the silicon substrate by deep reactive ion etching (DRIE). As illustrated in Fig. 1, this approach allows the creation of large arrays of well-defined blades that extend from the silicon substrate, which are most amenable to radial flow. An important outcome of this approach is that the flow area, A_f , increases linearly with radius, $A_f = 2\pi r h$, since the blade height, h , is defined during a single etch step and is therefore constrained to be uniform. Due to this fabrication approach, each stage operates at a different tangential speed proportional to radius, $U = \Omega r$, and the blades are constrained to 2D extruded shapes, without twist along the span.

2.2 Radial Multistage Design Approach. The design approach consists of a meanline analysis based on velocity triangles with loss, blockage, and deviation factors. This low order modeling approach is the basis for preliminary design of traditional multistage turbomachinery [6]. The flow is, however, purely radial through concentric rotor and stator stages of constant blade height. In this paper, the flow is considered to be compressible (ideal gas)

Contributed by the Fluids Engineering Division of ASME for publication in the JOURNAL OF FLUIDS ENGINEERING. Manuscript received February 26, 2008; final manuscript received July 14, 2008; published online September 23, 2008. Review conducted by Chunill Hah. Paper presented at the 2005 ASME International Mechanical Engineering Congress (IMECE 2005), Orlando, FL, November 5–11, 2005.

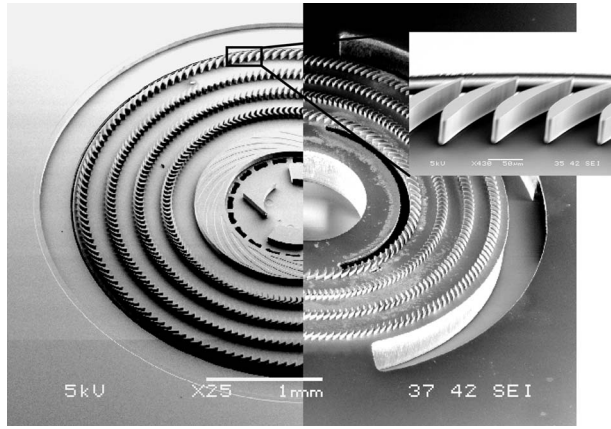


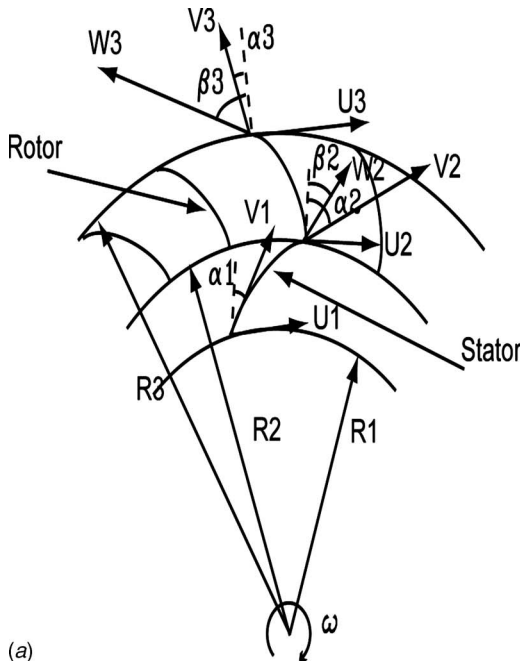
Fig. 1 Scanning electron microscopy (SEM) image of a typical radial multistage microturbine formed by DRIE, showing the rotors (left) and stators (right) on separate chips as well as a close-up view of one blade row (upper right). The turbine is assembled by laying the stator chip over the rotor chip in order to interdigitate the concentric blade rows.

and adiabatic. The nomenclature used to define the flow velocity components and the corresponding thermodynamic properties is illustrated in Fig. 2 for a stage composed of a stator and rotor. The process consists of conserving total enthalpy in a stator blade row or rothalpy in a rotor blade row, conserving mass, applying a loss coefficient correlation to define the total pressure, and applying a deviation correlation to define the exit flow angle. In addition, the blockage is applied to define the flow area in the mass conservation relation.

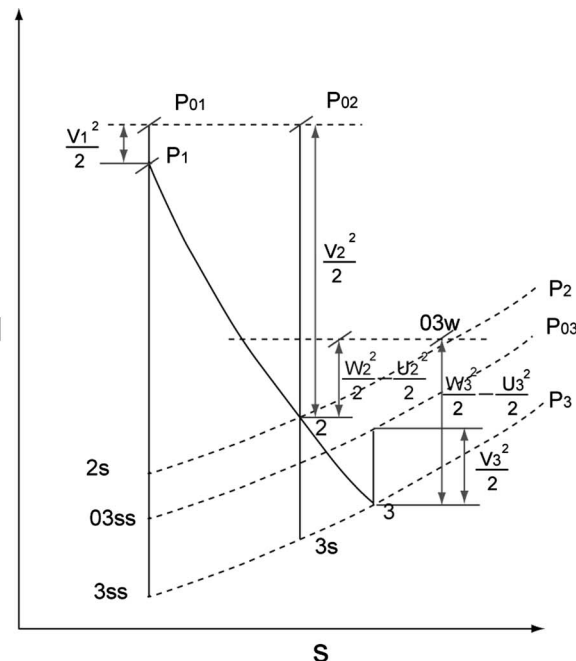
Stator. The pressure loss coefficient for a turbine stator is defined as

$$Y_N = \frac{P_{01} - P_{02}}{P_{02} - P_2} \quad (1)$$

where the subscripts represent inlet (1), exit (2), and total (0) properties in the stationary frame. At the exit, the isentropic relation for the compressible flow is



(a)



(b)

Fig. 2 Velocity triangles in one turbine stage: (a) velocity triangle diagram and (b) h - s diagram

$$\frac{P_{02}}{P_2} = \left(1 + \frac{K-1}{2} M_2^2\right)^{k/(k-1)} = C_2, \quad P_{02} = C_2 P_2 \quad (2)$$

where the Mach number is determined from mass conservation at the exit, as shown in Eq. (3).

$$M_2 = \frac{V_2}{\sqrt{kRT_2}}, \quad V_2 = \frac{\dot{m}}{2\pi r_2 \rho_2 h K \cos \alpha_2} \quad (3)$$

For mass conservation calculations, the density and mass flow rate are assumed at first. The exit velocity is calculated from mass conservation using velocity triangles to define the flow angles and considering the blockage.

The blockage was defined as the ratio of the effective flow area versus the geometric area ($K < 1$). The exit flow angle, α_2 , is defined as the blade angle minus deviation, δ .

The exit temperature is determined from the energy conservation for the adiabatic flow in the stator based on

$$T_2 = T_1 + \frac{1}{2C_p} V_1^2 - \frac{1}{2C_p} V_2^2, \quad V_1 = \frac{\dot{m}}{2\pi r_1 \rho_1 h \cos \alpha_1} \quad (4)$$

When Eq. (2) is substituted into Eq. (1), the static pressure at the exit is expressed as a function of the inlet total pressure and the loss coefficient:

$$P_2 = \frac{P_{01}}{\{Y_N(1 - 1/C_2) + 1C_2\}} \quad (5)$$

where the inlet total pressure is calculated from the given inlet static pressure and temperature and the assumed mass flow rate,

$$\frac{P_{01}}{P_1} = \left(1 + \frac{k-1}{2} M_1^2\right)^{k/(k-1)}, \quad M_1 = \frac{V_1}{\sqrt{kRT_1}} \quad (6)$$

Using the ideal gas relation

$$P_2 = \rho_2 RT_2 \quad (7)$$

pressure in Eqs. (6) and (7) can be equated:

$$\rho_2 RT_2 = \frac{P_1 \left(1 + \frac{k-1}{2} M_1^2 \right)^{k/(k-1)}}{\{Y_N(1 - 1/C_2) + 1\} C_2} \quad (8)$$

An iterative approach is then used to solve Eqs. (3)–(8) by changing the exit density until Eq. (8) is satisfied.

Rotor. In the rotor, the terms are redefined according to the relative coordinate and accounting for the centrifugal forces. The subscript 0 is replaced by 0_w . The absolute velocity, V , is replaced by the relative velocity, W .

In the rotating reference frame of the rotor, centrifugal forces will do work on the flow and therefore relative total enthalpy is not conserved. Instead, rothalpy, I_{0w} , which represents relative total enthalpy corrected for the centrifugal work, is the conserved quantity along a steady adiabatic streamtube in the rotating reference frame [7]:

$$I_{0w} = H + \frac{W^2}{2} - \frac{U^2}{2} \quad (9)$$

Equation (4) therefore changes to

$$T_3 = T_2 + \frac{W_2^2 - U_2^2}{2C_p} - \frac{W_3^2 - U_3^2}{2C_p} \quad (4')$$

Accordingly, the aerodynamic pressure loss, Y_R , must be defined with respect to the isentropic total pressure, which also changes across the blade row due to the centrifugal work. Using the isentropic relations, we can define the equivalent conserved pressure as the rotary stagnation pressure, P_{03w} :

$$\frac{P_{03w}}{P_3} = \left(1 + \frac{k-1}{2} M_{3w}^2 - \frac{U_3^2}{2C_p T_3} \right)^{k/(k-1)} = C_{3w} \quad (2')$$

The loss coefficient in the rotor, Y_R , is then redefined as

$$Y_R = \frac{P_{02w} - P_{03w}}{P_{03w} - P_3} \quad (1')$$

where the numerator is the change in the rotary stagnation pressure across the blade row.

The process to find the exit condition in the rotor is the same as the stator except for the above replacements. Through this process, all the exit conditions are calculated for the assumed flow rate, which is the same through all stages. The flow rate is adjusted by iteration until the exit static pressure at the final stage matches the desired value. Power produced by the turbine is obtained from the total enthalpy difference between inlet and outlet multiplied by the mass flow rate. For the microturbine system design, this calculation process is repeated to obtain the steady operating rotor speed (ω), which is obtained when the turbine power matches the power consumed through viscous drag by the surface area of the other parts.

2.3 Stage Configuration and Matching. For a turbine, work should be extracted from each stage with a similar loading distribution. The current radial outflow configuration results in the flow area and tangential speed that increase linearly with radius. Due to the work extracted from the flow, the pressure and density of the working fluid in the compressible flow decrease with radius. With the proper radial location of each stage, the density decrease can directly compensate for the through flow area increase and lead to approximately constant radial velocities in all stages. High velocities and hence power densities can therefore be maintained throughout the turbomachine. The desired layout should be such that the radius ratio between two locations is the inverse of the density ratio between those locations: $r_1/r_2 = \rho(r_2)/\rho(r_1)$. This leads to an outward flow turbine configuration, which is the opposite of normal practice. The centrifugal forces therefore pump the flow as we extract the work. For our typical operating conditions and multistage configuration, however, this opposing effect was found to be minimal compared with the advantage of operat-

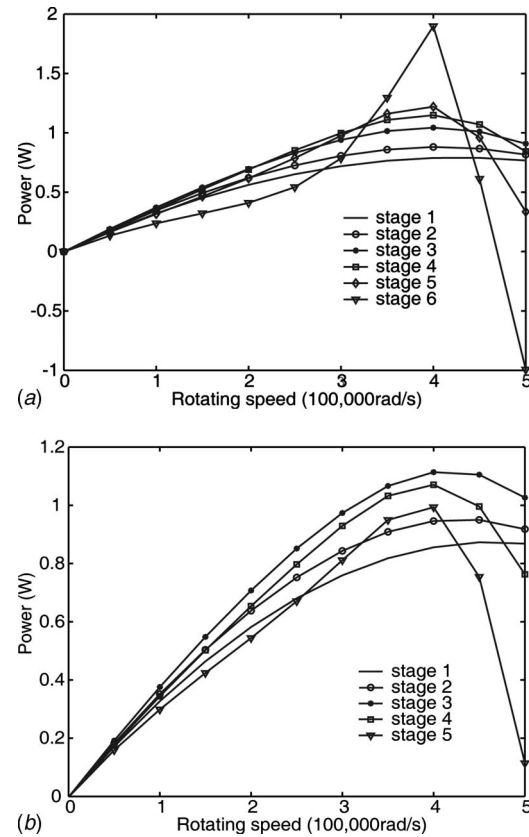


Fig. 3 Stage matching for two different stage designs. Baseline flow rate of 24 mg/s; 1.5 mm diameter rotor for both. Inlet pressure of 0.6 MPa and outlet pressure varies. (a) Six stage design and (b) five stage design.

ing all the stages at nearly constant high flow velocities. Given the constant blade height and the large radius ratio between the first and the last stage, we were forced to choose an outward flow configuration.

For a baseline mass flow of 24 mg/s, a power level of 1 W per stage is expected, which corresponds to 40 kJ/kg. In order to match the specific power levels defined in the cycle analysis of a Rankine steam turbine, 10–30 stages are expected to be required [5]. However, Fig. 3 suggests that it is difficult to design more than five stages on a single rotor. In the six stage design, it is noticed that most stages have relatively flat curves, suggesting good robustness, except the last stage (sixth stage). Although its power output is more than any other stage, it occurs over a narrow range and drops dramatically at higher speeds to significantly negative values. The flow velocity can also change significantly and in some cases can exceed the critical velocity. This implies that if the flow rate, heat transfer, and/or the fluid density change, the power output can change drastically. By changing the geometry of the sixth stage of the turbine, this problem can be avoided. However, in a stable condition, the last stage does not produce as much power and is better to be removed. Therefore, a single rotor is expected to provide on the order of 5 W of mechanical power (200 kJ/kg). Preliminary designs were also developed for a 28 W (1150 kJ/kg), which consists of five individual rotors in series with power levels ranging from 3.8 W to 8.4 W. It operates with an inlet pressure of 8 MPa and a temperature of 780°C [8].

3 Blade Passage Aerodynamics

Three main parameters are required as input for the above design process: the loss coefficient, deviation, and blockage. These aerodynamic parameters depend on the blade passage geometry

Table 1 Blade row configurations

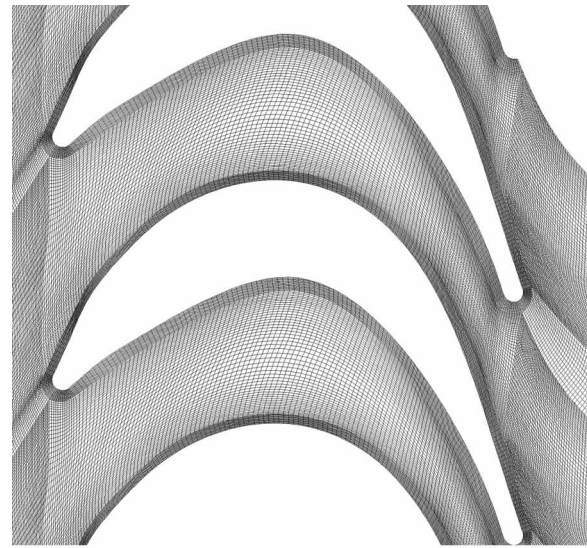
| NACA A3K7 | Rotor 1 | Rotor 3 |
|--------------|---------------------|----------------------|
| Chord length | 98.29 μm | 114.76 μm |
| Chord axial | 93.07 μm | 89.33 μm |
| Inlet angle | 56 deg | 22 deg |
| Outlet angle | -74 deg | -60 deg |
| Stagger | 19 deg | 39 deg |

and operating conditions. The geometry is defined by the airfoil profile, the stagger angle, and the solidity (i.e., the ratio of the blade chord to spacing, $\sigma=c/s$). Typically, correlations for loss and deviation are derived from experimental measurements and used in the initial design process. For a given geometry, they are found to depend on the incidence angle and Mach number of the incoming flow but are not a function of Reynolds number for traditional scale turbomachinery ($\text{Re} \sim 10^6$) [6]. In the operating regimes of microturbomachinery ($100 \text{ Re} < 100,000$) [9,10], the influence of Reynolds number is, however, expected to become important. As a first step, we have therefore chosen to use numerical simulations to explore the flow behavior in microturbomachinery cascades and to extract the main performance parameters (loss coefficient and deviation). These will enable the design of experiments to later validate the simulation results. This approach was mainly chosen since the size of microfluidic devices precludes the use of traditional instrumentation and requires the development of embedded sensors, not currently available. Scaled test apparatus have also been proposed and exhibit unique experimental challenges [11]. Fortunately at the microscale, flows are dominantly laminar and CFD solutions are expected to be increasingly accurate compared with large scale turbulent flows.

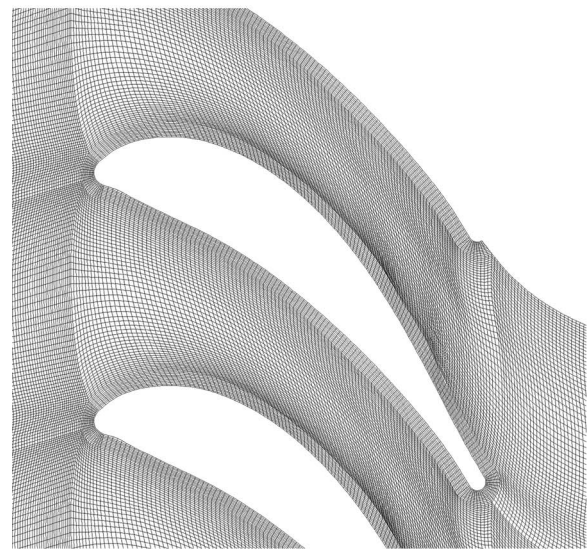
The current work is limited to the study of loss and deviation as a function of incidence and Reynolds number; the effect of Mach number will be studied subsequently since it was kept low in the current study and experiments ($M_{\text{inlet}} < 0.2$). Two blade passage geometries are considered, as described next.

3.1 Blade Passage Geometry. The geometry chosen for this study is based on the NACA A3K7 turbine airfoil [12]. The primary series A3K7 is for reaction blades in which there is acceleration through the cascades. The camber line shape gives rapid turning in the forward part of the blade, where the Mach numbers are low. The profile is defined by a series of points for the camber line (x_c, y_c) and a thickness distribution along that line (with a maximum thickness to chord of $t_{\text{max}}/c=20\%$). The stagger (angle of the blade to the radial direction) and camber (difference between leading and trailing edge angles) are adjusted in order to match the flow angles defined during the previous meanline analysis. Different levels of camber are achieved by scaling the tangential coordinate ($x_c, C \times y_c$), and the blade is tilted to match the incoming flow angle. High camber (Rotor 1) and low camber (Rotor 3) blades are analyzed here, with configurations summarized in Table 1. The nominal solidity is $\sigma=2$. The trailing edge is slightly modified in order to accommodate microfabrication limitations: It is shortened by 2% chord and kept to a minimum thickness of 4 μm .

3.2 Numerical Simulations. Commercial CFD software (FLUENT 6.1) is used for the numerical calculations. The steady-state Navier–Stokes equations are solved for the compressible laminar flow through a 2D section of the flow field near midspan with adiabatic walls. The blockage due to hub and shroud boundary layers is currently neglected, such that the flow passage is assumed to be of constant effective height. A segregated implicit solver is chosen with the SIMPLEC pressure-flow coupling algorithm and second order upwind schemes for the energy, momentum, and density equations. Cartesian grids were defined with 27,765 nodes (approximately 400×60) for Rotor 1 and 20,645



(a)



(b)

Fig. 4 Typical computational grid. Upstream and downstream areas are not shown and the blade passage is repeated for illustration purposes: (a) Rotor 1 and (b) Rotor 3

nodes (approximately 320×60) for Rotor 3, as shown in Fig. 4. The meshes were refined until the main parameter, which is the pressure loss coefficient, does not depend on the grid density for given boundary conditions. Because the calculations were done for low Reynolds numbers, leading to relatively thick boundary layers, the mesh density near the surface did not need to be as refined as for typical high Reynolds number calculations.

The working fluid was air with viscosity defined by Sutherland's law and with the following nominal operating conditions: inlet Mach number $M_1=0.14$, inlet total temperature $T_{01}=300 \text{ K}$, and exit static pressure $P_2=1 \text{ atm}$. The inlet static pressure is adjusted to maintain M_1 constant as the incidence or Reynolds number is changed. Calculations were done in a stationary reference frame in order to simulate cascade test conditions. The computational domain was limited to a single blade passage, with inlet and outlet regions extending one chord upstream and downstream, respectively.

3.3 Effect of Incidence. Incidence, defined as the angle between the incoming flow and the blade leading edge, is a key

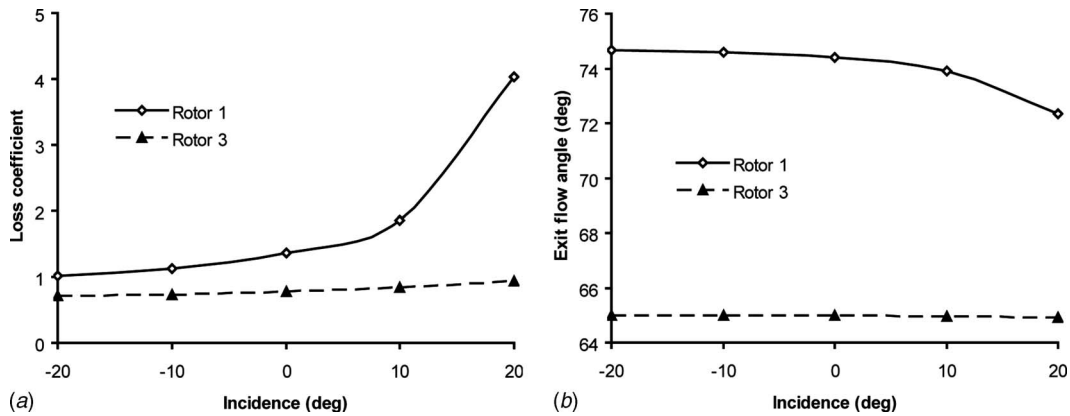


Fig. 5 Loss coefficient (a) and exit flow angle (b) as a function of incidence for high camber (Rotor 1) and low camber (Rotor 3) NACA A3K7 airfoils with solidity $\sigma=2$. In all cases $Re=350\pm 20$ and inlet Mach number $M_1=0.14\pm 0.02$. The blade exit angles of Rotors 1 and 3 are 74 deg and 60 deg. (a) Loss coefficient versus incidence and (b) exit flow angle versus incidence.

parameter that affects the aerodynamic performance of macroscale blade rows. The first set of calculations explores the effect of the inlet flow angle on the loss coefficient (Eq. (1)) and the exit flow angle (i.e., deviation). Numerical results are shown in Fig. 5 for both geometries studied here (Rotors 1 and 3). The exit total pressure and exit flow angle are taken as the mass-average values at the outlet boundary (i.e., one chord downstream of the trailing edge); this approach leads to a conservative mixed-out loss coefficient. Within the blade passage, the Mach number reaches $0.5 < M_{max} < 0.6$.

The main observations in Fig. 5 are the increase in loss coefficient and reduction in flow turning with increasing incidence. The effect is most important for the high camber blade row (Rotor 1), whereas the low camber blade row (Rotor 3) remains practically unaffected. Unlike high Re turbomachinery, which exhibits flow separation at high positive or negative incidence angles, flow separation was not present in the low Re simulations. Negative incidences even slightly reduced the loss coefficient instead of increasing it.

3.4 Effect of Reynolds Number. The second set of calculations explored the effect of Reynolds number on the loss coefficient and the exit flow angle. Here, Re is defined with blade inlet properties and blade chord length. Numerical results are shown in Fig. 6. During these calculations, the inlet Mach number was

maintained at $M_1=0.14\pm 0.02$ and the incidence was fixed to zero. The Reynolds number was varied by scaling the model and changing the inlet total pressure to maintain M_1 .

The most noticeable trend is the gradual increase in total pressure loss and reduction in flow turning as the Reynolds number is reduced. Below a critical Reynolds number of $Re_{crit}=200-300$, the loss coefficient and deviation start to increase dramatically. This behavior will be discussed later, but it should be noted that no flow separation was observed. As the Reynolds number increases, the loss coefficient and exit flow angle tend to asymptote and therefore become less a function of Reynolds number, as expected.

For design purposes, the following loss coefficient correlation is proposed:

$$Y = \frac{D_1}{\sqrt{Re}} + \frac{D_2}{Re} \quad (10)$$

The first term is inspired from the drag of a laminar boundary layer over a semi-infinite flat plate, while the second term stems from the consideration of the finite plate or airfoil length [13]. By fitting this expression to the numerical results, the following coefficients are found for the specific conditions listed in Secs 3.1 and 3.2: (a) Rotor 1: $D_1=6$, $D_2=400$ and (b) Rotor 3: $D_1=6$,

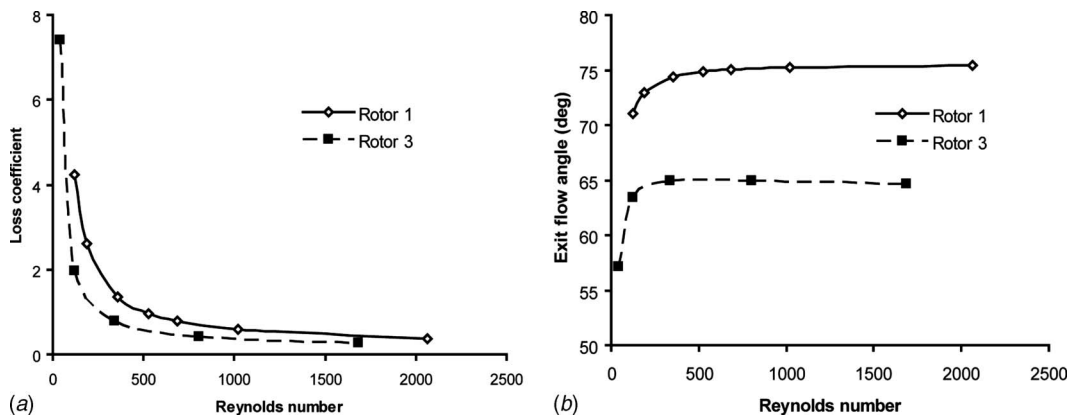


Fig. 6 Loss coefficient (a) and exit flow angle (b) as a function of Reynolds number for high camber (Rotor 1) and low camber (Rotor 3) NACA A3K7 airfoils with $\sigma=2$. In all cases incidence $i=0$ and inlet Mach number $M_1=0.14\pm 0.01$. (a) Loss coefficient versus Reynolds number and (b) exit flow angle versus Reynolds number.

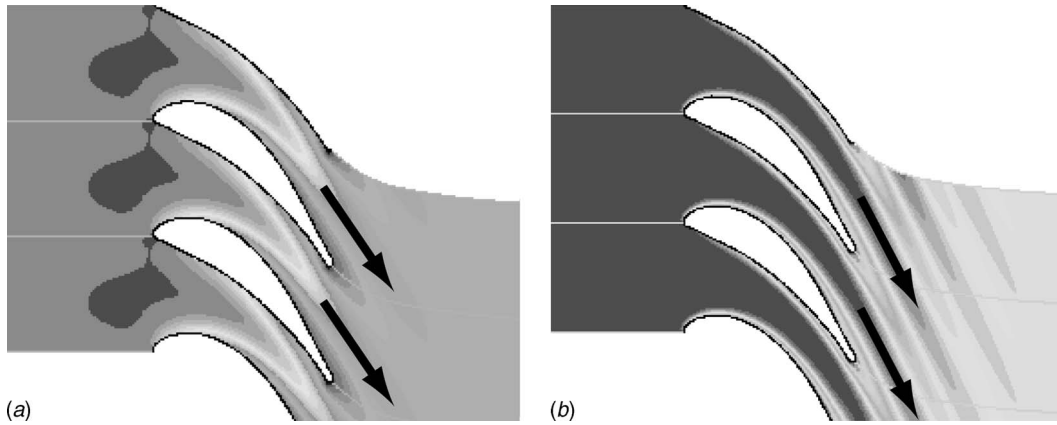


Fig. 7 Total pressure contours for NACA A3K7 turbine stage with solidity of 2 (Rotor 3), showing that low Reynolds numbers (a) lead to thick boundary layers and slightly shallower exit flow angles than higher Reynolds number flow (b). The nonuniformity of the total pressure at the entrance in (a) appears to be from the heat transfer due to acceleration of the flow. (a) $Re=60$ and (b) $Re=665$.

$D_2=170$. In general, the coefficients (D_1, D_2) will depend on blade geometry (profile, camber, and solidity) and operating conditions (incidence and Mach number).

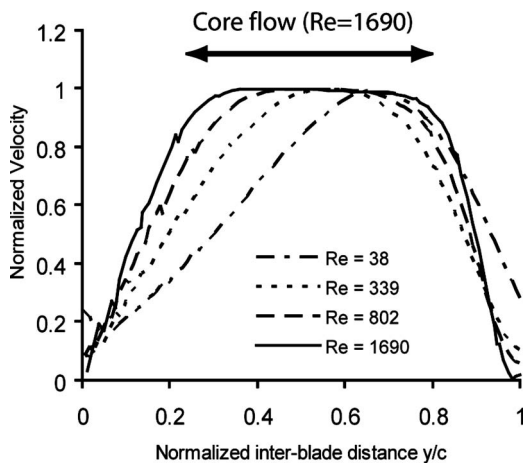


Fig. 8 Profile of the normalized velocity magnitude (V/V_{max}) across the flow passage (Rotor 3) taken at 5% chord downstream of the blade row. In x-axis, $y/c=0$ indicates the suction side and $y/c=1$ indicates the pressure side.

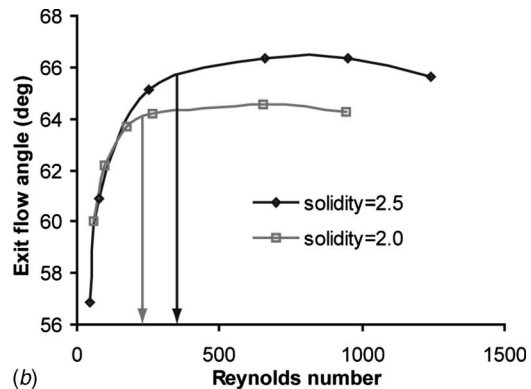
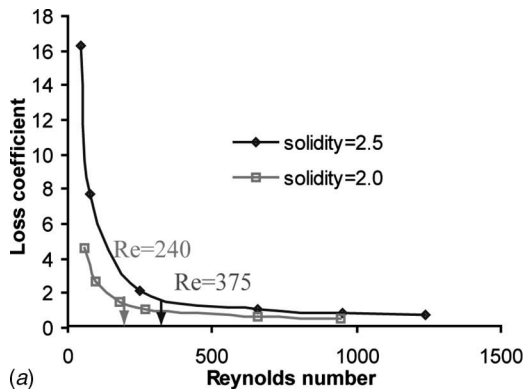


Fig. 9 Loss coefficient and exit flow angle as a function of Reynolds number for the same airfoil (Rotor 3) but with different solidities, $\sigma=c/s$: (a) pressure loss coefficient and (b) exit flow angle

3.5 Discussions

3.5.1 Critical Reynolds Number. The critical Reynolds number $Re_{crit}=200-300$ identified above appears to stem from the change in flow profile at the exit of the blade row, going from the boundary layer flow to the fully developed flow as the Re decreases. Total pressure contours are shown in Fig. 7 for two operating conditions: (a) $Re < Re_{crit}$ and (b) $Re > Re_{crit}$ to illustrate the boundary layer development along the blade passage. As better shown in Fig. 8, the profile of the velocity magnitude across the blade passage at the trailing edge (from suction to pressure side) shifts from the core flow at high Re to the merged boundary layers at low Re . This change in the regime appears to be associated with increased loss and reduced flow turning.

A first-order estimate of the critical Reynolds number can be derived from laminar flow relations. First, considering the Blasius solution for the laminar flow over a flat plate (with no pressure gradient), the boundary layer thickness at the trailing edge can be defined as [13]

$$\delta_c = 5.0 \sqrt{\frac{vc}{u}} = \frac{5.0c}{\sqrt{Re}} \quad (11)$$

Since the boundary layers will merge at the trailing edge when $\delta_c = s/2$ and solidity is defined as $\sigma = c/s$, we can solve for Re :

$$Re_{crit,1} = 100\sigma^2 \quad (12)$$

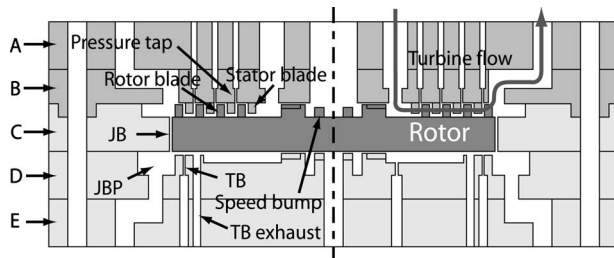


Fig. 10 Configuration of the demo microturbine device. The letters (A–E) identify the five wafers.

For the current configurations, $\sigma=2$, hence $Re_{crit,1}=400$. A similar estimate can be done by considering the blade passage as a channel and defining the Re required such that the entry length, x_{entry} , is equal to the blade chord, c [13]:

$$\frac{x_{entry}}{D} = \frac{c}{s} = 0.04 \frac{uD}{\nu} = 0.04 \frac{uc}{\nu c} = 0.04 \frac{Re}{\sigma} \quad (13)$$

Hence,

$$Re_{crit,2} = 25\sigma^2 \quad (14)$$

and $Re_{crit,2}=100$ for $\sigma=2$. These values appear to bound $Re_{crit}=200-300$ found from the numerical simulations. Based on these observations, one can suggest the following correlation for the critical Reynolds number:

$$Re_{crit} = 60\sigma^2 \quad (15)$$

3.6 Effect of Solidity. The above expressions suggest that blade rows of higher solidity would incur higher losses and deviation at low Reynolds number. Figure 9 illustrates this point by superposing results for $\sigma=2$ and $\sigma=2.5$. We can observe a ratio of approximately $(2.5/2)^2 \sim 1.5$ between the Re_{crit} (i.e., knee of the curve) for both solidities.

3.7 Effect of Blockage. Blockage is caused by many flow effects such as boundary layer on the endwalls and the blades, secondary flows, and tip leakage. In order to simplify the analysis and due to lack of relevant data at this small scale, only boundary layer on the endwalls was included in the calculations. The blockage was defined based on the boundary layer growth theory as follows:

$$K = 1 - a\sqrt{\Delta r} \quad (16)$$

where Δr represents radial position from the flow inlet and the constant a depends on the geometry and flow condition.

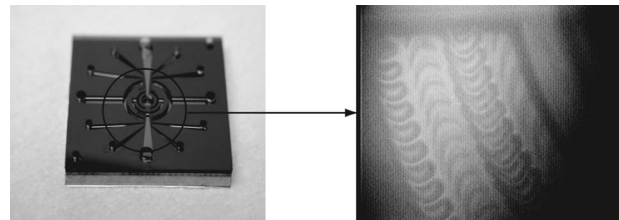


Fig. 11 Microturbine device: chip-scale view of the $15 \times 15 \text{ mm}^2$ device (left) and close-up infrared (IR) picture of interdigitated blade rows (right). Darker blades are rotors and brighter ones are stators.

4 Configuration of Silicon Microturbine Device

In order to prove the design concept of the multistage micro-turbomachinery, a demo microturbine was developed and fabricated using the silicon microtechnology, which is commonly used in the semiconductor industry. The device was designed to have four stages of blade rows producing about 1 W of mechanical power each from steam with 200°C and 3 atm at 1.3×10^6 rpm, which corresponds to 270 m/s of the rotor tip speed [8].

The fabricated device encloses a 4 mm diameter rotor and consists of the flow paths to the turbine and bearings, as shown in Fig. 10. The bearing system, which supports the rotor axially and laterally as it rotates, is composed of hydrostatic thrust and journal bearings (JBs). The JB, which corresponds to the circumferential gap surrounding the rotor, exploits the loss mechanisms at the entrance of the narrow channel and difference of pressure distribution between opposite sides of the bearing to create a restoring force [8]. The thrust bearing (TB), which consists of small circular nozzles underneath the rotor, utilizes the flow resistances between nozzles and a planar clearance to balance out the axial movement of the rotor. The rotor is a disk with four concentric blade rows on one side, each composed of 80–180 blades. Four rows of stator blades also extend out from the upper layer, between the rotor blade rows, making an interdigitated radial flow turbine, as shown in Fig. 11. The height of the rotor blades is $70 \mu\text{m}$ and that of the stator blades is $50 \mu\text{m}$. The profile details of the fabricated blades and their shapes are described in Table 2 and Fig. 12, respectively. The geometry chosen for this study is based on the NACA A3K7 turbine airfoil, as in Sec. 2 [12]. The solidity of each blade row (chord-to-pitch ratio) is 2, and the radial gap between the blade rows is $25 \mu\text{m}$. The base tip clearance of the rotor blade is $1.5 \mu\text{m}$ and that of the stator is $20 \mu\text{m}$, which stems from the excessive etching during the fabrication process [8].

As illustrated in Fig. 10, the high pressure flow is fed from the top, does a right angle turn into the first blade row, and flows outward through the subsequent blade rows. Expansion of the working fluid provides the energy to drive the rotor. The increas-

Table 2 Specifications of the stator and rotor blade rows

| Stage | Inlet angle (deg) | Outlet angle (deg) | Radial length (μm) | Chord length (μm) | No. of blades |
|--------|-------------------|--------------------|---------------------------------|--------------------------------|---------------|
| Stator | | | | | |
| 1 | 14 | 67 | 96.4 | 140.8 | 87 |
| 2 | 53 | 66 | 93.3 | 98 | 155 |
| 3 | 33 | 61 | 93.4 | 96.4 | 168 |
| 4 | 16 | 59 | 92 | 94.2 | 181 |
| Rotor | | | | | |
| 1 | 53 | 70 | 94.1 | 98.9 | 139 |
| 2 | 37 | 62 | 93.8 | 106.9 | 158 |
| 3 | 16 | 57 | 92.2 | 116.3 | 168 |
| 4 | -9 | 65 | 90.3 | 147.6 | 152 |

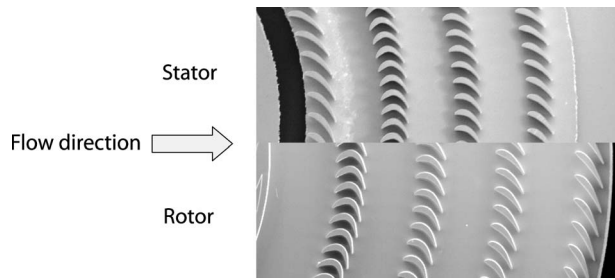


Fig. 12 Fabricated stator and rotor blade rows. Upper rows are the stator, and lower ones the rotor. After device assembly, these become interdigitated.

ing flow area along the stages maintains a nearly constant flow velocity, which can prevent premature choking in the flow passages. The bearing flows are supplied from the bottom. The journal bearing flow goes to the journal bearing plenum (JBP) and joins the turbine exit flow to be discharged after passing through the narrow gap. The thrust bearing flow splits into two directions and is discharged to the journal bearing plenum and to the atmosphere through the exhaust channel beside the nozzles.

The complete device is composed of five wafers, as shown in Fig. 10: one Pyrex glass wafer (wafer A), one silicon-on-insulator (SOI) (wafer B), and three silicon wafers (wafers C–E). The glass wafer, which is the first layer, was machined by ultrasonic drilling. The other four wafers are fabricated using silicon micromachining techniques such as photolithography, reactive ion etching (RIE), deep reactive ion etching (DRIE), and plasma-enhanced chemical vapor deposition (PECVD) to create channels, nozzles, bearings, and turbine blades. The machined layers are then anodically bonded (between wafers A and B) and fusion bonded (between wafers C–E). Details about the bearing system design, the fabrication process, and the operating procedures are beyond the scope of this paper; they are presented elsewhere [8,14,15].

5 Experimental Testing and Analysis

5.1 Experimental Setup and Operating Procedures. The test setup is composed of a gas flow control system and measurement sensors adopted from the previous microturbine development [16]. The working fluid is air for the experiments. The gas test consists of six separate pressure sensors (OMEGA® PX4202) and five mass flow controllers (MKS® 1179A) for bearing and turbine operation, an eight-channel pressure sensor (Scanivalve® Zoc17IP/8PX-APC 100PSID) for turbine interblade row pressure measurement, and one optical displacement probe (Philtec® Model 6D) for the measurement of the rotational speed of the rotor.

The eight pressure sensors are connected to interblade row static pressure taps, which correspond to the exit points of each blade row. The turbine inlet pressure, which is the first stator inlet pressure, could not be directly measured due to the lack of space for the pressure tap in the device but was derived by assuming the inlet pressure in the modeling and calculating interblade row pressures. The inlet pressure is defined when the calculated first stator exit pressure closely matches the measured one. The device is operated by maintaining the thrust bearing flow rate constant with a fixed feed pressure. The turbine flow rate is then increased by regulating the differential pressure between the supply and exhaust of the turbine using the metering valves.

5.2 Measured Performance and Predictions. During operation, pressure, flow rate, and rotation rate data were obtained. Figure 13 shows the turbine flow rate as a function of differential pressure between turbine inlet and outlet (dP). The uncertainty of the flow rate comes from the measurement error of the sensor. Figure 14 shows the rotational speed in rpm as a function of the

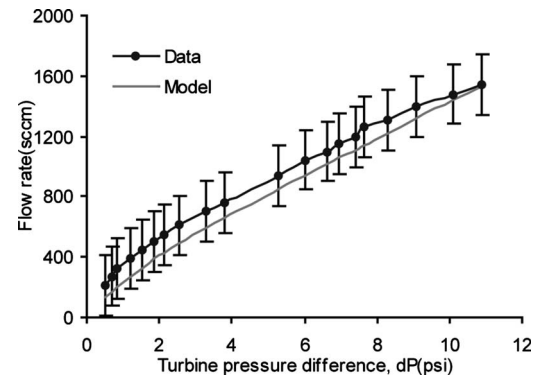


Fig. 13 Flow rate as a function of the differential pressure across the turbine

turbine flow rate. The maximum speed measured from the test was 330,000 rpm, which corresponds to 70 m/s in tip speed for the 4 mm diameter rotor. Up to this speed, no instability in the rotor operation was observed. Currently, the maximum rotational speed achieved has been limited largely due to device failures, stemming from bearing limitations and mechanical failure [8].

Prediction. The model calculates the speed and turbine flow rate using the estimated pressure differential as an input. The speed results from the balance between the turbine power and surface drag torques acting on the rotor. The power generated by the turbine is estimated as the product of the mass flow rate and enthalpy difference between inlet and outlet. Detailed calculation procedure of the speed and power is beyond the scope of this paper but can be found in Ref. [8].

In this calculation, the loss coefficient and blockage were included in the meanline analysis. The correlation for the profile loss of the turbine blades was obtained by the 2D CFD calculations and expressed as a function of Reynolds number, as mentioned in Sec. 3. The coefficients in Eq. (10) were only predicted for Rotors 1 and 3 using the CFD calculations. For the other blade rows, they were linearly interpolated according to their camber angles assigning higher values for bigger angles.

Based on the CFD data, the impact of incidence was found to be relatively small compared with Reynolds number effects. For simplicity here, the constants are considered as functions of geometry only, especially camber angle, assuming negligible incidence effects and low Mach numbers ($M < 0.2$).

The loss may be split into several categories such as profile loss, endwall loss, secondary loss, and tip clearance loss [17]. The correlation mentioned above corresponds to the profile loss, which is associated with boundary layer growth over the blade profile, a

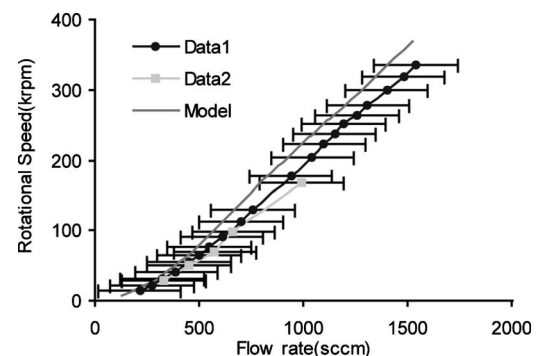


Fig. 14 Rotation rate as a function of the flow rate of pressurized air. Data are presented for two different devices showing repeatability. These data come from Ref. [14], but shown here for completeness.

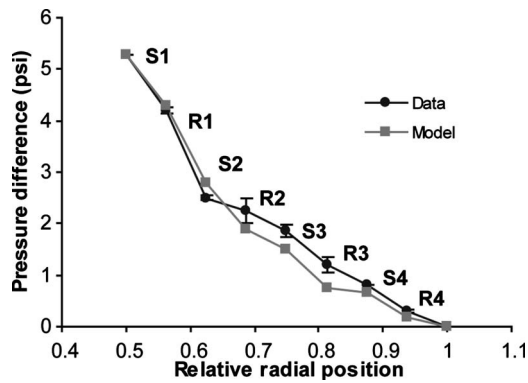


Fig. 15 Pressure distribution throughout the multistage microturbine. The relative radial position indicates the distance from the center of the rotor divided by the disk radius, and the pressure difference is the measured pressure subtracted by the exit pressure. The rotors and stators for each of the four stages are identified by R# and S#, respectively.

characteristic of the two-dimensional flow around the airfoil. The other losses are related to 3D effects of the turbine flow. In the current modeling, these 3D effects were not predicted but were considered by multiplying the profile loss coefficient in Eq. (10) by a factor greater than unity. A factor of 1.4 was found to fit the calculation to the measured data as closely as possible. This approach assumes that the total loss is proportional to the profile loss, as suggested in large scale turbine research [17] and micro-scale investigations [9]. Furthermore, the factor of 1.4 used here is similar to that extracted from the comparison between 2D and 3D CFD calculations done for other microturbomachines [9].

The coefficient a in Eq. (16) for blockage in each blade row was fixed to 8 based on previously published CFD results, which were obtained for higher Reynolds number range [9].

Although CFD investigations (Sec. 3) suggest that the exit flow angle varies at low Reynolds number range, deviation effects were not included in this model due to the difficulty in generalization for different angles from the limited CFD data. These simplifications are also applied to the calculations for characterization and projected performance at higher speeds in Secs. 5.3, 6.1, and 6.2.

The modeling results show slightly higher values for the same flow rate compared with the experimental data. As mentioned previously, the model does not include the loss factors for changing incidence and high Mach number and simply accounts for 3D losses by applying a correction factor. This may contribute to the higher prediction of the model. Also, the excessive tip clearance of the stator could be a cause. The clearance between the stator blade tips and the rotor surface was about 40% of the blade height, which resulted from the device fabrication process. That portion of the turbine flow can pass through the stator blade rows without appropriate turning, which would in turn reduce the fluid-to-mechanical energy conversion in the rotor, hence resulting in lower speed and power per unit flow.

5.3 Turbine Characterization. The pressures between the blade rows were measured at each operating condition. Figure 15 shows the pressure distribution at one operating point. The trend of the other data points is typically similar to that illustrated here. Generally the mechanical power generated by the flow is proportional to the pressure drop across the rotor blades. The pressure distribution shows that there is higher pressure drop in the first rotors than the last: $\Delta P(R1) > \Delta P(R2) > \Delta P(R3/R4)$, which reflects power production in the same order, as shown in Fig. 16.

The power produced from each stage is around 0.1 W in average, totaling 0.38 W at the highest measured speed.

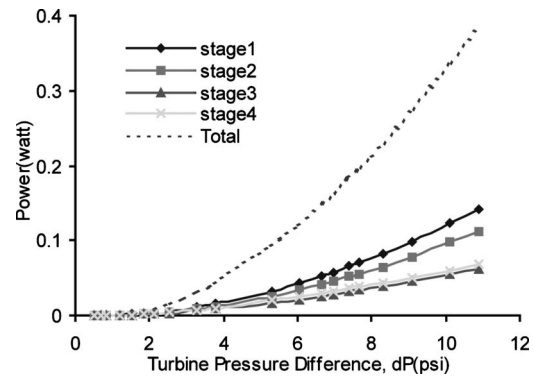


Fig. 16 Estimated power production from each stage

6 Discussion

6.1 Loss and Efficiency. Unlike large scale turbomachinery, which operates usually at high Reynolds numbers ($10^7 \text{ Re} < 10^8$), this microturbine runs at very low Reynolds number ranging from $\text{Re} = 10^2$ to 10^3 . The viscous loss effects are clearly expected to become dominant in the microturbine. The turbine cascade CFD calculation for microscale turbines showed that the pressure loss is at least one order of magnitude higher than for conventional machines [17]. Figure 17 shows the averaged loss coefficient as a function of the averaged Reynolds number for the current geometry and flow condition, using the meanline model and correlations proposed herein. As expected, the loss decreases as Re increases.

The total adiabatic efficiency of the turbine, which is defined as the ratio of the actual total enthalpy differential to isentropic total enthalpy differential, reaches 35.7% at $\text{Re} = 266$, as shown in Fig. 18. When the Reynolds number increases, the viscous loss coefficient decreases so the adiabatic turbine efficiency should increase, as shown in Figs. 17 and 18. They reveal the significant impact of the Reynolds number, especially in this low range, and the benefit of higher-speed operation for better efficiency.

6.2 Prediction for Higher-Speed Operation. As shown in Sec. 6.1, the efficiency at the measured speed is still much lower than that of large scale turbines, which are normally over 80–90%. Although it is not expected that small devices can reach efficiency levels of large machines due to fundamental scaling [10], it is desirable to increase the turbine efficiency up to a certain level to achieve reasonable performance of the overall power production microsystem.

Figures 19 and 20 show the projected turbine efficiency and the power produced from each stage. In the calculation process, the

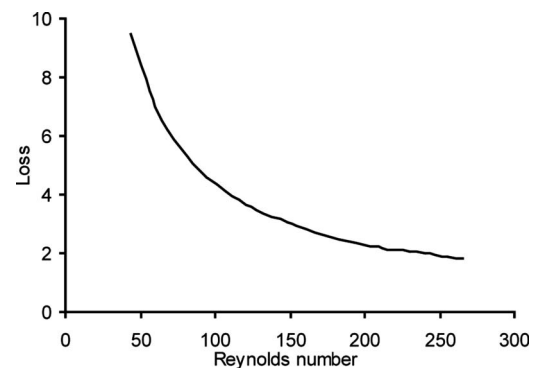


Fig. 17 Estimated pressure loss coefficient, γ , as a function of Reynolds number. The numbers are averaged values across the blade rows.

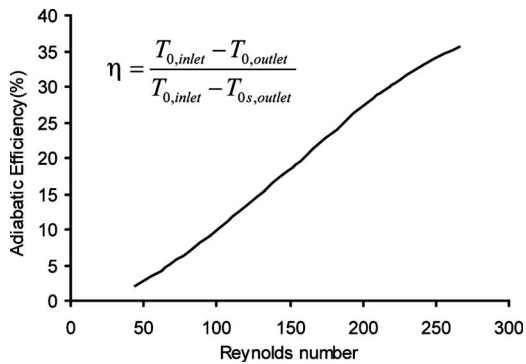


Fig. 18 Estimated total adiabatic efficiency of the turbine as a function of averaged Reynolds number

static pressure at the outlet is fixed at atmospheric conditions and the inlet static pressure varies. The speed and flow rate at the highest performance point are 1.1×10^6 rpm and 3500 SCCM (SCCM denotes cubic centimeter per minute) with a turbine pressure ratio of 3:1. The projected efficiency reaches up to 63% at $Re=674$ for a total turbine power of 3.2 W. The estimated efficiency appears to be acceptable considering the micro-Rankine power cycle analysis [5]. Therefore, high-speed operation over 1×10^6 rpm or $Re > 600$ is recommended for the current design to achieve the required levels of performance.

These predictions suggest that the current multistage turbine configuration may need to be revised since the power production distribution at high pressure range is different from the low pressure range, as shown in Fig. 20. The increasing production of the second stage over the first stage comes from higher expansion in that stage. This phenomenon could be undesirable because the

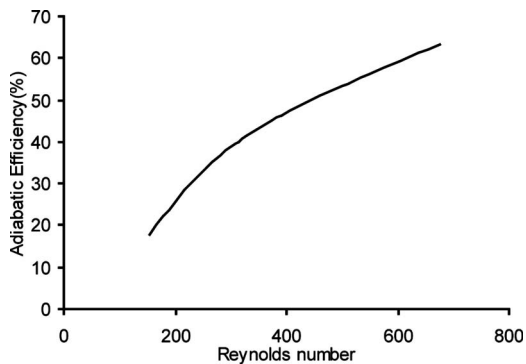


Fig. 19 Model prediction of the total adiabatic efficiency at extended Re range

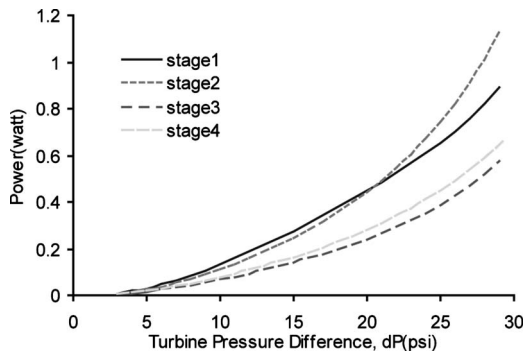


Fig. 20 Model prediction of the power production from each stage at higher differential pressure

unexpected expansion can cause premature choking and can deteriorate the overall performance of the turbine. In this perspective, further analysis of blockage, loss, deviation, and heat transfer in low Reynolds turbomachinery and high-speed testing seem to be necessary to guide future designs.

7 Conclusion

In this paper, we have presented an approach for the design of radial flow multistage silicon microturbomachinery and validated it through experimental demonstration of a microturbine with four stages. Using a model based on the meanline analysis, it is suggested that a planar radial flow configuration is appropriate but that a limited number of stages can be implemented per rotor in practice because it is hard to match the loading across the stages. The main aerodynamic parameters required for the design process (loss coefficient and deviation) were defined using computational fluid dynamics of the laminar flow through standard blade profiles but in the low Reynolds number range ($100 < Re < 1000$). It was found that dramatic increases in loss and deviation occur below a critical Reynolds number of approximately $Re_{crit} = 200-300$. This behavior is associated with merging of the boundary layers at the exit of the blade passage. To maintain acceptable efficiency, it is therefore preferable to limit the scale of microturbomachinery beyond this threshold, setting a minimal scale on the order of $100 \mu m$ for flow velocities in the hundreds of m/s. Microturbomachinery must therefore operate at high speed to achieve acceptable efficiencies.

A demo four-stage microturbine device was fabricated out of five wafers using photolithography, shallow and deep etching, and silicon and glass bonding techniques. The turbine rotor with 4 mm in diameter is supported by gas lubricated bearings and was spun up to 330,000 rpm, producing 0.38 W of mechanical power. The measured pressure distribution between the blade rows shows close agreement with the modeling results. The modeling suggests 35% of total adiabatic efficiency with an average $Re=266$ in the turbine. The efficiency at 1.1×10^6 rpm is estimated to reach 63%, producing 3.2 W of total power at $Re=674$.

Considering the unprecedented small scale of the blades and low Reynolds numbers, the power production and efficiency level at the recommended operating range are quite encouraging in the perspective of the whole Rankine cycle efficiency. This research is expected to provide a guideline on the smallest size and lowest Reynolds number range for practical microturbines and to contribute to the development of other types of multistage microscale turbomachinery, such as pumps and compressors.

Acknowledgment

This work was supported by the NASA Glenn Research Center, Alternate Fuels Foundation Technologies program (Contract Nos. NAS3-02118 and NAS3-03105) monitored by Dr. Glenn Beheim. The authors gratefully acknowledge this support. The fabrication work was performed in part at the Cornell NanoScale Science and Technology Facility (CNF), a member of the National Nanotechnology Infrastructure Network, which is supported by the National Science Foundation (Grant No. ECS 03-35765).

Nomenclature

- a = blockage coefficient
- c = chord length
- C_p = heat capacity
- D = channel height
- H = enthalpy
- h = blade height
- I = rothalpy
- i = incidence
- K = blockage
- k = heat capacity ratio
- M = Mach number

\dot{m} = flow rate
 P = pressure
 R = gas constant
 Re = Reynolds number
 r = radius
 s = space between two blades
 T = temperature
 t_{\max} = maximum thickness of blade
 U = tangential speed
 u = entry flow velocity
 V = absolute flow velocity
 W = relative flow velocity
 x_{entry} = entry length
 \dot{Y} = pressure loss coefficient
 α = inlet flow angle
 β = relative flow exit angle
 δ = deviation angle
 δ_c = boundary layer thickness
 Δr = radial position from the flow inlet
 ρ = density
 ω = rotational speed
 σ = solidity
 ν = dynamic viscosity

Subscripts

0 = total property
 1 = inlet of the stator blade
 2 = exit of the stator or inlet of the rotor blade
 N = stationary frame
 R = rotating frame
 w = property in the rotating frame

References

- [1] Epstein, A. H., 2004, "Millimeter-Scale, Micro-Electro-Mechanical Systems Gas Turbine Engines," *ASME J. Eng. Gas Turbines Power*, **126**, pp. 205–226.
- [2] Isomura, K., Murayama, M., Yamaguchi, H., Ijichi, N., Asakura, H., Saji, N., Shiga, O., Takahashi, K., Tanaka, S., Genda, T., and Esashi, M., 2002, "Development of Microturbocharger and Microcombustor for a Three-Dimensional Gas Turbine at Microscale," *Proceedings of the ASME IGTI*

- Turbo Expo 2002, Amsterdam, Netherlands, Jun. 6, Paper No. GT-2002-30580.
- [3] Epstein, A. H., and Senturia, S. D., 1997, "Macro Power From Micro Machinery," *Science*, **276**, p. 1211.
- [4] Epstein, A. H., Senturia, S. D., Al-Midani, O., Ayon, A., Breuer, K., Chen, K.-S., Ehrich, F. E., Esteve, E., Fréchet, L., Gauba, G., Ghodssi, R., Groshenry, C., Jacobson, S., Kerrebrock, J. L., Lang, J. H., Lin, C.-C., London, A., Lopata, J., Mehra, A., Mur Miranda, J. O., Nagle, S., Orr, D. J., Piekos, E., Schmidt, M. A., Shirley, G., Spearing, S. M., Tan, C. S., Tzeng, Y.-S., and Waitz, I. A., 1997, "Micro-Heat Engines, Gas Turbines, and Rocket Engines: The MIT Microengine Project," *Proceedings of the 28th AIAA Fluid Dynamics Conference, Snowmass Village, June 29–July 2, AIAA Paper No. 97-1773*.
- [5] Fréchet, L. G., Lee, C., Arslan, S., and Liu, Y.-C., 2003, "Design of a Microfabricated Rankine Cycle Steam Turbine for Power Generation," *Proceedings of the ASME International Mechanical Engineering Congress and Exposition, Washington, DC, Nov. 16–21*.
- [6] Kerrebrock, J. L., 1992, *Aircraft Engines and Gas Turbines*, 2nd ed., MIT, Cambridge, MA, p. 478.
- [7] Greitzer, E. M., 2004, *Internal Flow: Concepts and Applications*, Cambridge University Press, Cambridge, England.
- [8] Lee, C., 2006, "Development of a Microfabricated Turbopump for a Rankine Vapor Power Cycle," Ph.D. thesis, Columbia University, New York.
- [9] Mehra, A., 1997, "Computational Investigation and Design of Low Reynolds Number Micro-Turbomachinery," MS thesis, Massachusetts Institute of Technology, Cambridge, MA.
- [10] Jacobson, S. A., 1998, "Aerothermal Challenges in the Design of a Microfabricated Gas Turbine Engine," *Proceedings of the 29th Fluid Dynamics Conference, Albuquerque, NM, June 15–18, AIAA Paper No. 98-2445*.
- [11] Shirley, G., 1998, "An Experimental Investigation of a Low Reynolds Number, High Mach Number Centrifugal Compressor," MS thesis, Massachusetts Institute of Technology, Cambridge, MA.
- [12] Dunavant, J. C., and Erwin, J. R., 1956, "Investigation of a Related Series of Turbine Blade Profiles in Cascades," *NACA Technical Note No. 3802*.
- [13] Schlichting, H., 1979, *Boundary-Layer Theory*, 7th ed., McGraw-Hill, New York, p. 817.
- [14] Lee C., Liamini M., and Fréchet, L. G., "Design, Fabrication and Characterization of a Micro Turbopump for a Rankine Power Generation—Part II: Fabrication and Characterization," *J. Microelectromech. Syst.*, submitted.
- [15] Fréchet, L. G., Jacobson, S. A., Breuer, K. S., Ehrich, F. F., Ghodssi, R., Khanna, R., Wong, C. W., Zhang, X., Schmidt, M. A., and Epstein, A. H., 2005, "High-Speed Microfabricated Silicon Turbomachinery and Fluid Film Bearings," *J. Microelectromech. Syst.*, **14**(1), pp. 141–152.
- [16] Fréchet, L. G., 2000, "Development of a Microfabricated Silicon Motor-Driven Compression System," Ph.D. thesis, Massachusetts Institute of Technology, Cambridge, MA.
- [17] Horlock, J. H., 1966, *Axial Flow Turbines*, Krieger, Malabar, FL.

A Parametric Study of Passive Flow Control for a Short, High Area Ratio 90 deg Curved Diffuser

T. P. Chong¹

e-mail: t.p.chong@soton.ac.uk

P. F. Joseph

P. O. A. L. Davies

ISVR,
University of Southampton,
University Road,
Southampton SO17 1BJ, UK

This paper represents the results of an experimental program with the aim of controlling the flow in a highly unstable 90 deg curved diffuser. The diffuser, which is an integral part of an open jet wind tunnel at the University of Southampton, has the unique configuration of extreme shortness and high area ratio. In this study, several passive flow control devices such as vortex generators, woven wire mesh screens, honeycomb, and guide vanes were employed to control the three-dimensional diffusing flow in a scaled-down model. Although less successful for vortex generators, the other devices were found to improve significantly the uniformity of the flow distribution inside the curved diffuser and hence the exit flow. This study suggests that a cumulative pressure drop coefficient of at least 4.5 at the diffuser exit with at least three guide vanes is required to achieve adequate flow uniformity at the diffuser exit. These flow conditioning treatments were applied to the full-scale diffuser with exit dimensions of $1.3 \times 1.3 \text{ m}^2$. Flow with comparable uniformity to the scale-model diffuser is obtained. This study provides valuable guidelines on the design of curved/straight diffusers with nonseparated flow and minimal pressure distortion at the exit. [DOI: 10.1115/1.2969447]

Keywords: flow control, curved diffuser, secondary flow, vortices

1 Introduction

The use of “diffusers” is common in aeroengineering applications. In its simplest form a diffuser has an expanding area in the flow direction. A wind tunnel is one of the many installations that incorporate a diffuser. A typical closed-circuit wind tunnel would normally incorporate a wide-angle diffuser before the nozzle in order to transform the geometry from a smaller to a larger area. An additional diffuser, albeit with a smaller divergence angle than the wide-angle diffuser, is also installed behind the working section to recover static pressure from the kinetic energy to increase the efficiency of the power source. Similarly, higher propulsion efficiency can be achieved as the result of pressure recovery obtained by installing a diffuser at the inlet of an aircraft engine. The use of diffusers to increase the handling stability for racing cars is also well established. Unfortunately, the desired performance of a diffuser is often compromised by detrimental flow phenomena induced by the very nature of its geometry.

Bernoulli's principle implies that an increasing area along the path of an incompressible flow, as in a diffuser, causes the velocity to decrease ($\partial u / \partial x < 0$) and the pressure to increase ($\partial p / \partial x > 0$). Under a strong adverse pressure gradient, the boundary layer on the diffuser wall is likely to separate because the flow cannot sustain the momentum required to maintain a stable boundary layer. Ultimately, flow detachment occurs because the fluid particles at the near wall region experience a greater retarding shearing force than the pressure force pushing it. Flow separation is undesirable in many fluid systems as it would increase the pressure drag, decrease the core flow area, reduce the handling stabil-

ity, and enhance the structural vibration. In our case, flow separation is particularly unwanted as it leads to the generation of noise and turbulence levels.

The use of a “curved” diffuser is common in engineering applications. Considerable research and development efforts have been invested into their design. A 90 deg-bent diffuser can sometimes be found in some closed-circuit wind tunnel designs [1], whereas an S-shaped diffusing duct is often adopted in combat aircraft engine intakes when a shift of axis between the intake and the engine exists. The presence of a constant area, curved duct introduces centrifugal forces to deflect the core flow toward its outer-wall region (concave part). The deflected flow subsequently encounters an adverse pressure gradient and is slowed down at the outer wall. As a result the low energy fluid moves around the sidewalls toward the low-static pressure inner-wall region (convex part). This movement creates a cross-stream pressure gradient that eventually leads to the formation of pressure-driven secondary flows. When this secondary flow (moving toward the inner wall) couples with the fast-moving deflected core flow by the centrifugal force (moving toward the outer wall), two cells of pressure-driven vortices will be formed. Similar observations can also be found in curved diffusers, when the flow field becomes more complex. For instance, the secondary flow will inject low momentum fluid and consequently thicken the inner-wall boundary layer, which makes it susceptible to flow separation when a streamwise adverse pressure gradient is present. Sagi and Johnston [2] indicated that the convex nature of the inner wall also decreases mixing there, thereby inhibiting the momentum exchange between the inner and outer parts of the boundary layer. Therefore, the inner-wall boundary layer growth becomes more crucial than the outer-wall counterpart of a curved diffuser. Figure 1(a) depicts the parameters needed to describe a two-dimensional curved diffuser.

The performance of a curved diffuser is often dictated by just three dimensionless parameters, namely, W_2/W_1 (area ratio, AR), L_{in}/W_1 (scaled inner-wall length), and $\Delta\phi$ (turning angle) [2]. The influences of these dimensionless parameters to the first stall lim-

¹Corresponding author.

Contributed by the Fluids Engineering Division of ASME for publication in the JOURNAL OF FLUIDS ENGINEERING. Manuscript received September 21, 2007; final manuscript received June 9, 2008; published online September 23, 2008. Assoc. Editor: Chunill Hah.

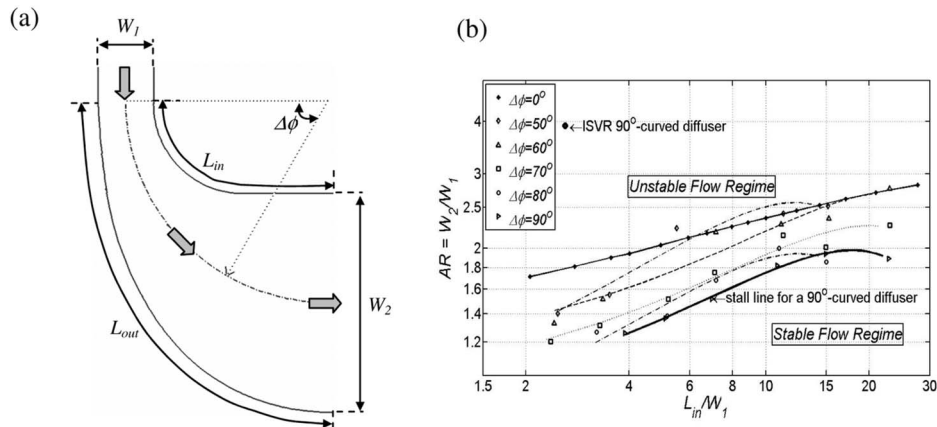


Fig. 1 (a) A schematic depicting the parameters needed to describe a curved diffuser. (b) Location of the first appreciable stall as a function of $\Delta\phi$ for circular-arc centerline curved diffusers (data tabulated from Ref. [3]).

its for curved diffuser with a circular-arc centerline were compiled by Fox and Kline [3]. Their correlations are shown in Fig. 1(b). From this figure, curved diffusers with a geometry situated below the first stall limit line are likely to be separation-free and unstalled; while the opposite is true for geometries above this line. It is clear from the figure that the allowance for a higher AR and a lower value of L_{in}/W_1 decreases when $\Delta\phi$ increases.

A common design rule for straight and conical diffusers is that the angle of divergence does not exceed roughly 5 deg in order to restrain the adverse pressure gradient level [4]. However, this rule introduces difficulties in a diffuser design when a large AR value is required since it implies a high diffuser length, thereby requiring a large space to accommodate it. Moreover, the additional losses due to skin friction and growth of boundary layer displacement thickness in a long diffuser require a higher power plant, which ultimately increases both initial and running costs. For the curved diffuser, Sagi and Johnston [2] developed a procedure to convert inner- and outer-wall potential-flow pressure distributions from a curved diffuser to a combination of straight-wall diffusers for the same AR. This has the advantage that, since the flow regime data for straight-wall diffusers are widely available, suitable inner- and outer-wall curved diffuser shape profiles can subsequently be evaluated. However, this practice also has its limitations especially when the curved diffuser to be designed is short and of large $\Delta\phi$. They have concluded that no wall shapes are possible that allow one to achieve separation-free flow for a curved diffuser with $L_{in}/W_1 < 4$. Note that the diffuser under investigation here has $L_{in}/W_1 = 2.6$.

In the practical application of active and passive devices to control the three-dimensional flow in a diffuser with a large divergence angle and short length, or with a large turning angle, a compromise is frequently made between acceptable pressure loss and having fully attached flow. A common approach is to install gauze screens inside the diffuser. The screen works in two ways to prevent flow separation. First, a suitably selected screen can break off an unstable boundary layer caused by the adverse pressure gradient and increase the flow mixing. In this way the momentum exchange within the viscous layers is enhanced and the tendency of flow separation is reduced. Second, the screen can cause a pressure drop when flow passes through it. The amount of pressure loss depends on the screen characteristics (discussion on this issue can be found in the later section). The introduction of pressure loss in a flow is analogous to an increase in flow resistance, which has the profound effect of redistributing more evenly the upstream flow streamlines. Sahin et al. [5] and Seltsam [6] used gauze screens to control the flow inside their wide-angle diffusers in which they achieved improved flow uniformity and reasonable

pressure recovery. Based on the data collected from a number of wide-angle diffuser designs, Mehta and Bradshaw [4] compiled design guidelines on the basis of AR, divergence angle, pressure-drop characteristics, and number of screens for straight diffusers. In contrast, very few studies have been undertaken on the use of screens in curved diffusers, except that improvement in pressure recovery in S-shaped diffusers by boundary layer fences has been reported by Sullerey et al. [7].

A guide vane, or a flow splitter, represents another attractive device for diffuser flow control. Moore and Kline [8] successfully maintained a separation-free 45 deg wide-angle diffuser by installing five equally spaced flat vanes. Weng and Gou [9] employed a so-called automatic adjustable blade (AAB) to control swirl in an S-duct diffuser. The principle of this method is to use the AAB to deflect inlet flow toward the inner-wall region, thereby enhancing local flow momentum at the expense of acceptable total pressure loss at the diffuser exit. Majumdar et al. [10] employed five adjustable splitter vanes, similar to the AAB, in a large AR, 90 deg-curved diffuser. Significant improvements were reported in the overall flow uniformity and performance for this otherwise unstable curved diffuser.

Brunn and Nitsche [11] used synthetic jets to energize the adverse pressure gradient boundary layers pertinent to their straight-wall diffuser. They found that the longitudinal vortices produced by the synthetic jets could effectively delay the onset of separation or reduce the separation bubble lengths due to the more rigorous momentum exchange between the inner and outer boundary layers. A major drawback of this active approach is that to perform optimally it requires a thorough knowledge of the excitation frequency, optimal slot or port dimensions on the wall to allow the synthetic jet to be injected into the boundary layer, the local boundary layer characteristics, as well as the ability to respond to transient changes. Following the same line of approach, an array of inclined or triangular-shaped devices can be mounted on flow surface to continuously generate longitudinal co- or counter-rotating vortices to re-energize the boundary layer. Lin [12] presented a comprehensive review of the use of small-scale vortex generators (VGs) to control boundary layer separation. Recently, Godard and Stanislas [13] utilized hot wire and particle image velocimetry (PIV) techniques in an attempt to study flow improvement produced by vortex generators. They quantified the distributions and growth of high and low momentum fluids created by vortex generators within a decelerating boundary layer. However, this momentum mixing technique has not yet been extensively applied to curved diffusers. A notable example is the one

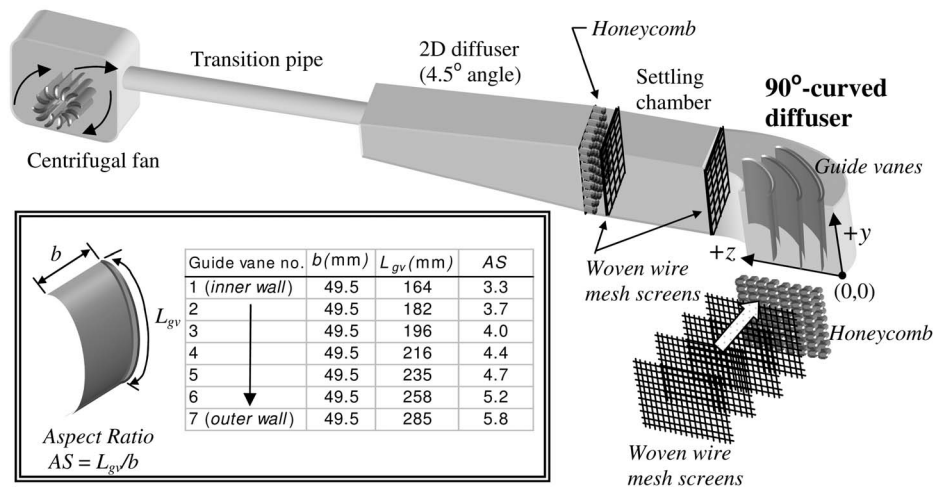


Fig. 2 Schematic of the experimental facility for the flow control study on the 90 deg-curved diffuser model. Coordinate system for the diffuser exit flow is also shown. Insert diagram: Schematic of a typical guide vane profile. Guide vanes with different aspect ratios employed in this study were also shown in the table.

described by Reichert and Wendt [14] where tapered-fin vortex generators were shown to improve aerodynamic performance in a relatively mild S-shaped subsonic diffuser.

A new large scale, low flow-noise, open-jet blow-down wind tunnel has been designed, built, and tested at the Institute of Sound and Vibration Research (ISVR), at the University of Southampton in the UK [15]. Of significance in its design is the construction of a high AR (3.9) and an extremely short ($L_{in}/W_1 = 2.6$) two-dimensional 90 deg-curved diffuser with a circular-arc centerline and exit dimensions of $1.3 \times 1.3 \text{ m}^2$. These extreme values were necessary due to the limited space of the anechoic chamber in which the wind tunnel was housed [15]. Figure 1(b) makes clear that this diffuser will be intrinsically unstable and prone to large-scale flow separations. The literature suggests that this particular 90 deg-curved diffuser is the shortest and most unfavorable ever reported. The space constraints of the building and the required expansion ratio of the diffuser did not allow relaxation of these parameters and so it was imperative to introduce flow control methods to control the flow such as those discussed above. Due to the absence of guidelines on the use of the above techniques in a 90 deg-curved diffuser, a small test tunnel was built specifically to optimize the passive control devices before applying them to the full-scale facility.

2 Experimental Setup

Aerodynamic testing of the scale-model diffuser was conducted in a purpose-built low-speed wind tunnel, as shown in Fig. 2. A centrifugal blower discharged air through a 49.5 mm diameter transition pipe into a two-dimensional straight diffuser. This diffuser, with a divergence angle of 4.5 deg, expands to a rectangular duct with cross-sectional area of $195 \times 49.5 \text{ mm}^2$. It is then followed by a 400 mm long settling chamber with a honeycomb and a woven wire screen installed to straighten the flow and to reduce velocity fluctuations, respectively. A 90 deg-curved diffuser model was then attached to the settling chamber outlet. Also shown in the figure is the coordinate system in relation to the exit of the curved diffuser. Efforts were also made to ensure that uniform flow exists at the inlet of the 90 deg-curved diffuser. The Reynolds number was 52,640 based on the hydraulic diameter of the diffuser inlet with an average turbulence intensity of the flow at about 0.1%.

2.1 90 deg-Curved Diffuser Model. The geometry of the 90 deg-curved diffuser examined in this study is shown in Fig. 3.

It has an inlet area of $195 \times 49.5 \text{ mm}^2$ and an outlet area of $195 \times 195 \text{ mm}^2$. This model is about 1/6 of the full size of the 90 deg-curved diffuser planned for the low noise wind tunnel, thereby retaining the same AR and L_{in}/W_1 (3.9 and 2.6, respectively). As shown in the figure both the inner wall and centerline are quadrant circles with radii equal to 79.5 mm and 180 mm, respectively. The outer wall is shaped such that equal area distributions are established for the inner- and outer-wall passages relative to the centerline. Since the boundary layer growth on the inner wall is more important, 19 static pressure tappings were distributed along the centerline of the inner wall; whereas no pressure tappings were installed at the outer wall. A special screen adapter to accommodate a honeycomb and up to four mesh screens was attached at the curved-diffuser exit. These are then followed by an extension of a 110 mm straight duct to ensure that the flow across the last screen does not discharge into the atmosphere immediately. In this case accurate velocity and total pressure measurements can be made inside the straight duct.

2.2 Woven Wire Mesh Screens and Guide Vanes. The

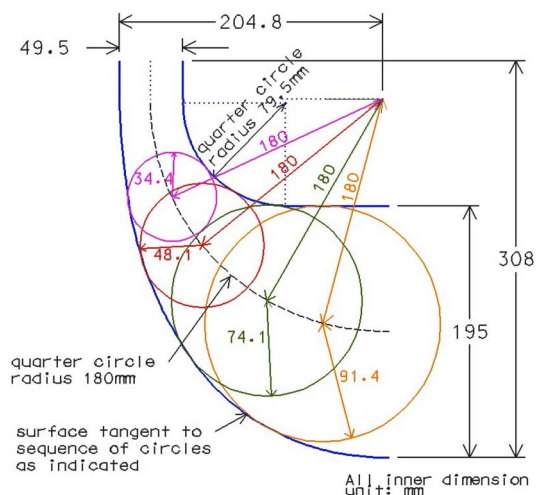


Fig. 3 Schematic showing the design of the 90 deg-curved diffuser model. All dimensions are in millimeters.

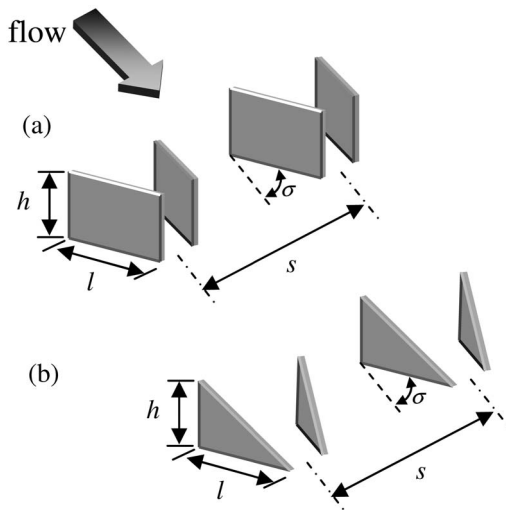


Fig. 4 Schematics showing the parameters required to describe the (a) rectangular and (b) triangular-shaped vortex generators

pressure-drop coefficient, K , is an important parameter for assessing the aerodynamic performance of a screen. In incompressible flow, K can be expressed as [16]

$$K = \frac{\Delta p}{q} = A \left(\frac{1}{\beta^2} - 1 \right)^B \quad (1)$$

where Δp is the static pressure drop across the screen, q is the upstream dynamic pressure, and β is the screen porosity. Constants A and B are usually taken as 0.52 and 1, respectively, for a square woven type of screen. Equation (1) suggests that the pressure drop produced by a screen is determined solely by its porosity. An important criterion is that the use of screens with porosity less than 0.5, which corresponds to K more than 1.56, should be avoided in order to prevent exit flow instability as the result of jet coalescence [17]. To produce a total pressure drop of more than 1.56 at the diffuser exit, several screens with small K were added in series to achieve the required cumulative values (see Fig. 2). A honeycomb was also installed at the curved-diffuser exit in order to straighten the flow and to reduce lateral velocity fluctuations.

To assess the effectiveness of guide vanes inside the curved diffuser model, up to seven vanes with different profiles and aspect ratios, AS were tested (see Fig. 2 for definition of AS). The vane with the smallest AS was placed nearest to the inner-wall region and the AS of vanes increase toward the outer-wall region.

The vanes were made from a thin 0.8 mm aluminum sheet in order to help reduce any impact of leading edge irregularities on boundary layer separation on the vane surfaces. To minimize boundary layer growth, and hence the exit shear layer, the leading edge of the guide vanes was placed at the line in tangent with $L_{(i)}/W_1=1.2$, where $L_{(i)}/W_1$ is the normalized distance from the curved-diffuser inlet at the inner wall. This location is chosen because it is slightly upstream of where the locus of flow separation occurred at the inner wall for the base line case without flow treatment (see Sec. 3.1). Another advantage of locating the vane leading edges in this position is that the AR of the passage between adjacent vanes is slightly reduced.

2.3 Vortex Generator Arrays. The VGs used in this study comprise configurations of rectangular and triangular shapes. Parameters associated with the VG arrays such as the location, height, length, skew angle, and spacing are chosen based on the suggestion by Lin [12] and the schematic showing these parameters is shown in Fig. 4 for both the rectangular and triangular shapes. The VG arrays were manufactured from a thin Perspex sheet from which each individual generator was cut into the required shape. They were glued onto the surface by a thin double-sided tape that spanned across the whole diffuser width. To avoid excessive dissipation of the strength of the VG-induced longitudinal vortices, special care was taken to place the VG array not too far upstream from the locus of the boundary layer separation on the inner wall for the base line case.

Various combinations of screens, guide vanes, and vortex generators were tested on the 90 deg-curved diffuser model. A selection of representative cases was chosen for presentation in this paper, a summary of which is given in Table 1. From the table, abbreviations q , gv , and vg refer to the cumulative K at the diffuser exit, number of guide vanes, and type of vortex generators, respectively. The table also include the parameters associated with the VG configurations used in this study.

2.4 Instrumentation and Measurement Techniques. A $3.8 \mu\text{m}$ TSI 1210-T1.5 single hot wire probe was used to measure the mean and fluctuating velocities at 135 mm from the 90 deg-curved diffuser exit. The hot wire was heated by a constant-temperature anemometer (TSI IFA300) with an overheat ratio of 1.8. To measure the velocity at the cross-sectional area perpendicular to the direction of flow at the curved-diffuser exit (y - z plane), the hot wire was attached to a computer-controlled two-dimensional traverse mechanism. The accuracy of the traverse is within ± 0.01 mm in both directions. In the current study, a traverse matrix of 20×38 measurement points was selected in the y and z directions at separation intervals of 10 mm

Table 1 Summary of cases presented in this study. Note that each case is represented by abbreviations with q as the cumulative K at the diffuser exit, gv as the number of guided vanes, and vg as the type of vortex generators. δ is the boundary layer thickness at the diffuser inlet.

| Abbreviations | Cumulative K at diffuser exit | No. of guided vanes | Types of vortex generators | Length, l/h | Height, h/δ | Spacing, s/h | σ (deg) |
|---------------------|---------------------------------|---------------------|----------------------------|---------------|--------------------|----------------|----------------|
| $q=0, gv=0, vg=0$ | 0 | 0 | — | — | — | — | — |
| $q=0, gv=7, vg=0$ | 0 | 7 | — | — | — | — | — |
| $q=5.5, gv=0, vg=0$ | 5.5 | 0 | — | — | — | — | — |
| $q=3, gv=3, vg=0$ | 3 | 3 | — | — | — | — | — |
| $q=3, gv=7, vg=0$ | 3 | 7 | — | — | — | — | — |
| $q=5.5, gv=3, vg=0$ | 5.5 | 3 | — | — | — | — | — |
| $q=4.5, gv=7, vg=0$ | 4.5 | 7 | — | — | — | — | — |
| $q=5.5, gv=7, vg=0$ | 5.5 | 7 | — | — | — | — | — |
| $q=0, gv=0, vg=1$ | 0 | 0 | Rectangular | 4 | 0.2 | 9 | 45 |
| $q=0, gv=0, vg=2$ | 0 | 0 | Triangular | 4 | 0.2 | 9 | 45 |

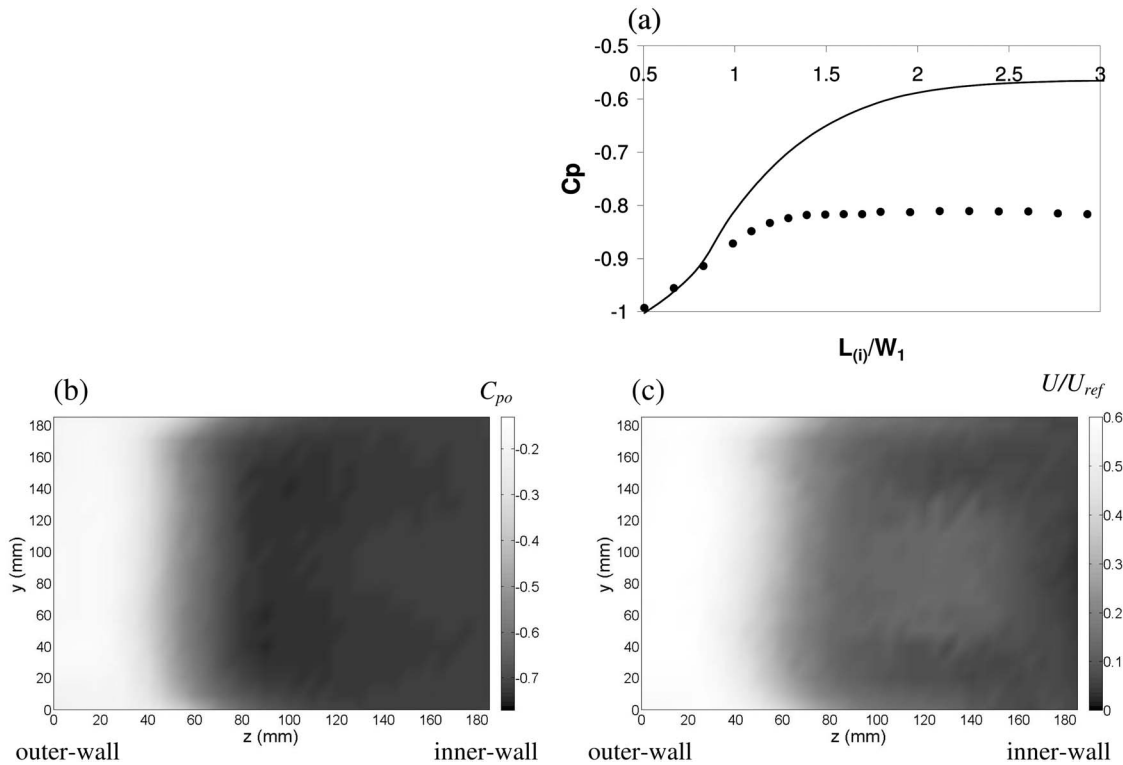


Fig. 5 (a) Comparison of (—) theoretical and (●) measured C_p for the base line case ($q=0$, $gv=0$, $vg=0$). (b) and (c) Measured C_{p0} and velocity contours for the base line case, respectively.

and 5 mm, respectively.

The signals from the hot wire were sampled for 6.6 s at a frequency of 5 kHz after passing through a 2.5 kHz anti-aliasing filter and digitized using a 12 bit analog-to-digital (A/D) converter. The digitized voltage from the hot wire was converted to velocity by interpolating the fifth-order polynomial velocity-voltage calibration curve. The streamwise rms values of velocity fluctuations were calculated from

$$u_{rms}(y,z) = \sqrt{\sum_n^N [U(y,z,t_n) - \bar{U}(y,z)]^2 / N} \quad (2)$$

where $U(y,z,t_n)$ and $\bar{U}(y,z)$ are the instantaneous (at sampled time t_n) and the time-averaged velocities, respectively. Note that both $\bar{U}(y,z)$ and u_{rms} measured in the current study may be ambiguous in the separation region due to the rectification errors of the hot wire signals caused by the reversed flow. This limitation has no consequence in the present work because one can still interpret qualitatively the velocity contours with regard to the flow physics, especially the cases involving the exit mesh screens. To ensure the validity of such interpretation, each velocity contour was examined in conjunction with the corresponding total pressure contours.

To allow a satisfactory spatial resolution, a miniature aluminum tube of 0.8 mm diameter was used to measure the total pressure distributions at 135 mm from the 90 deg-curved diffuser exit. Since this miniature tube cannot be held firmly by the traversing probe holder due to its small size, one side of the miniature tube was joined together with a larger tube of 4 mm diameter and the other side was retained for the total pressure measurements. The 4 mm diameter tube was then held by the same traverse system as the hot wire to allow mapping of the total pressure in the $y-z$ plane. This configuration also has the advantage that the measured pressure requires a shorter equalization time because of the larger size tube. A vinyl tube is used to connect the pressure probe to a

differential pressure transducer (SensorTechnics HCXM010D6H).

To allow a more meaningful comparison between different test cases, nondimensional static and total pressures, denoted by C_p and C_{p0} , respectively, are defined as

$$C_p = \frac{P\left(\frac{L_{(i)}}{W_1}\right) - P_{ref}}{P_{0,ref} - P_{ref}} \quad (3a)$$

$$C_{p0} = \frac{P_0(y,z) - P_{ref}}{P_{0,ref} - P_{ref}} \quad (3b)$$

where $P(L_{(i)}/W_1)$ is the axial distribution of static pressure measured at the inner wall and $P_0(y,z)$ is the total pressure measured at the cross-sectional area of the diffuser exit. $P_{0,ref}$ and P_{ref} are the reference total and static pressures, respectively, at 30 mm before the curved-diffuser inlet. Note that, as shown in Fig. 2, a mesh screen was placed at the curved-diffuser inlet to ensure a uniform flow. This screen was regarded as an integral part of the flow control mechanism for the 90 deg-curved diffuser. Because this screen was situated between the reference and the measurement points, the subsequently measured C_p and C_{p0} values will remain predominantly negative.

3 Results

3.1 Base Line Case. Figure 5(a) shows the axial static pressure distribution at the inner-wall region for the base line case in which no screens (q), guide vanes (gv), and vortex generators (vg) were used. This case will be represented by the notation ($q=0$, $gv=0$, $vg=0$). From hereon, this style of notation will also be used to represent the other cases. Also shown in the figure is the theoretical C_p distribution pertinent to the present 90 deg-curved diffuser. The C_p distribution is derived from potential flow theory by converting the 90 deg-curved diffuser into an equivalent two-

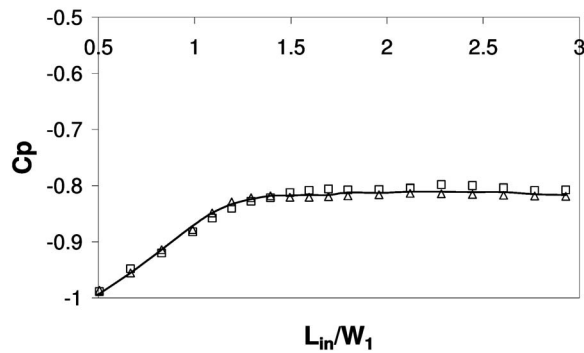


Fig. 6 C_p distributions for (—) base line, (Δ) ($q=0$, $gv=0$, $vg=1$), and (\square) ($q=0$, $gv=0$, $vg=2$) cases

dimensional straight diffuser. From the figure, the calculated C_p value increases almost monotonically over the range of $0.5 < L_{(i)}/W_1 < 0.8$. Beyond this range there is an inflexion point and C_p increases continuously before reaching saturation at $L_{(i)}/W_1 > 2$. Indeed, the measured C_p values also increase monotonically over the range of $0.51 < L_{(i)}/W_1 < 1.19$, but remain constant thereafter. The deviation between the theoretical and measured results for $L_{(i)}/W_1 > 0.83$, coupled with the absence of measured C_p increment at $L_{(i)}/W_1 > 1.19$, indicate that the boundary layer on the inner wall becomes unstable at $L_{(i)}/W_1 \approx 0.99$ and eventually separates at $L_{(i)}/W_1 \approx 1.29$. The unchanging values of measured C_p at $L_{(i)}/W_1 > 1.29$ are associated with a large-scale nonrecoverable flow separation. This observation is consistent with the classical design criteria presented in Fig. 1(b) in that the current 90 deg-curved diffuser geometry lies in the stall region over a wide range of Reynolds numbers.

Figure 5(b) shows the contour map of total pressure coefficient, C_{p0} , at 135 mm from the 90 deg-curved diffuser exit. It is apparent that a significant total pressure deficit (darker color) encompasses more than 50% of the flow area at the exit. This pressure deficit region is associated with the large-scale nonrecoverable flow separation that originated from the inner-wall region near $L_{(i)}/W_1 = 1.29$. The corresponding velocity contour in Fig. 5(c), which is scaled with the reference velocity U_{ref} at the diffuser inlet, also exhibits a similar pattern. A consequence of the “dead flow” regions shown in Figs. 5(b) and 5(c) is that most of the mass flow is transferred to a fast stream flow toward the outer-wall region. Without flow control treatment, incorporating the current 90 deg-curved diffuser into a fluid flow system, such as a wind tunnel, would require a substantial distance before the separated flow from the diffuser inner wall reattaches again. This will not only increase the overall running cost but also will undesirably increase the turbulence intensity and flow unsteadiness in the fluid flow system.

3.2 Vortex Generators. Figure 6 compares the C_p distributions for the base line case to ($q=0$, $gv=0$, $vg=1$) and ($q=0$, $gv=0$, $vg=2$), with rectangular and triangular surface-mounted vortex generator arrays, respectively. This figure demonstrates that the C_p distribution for the case ($q=0$, $gv=0$, $vg=1$) is markedly similar to the base line case. For the case ($q=0$, $gv=0$, $vg=2$), although the inception of constant C_p occurs at a slightly larger $L_{(i)}/W_1$ value, the overall pressure recovery pattern remains almost unchanged compared to the base line case. The velocity contour in Fig. 7 for the case ($q=0$, $gv=0$, $vg=2$) also exhibits little difference compared to the base line case. The above results imply that the inclusion of either a rectangular or a triangular vortex generator array to produce counter-rotating vortex pairs at the inlet of the present curved-diffuser’s inner wall has no significant effect on the suppression or delay of flow separation. Similar

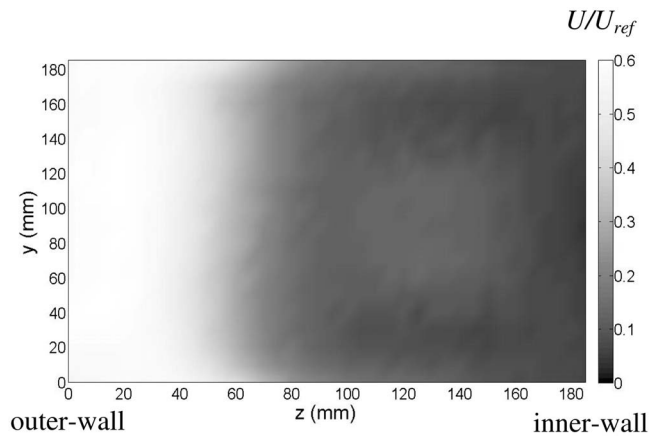


Fig. 7 Velocity contour for the ($q=0$, $gv=0$, $vg=2$) case

results are also observed when the VG numbers were doubled or the VG arrays changed to a corotating configuration. It has been reported that the main mechanism of improving the aerodynamic performance for a curved diffuser by a counter-rotating VG is through the production of counter-rotating vortices of greater vortex strength and in opposite direction compared to the pressure-driven vortices (natural vortices produced by the curvature-induced secondary flow) in order that the latter is suppressed [14]. However, a counter-rotating VG configuration can produce vortices that tend to move away from a flat plate wall region due to mutual interaction while developing downstream [18]. Therefore, in the present case, the VG vortices are even more likely to lift away from the inner wall due to the presence of exceptionally large centrifugal forces. The consequence of this is that the redirecting/near wall re-energizing effects of the VG vortices becomes less effective in inhibiting the detrimental secondary flow caused by the pressure-driven vortices.

3.3 Guide Vanes. This section describes the influence of the guide vanes alone in the flow control of the 90 deg-curved diffuser. Guide vanes are primarily used for diverting flow paths but can also potentially decrease the effective AR provided that the leading edges of the vanes do not begin at the inlet. The addition of guide vanes can bring the design limit closer to the stable flow regime at a given L_{in}/W_1 value in Fig. 1(b). Figure 8 shows the C_p distribution on the inner wall for the case ($q=0$, $gv=7$, $vg=0$). The introduction of seven exit guide vanes can be seen to produce a significant improvement in the pressure recovery compared to the base line case. However, flow is still observed to separate at $L_{(i)}/W_1 \approx 1.39$ as indicated by the ensuing constant C_p value. Further examination of the exit total pressure and velocity contours in

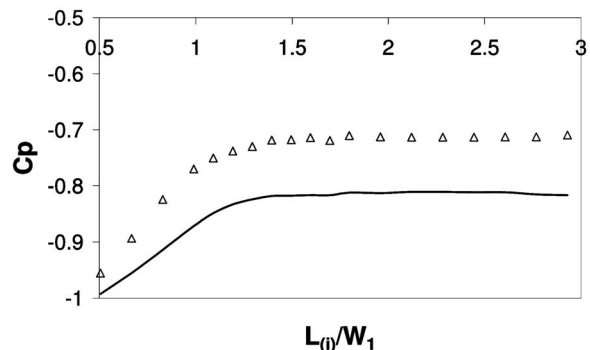


Fig. 8 C_p distributions between (—) base line and (Δ) ($q=0$, $gv=7$, $vg=0$) cases

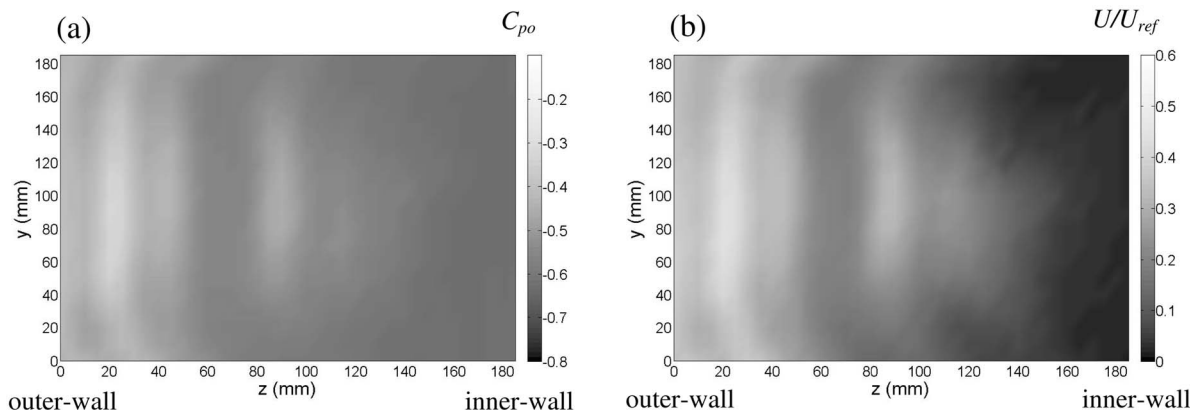


Fig. 9 (a) Measured C_{p0} and (b) velocity contours for the $(q=0, gv=7, vg=0)$ case

Figs. 9(a) and 9(b), respectively, confirm this behavior.

The contours in these figures also reveal that, starting closest to the inner wall, the boundary layers at the pressure sides of the first three guide vanes were separated. However, the boundary layers remained attached for the remaining guide vanes. The overall separation region for the case $(q=0, gv=7, vg=0)$ is thus smaller than the base line case as indicated by Figs. 9(a) and 9(b). Consequently, flow uniformity at the diffuser's exit has been slightly improved. Therefore, the addition of evenly spaced guide vanes is an effective way of redistributing the flow in the stages, but they may not be enough to completely suppress flow separation at the inner-wall region for an extreme 90 deg-curved diffuser configuration such as in the present case.

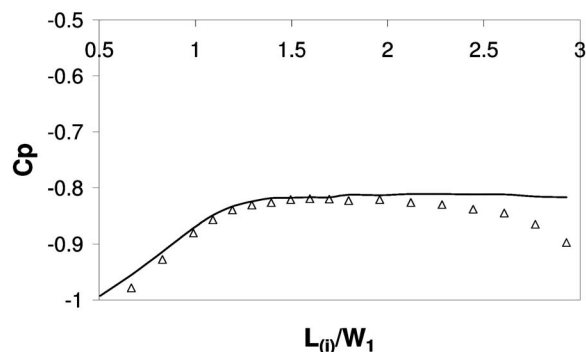


Fig. 10 C_p distributions between (—) base line and (Δ) $(q=5.5, gv=0, vg=0)$ cases

3.4 Mesh Screens. A cumulative pressure-drop coefficient of 5.5 was introduced at the 90 deg-curved diffuser exit to examine the effect of wire mesh screens on the internal flow. Because of the existence of pressure-driven vortices, a honeycomb was also added to reduce lateral velocity fluctuations. Figure 10 shows the C_p distribution on the inner wall for the case $(q=5.5, gv=0, vg=0)$. From the figure, one can observe that the pressure recovery pattern resembles closely the base line case in Fig. 5(a) up to $L(i)/W_1=1.7$. Thereafter, rather unexpectedly, C_p begins to drop. The reason for this drop will be explained in Sec. 4. The corresponding exit total pressure and velocity contours are shown in Figs. 11(a) and 11(b), respectively.

As expected, the overall total pressure and velocity level distributions are now lower compared to the previous cases, due to extra losses caused by the presence of the screens (take note of the changes of contour scales for both pressure and velocity from here on). However, another feature of the case $(q=5.5, gv=0, vg=0)$ is that the distributions of total pressure and velocity from the outer to inner walls at the diffuser exit are more progressive and gradual than the base line case. Although still not the optimum configuration, the case $(q=5.5, gv=0, vg=0)$ demonstrates that the introduction of pressure drop at the diffuser exit yields beneficial effects to flow uniformity.

3.5 Mesh Screens+Guide Vanes. The results presented above suggest that the guide vanes and mesh screens, when introduced independently, produce limited but useful flow control capabilities for the present 90 deg-curved diffuser configuration. This section investigates the simultaneous use of both devices with different combinations of vane number and pressure-drop

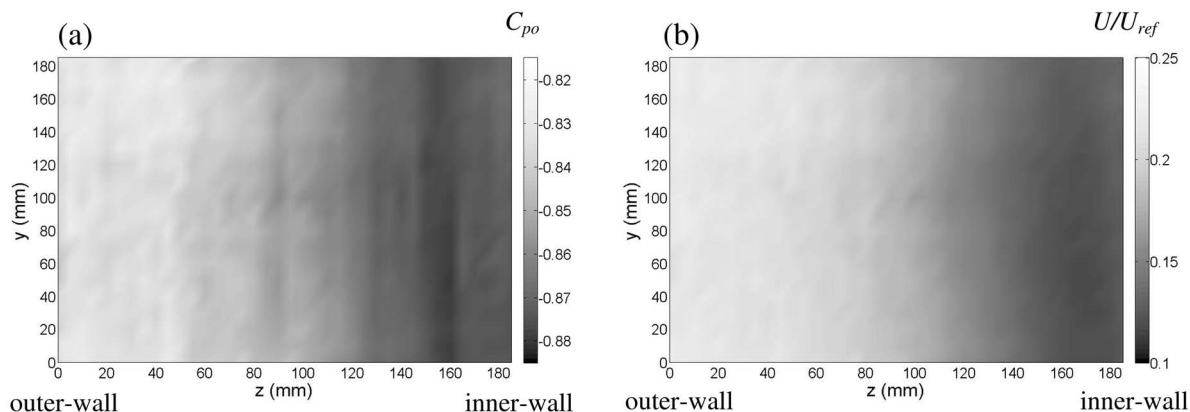


Fig. 11 (a) Measured C_{p0} and (b) velocity contours for the $(q=5.5, gv=0, vg=0)$ case

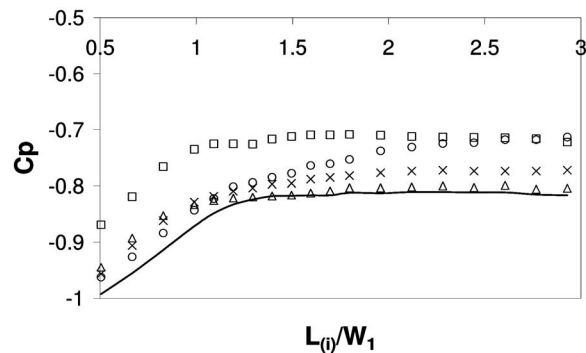


Fig. 12 C_p distributions for (Δ) ($q=3$, $gv=3$, $vg=0$), (\square) ($q=3$, $gv=7$, $vg=0$), (\times) ($q=5.5$, $gv=3$, $vg=0$), (\circ) ($q=5.5$, $gv=7$, $vg=0$), and (—) base line cases

level. Figure 12 shows the inner-wall C_p distributions for cases ($q=3$, $gv=3$, $vg=0$), ($q=3$, $gv=7$, $vg=0$), ($q=5.5$, $gv=3$, $vg=0$), and ($q=5.5$, $gv=7$, $vg=0$) as well as the base line case ($q=0$, $gv=0$, $vg=0$). Generally speaking, the pressure recovery pattern becomes more favorable as both the number of guide vanes and the pressure-drop levels increase. Among the various cases the best pressure recovery is achieved for the configuration ($q=5.5$, $gv=7$, $vg=0$), where it was found that the static pressures continue to increase along the inner wall. The correlation between the number of guide vanes, pressure-drop level, and the inner-wall pressure recovery improvement is also exhibited in the exit total pressure and velocity distributions as shown in Fig. 13. The effect of the number of guide vane on the exit flow uniformity with fixed pressure-drop levels (q) was first investigated. Then, with the same number of guide vanes, the exit pressure-drop levels were varied. It was shown that by increasing the numbers of guide vane the exit flow can be improved and distributed more evenly. However, the overall total pressure recovery remains virtually unchanged regardless of the numbers of guide vanes introduced. With seven guide vanes introduced (and no vortex generators), comparisons of the flow uniformity were made for screens with the following q values: $q=3$, 4.5, and 5.5. As expected, the overall total pressure recovery decreases with the cumulative screen pressure-drop level. However, the use of screens seems to have a greater effect on flow uniformity improvement than the use of guide vanes. The configuration ($q=5.5$, $gv=7$, $vg=0$) provides superior flow uniformity for the present 90 deg-curved diffuser. The obvious disadvantage for this case is the reduced performance of pressure recovery since a heavily loaded screen pack was used.

Another beneficial effect of adding mesh screens at the end of a diffuser is a reduction in turbulence levels. Figures 14(a) and 14(b) show the turbulence intensity contours for ($q=3$, $gv=7$, $vg=0$) and ($q=5.5$, $gv=7$, $vg=0$) cases, respectively. These figures reveal patches of high turbulence levels for the ($q=3$, $gv=7$, $vg=0$) case; whereas for the case ($q=5.5$, $gv=7$, $vg=0$), not only does the exit flow have a much lower overall turbulence intensity level but it also remains more uniform.

4 Discussion

In the process of flow turning, fluid motion can no longer be adequately described using two-dimensional theory. Evidence for this is that C_p plotted in Fig. 5(a) assuming two-dimensional flow deviates from the measured C_p values from $L(i)/W_1=0.83$, although the boundary layer has not yet separated at this point. Initially deflected by the centrifugal forces, the fluid approaching the outer wall experiences an adverse pressure gradient and begins to slow down. Because of the lower static pressure at the inner-wall region, this energy deficient fluid at the outer wall tends toward the inner-wall region from the sidewall. This results in a naturally occurring pair of pressure-driven counter-rotating vorti-

ces on the inner wall that convects low momentum fluid away from the surface. The injection of low momentum fluid into the outer layer of the boundary layer will inhibit the mixing process required for sustaining a stable boundary layer growth under an adverse pressure gradient flow regime. Ultimately, flow separation becomes inevitable. It is worth citing the findings of Majumdar et al. [19] here, where they still observed strong secondary flow even in a high aspect ratio 90 deg-curved diffuser.

Although the vortex generators failed to control the diffuser internal flow, guide vanes and mesh screens were shown to be more effective. The mesh screens at the diffuser exit can induce extra flow resistance where the velocity is high and hence slow down the flow in that region. The amount of pressure loss depends on the specifications of the screens (see Eq. (1)), but generally the pressure loss will tend toward uniformity over the screen area because of the redistribution of upstream flow path in response to the exit pressure loss. As a result, the flow through the screen will be forced to be more uniform. This could explain the drop of C_p at $L(i)/W_1 > 1.7$ in Fig. 10 with screen alone in that low static pressures at the inner wall close to the exit screen are required in order to generate a cross-stream pressure gradient to divert some of the mass flow from the outer wall to the inner wall. A correlation between the use of exit screens and exit flow uniformity is also evident in the turbulence intensity contours shown in Figs. 14(a) and 14(b). However, with the rather extreme conditions of the present case, significant flow guidance by guide vanes was also found to be essential to obtain a satisfactory flow distribution.

The use of guide vanes was shown to have no effect on the overall exit pressure recovery levels. Indeed the guide vane acts more like a "flow divider" to divert some of the higher mass flow from the outer-wall region and inject it into the inner-wall region. In this way the internal flow can be more uniformly distributed. Majumdar et al. [10], Lindgren et al. [20], and many others have successfully employed guide vanes to aid turning the flow inside their 90 deg-curved diffusers or expanding bends with different values of AR and L_{in}/W_1 . However, it is less successful for the present situation because of the large curvature and extreme shortness of the inner wall and large AR involved. Nonetheless, significant improvements can still be pursued if further pressure drop is introduced by screens at the exit of the curved diffuser with guide vanes installed. Of all the cases studied, the case ($q=5.5$, $gv=7$, $vg=0$) has produced the most uniform flow distribution, with minimum pressure distortion and low turbulence intensity of exit flow compared to the untreated base line case. Overall it is believed that the degree of flow uniformity is strongly related to the level of cumulative pressure drop at the diffuser exit. However, this statement should be treated cautiously since an unrealistically large pressure-drop value is also not recommended. This is because the subsequent penalty of large total pressure loss would negate the objectives of having a diffuser in the first place, which is to increase static pressure downstream.

It has already been established elsewhere that the use of multiple screens can effectively control flow inside diffusers with adverse geometries such as those with highly diverging angles and large curvature. Common practice with this approach is to place the screens inside the diffuser to achieve pressure drop in stages. From a construction viewpoint, especially for a curved diffuser, this practice tends to be complicated because issues such as air leakage, joint-surface continuity, and high cost also need to be addressed first. Another issue that must be considered is the optimum locations of the screens. This requires a thorough knowledge of the base line flow characteristic pertinent to the diffuser concerned. This study offers a unique and simpler approach for obtaining improved exit flow uniformity by locating a series of screens at the 90 deg-curved diffuser exit, with the great flexibility of increasing and decreasing the values of the cumulative pressure loss if needed.

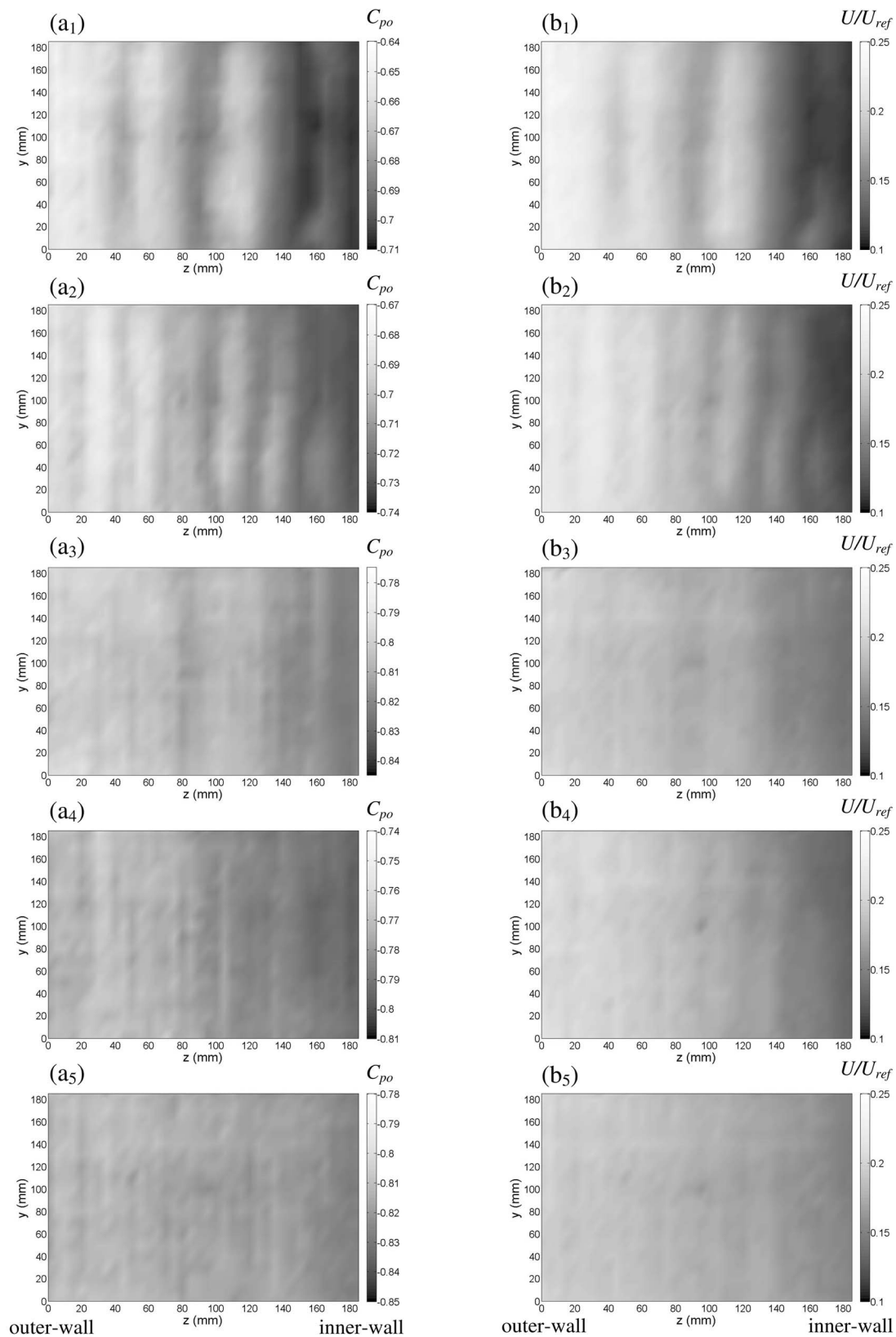


Fig. 13 Comparison of $(q=3, gv=3, vg=0)$, $(q=3, gv=7, vg=0)$, $(q=5.5, gv=3, vg=0)$, $(q=4.5, gv=7, vg=0)$, and $(q=5.5, gv=7, vg=0)$ cases for (a1)–(a5) measured C_{p0} and (b1)–(b5) velocity contours, respectively

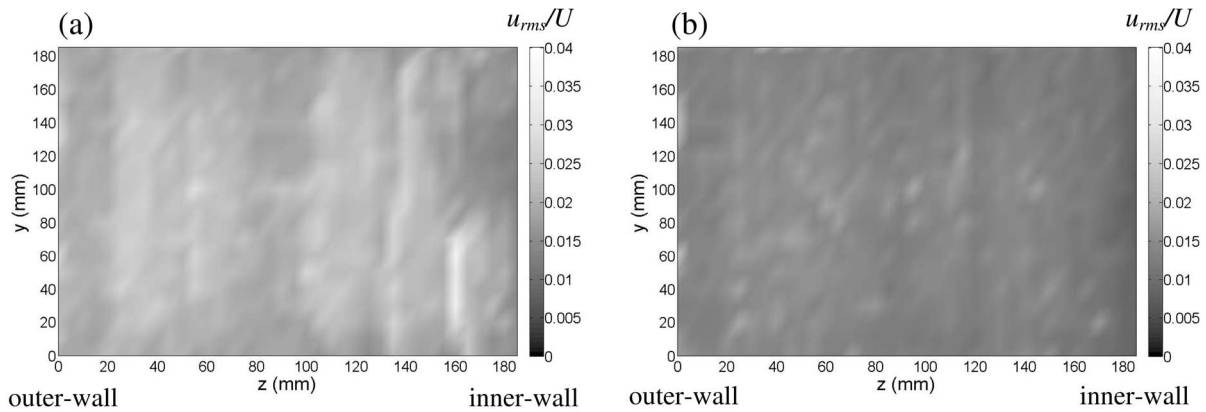


Fig. 14 Comparison for turbulence intensity contours between (a) ($q=3$, $gv=7$, $vg=0$) and (b) ($q=5.5$, $gv=7$, $vg=0$) cases

5 Validation of Control Techniques on a Full-Scale Diffuser

So far, promising but limited guidelines have been established for passive flow control techniques applied to the current 90 deg-curved diffuser configuration based on experiments on a scale model. It was demonstrated that satisfactory exit flow can be achieved by adhering to the criteria $q > 4.5$ and $gv > 3$. For the design of the full-size 90 deg-curved diffuser, only three guide vanes were employed to minimize the cumulative weight (Fig. 15(a)). Composite drawer adapters for honeycomb and mesh screens were also installed at the inlet and exit of the diffuser. This drawer adapter features a rail type handling system that allows a simple changeover of mesh screens. In this installation, a cumulative pressure drop of $5.5q$ was chosen at the diffuser exit. The full-scale diffuser has an inlet area of $0.33 \times 1.3 \text{ m}^2$ and an outlet area of $1.3 \times 1.3 \text{ m}^2$ over an axial distance of 1.4 m. It retains the same AR and L_{in}/W_1 , and AS as the scale model. More descriptions of the curved diffuser as part of the open-jet blow-down wind tunnel can be found in Ref. [15].

Figure 15(b) shows the 90 deg-curved diffuser when it was attached to a vertical air duct inside an anechoic chamber. Under normal operation, the Reynolds number at the diffuser inlet is about 3.5×10^5 based on the hydraulic diameter. A rake of pitot tubes covering the distance from the outer to inner walls of the full-size 90 deg-curved diffuser was used to simultaneously measure the exit flow total pressures. Measurements were taken at several spanwise (y) locations to determine the uniformity of the

exit flow. Since the full-size and scale-model experiments were performed at different flow speeds, collapse of data between the two is not possible. A more meaningful approach would be to determine the velocity deviations, U_{dev} , of measured velocity compared with the flow at the outer-wall region where it is usually of maximum. This quantity can be expressed as

$$U_{dev} = \frac{U_{(Z \rightarrow 0, Y=0.5)} - U_{(Z, Y=0.5)}}{U_{(Z \rightarrow 0, Y=0.5)}} \quad (4)$$

where $U_{(Z \rightarrow 0, Y=0.5)}$ is the velocity near the outer-wall region at the center-plane of the diffuser exit, $Y=0.5$; whereas $U_{(Z, Y=0.5)}$ is the velocity from the outer to inner walls (in Z direction), also at $Y=0.5$. Here Y and Z are the normalized distances of y and z respectively, and both have values from 0 to 1. Figure 16(a) compares the aerodynamically treated full-size (\square) and scale-model (\circ) velocity deviations at $Y=0.5$ of the 90 deg-curved diffuser exits. Also shown in the figure is the corresponding velocity deviation for a bare, untreated, scale-model 90 deg-curved diffuser (\triangle). Good agreement is observed between the flow uniformities of the full-size and scale-model diffusers with flow treatment. For the treated case, the velocity deviations of exit flow from the outer to the inner walls for both of the full-size and scale-model diffusers are significantly lower than the untreated case. This implies that the addition of splitter vanes, honeycomb, and pressure-reducing screens has successfully maintained uniform flow over a relatively wide range of Reynolds numbers by inhibiting large-

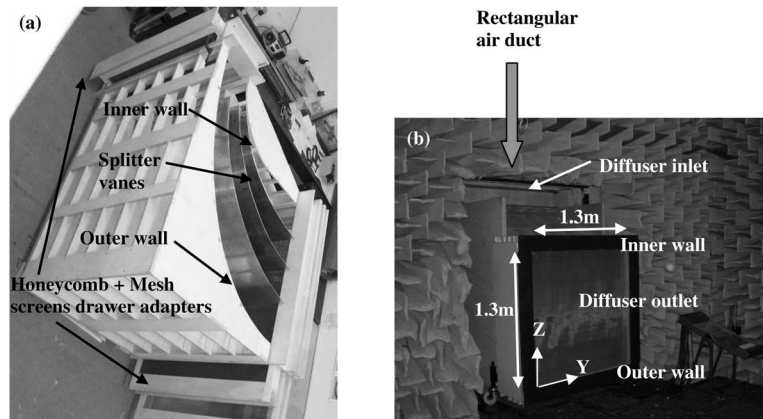


Fig. 15 (a) Inner structure of the full-size 90 deg-curved diffuser. (b) Curved diffuser installed inside the ISVR anechoic chamber.

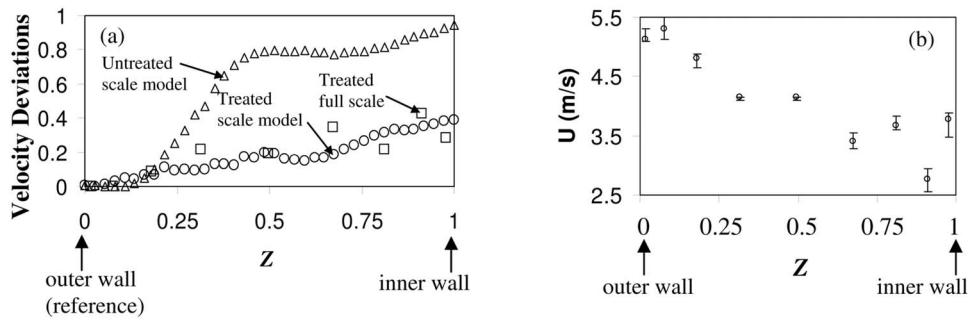


Fig. 16 (a) Comparison of velocity deviations from the outer to the inner walls at $Y=0.5$ of the 90 deg-curved diffuser exit for (○) treated scale model, (△) bare, untreated scale-model, and (□) treated full-size 90 deg-curved diffusers. (b) Distributions of the exit velocity at different spanwise locations, z , from the outer to the inner walls of the full-size 90 deg-curved diffuser.

scale flow separation at the inner wall. Finally, error bars that correspond to the distributions of exit velocity at different spanwise locations (Y) from the outer to inner walls are shown in Fig. 16(b). The deviations are generally small, which implies that a satisfactory two-dimensional exit flow has been achieved by the uses of both guide vanes and mesh screens.

6 Conclusions

A high AR, short L_{in}/W_1 90 deg-curved diffuser model with an inherently unstable flow has been studied parametrically with various passive flow control devices such as vortex generators, guide vanes, honeycomb, and mesh screens. The experiments were carried out in a specially built tunnel to provide uniform inlet air flow to the scale-model 90 deg-curved diffuser. The purpose of this investigation is to determine the optimal configurations of the above flow control devices and implement them on a full-size 90 deg-curved diffuser, which is an integral part of the open-jet, low noise, blow-down wind tunnel at the University of Southampton.

A base line study undertaken using the 90 deg-curved diffuser model confirms the estimates obtained with the classical empirical correlation [3] in that flow separates quite early on the inner wall and the ensuing separated flow encompassed a large cross-sectional area downstream. Also, severe pressure distortion dominated the exit area when more than 50% of it was covered by reversed flow. At first, vortex generator (VG) arrays were used at the 90 deg-curved-diffuser inlet to produce counter-rotating longitudinal vortices to energize the inner part of the boundary layer with a high adverse pressure gradient and to redirect the pressure-driven vortices. However, no clear improvement was observed. While there are reports of satisfactory reduction of total pressure distortion by VG arrays in S -shaped diffusers [7,14,21], it is felt that for short 90 deg-curved diffusers with a large inner-wall curvature, the potentially superior aerodynamic performance with VG arrays is more difficult to achieve due to the presence of large centrifugal forces. Consequently the VG vortices become less capable of producing a flow that remains attached to the wall in such cases.

Effective flow control was achieved using combinations of guide vanes and honeycomb and mesh screens. Although by themselves guide vanes are not capable of preventing large-scale pressure distortion, they were shown to have the effect of distributing the velocity and total pressure more evenly at the diffuser exit. On the other hand, it was shown that a better diffuser performance could be achieved by introducing a pressure drop at the diffuser exit with the addition of a honeycomb and a set of wire mesh screens. Similarly, the investigation demonstrated that heavily loaded screen packs by themselves without guide vanes did not significantly improve the exit flow of the present 90 deg-curved diffuser. Although it is conjectured that a further increase in the

pressure-drop level at the diffuser exit can proportionally enhance the uniformity and minimize the pressure distortion of the exit flow, this practice is shown to be potentially costly as it reduces the pressure recovery of the diffuser. Instead, it is proposed that the guide vanes should be used in conjunction with an acceptable level of pressure drop at the diffuser exit to strike an appropriate balance between effective flow control and minimal loss of total pressure. Guided by the results from the model-scale results, guide vanes, honeycomb and mesh screens were eventually employed in the final design of the full-size 90 deg-curved diffuser. Assessment of the full-size diffuser was performed, which showed satisfactory exit flow uniformity with acceptable pressure loss caused by the screens. Most importantly, no large-scale flow separation was observed in a normally unstable 90 deg-curved diffuser.

Acknowledgment

The work reported in this paper is sponsored by MSTAR DARP in the United Kingdom.

In Memoriam

Professor Peter Davies, the co-author of this paper, passed away on February 2008 at the age of 85. He was one of the founders of the Institute of Sound and Vibration Research (ISVR) at the University of Southampton, UK. This paper is dedicated to his memory. He was an outstanding academic who worked on a wide range of aeroacoustic problems. We got to know and appreciate him as a kind, gentle, and intelligent person. Apart from his professional help, he also became our personal friend. His passing is therefore not only a great loss to the department but also a sad personal loss.

Nomenclature

| | |
|------------------|--|
| AR | = area ratio, W_2/W_1 |
| AS | = aspect ratio of guide vanes, L_{gv}/b |
| b | = width of guide vanes, mm |
| C_p | = nondimensional static pressure along the inner wall |
| C_{p0} | = nondimensional total pressure coefficient at diffuse exit plane |
| gv | = guide vanes |
| h | = height of the vortex generators, mm |
| K | = pressure drop coefficient caused by the screens |
| l | = length of the vortex generators, mm |
| L_{gv} | = arclength of guide vane profiles, mm |
| L_{in} | = length of the inner wall arc, m |
| $P(L_{(i)}/W_1)$ | = axial distribution of static pressure measured at the inner wall, Pa |

P_0 = total pressure measured at the curved-diffuser exit, Pa
 $P_{0,\text{ref}}, P_{\text{ref}}$ = reference total and static pressures, respectively, at 30 mm before the curved-diffuser inlet, Pa
 q = dynamic pressure, $\frac{1}{2}\rho U^2$, Pa; also the cumulative K caused by the screens at the diffuser exit
 s = distance between each successive vortex generator pairs, mm
 U_{dev} = deviation of velocity compared with the flow at the outer-wall region, see Eq. (4)
 U_{ref} = reference velocity at the diffuser inlet, m/s
 $U_{(Z \rightarrow 0, Y=0.5)}$ = velocity near the outer wall at $Y=0.5$, m/s
 $U_{(Z, Y=0.5)}$ = velocity from the outer wall to the inner walls at $Y=0.5$, m/s
 vg = vortex generators
 W_1, W_2 = diffuser widths at the inlet and outlet, respectively, m
 y = spanwise distance from the origin defined in Fig. 2, m
 Y = normalization of y , $y/0.195$ (scale model) or $y/1.3$ (full size)
 z = normal distance from the origin defined in Fig. 2, m
 Z = normalization of z , $z/0.195$ (scale model) or $z/1.3$ (full size)
 $\Delta\phi$ = diffuser turning angle, deg
 Δp = static pressure drop across mesh screens, Pa
 β = screen porosity, see Eq. (1)
 σ = skew angle of vortex generator relative to the plane of symmetry, deg
 ρ = density of air, kg/m^3

References

- [1] Lindgren, B., and Johansson, A. V., 2002, "Design and Evaluation of a Low-Speed Wind-Tunnel With Expanding Corners," Royal Institute of Technology, Technical Report No. TRITA-MEK 2002:14.
- [2] Sagi, C. J., and Johnston, J. P., 1967, "The Design and Performance of Two-Dimensional, Curved Diffusers," *ASME J. Basic Eng.*, **89**, pp. 715–731.
- [3] Fox, R. W., and Kline, S. J., 1962, "Flow Regime Data and Design Methods for Curved Subsonic Diffusers," *ASME J. Basic Eng.*, **84**, pp. 303–312.
- [4] Mehta, R. D., and Bradshaw, P., 1979, "Design Rules for Small Low Speed Wind Tunnels," *Aeronaut. J.*, **83**(827), pp. 443–449.
- [5] Sahin, B., Ward-Smith, A. J., and Lane, D., 1995, "Pressure Drop and Flow Characteristics of Wide-Angle Screened Diffusers of Large Area Ratio," *J. Wind. Eng. Ind. Aerodyn.*, **58**(1–2), pp. 33–50.
- [6] Seltam, M. M., 1995, "Experimental and Theoretical Study of Wide-Angle Diffuser Flow With Screens," *AIAA J.*, **33**(11), pp. 2092–2100.
- [7] Sullerey, R. K., Mishra, S., and Pradeep, A. M., 2002, "Application of Boundary Layer Fences and Vortex Generators in Improving Performance of S-Duct Diffusers," *ASME J. Fluids Eng.*, **124**(1), pp. 136–142.
- [8] Moore, C. A., and Kline, S. J., 1958, "Some Effects of Vanes and of Turbulence in Two-Dimensional Wide-Angle Subsonic Diffusers," NACA, Report No. TN-4080.
- [9] Weng, P. F., and Guo, R. W., 1994, "Swirl Control in an S-Duct at High Angle of Attack," *AIAA J.*, **32**(6), pp. 1321–1322.
- [10] Majumdar, B., Singh, S. N., and Agrawal, D. P., 1996, "Flow Characteristics in a Large Area Ratio Curved Diffuser," *J. Aerospace Eng.*, **210**(1), pp. 65–75.
- [11] Brunn, A., and Nitsche, W., 2003, "Separation Control by Periodic Excitation in a Turbulent Axisymmetric Diffuser Flow," *J. Turbul.*, **4**(1), pp. 1–13.
- [12] Lin, J. C., 2002, "Review of Research on Low-Profile Vortex Generators to Control Boundary-Layer Separation," *Prog. Aerosp. Sci.*, **38**(4–5), pp. 389–420.
- [13] Godard, G., and Stanislas, M., 2006, "Control of a Decelerating Boundary Layer. Part 1: Optimization of Passive Vortex Generators," *Aerosp. Sci. Technol.*, **10**(3), pp. 181–191.
- [14] Reichert, B. A., and Wendt, B. J., 1996, "Improving Curved Subsonic Diffuser Performance With Vortex Generators," *AIAA J.*, **34**(1), pp. 65–72.
- [15] Chong, T. P., Joseph, P. F., and Davies, P. O. A. L., 2008, "Design and Performance of an Open Jet Wind Tunnel for Aero-Acoustic Measurement," *Appl. Acoust.*, in press.
- [16] Pinker, R. A., and Herbert, M. V., 1967, "Pressure Loss Associated With Compressible Flow Through Square-Mesh Wire Gauzes," *J. Mech. Eng. Sci.*, **9**(1), pp. 11–23.
- [17] Bradshaw, P., 1964, "Wind Tunnel Screens: Flow Instability and Its Effect on Aerofoil Boundary Layers," *J. R. Aeronaut. Soc.*, **68**, p. 198.
- [18] Betterton, J. G., Hackett, K. C., Ashill, P. R., Wilson, M. J., Woodcock, I. J., Tilman, C. P., and Langan, K. J., 2000, "Laser Doppler Anemometry Investigation on Sub-Boundary Layer Vortex Generators for Flow Control," *Tenth International Symposium on Applications of Laser Techniques to Fluid Mechanics*, Lisbon, Portugal, Jul. 10–13.
- [19] Majumdar, B., Mohan, R., Singh, S. N., and Agrawal, D. P., 1998, "Experimental Study of Flow in a High Aspect Ratio 90 deg Curved Diffuser," *ASME J. Fluids Eng.*, **120**(1), pp. 83–89.
- [20] Lindgren, B., Oesterlund, J., and Johansson, A. V., 1998, "Measurement and Calculation of Guide Vane Performance in Expanding Bends for Wind-Tunnels," *Exp. Fluids*, **24**(3), pp. 265–272.
- [21] Anabtawi, A. J., Blackwelder, R. F., Lissaman, P., and Liebeck, R. H., 1999, "An Experimental Study of Vortex Generators in Boundary Layer Ingesting Diffusers With a Centerline Offset," *AIAA Paper No. 99-2110*.

Strategies for Simulating Flow Through Low-Pressure Turbine Cascade

Andreas Gross

e-mail: agross@email.arizona.edu

Hermann F. Fasel

Department of Aerospace and Mechanical
Engineering,
University of Arizona,
Tucson, AZ 85721

Laminar separation on the suction side of low-pressure turbine blades at low Reynolds number operating conditions deteriorates overall engine performance and has to be avoided. This requirement affects the blade design and poses a limitation on the maximum permissible blade spacing. Better understanding of the flow physics associated with laminar separation will aid in the development of flow control techniques for delaying or preventing flow separation. Simulations of low-pressure turbine flows are challenging as both unsteady separation and transition are present and interacting. Available simulation strategies have to be evaluated before a well-founded decision for the choice of a particular simulation strategy can be made. With this in mind, this paper provides a comparison of different flow simulation strategies: In particular, "coarse grid" direct numerical simulations, implicit large-eddy simulations, and simulations based on a hybrid turbulence modeling approach are evaluated with particular emphasis on investigating the dynamics of the coherent structures that are generated in the separated flow region and that appear to dominate the entire flow. It is shown that in some instances, the effect of the dominant coherent structures can also be predicted by unsteady Reynolds-averaged Navier–Stokes calculations. [DOI: 10.1115/1.2969463]

1 Introduction

Low-pressure turbine (LPT) stages are important components of many modern jet engines. At low operating Reynolds numbers as encountered at high altitude cruise and/or for small jet engines such as those used in unmanned aerial vehicles, LPT boundary layers remain essentially laminar, even in the presence of elevated freestream turbulence (FST) levels. Laminar separation can occur, causing substantial losses in turbine and overall engine performance. Since off-design conditions are often unavoidable, conservative design margins have to be adopted in the design of LPT stages to guarantee safe and reliable operation. The understanding of the transition process and its interaction with the separation is still incomplete, especially when the separation process is unsteady and three dimensional (3D) as in the LPT application investigated here. Transition to turbulence in the separated region can be initiated by an inviscid Kelvin–Helmholtz (KH) instability (the velocity profiles are inflectional), which results in a "rollup" of the separated boundary layer, or for large enough disturbance amplitudes, by a "by-pass" transition process [1]. Insight into the fluid dynamics of the LPT flow can be obtained from experiments or computational fluid dynamics (CFD).

The experimental research focused to a large extent on methods for active flow control (AFC) of the separation resulting in a large body of publications on steady and pulsed vortex generator jets (VGJs) [2–5] and plasma actuators [6–9]. Particular focus was also on the effect of FST [4,6,7,10], surface roughness [10,11], separation control by carefully placed roughness elements [7,12], and the effect of unsteady wakes generated by upstream stages. The FST effect was also investigated for laminar separation bubbles on a flat plate at LPT conditions [13–15]. While for low freestream turbulence intensity (FSTI) conditions (less than 1%) transition was found to occur through the amplification of disturbances by a KH instability of the wall-bounded shear layer, for higher FSTI conditions, transition was found to occur through a

"by-pass" mode and to set in earlier. The earlier transition resulted in an earlier reattachment and a smaller separated flow region.

In addition to the experimental investigations, numerical simulations were performed by several research groups. Particular challenges for CFD are the transitional nature of the flow and the associated numerical resolution requirements. The relevant Reynolds number range is barely accessible for direct numerical simulations (DNS). The computational expense of numerical simulations may be lowered by employing turbulence modeling. These models must, however, correctly account for the low Reynolds number transitional nature of the flow. So far, five different turbulence modeling approaches have been applied to LPT flows: DNS, large eddy simulation (LES), implicit LES (ILES) where the diffusion of the numerical scheme resembles the model contribution of typical LES subgrid stress models [16], Reynolds-averaged Navier–Stokes (RANS), Unsteady RANS (URANS), RANS coupled with a transport equation for the intermittency factor, or RANS coupled with transition models.

Using DNS, Wu and Durbin [17] showed that periodic turbulent upstream wakes can trigger by-pass transition of the suction side boundary layer and generate longitudinal vortices on the pressure side of the blade. Results by Kalitzin et al. [18] and Wissink and Rodi [19] indicate that both FST and upstream wakes can trigger by-pass transition. High-resolution DNS of laminar separation bubbles on a flat plate at LPT conditions, a related model problem, were performed by Wu et al. [20], Postl et al. [21,22], and Wissink and Rodi [19]. Other than DNS, the least amount of modeling is required by ILES and LES. An ILES of the T106 LPT blade with relatively limited flow separation by Raverdy et al. [23] matched the experimental mean velocity profiles and wall pressure distribution for the chosen Reynolds number surprisingly well. A LES of the same geometry with periodic upstream wakes by Michellasi et al. [24] produced velocity and turbulent kinetic energy profiles that were in good agreement with DNS results by Wu and Durbin [17]. Rizzetta and Visbal [25,26] employed ILES for studying the fluid dynamics of separation control by pulsed VGJs for a Pack B cascade. Standard turbulence models, such as the k - ϵ and k - ω models when applied in a RANS context, may in some instances yield reasonable results [27–29]. It is, however, surprising that such simple models can capture the complex 3D dynam-

Contributed by the Fluids Engineering Division of ASME for publication in the JOURNAL OF FLUIDS ENGINEERING. Manuscript received November 5, 2007; final manuscript received July 2, 2008; published online September 23, 2008. Assoc. Editor Chunill Hah.

ics of the transitional flow. It appears that at least the more energetic unsteady flow components have to be resolved if more realistic predictions of the transitional flow are sought. Quite encouraging results by Lardeau and Leschziner [30] showed that this can be accomplished, at least in a qualitative manner, by URANS. Turbulence models coupled with additional transport equations for intermittency and other quantities (e.g., Refs. [31–34] show great potential but are not broadly used yet.

The geometry chosen for the present studies is the Pratt and Whitney Pack B LPT blade. The simulations were set up according to the earlier experiments by Bons and co-workers at the Air-Force Research Laboratory (AFRL) [2–4] where upstream wakes, surface roughness, and freestream wakes were not considered. This deliberate simplification, when compared to the environment in real jet engines, allows focusing on the flow physics of the laminar separation and transition without the complicating interference of other secondary effects. This paper is organized as follows: First, the results from a “coarse grid” DNS are compared with the results obtained from an ILES and results obtained with a hybrid turbulence model, the flow simulation methodology (FSM) [35]. Second, as a reference, the flow was also computed using RANS. Finally, the dynamical behavior of the unsteady flow structures obtained from the various approaches is analyzed and compared.

2 Numerical Method

2.1 Governing Equations. The compressible Navier–Stokes equations are solved in conservative form and curvilinear coordinates. For our FSM [35], which was originally developed in collaboration with Speziale [36,37], additional turbulence model equations are solved and the turbulence quantities are scaled by a contribution function

$$f = 1 - \exp\left(-\frac{\max\left(0, \frac{\Delta}{L_k} - 2\right)}{1000}\right) \quad (1)$$

where Δ is a measure of the local grid spacing and $L_k = ((\mu/\rho)^3/\varepsilon)^{0.25}$ is the Kolmogorov length scale. Effectively, FSM calculations can be considered to be locally and temporally DNS, LES, or RANS depending on the ratio Δ/L_k . Here, for the FSM, the 1998 version of the k - ω model [38] was employed in combination with an explicit algebraic stress model (EASM) as described by Rumsey and Gatski [39].

In addition, for RANS and URANS simulations, the following turbulence models were employed in combination with either the Boussinesq-approximation (BA) or the EASM by Rumsey and Gatski [39]: The k - ε model [40] with EASM (in the following referred to as “ k - ε EASM”), the low Reynolds number variant of the k - ε model by Lam and Bremhorst [41] (LB) with BA, the 1998 version of the k - ω model by Wilcox [38], both with BA (“ k - ω ”) or EASM (“ k - ω EASM”), the shear stress transport (SST) model by Menter [42] with BA, and the Spalart–Allmaras (SA) model [43]. For the SA model, the tripping terms were omitted.

2.2 Boundary Conditions. The blade surface was treated as an adiabatic no-slip wall. A nonreflecting boundary condition was employed at the inflow and outflow boundaries [44]. Turbulence quantities were extrapolated at the outflow and prescribed at the inflow. Flow periodicity was imposed at all other boundaries. The turbulent fluctuations are zero at the wall, $k=0$. For the k - ε turbulence model, $\partial\varepsilon/\partial y=0$ was prescribed at the wall. Wilcox [38] gave a relation for the dependence of ω on the wall distance in close vicinity of a hydraulically smooth wall. This relationship was employed for computing the value of ω for the wall next grid cell. The computed value was then multiplied by 10 and prescribed as wall value for ω . In principle, for a perfectly smooth wall, ω becomes infinite at the wall. Prescribing arbitrarily large values of ω at the wall may result in accurate model predictions;

it can, however, reduce the robustness of the numerical method. The procedure mentioned above yields accurate results without compromising robustness.

2.3 Discretization. The governing equations were solved in the finite volume formulation to guarantee conservation of mass on distorted grids. For the FSM, RANS, and URANS calculations, the convective terms of the Navier–Stokes equations were discretized with a fifth-order-accurate upwind scheme based on a weighted essentially nonoscillatory extrapolation of the characteristic variables and the Roe scheme [45,46]. An analogous ninth-order-accurate scheme was employed for the DNS results. Fourth-order-accurate finite differences were used for the Navier–Stokes viscous terms. According to investigations by Margolin and Rider [16] the diffusion characteristics of second-order-accurate nonoscillatory finite volume schemes can mimic the diffusion properties of Smagorinsky-type subgrid stress models used in traditional LES. Here, the second-order-accurate symmetric total variation diminishing (TVD) scheme by Yee [47] was employed for the ILES simulations. This scheme is not identical to the specific discretization proposed by Margolin and Rider [16]. It does, however, exhibit similar properties and falls under the same category of schemes (nonoscillatory finite volume schemes) that Margolin and Rider considered appropriate for ILES. The viscous terms were then discretized with second-order-accurate finite differences. The convective terms of the turbulence model equations were discretized with a second-order-accurate scheme analogous to the TVD scheme by Yee [47] for the FSM calculations and with a first-order-accurate upwind scheme for the RANS and URANS calculations. A second-order-accurate implicit Adams–Moulton method was employed for time integration. The resulting system of equations was solved iteratively by a Newton method based on a line Gauss–Seidel algorithm.

3 Setup

3.1 Case Description. The present results are for the Pack B LPT blade. The experimental linear Pack B cascade by Bons and co-workers [2–4] consisted of eight blades with a span of $\approx 5C_x$. The ratio of blade spacing, d , and axial chord length, C_x , was 0.88. The inflow and design exit angle (both measured relative to the plane of the cascade) were 55 deg and 30 deg. In our Pack B simulations, both the number of blades and the span were assumed to be infinite (using periodicity conditions). In the experiments, the flow was most susceptible to laminar separation for an inflow Reynolds number based on axial chord of 25,000. The same case was investigated here. The inflow Mach number, which was 0.0064 in the experiments, was raised to 0.1 to accelerate the convergence of the numerical method. The same inflow Mach number was also chosen by Rizzetta and Visbal [25,26] for their simulations. In a separate investigation (omitted here) it was shown that compressibility effects played an insignificant role for Mach numbers of $M=0.1$ or smaller. Inflow temperature and Prandtl number were set to 300 K and 0.72 and the viscosity was computed from Sutherlands law. Length scales, velocities, and time were nondimensionalized with the axial chord length, C_x , and the inlet velocity, v_{in} . The RANS and URANS calculations were computed with a nondimensional time step of $\Delta t=0.001$. All other cases were computed with a nondimensional time step of $\Delta t=0.0005$ resulting in a more accurate time integration.

3.2 Inflow Turbulence. For two-equation turbulence models two parameters such as the FSTI, Tu , and a second parameter, such as the integral turbulence length scale, l_T , have to be provided at the inflow boundary. The turbulence intensity can be measured directly and is often reported. The integral turbulence length scale, on the other hand, is often not reported and needs to be assumed. To be even more accurate, the distance between inflow boundary and cascade plane would also have to be matched since the freestream turbulence intensity decays in downstream

direction. The turbulence spectrum also plays a role as peaks in the spectrum can excite flow instabilities. However, most turbulence models are relatively insensitive to the inflow turbulence values as long as they are within a certain parameter range. Menter [48] showed that for ill-chosen inflow parameters unphysical solutions can be obtained. The freestream eddy viscosity, μ_T , was found to not affect the solution as long as its freestream value was small compared to its maximum value in the boundary layer. In addition, Wilcox [38] stated that the freestream value of either ω or ε should be less than 1% of their respective peak value in the boundary layer.

The freestream eddy viscosity

$$\frac{\mu_T}{\mu_{in}} = \sqrt{\frac{3}{2}} Tu Re \frac{l_T}{C_x} \quad (2)$$

can be computed from the turbulence intensity

$$Tu = \sqrt{\frac{2}{3} \frac{k}{v_{in}^2}} \quad (3)$$

and from the integral turbulence length scale

$$l_T = \frac{\sqrt{k}}{\omega} = c_\mu \frac{k^{3/2}}{\varepsilon} = \sqrt{\frac{3}{2}} Tu \frac{v_{in}}{\omega} = c_\mu \left(\frac{3}{2}\right)^{3/2} Tu^3 \frac{v_{in}^3}{\varepsilon} \quad (4)$$

The freestream integral turbulence length scale influences the downstream decay of k upstream of the cascade. Wilcox [38] provided relationships describing the freestream downstream development of k and ω for the $k-\omega$ model. In fact, Suzen and Huang [31] estimated the freestream eddy viscosity for a specific experiment by adjusting it such that the measured turbulence intensity decay was matched.

Various experiments indicate that at very low Reynolds numbers (25,000 and below) and for FSTIs less than 1%, the separated boundary layer transitions through a KH instability mechanism [49]. In the experiments at the AFRL [2–4] honeycomb flow straighteners located in the inlet together with a 6:1 contraction resulted in an inflow turbulence intensity, Tu , of 1% at the cascade plane. In separate Pack B experiments by Huang et al. [6–8] an inflow turbulence intensity of 0.08% was achieved. For both experiments, turbulence length scales were not reported. In the flat plate LPT experiments by Simon et al. [50] FSTIs of 0.5%, 2.5%, and 10% were investigated. The integral turbulence length scale, l_T/C_x , computed from the measured dissipation rate, ε , was 1.4×10^{-3} for $Tu=2.5\%$ and 1.9×10^{-3} for $Tu=10\%$. No turbulence length scales were reported for the low FSTI case. Dorney [29] observed a dependence of the predicted wall skin friction on the freestream eddy viscosity in his low Reynolds number Pack B RANS calculations with the $k-\varepsilon$ model. For $\mu_T/\mu_{in}=1$ the boundary layers were too laminar. Good agreement with a Baldwin-Lomax reference solution was obtained for $\mu_T/\mu_{in}=10$. With a turbulence intensity of 3% and a Reynolds number of 80,000 the integral turbulence length scale, l_T/C_x , was 3.4×10^{-4} for $\mu_T/\mu_{in}=1$ and 3.4×10^{-3} for $\mu_T/\mu_{in}=10$. Garg [28] assumed a FSTI of 1% and $l_T/C_x=0.05$ in his LPT calculations. Langtry et al. [51] in their Pack B simulations at $Re=50,000$ considered freestream turbulence intensities of 0.08%, 2.35%, and 6%. For the low FST case the nondimensionalized eddy viscosity at the inflow was set to $\mu_T/\mu_{in}=10$. With a Reynolds number of 50,000 and a FSTI of 0.08% $l_T/C_x=0.20$ is obtained.

At this point we were not interested in the effect of FST on separation and transition. Therefore, for the DNS, ILES, and the resolved part of the FSM we prescribed laminar inflow conditions (no velocity fluctuations). For the RANS calculations and for the unresolved part of the FSM we chose an inflow FSTI of 0.1%, which is a typical experimental value. For this FSTI, transition can be expected to be initiated through a KH instability mechanism. Since the inflow integral turbulence length scale was not reported for any of the low FSTI LPT experiments we had to guess its value. We decided on an integral turbulent length scale,

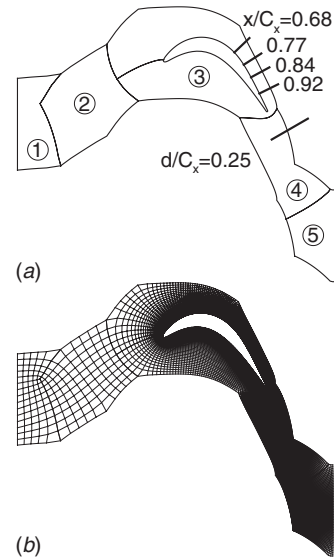


Fig. 1 Coarse grid. (a) Block structure (blocks 1–5 from left to right) and (b) entire grid. The lines indicate where profiles in Figs. 9–11, 16, and 17 were taken.

l_T/C_x , of 0.002. In our calculations with this choice of l_T/C_x the resulting freestream eddy viscosity, $\mu_T/\mu_{in}=0.061$, was considerably lower than the peak eddy viscosity (~ 10 in the boundary layer) and the nondimensional inflow turbulent specific dissipation $\omega \mu_{in}/(\rho_{in} v_{in}^2) = \sqrt{3/2} Tu C_x / (Re l_T) = 2.4 \times 10^{-5}$ was significantly lower than its peak value in the boundary layer (~ 0.005). As both the Menter [48] and the Wilcox [38] conditions were satisfied and the computed flow fields appeared reasonable we deemed this particular choice of l_T/C_x adequate for our present simulations.

3.3 Computational Grid. The computational domain was split into five blocks as shown in Fig. 1. In the same figure, the lines along which the wall normal and wake profiles in Figs. 9–11, 16, and 17 were taken are indicated. The grid was designed to be periodic in the plane of the cascade and in the spanwise direction. Cells were densely clustered at the wall, in the separated flow region on the suction side of the blade, and in the wake region. The near wall grid resolution in wall units, y^+ , was below 1. For the three-dimensional (3D) simulations, the two-dimensional (2D) grids were extended in the spanwise direction. The grid line spacing in the spanwise direction was constant. According to the numerical studies by Rizzetta and Visbal [25,26] the spanwise grid extent, ΔZ , was set to $0.2 C_x$. Both a coarse grid and a fine grid were employed (Table 1). The coarse grid was obtained from the fine grid by removing every other grid line.

4 Results

4.1 DNS, ILES, and FSM Results. Instantaneous visualizations of the time-dependent 3D flow data obtained from the DNS, ILES, and FSM simulations are shown in Fig. 2. For these visu-

Table 1 Block grid resolutions

| Block | Coarse grid | Fine grid |
|-------|---------------------------|----------------------------|
| 1 | $5 \times 15 \times 16$ | $10 \times 30 \times 32$ |
| 2 | $10 \times 10 \times 16$ | $20 \times 20 \times 32$ |
| 3 | $250 \times 50 \times 16$ | $500 \times 100 \times 32$ |
| 4 | $130 \times 50 \times 16$ | $260 \times 100 \times 32$ |
| 5 | $52 \times 55 \times 16$ | $105 \times 110 \times 32$ |

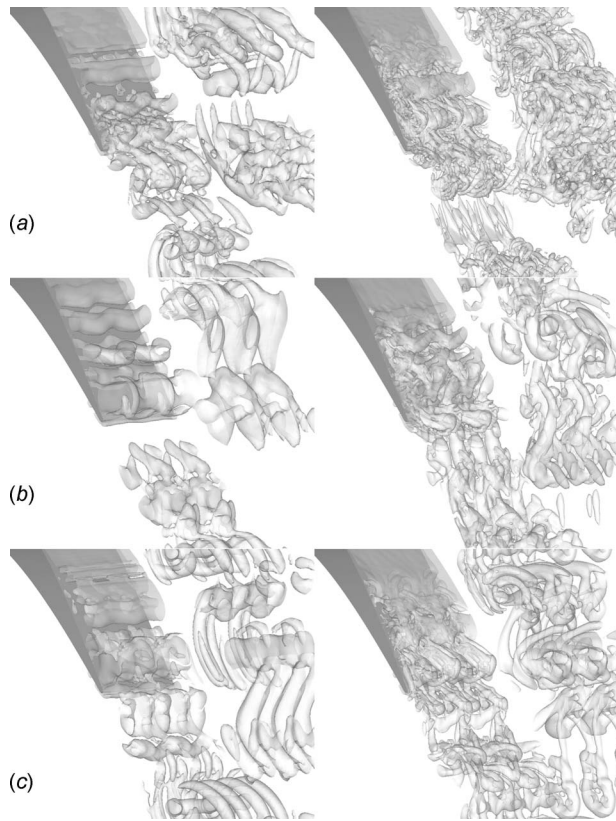


Fig. 2 Isosurfaces of Q -criterion, $Q=1$. Results for (a) DNS, (b) ILES, and (c) FSM. (Left) coarse grid and (right) fine grid.

alizations the flow domain was repeated once in the spanwise direction and twice in the normal direction. Here, isosurfaces of the vortex identification criterion [52],

$$Q = \frac{1}{2}(W_{ij}W_{ij} - S_{ij}S_{ij}) \quad (5)$$

are shown. A positive Q -criterion indicates areas where rotation dominates strain. When interpreting the results in Fig. 2, one has to keep in mind that the amount of turbulence modeling is different. Some of the small scale structures that are visible in the separated flow region in the DNS are not resolved in the ILES and FSM. A strong amplification of 2D disturbances caused by the shear layer instability of the separated boundary layer (inflectional velocity profile and KH instability) results in a rollup of the separated boundary layer into spanwise vortical structures, which are subject to a secondary instability mechanism (indicated by the spanwise modulation of the spanwise structures) leading to transition. From previous simulations it is known that the strength of the spanwise coherent structures is overpredicted in 2D simulations [53], resulting in a delayed separation and earlier reattachment when compared with the 3D simulations where small scale turbulent motion weakens the coherence of the spanwise coherent structures.

Instantaneous visualizations of eddy viscosity, μ_T/μ , levels of the contribution function, f , and “effective eddy viscosity,” $f\mu_T/\mu$, in the $z=0$ plane for the FSM cases are shown in Fig. 3. Eddy viscosity is produced in the separation bubble and around the flow structures in the wake (Fig. 3(a)). A significant buildup of eddy viscosity can also be detected in between the wakes. The instantaneous spatial distribution of the contribution function (Fig. 3(b)) is clearly coupled to the unsteady flow structures. Since the grid resolution is relatively good (or since the Reynolds number is relatively low) the turbulence model contribution is small and less than 6% for the coarse grid and less than 3% for the fine grid. The “effective” eddy viscosity (Fig. 3(c)) is less than ten times the

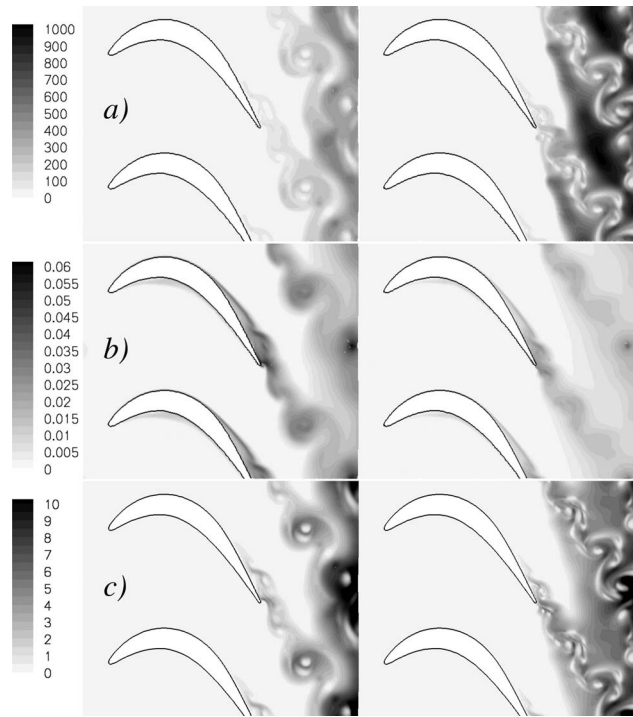


Fig. 3 Isocontours of (a) eddy viscosity, μ_T/μ , (b) contribution function, f , and (c) effective eddy viscosity, $f\mu_T/\mu$, for (left) coarse grid and (right) fine grid FSM

laminar viscosity in the wake and less than three times the laminar viscosity in the separation bubble for the coarse grid (with half the respective numbers for the fine grid). Based on the FSM results, a resolution requirement estimate for a true DNS can be obtained. The ratio of local grid resolution, Δ , and smallest turbulence length scale, L_k , can be computed from the local contribution function, f . The results shown in Fig. 4 were computed from the time-averaged flow data (averaged in time over a time interval of $\Delta T=10$ and in the spanwise direction). Here and in the following, time averages were computed from the time-averaged density and the Favre-averaged velocities, total energy, turbulence kinetic energy, and turbulence dissipation rate or specific dissipation. The time averaging was initiated after the flow had settled into a time-periodic behavior. For the fine grid, the maximum value of Δ/L_k is about 15 in the separated flow region and 20 close to the trailing edge with double the numbers for the coarse grid. This means that the grid resolution of the current fine grid DNS is too low by a factor of roughly 80 in the separated flow region and the wake, assuming that a ratio, Δ/L_k , of 1/4 is sufficient for resolving the smallest eddies [38]. The current fine grid had 2.8×10^6 cells.

A comparison of the computed wall pressure coefficient

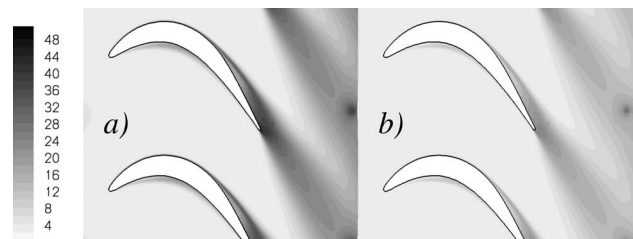


Fig. 4 Isocontours of grid resolution, Δ/L_k , for (a) coarse grid and (b) fine grid FSM

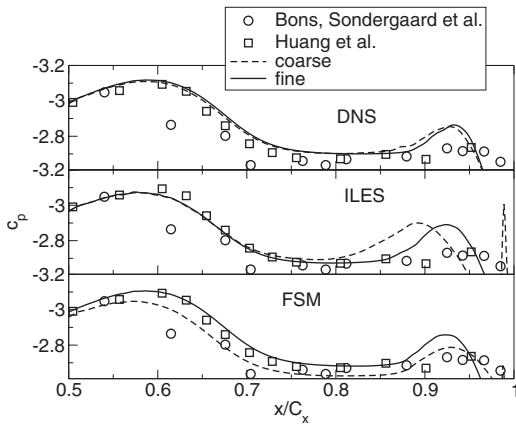


Fig. 5 Wall pressure coefficient, c_p

$$c_p = \frac{p - p_{in}}{\frac{1}{2} \rho_{in} v_{in}^2} \quad (6)$$

with the experimental data [2–4,6,7] is shown in Fig. 5. Except for the coarse grid ILES, the difference between the computed wall pressure distributions is small, indicating that the wall pressure coefficient is not a good choice for comparing results. A slight pressure drop-off or “hump” close to the trailing edge, indicating strong spanwise coherent structures [21,22,53], can be observed for all cases. This hump is especially pronounced for the coarse grid ILES result. In the experiment the “pressure plateau” in the separated flow region is flatter leading to the conclusion that the spanwise coherent structures were not as energetic or pronounced as in the simulations. The weaker coherence of the spanwise structures in the aft part of the blade is likely a consequence of the flow being more turbulent, which may be attributed to a larger FSTI or wall roughness in the experiments, or a lack of grid resolution for the DNS, insufficient model contribution for the ILES and FSM, or an insufficient spanwise grid extent of the computational domain, which effectively suppresses spanwise modes with larger wavelengths. Although a low inflow turbulence intensity was prescribed for the FSM, a time-dependent random freestream disturbance that could “seed” the primary and secondary instabilities of the separated boundary layer was not introduced for all of the current 3D simulations. Also as a consequence of the lack of a defined disturbance input, the results become somewhat nondeterministic and dependent on numerical errors, which may be a reason why grid convergence is difficult to obtain.

Figure 6 shows isocontours of the streamfunction computed from the temporal and spanwise average of the FSM data. Three recirculating flow regions are visible: A separation bubble on the pressure side and a separation bubble on the suction side which encloses a secondary separation bubble. Although the coarse and fine grid results look qualitatively similar, the suction side separation bubble is shallower for the fine grid indicating that full grid convergence was not achieved. The secondary separation bubble can only be seen in the time mean. Instantaneous flow visualizations reveal that the strong spanwise coherent structures with clockwise rotation that result from the rollup of the shear layer

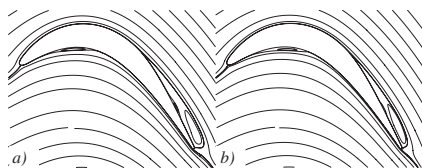


Fig. 6 Isocontours of streamfunction. Results for (a) coarse grid and (b) fine grid FSM

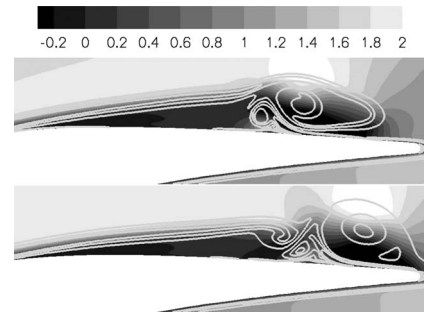


Fig. 7 Instantaneous flow visualizations near the trailing edge. Isocontours of velocity in the cascade exit flow direction superimposed with isocontours of spanwise vorticity (gray lines, $\omega_z = -100, \dots, 100$, $\Delta\omega_z = 40$).

transport counterclockwise vorticity off the wall leading to the formation of spanwise vortices with counterclockwise rotation in between the primary spanwise vortices (Fig. 7). These vortices with counter-clockwise rotation are strong enough to cause a local reversal of the wall skin friction direction.

Temporal and spanwise averages of the skin friction coefficient

$$c_F = \frac{\mu \frac{\partial v}{\partial y}}{\frac{1}{2} \rho_{in} v_{in}^2} \quad (7)$$

are plotted in Fig. 8. The waviness of the skin friction coefficient curves in the region of the secondary separation bubble can be attributed to short time-averaging intervals. The coarse grid ILES result is noticeably different from the other results. This is likely the consequence of (when compared with the other simulations) stronger spanwise coherent structures due to strong numerical diffusion, which dampens out much of the small scale turbulent motion thereby resulting in a flow with a lower “effective Reynolds number,” which is less turbulent. The locations of primary and secondary separation and reattachment on the suction side of the blade as obtained from Fig. 8 are listed in Table 2. The primary separation locations computed with the various approaches appear to converge toward each other as the grid resolution is increased.

Computed shape factors, $H = \delta^* / \theta$, at $x/C_x = 0.68$ are listed in Table 3. Displacement thickness, δ^* , and momentum thickness, θ , were computed from the wall tangential velocity component and the boundary layer edge velocity was taken to be the maximum velocity of the profile. The shape factor is larger for the cases where the flow separates earlier, e.g., the coarse grid FSM. The

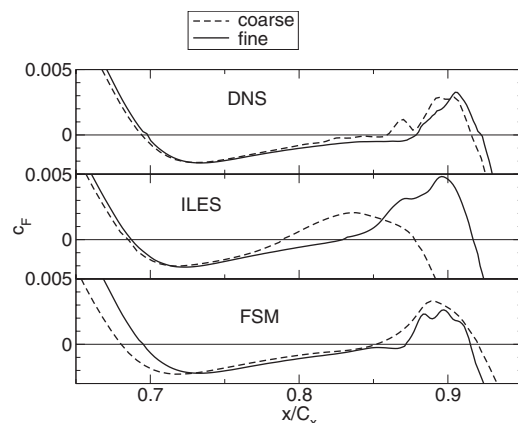


Fig. 8 Skin friction coefficient, c_F

Table 2 Locations, x/C_x , of primary and secondary separation and reattachment. The numbers in parentheses are coarse grid results.

| Model | Primary sep. | Secondary sep. | Secondary reat. | Primary reat. |
|-------|------------------|------------------|------------------|------------------|
| DNS | 0.698 (0.694) | 0.879 (0.859) | 0.922 (0.916) | 1.000 (1.000) |
| ILES | 0.687 (0.685) | 0.829 (0.789) | 0.917 (0.878) | 1.000 (0.995) |
| FSM | 0.695 (0.680) | 0.872 (0.852) | 0.915 (0.920) | 1.000 (1.000) |

additional numerical diffusion of the lower-order scheme employed for the ILES and the turbulence model contribution for the FSM have a similar effect and increase the shape factor when compared with the DNS. Also, lower grid resolution does in all instances result in a larger shape factor, indicating that numerical diffusion for the coarser grid makes the velocity profiles less full and reduces the wall shear stress.

Time-averaged wall normal profiles of the total velocity

$$v_{tot} = \sqrt{u^2 + v^2} \quad (8)$$

averaged in the spanwise direction are shown in Fig. 9. The profiles were normalized with their respective velocity maxima to allow for a comparison with the normalized experimental data [2,4]. At $x/C_x=0.68$, the computed velocity profiles are slightly less full than the measured profiles indicating that the flow is closer to separation. This is surprising, since judging from the wall pressure distribution (Fig. 5), the flow separated earlier in the experiment [2,4] when compared with the simulations. Downstream, at $x/C_x=0.77$, the computed velocity profiles match the experimental data very well. The thickness of the separation bubble is underpredicted at the following two downstream stations: $x/C_x=0.84$ and $x/C_x=0.92$. With the current limited amount of available experimental data, a more thorough investigation of the differences responsible for this discrepancy is impossible. However, since the numerical results appear to converge toward a unique solution as the grid resolution is increased, a fundamental difference in the setup between the simulations and the experiment may also be the reason for the observed differences. This may include differences in the FSTI, or differences in the setup with respect to, for example, the inflow and outflow angles. It is worth noting that although the velocity profiles obtained from the ILES appear to be almost grid converged, the c_p - and c_F -distributions are not (Figs. 5 and 8).

Wall-normal profiles of the model contribution for the FSM computed from the time-averaged flow data and averaged in the spanwise direction are shown in Fig. 10. The model contribution at $x/C_x=0.68$ obtains a maximum of about 2.5% for the coarse grid and 1% for the fine grid in the outer region of the boundary layer. As the velocity profiles at this downstream location are not inflectional most of the turbulence production is expected to take place near the wall. At the separated flow locations, $x/C_x=0.77$, 0.84, 0.92, the contribution function distributions exhibit two distinctive maxima, one near the wall in the boundary layer of the

Table 3 Shape factor, H , at $x/C_x=0.68$. The numbers in parentheses are coarse grid results.

| Model | H |
|-------|-------------|
| DNS | 1.42 (1.46) |
| ILES | 1.48 (1.53) |
| FSM | 1.43 (1.56) |

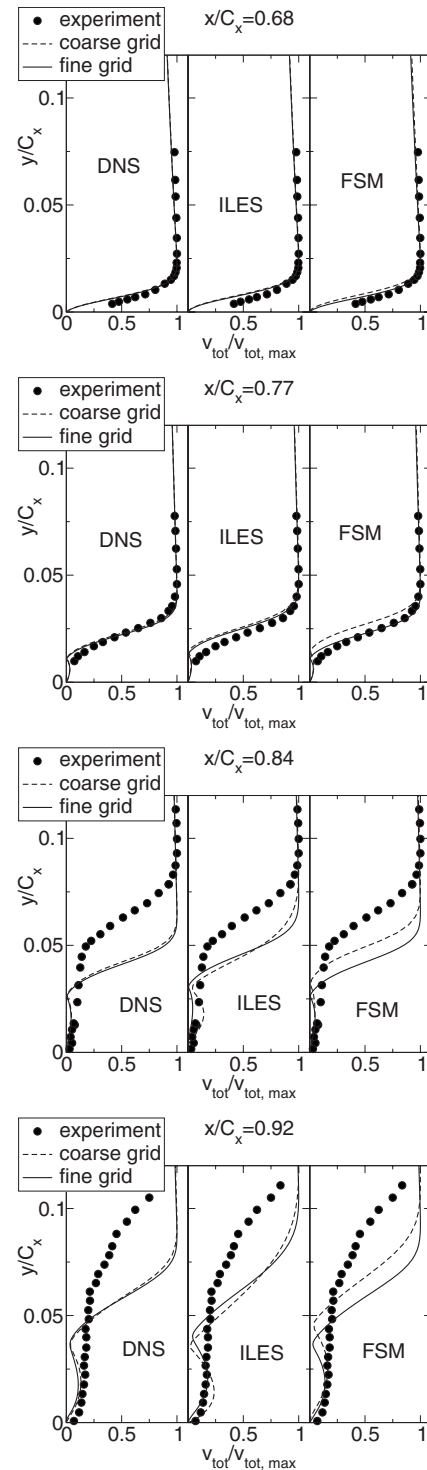


Fig. 9 Wall-normal profiles of the total velocity. Comparison with experimental data [2,4].

reverse flow and one in the vicinity of the inflection point of the velocity profile (both locations are regions of turbulence production). Finally, wake velocity profiles taken downstream of the trailing edge of the blade and computed from the temporal average of the flow data and averaged in the spanwise direction are shown in Fig. 11. The DNS and FSM results appear to converge to the same result as the grid resolution is increased with the ILES yielding a slightly wider wake.

4.2 RANS and URANS Results. The current 3D results may

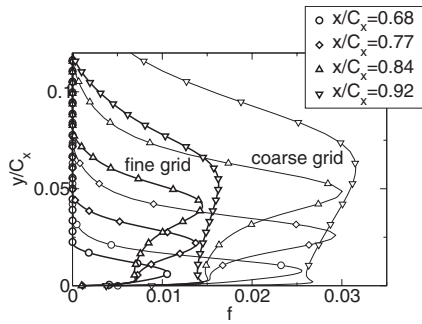


Fig. 10 Wall-normal profiles of model contribution obtained from the FSM simulation

be sufficiently accurate for analyzing existing LPT blade geometries. They are, however, computationally expensive with large turnaround times and, therefore, out of the question during the design process of new blade geometries. Computationally less expensive alternatives such as URANS and RANS or design codes based on the Euler equations such as MISES [54] have to be considered. With URANS the dynamics of the unsteady flow structures may be captured while for RANS all unsteady flow motion has to be modeled, imposing a large burden on the turbulence model. As the flow is transitional, low Reynolds number models such as the LB model are expected to work better. Here, other common turbulence models such as the $k-\omega$, $k-\varepsilon$, and SA models are considered as well. As shown by Praisner and Clark [55], the accurate prediction of the FST properties and its interaction with the laminar boundary layer, as well as the accurate prediction of the attached and separated flow transition, pose the largest challenges in RANS calculations of LPT flows. For our present studies the FSTI was assumed to be small. Flow transition was not forced based on a transition criterion but left to the turbulence model. Although this approach may appear a little naive it is shown that for the test case considered here where the flow does not reattach to the blade, URANS can yield relatively accurate results. For the same reason, because the flow does not reattach the performance of the models is not fully tested.

Figure 12 shows a comparison of some of the 2D RANS and URANS results. Shown are isocontours of spanwise vorticity

$$\omega_z = \frac{\partial v}{\partial x} - \frac{\partial u}{\partial y} \quad (9)$$

All cases were computed on the fine grid. When the LB and $k-\varepsilon$ EASM models were employed, the flow became unsteady (therefore, these simulations are referred to as URANS) and a separation bubble developed on the suction side close to the trailing edge, which is in qualitative agreement with the experiments and the 3D simulations. The results obtained with the $k-\omega$, SST, and SA models indicate no discernible flow separation on the suction

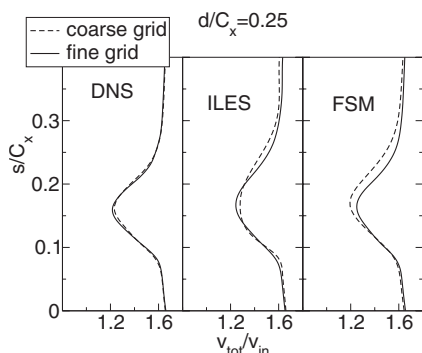


Fig. 11 Wake profiles of the total velocity

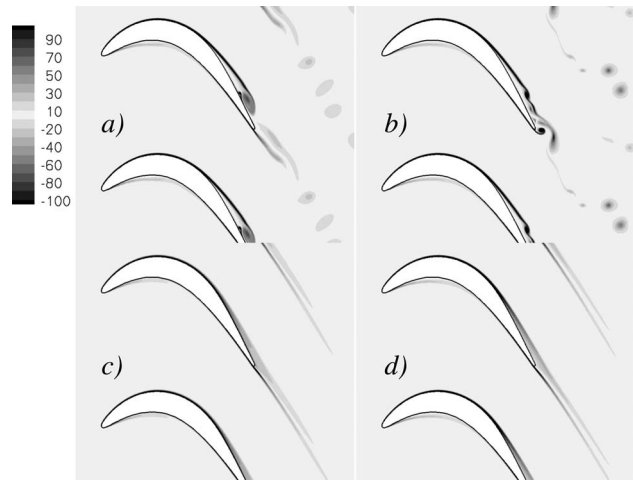


Fig. 12 Isocontours of spanwise vorticity, ω_z . The results were obtained with (a) LB, (b) $k-\varepsilon$ EASM, (c) $k-\omega$, and (d) $k-\omega$ EASM model.

side, which is contradicting the experimental results. With all models, a shallow separation bubble is predicted on the pressure side of the blade.

Figure 13 shows the computed distributions of eddy viscosity for all four models. Owing to the low Reynolds number conditions, the flow upstream of the separation is almost laminar for the LB and $k-\varepsilon$ EASM models. For both the LB and $k-\varepsilon$ EASM models, eddy viscosity is produced in the spanwise structures and in the wake (Figs. 13(a) and 13(b)). This is in qualitative agreement with the FSM results and with the real flow where (through a secondary instability mechanism) the flow transitions to turbulence near the trailing edge. The increased entrainment caused by the spanwise structures and also due to turbulent mixing leads to flow reattachment near the trailing edge (closing the laminar separation bubble). For all other models, an accumulation of eddy viscosity can be observed close to the leading edge (slightly less, though, for the $k-\omega$ EASM model). This unphysical behavior can be attributed to the stagnation point anomaly of linear eddy viscosity models [56].

A comparison of the wall pressure coefficient is shown in Fig. 14. For the URANS results (LB and $k-\varepsilon$ EASM models) the data were time-averaged over a time interval of $\Delta T=10$. The upper

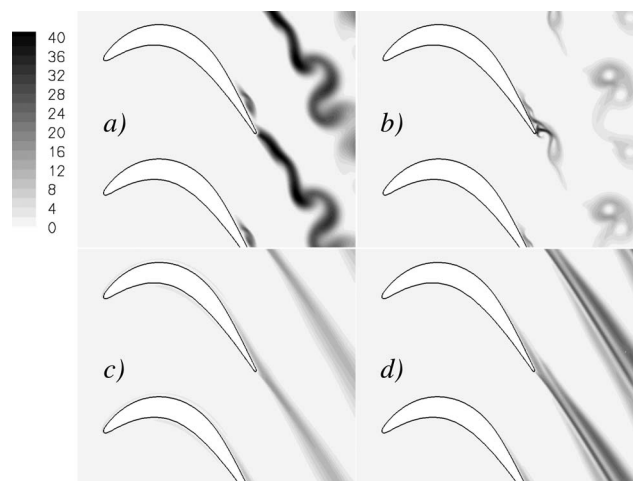


Fig. 13 Isocontours of eddy viscosity μ_T/μ . The results were obtained with (a) LB, (b) $k-\varepsilon$ EASM, (c) $k-\omega$, and (d) $k-\omega$ EASM model.

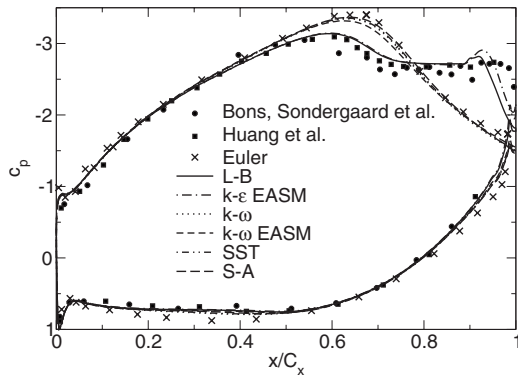


Fig. 14 Wall pressure coefficient, c_p

part of the curves represents the suction side of the blade. The results are compared with the experimental data by Bons et al. [2], Sondergaard et al. [4], and Huang et al. [6] and with an inviscid (Euler) solution [6]. In the experiments, the laminar boundary layer separates from the blade at approximately $x/C_x=0.6$ (roughly the beginning of the “uncovered turning”) leading to a deviation of the wall pressure distribution from the Euler prediction. The resulting pressure plateau can be associated with the separated flow region. Another deviation from the inviscid flow solution, which can be observed on the pressure side of the blade around $x/C_x=0.2 \dots 0.4$, is caused by the pressure side separation bubble. Aside from a hump close to the trailing edge, the wall pressure distributions computed with the LB and $k-\epsilon$ EASM models are in reasonably good agreement with the experimental data. This hump or pressure drop can be attributed to strong spanwise coherent structures, which are a consequence of the two dimensionality of the simulations. [53]

A comparison of the time-averaged skin friction coefficient shows a very shallow separation bubble for the $k-\omega$ EASM model (Fig. 15). Also, a secondary separation (in the temporal mean) can be observed for the LB and $k-\epsilon$ EASM models (URANS results). Fully attached flow is predicted with all other models (steady RANS). Table 4 lists computed separation and reattachment locations as obtained from the zero skin friction locations. The results obtained with the various turbulence models vary considerably.

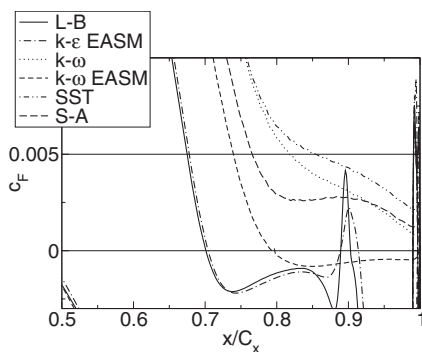


Fig. 15 Skin friction coefficient, c_f

Table 4 Locations, x/C_x , of primary and secondary separation and reattachment

| Model | Primary sep. | Secondary sep. | Secondary reat. | Primary reat. |
|-------------------|--------------|----------------|-----------------|---------------|
| LB | 0.690 | 0.881 | 0.906 | 1.000 |
| $k-\epsilon$ EASM | 0.706 | 0.887 | 0.916 | 0.995 |
| $k-\omega$ EASM | 0.797 | — | — | 0.998 |

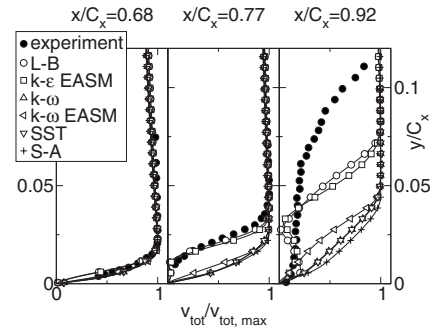


Fig. 16 Wall-normal profiles of the total velocity. Comparison with experimental data [2,4].

However, the URANS results (LB and $k-\epsilon$ EASM) are close to the 3D fine grid results (Table 2). Time-averaged wall normal profiles of the total velocity are shown in Fig. 16. The computed profiles match the experimental profiles well at $x/C_x=0.68$ with the profiles obtained with the LB and $k-\epsilon$ EASM models being slightly less full. At $x/C_x=0.77$, the LB and $k-\epsilon$ EASM results (unsteady RANS) still match the experimental data very well. With the same models, the thickness of the separation bubble is, however, under-predicted at $x/C_x=0.92$. With the $k-\omega$, $k-\omega$ EASM, SST, and SA models attached flow profiles are predicted for $x/C_x=0.77$ and $x/C_x=0.92$. The shape factor at $x/C_x=0.68$ for the various cases is given in Table 5. When compared with the other models, the shape factor is the largest for both the LB and the $k-\epsilon$ EASM model, indicating that the flow is closer to separation. Additional insight can be obtained from time-averaged wall-normal profiles of the turbulence intensity (see Fig. 17). For the LB and $k-\epsilon$ EASM models the boundary layers at $x/C_x=0.68$ and $x/C_x=0.77$ are fully laminar. The laminar boundary layer separates and “transition” takes place within the separation bubble (Fig. 13).

Overall, it appears that none of the models can accurately capture all aspects of the flow. The applicability of such models is questionable as they were not calibrated to predict transition for flows as complicated (curvature, pressure gradient, and separation) as the LPT flow. Important aspects of the transition process, such as the primary and secondary stages of transition, are not reproduced, of course. For the low Reynolds number conditions

Table 5 Shape factor, H , at $x/C_x=0.68$

| Model | H |
|-------------------|------|
| LB | 1.40 |
| $k-\epsilon$ EASM | 1.38 |
| $k-\omega$ | 1.25 |
| $k-\omega$ EASM | 1.28 |
| SST | 1.25 |
| SA | 1.27 |

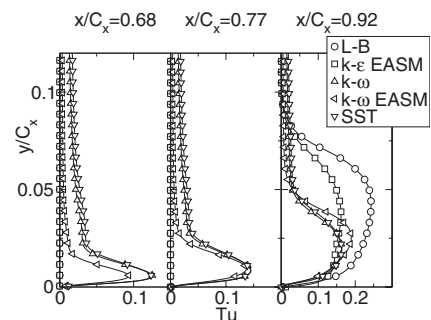


Fig. 17 Wall-normal profiles of turbulence intensity, Tu

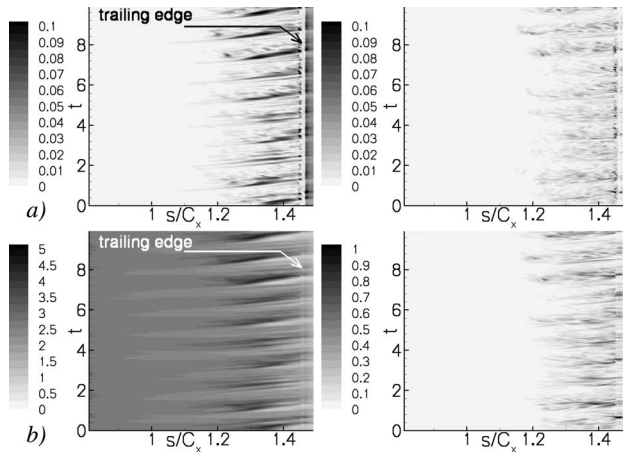


Fig. 18 Fourier mode amplitude, $A^{(k)}(s, t)$, of (a) skin friction coefficient, c_F , and (b) wall pressure coefficient, c_p , for modes $k=0$ (left) and $k=1$ (right) obtained from fine grid DNS data

considered here, the flow is transitional and may, depending on the boundary conditions (FST, etc.) not become fully turbulent. More advanced turbulence models that capture the transitional nature of the flow [31–34,51,55] or DNS and hybrid turbulence modeling approaches have to be considered if more reliable and accurate results are sought.

5 Analysis of Flow Dynamics

For analyzing the time-dependent behavior of the flow data, the wall skin friction coefficient, $c_F(s, z, t)$, and the wall pressure coefficient, $c_p(s, z, t)$, can be Fourier decomposed in the spanwise direction, z , as follows:

$$c_{F,p}(s, z, t) = \sum_k c_c^{(k)}(s, t) \cos \frac{2\pi kz}{\Delta Z} + c_s^{(k)}(s, t) \sin \frac{2\pi kz}{\Delta Z} \quad (10)$$

where the respective spanwise wavelengths are $\lambda_z^{(k)} = \Delta Z/k$. Results were computed from data taken over a time period of $\Delta T = 10$ at a sampling rate of $1/\Delta t = 1/0.004 = 250$. All simulations were first advanced over a sufficiently long period of time to ensure that initial flow transients were excluded before the time-dependent data were recorded. In Fig. 18(a), t versus s diagrams of the Fourier mode amplitudes,

$$A^{(k)}(s, t) = \sqrt{c_c^{(k)}(s, t)^2 + c_s^{(k)}(s, t)^2} \quad (11)$$

of the skin friction coefficient for the fine grid DNS are shown for modes $k=0$ (the spanwise average) and $k=1$ (the first spanwise mode). The corresponding figures for the ILES and FSM look very similar and are omitted to save space. The arclength along the blade, s , was measured from the leading edge. Mode $k=0$ amplitudes illustrate the “footprints” or wall traces of the spanwise coherent structures. The time-derivative of the traces is equivalent to the wave speed of the spanwise coherent structures and approximately the same for all cases. The vortex shedding frequency, which can be determined by measuring the time-difference between the wall traces in Fig. 18(a), is about 1 and almost identical for all cases.

According to Ho and Huerre [57], the nondimensional frequency of the most unstable KH mode is approximately

$$St = \frac{f\vartheta}{v_e} = 0.016 \quad (12)$$

where ϑ is the shear layer momentum thickness $\int (v-v_1)/(v_2-v_1)[1-(v-v_1)/(v_2-v_1)]dy$ and v_e is the local boundary layer edge velocity. Velocity profiles were taken from the fine grid DNS data in the separated flow region at $x/C_x = 0.80, 0.83, \text{ and } 0.86$

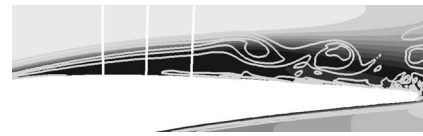


Fig. 19 Flow visualization near the trailing edge (fine grid DNS). Isocontours of the total velocity of time-averaged data ($v_{tot}=0, \dots, 2, \Delta v_{tot}=0.2$) superimposed with isocontours of spanwise vorticity of instantaneous data (gray lines, $\omega_z = -100, \dots, 100, \Delta \omega_z = 40$). Indicated in white are lines along which velocity profiles were obtained.

upstream of the location where the spanwise vortices appear (Fig. 19). The shear layer momentum thickness, which was computed by integration from the near wall velocity minimum to the velocity maximum, was $0.0038, 0.0042, \text{ and } 0.0048C_x$ at the three downstream stations. The edge velocity was $1.88v_{in}$ at all three stations. With these numbers the frequency of the most unstable KH mode normalized by inlet velocity and axial chord length, $0.016v_e/v_{in}C_x/\vartheta$, becomes $7.9, 7.2, \text{ and } 6.3$, respectively. These numbers are larger than the nondimensional frequency of 1 observed in the simulations. This discrepancy is presently not understood and subject of future investigations.

Vortex merging (subharmonic) resonance of the spanwise structures, where the wall traces of two spanwise coherent structures merge into one, cannot be observed. When considering the mode $k=1$ amplitudes (right hand side of Fig. 18) it becomes clear that the appearance of the $k=1$ mode (or first 3D mode) is linked to the presence of the 2D mode ($k=0$). It can be speculated that the growth of the 3D mode is caused by a secondary instability of the time-dependent 2D flow. Although not proven here, the observed time-periodic vortex shedding may be the result of an absolute instability of the separation bubble. This conjecture is based on two observations: In time-dependent flow visualizations of the simulation data, disturbances can be seen to travel upstream in the reverse flow region of the separation bubble. Also, acoustic noise associated with the vortical structures was found to propagate upstream and disturb the approach boundary layer. A definitive answer to the question if an absolute instability was present can potentially be obtained from a BiGlobal stability analysis [58]. For a global bubble instability, the nondimensional frequency based on bubble length, L , and local freestream velocity is about 1,

$$f \frac{L}{v_e} \approx 1 \quad (13)$$

With a bubble length of about $0.5C_x$ and an edge velocity of $1.88v_{in}$ a frequency of $v_e/v_{in}C_x/0.5C_x = 3.8$ is obtained.

When the wall pressure coefficient, c_p , is Fourier decomposed in the spanwise direction, the graphs in Fig. 18(b) are obtained. As the pressure in the vortex cores of the spanwise structures is below the local freestream pressure, the minima of the wall pressure (light shaded areas in Fig. 18(b)) can be associated with the wall traces of the spanwise (or 2D) vortices. In addition, Fig. 18(b) clearly illustrates that the spanwise structures have an upstream influence. The light shaded areas extend upstream up to approximately $s/C_x = 0.9$. This upstream influence is not caused by upstream traveling acoustic waves which have a negative wave speed of $\partial s/\partial t = v - c \approx 1 - 1/M = -9$ (where c is the speed of sound) but may instead be attributed to a time-periodic oscillation of the circulation around the entire turbine blade. Figure 20 demonstrates that the separation and reattachment locations of the separation bubbles on the pressure and suction sides are unsteady and oscillating with the same frequency as the spanwise structures on the suction side. The separation and reattachment locations were taken as the locations of instantaneous zero skin friction of

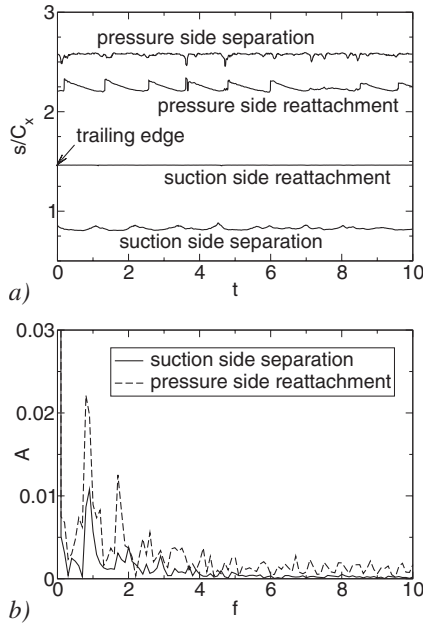


Fig. 20 Separation and reattachment locations obtained from the fine grid FSM in (a) time and (b) frequency domains

the spanwise mean of the flow. Similar results were obtained for the DNS and ILES. Clearly, the spanwise structures on the suction side influence the flow around the entire blade.

In the following only the time-dependent data of the wall pressure coefficient is analyzed because it was found to better reflect the dynamics of the coherent structures. The skin friction coefficient appeared to be more biased toward the structures in direct vicinity of the wall. The wall pressure coefficient, $c_p(s, z, t)$, can additionally be Fourier decomposed in time, t , as follows:

$$c_p(s, z, t) = \sum_n \sum_k \left(c_{cc}^{(n,k)}(s) \cos \frac{2\pi n t}{\Delta T} + c_{cs}^{(n,k)}(s) \sin \frac{2\pi n t}{\Delta T} \right) \cos \frac{2\pi k z}{\Delta Z} + \left(c_{sc}^{(n,k)}(s) \cos \frac{2\pi n t}{\Delta T} + c_{ss}^{(n,k)}(s) \sin \frac{2\pi n t}{\Delta T} \right) \sin \frac{2\pi k z}{\Delta Z} \quad (14)$$

where the respective spanwise wavelengths and frequencies are $\lambda_z^{(k)} = \Delta Z/k$ and $f^{(n)} = n/\Delta T$. Since the original data were not exactly periodic in time the frequency spectra may exhibit high frequency ringing (Gibbs phenomenon). For the current results, data-windowing techniques were not employed. In Fig. 21, $f^{(n)}$ versus s diagrams of the Fourier mode amplitudes,

$$A^{(k)}(s, f^{(n)}) = \sqrt{c_{cc}^{(n,k)}(s)^2 + c_{cs}^{(n,k)}(s)^2 + c_{sc}^{(n,k)}(s)^2 + c_{ss}^{(n,k)}(s)^2} \quad (15)$$

for modes $k=0$ and $k=1$ are shown for the fine grid DNS. Mode $k=0$ attains its global maximum for $f \approx 1$. This dominant or fundamental frequency can be identified as the natural shedding fre-

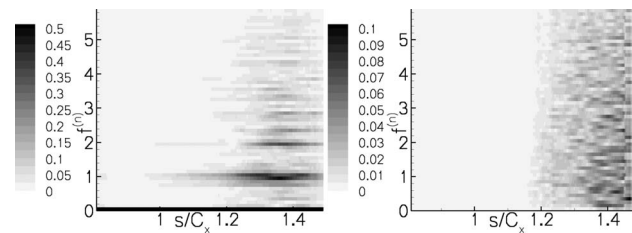


Fig. 21 Fourier mode amplitude, $A^{(k)}(s, f^{(n)})$, of wall pressure coefficient, c_p , for modes $k=0$ (left) and $k=1$ (right) obtained from fine grid DNS data

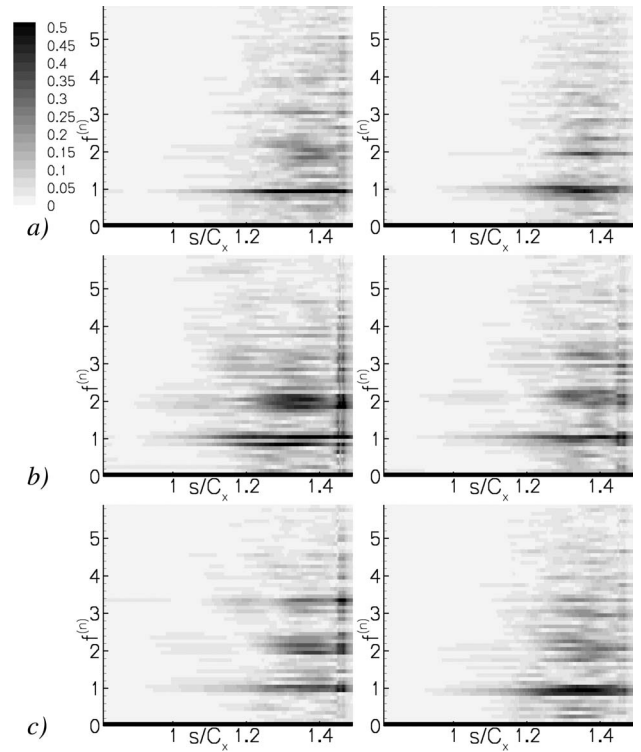


Fig. 22 Fourier mode amplitudes, $A(s, z=0, f^{(n)})$, of wall pressure coefficient, c_p , for coarse grid (left) and fine grid (right). Results for (a) DNS, (b) ILES, and (c) FSM.

quency of the separation bubble. Higher harmonics with $f \approx 2$ and $f \approx 3$ appear downstream of $s/C_x \approx 1.2$. Since the vortex shedding is not exactly time-periodic and as the time intervals used for the Fourier transforms were relatively short, the peaks in the frequency spectra are not very pronounced. In fact, the high frequency end of the spectra for the $k=0$ mode begins to fill up as the trailing edge is approached indicating that the flow is transitioning. The most pronounced energy drop off toward the higher frequencies, $f^{(n)}$, and spanwise mode numbers, k , was obtained with the FSM. Here, the model contribution is dependent on the local and time-dependent ratio of grid resolution to smallest turbulence length scale. Structures with higher spanwise mode number, k , or larger frequency, $f^{(n)}$, experience a larger model contribution and therefore stronger damping, which explains the energy drop-off in the spectra. The frequency spectrum of the higher spanwise mode, $k=1$, show no distinctive amplitude maxima but an overall growth in amplitude downstream of $s/C_x \approx 1.2$.

Finally, frequency spectra at $z=0$ (arbitrarily chosen z -location) were computed as

$$c_p(s, z=0, t) = \sum_n \left(\sum_k c_{cc}^{(n,k)}(s) \cos \frac{2\pi n t}{\Delta T} + \left(\sum_k c_{cs}^{(n,k)}(s) \right) \sin \frac{2\pi n t}{\Delta T} \right) = \sum_n c_{cc}^{(n)}(s, z=0) \cos \frac{2\pi n t}{\Delta T} + c_{cs}^{(n)}(s, z=0) \sin \frac{2\pi n t}{\Delta T} \quad (16)$$

In Figs. 22 and 23 $f^{(n)}$ over s graphs of

$$A(s, z=0, f^{(n)}) = \sqrt{c_{cc}^{(n)}(s, z=0)^2 + c_{cs}^{(n)}(s, z=0)^2} \quad (17)$$

are shown for the 3D simulations and for the 2D LB and $k-\varepsilon$ EASM URANS results. Due to the comparatively small contribu-

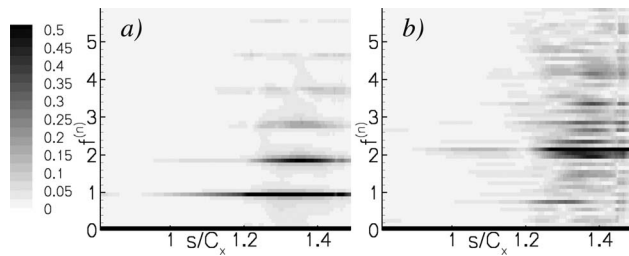


Fig. 23 Fourier mode amplitudes, $A(s, z=0, f^n)$, of wall pressure coefficient, c_p . URANS results obtained with (a) LB and (b) $k-\epsilon$ EASM model.

tion of the higher spanwise modes the spectra obtained from the 3D simulations in Fig. 22 resemble those in Fig. 23 from the URANS calculations. Disturbances with a frequency of $f \approx 1$ (with higher harmonics at $f \approx 2$ and $f \approx 3$) are most amplified. The frequency spectra obtained with the coarse and fine grids are roughly identical, indicating that the dynamics of the flow are similar. Figure 23 illustrates that with the LB model (and probably also as a result of the 2D nature of the URANS calculations) the flow is very time-periodic and very pronounced peaks in the frequency spectra can be detected at $f \approx 1$. A completely different result is obtained with the $k-\epsilon$ EASM model. Although wall pressure distribution and velocity profiles resemble the LB results, a dominant frequency of $f \approx 2$ is predicted, which is not in agreement with the other data. This difference may be explained by the larger amount of eddy viscosity computed with the LB model (Fig. 13), which results in a lower “effective Reynolds” number, which in turn lowers the frequency of the most unstable bubble instability mode. In other words, the $k-\epsilon$ EASM turbulence model contribution is too low for predicting the right shedding frequency.

Finally, frequency spectra taken at three different downstream locations (fine grid results) are compared in Fig. 24. When analyzing the spectra one has to keep in mind that the sampling rate of the time-dependent data was 250. The fundamental ($f \approx 1$) grows in amplitude by a factor of roughly 10 between $s/C_x=1.0$ and 1.4. At $s/C_x=1.4$ higher harmonics appear in the spectra and the frequency range of the energy containing eddies becomes wider. For the DNS, the amplitude of the disturbances does not diminish toward the higher frequency end of the spectra. The reason for this behavior may be numerical instabilities (“grid mesh oscillations”) due to insufficient grid resolution (the grid is not fine enough to resolve the dissipative length scales) or pertinent acoustic noise in the computational domain. For the ILES and FSM, high frequency disturbances are damped by the inherent diffusion of the discretization and the model contribution, respectively. With the LB model and for the ILES and FSM, an exponential decay in the fluctuation amplitudes akin to the Kolmogorov $-5/3$ law that characterizes the inertial turbulent subrange can be observed near the high frequency end of the spectrum.

Several correlations for the Reynolds number based on the downstream distance from the laminar separation point to the point of transition onset, Re_{st} , were proposed. The correlation by Davis et al. [59],

$$Re_{st} = 25,000 \log_{10}(\coth(17.32Tu)) \quad (18)$$

was shown to be in good agreement with the experimental data by Sohn et al. [13,14] and Volino and Hultgren [15]. For $Tu=0.1\%$ this Reynolds number obtains a value of 44,000, indicating that for the Pack B geometry at $Re=25,000$ the flow is beginning to transition downstream of the trailing edge. A more recent correlation by Suzen et al. [33] also takes the momentum thickness Reynolds number at the separation point, Re_{θ_s} , into account,

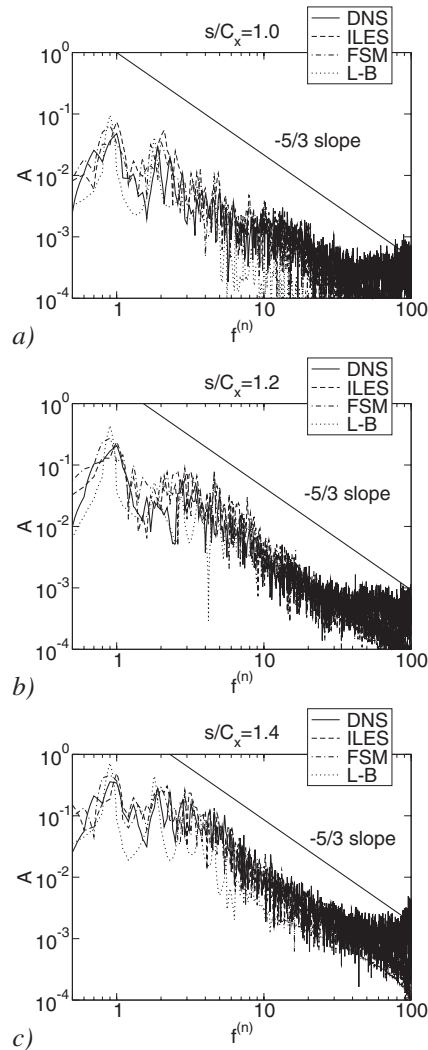


Fig. 24 Frequency spectra, $A(s, z=0, f^n)$, of wall pressure coefficient, c_p , at (a) $s/C_x=1$ ($x/C_x=0.80$), (b) $s/C_x=1.2$ ($x/C_x=0.89$), and (c) $s/C_x=1.4$ ($x/C_x=0.98$)

$$Re_{st} = 874 Re_{\theta_s}^{0.71} \exp(-0.4Tu) \quad (19)$$

For the fine grid DNS, the boundary layer momentum thickness and edge velocity near the separation location ($x/C_x=0.695$) are $0.0024C_x$ and $1.9v_{in}$ resulting in $Re_{\theta_s}=0.0024 \times 1.9 \times Re=114$. From this $Re_{st}=25,200$ is obtained, again indicating that the flow is beginning to transition downstream of the trailing edge. Although the present data (e.g., Figs. 2, 18, and 21) provide some evidence that the flow is transitioning near the trailing edge the exact transition onset location is not available. Many other similar correlations exist [15,29]. As shown by, e.g., Volino for the Pack B blade, the level of agreement between measurements and the predictions made by such models can vary strongly with Reynolds number [49].

6 Conclusions

Laminar separation in low-pressure turbine (LPT) stages can lead to significant performance losses. Numerical simulations are challenged by the complicated nature of the flow. Both separation and transition are unsteady and interacting with each other. The separated flow is dominated by energetic coherent structures. Simulations that reliably capture these phenomena could aid in the design of new blade geometries and in the development of active flow control devices. In this paper, coarse and fine grid results

obtained with three different simulation strategies, DNS, ILES, and FSM, are compared. The fine grid results were almost identical with each other and formed the basis for an analysis of the flow dynamics. The coarse grid results helped assess the properties of the various simulation techniques. With the FSM, the predicted dynamical behavior of the flow was approximately the same for the coarse and the fine grid. For the coarse grid ILES, stronger numerical diffusion was shown to noticeably alter the flow dynamics.

Attempts were made to compute the flow using 2D steady and unsteady RANS. The advantage of this approach is a lower computational expense when compared to the 3D simulations. With steady RANS, the correct extent of the laminar separation bubble near the trailing edge of the blade could not be obtained. With URANS, both the laminar separation and the bubble vortex shedding were captured. This was attributed to the dominance of the 2D mode (spanwise vortices) in the flow (analysis of 3D flow data) which can be captured qualitatively in 2D URANS calculations. However, as the models are not tailored for separating transitional flows, this success is likely a coincidence and should not lead to the conclusion that such models work reliably for LPT flows.

Analysis of the time-dependent data obtained from the simulations showed the flow to be dominated by energetic spanwise coherent structures and to be transitioning near the trailing edge. Although the 3D structures were amplified in downstream direction their amplitudes were still relatively small when compared with the amplitudes of the 2D structures. Forcing of the 3D modes (such as by pulsed vortex generator jets) with the right frequency and amplitude will increase the initial amplitude of the 3D modes resulting in an accelerated breakdown to turbulence. An earlier transitioning of the flow would result in an increased wall normal mixing and entrainment of freestream fluid and thus delay or prevent separation as has been shown in the experiments [2–4]. However, the present results indicate that the 2D mode experiences a stronger amplification than the 3D modes. Therefore, it may also be concluded that excitation of the 2D mode by in-phase pulsed actuation may strengthen the spanwise coherent structures, which also entrain freestream fluid and counteract separation.

Acknowledgment

This work was supported by the Air Force Office of Scientific Research (AFOSR) under Grant No. F9550-05-1-0166 with Rhett Jefferies serving as a program manager. The 3D simulations became possible through pilot user time provided at the NRL.

Nomenclature

| | |
|------------|---|
| A | = amplitude |
| c_F | = skin friction coefficient |
| c_p | = wall pressure coefficient |
| C_x | = axial chord length |
| f | = contribution function, frequency |
| H | = shape factor |
| k | = turbulent kinetic energy, spanwise mode |
| l_T | = integral turbulence length scale |
| L_k | = Kolmogorov length scale |
| n | = temporal mode |
| Q | = vortex identification criterion |
| s | = arclength along blade |
| t | = time |
| ΔT | = time interval for data analysis |
| Tu | = turbulence intensity |
| u, v | = velocity components |
| x | = axial coordinate |
| y | = wall normal coordinate |
| z | = spanwise coordinate |
| Δ | = grid line spacing |
| ΔZ | = spanwise extent of computational domain |

| | |
|---------------|---|
| ε | = dissipation rate of k |
| δ | = momentum thickness |
| λ | = wavelength |
| μ | = molecular viscosity |
| μ_T | = eddy viscosity |
| ρ | = density |
| ω | = turbulent specific dissipation, vorticity |

References

- [1] Morkovin, M., 1969, "The Many Faces of Transition," *Viscous Drag Reduction*, C. S. Wells, ed., Plenum, New York.
- [2] Bons, J., Sondergaard, R., and Rivir, R., 2001, "Turbine Separation Control Using Pulsed Vortex Generator Jets," *ASME J. Turbomach.*, **123**(2), pp. 198–206.
- [3] Bons, J., Sondergaard, R., and Rivir, R., 2002, "The Fluid Dynamics of LPT Blade Separation Control Using Pulsed Jets," *ASME J. Turbomach.*, **124**(1), pp. 77–85.
- [4] Sondergaard, R., Bons, J., and Rivir, R., 2002, "Control of Low-Pressure Turbine Separation Using Vortex Generator Jets," *J. Propul. Power*, **18**(4), pp. 889–895.
- [5] Hansen, L., and Bons, J., 2006, "Flow Measurements of Vortex Generator Jets in Separating Boundary Layer," *J. Propul. Power*, **22**(3), pp. 558–566.
- [6] Huang, J., Corke, T., and Thomas, F., 2003, "Plasma Actuators for Separation Control of Low Pressure Turbine Blades," AIAA Paper No. 2003-1027.
- [7] Huang, J., Corke, T., and Thomas, F., 2006, "Plasma Actuators for Separation Control of Low-Pressure Turbine Blades," AIAA J., **44**(1), pp. 51–57.
- [8] Huang, J., Corke, T., and Thomas, F., 2006, "Unsteady Plasma Actuators for Separation Control of Low-Pressure Turbine Blades," AIAA J., **44**(7), pp. 1477–1487.
- [9] Corke, C., and Post, M., 2005, "Overview of Plasma Flow Control: Concepts, Optimization, and Applications," AIAA Paper No. 2005-0563.
- [10] Roberts, S., and Yaras, M., 2005, "Boundary-Layer Transition Affected by Surface Roughness and Free-Stream Turbulence," *ASME J. Fluids Eng.*, **127**(5), pp. 449–457.
- [11] Roberts, S., and Yaras, M., 2006, "Effects of Surface-Roughness Geometry on Separation-Bubble Transition," *ASME J. Turbomach.*, **128**(2), pp. 349–356.
- [12] Lake, J., King, P., and Rivir, R., 1999, "Reduction of Separation Losses on a Turbine Blade With Low Reynolds Number," AIAA Paper No. 99-0242.
- [13] Sohn, K.-H., Shyne, R., and DeWitt, K., 1998, "Experimental Investigation of Boundary Layer Behavior in a Simulated Low Pressure Turbine," NASA, Technical Memorandum No. 207921.
- [14] Sohn, K.-H., and DeWitt, K., 2007, "Experimental Study of Transitional Flow Behavior in a Simulated Low Pressure Turbine," NASA, Technical Memorandum No. 214670.
- [15] Volino, R., and Hultgren, L., 2001, "Measurements in Separated and Transitional Boundary Layers Under Low-Pressure Turbine Airfoil Conditions," *ASME J. Turbomach.*, **123**(2), pp. 189–197.
- [16] Margolin, L., and Rider, W., 2002, "A Rationale for Implicit Turbulence Modeling," *Int. J. Numer. Methods Fluids*, **39**(9), pp. 821–841.
- [17] Wu, X., and Durbin, P., 2001, "Evidence of Longitudinal Vortices Evolved From Distorted Wakes in a Turbine Passage," *J. Fluid Mech.*, **446**, pp. 199–228.
- [18] Kalitzin, G., Wu, X., and Durbin, P., 2003, "DNS of Fully Turbulent Flow in a LTP Passage," *Int. J. Heat Fluid Flow*, **24**(4), pp. 636–644.
- [19] Wissink, J., and Rodi, W., 2006, "Direct Numerical Simulations of Transitional Flow in Turbomachinery," *ASME J. Turbomach.*, **128**(4), pp. 668–678.
- [20] Wu, X., Jacobs, R., Hunt, J., and Durbin, P., 1999, "Simulation of Boundary Layer Transition Induced by Periodically Passing Wakes," *J. Fluid Mech.*, **398**, pp. 109–153.
- [21] Postl, D., Gross, A., and Fasel, H., 2003, "Numerical Investigation of Low-Pressure Turbine Blade Separation Control," AIAA Paper No. 2003-0614.
- [22] Postl, D., Gross, A., and Fasel, H., 2004, "Numerical Investigation of Active Flow Control for Low-Pressure Turbine Blade Separation," AIAA Paper No. 2004-0750.
- [23] Raverdy, B., Mary, I., and Sagaut, P., 2003, "High-Resolution Large-Eddy Simulation of Flow Around Low-Pressure Turbine Blade," AIAA J., **41**(3), pp. 390–397.
- [24] Michelassi, V., Wissink, J., Fröhlich, J., and Rodi, W., 2003, "Large-Eddy Simulation of Flow Around Low-Pressure Turbine Blade With Incoming Wakes," AIAA J., **41**(11), pp. 2143–2156.
- [25] Rizzetta, D., and Visbal, M., 2003, "Numerical Investigations of Transitional Flow Through a Low-Pressure Turbine Cascade," AIAA Paper No. 2003-3587.
- [26] Rizzetta, D., and Visbal, M., 2005, "Numerical Simulation of Separation Control for Transitional Highly Loaded Low-Pressure Turbines," AIAA J., **43**(9), pp. 1958–1967.
- [27] Chernobrovkin, A., and Lakshminarayana, B., 1999, "Turbulence Modeling and Computation of Viscous Transitional Flows for Low Pressure Turbines," *ASME J. Fluids Eng.*, **121**(4), pp. 824–833.
- [28] Garg, V., 2002, "Low-Pressure Turbine Separation Control—Comparison With Experimental Data," *Proceedings of ASME Turbo Expo 2002*, Amsterdam, The Netherlands, June 3–6, pp. 621–627.
- [29] Dorney, D., 1996, "Reynolds-Averaged Navier-Stokes Studies of Low Rey-

- nolds Number Effects on the Losses in a Low Pressure Turbine," NASA, Contractor Report No. 198534.
- [30] Lardeau, S., and Leschziner, M., 2004, "Unsteady Reynolds-Averaged Navier-Stokes Computations of Transitional Wake/Blade Interaction," *AIAA J.*, **42**(8), pp. 1559–1571.
- [31] Suzen, Y., and Huang, P., 2000, "Modeling of Flow Transition Using an Intermittency Transport Equation," *ASME J. Fluids Eng.*, **122**(2), pp. 273–284.
- [32] Suzen, Y., and Huang, P., 2005, "Numerical Simulation of Unsteady Wake/Blade Interactions in Low-Pressure Turbine Flows Using an Intermittency Transport Equation," *ASME J. Turbomach.*, **127**(3), pp. 431–444.
- [33] Suzen, Y., Huang, P., Ashpis, D., Volino, R., Corke, T., Thomas, F., Huang, J., Lake, J., and King, P., 2007, "A Computational Fluid Dynamics Study of Transitional Flows in Low-Pressure Turbines Under a Wide Range of Operating Conditions," *ASME J. Turbomach.*, **129**(2), pp. 527–541.
- [34] Menter, F., Langtry, R., Likki, S., Suzen, Y., and Huang, P., 2006, "A Correlation-Based Transition Model Using Local Variables—Part I: Model Formulation," *ASME J. Turbomach.*, **128**(3), pp. 413–422.
- [35] Fasel, H., Seidel, J., and Wernz, S., 2002, "A Methodology for Simulations of Complex Turbulent Flows," *ASME J. Fluids Eng.*, **124**(4), pp. 933–942.
- [36] Spalart, P., Jou, W.-H., Strelets, M., and Allmaras, S., 1997, "Comments on the Feasibility of LES for Wings, and on a Hybrid RANS/LES Approach," *Proceedings of the First AFOSR International Conference on DNS/LES*, Ruston, LA, Aug. 4–8, Advances in DNS/LES, C. Liu and Z. Liu, eds., Greyden Press, Columbus, OH.
- [37] Speziale, C., 1998, "Turbulence Modeling for Time-Dependent RANS and VLES: A Review," *AIAA J.*, **36**(2), pp. 173–184.
- [38] Wilcox, D., 2006, *Turbulence Modeling for CFD*, 3rd ed., DCW Industries, La Cañada, CA.
- [39] Rumsey, C., and Gatski, T., 2001, "Recent Turbulence Model Advances Applied to Multielement Airfoil Computations," *J. Aircr.*, **38**(5), pp. 904–910.
- [40] Launder, B., and Sharma, B., 1974, "Application of the Energy Dissipation Model of Turbulence to the Calculation of Flow Near a Spinning Disc," *Let. Heat Mass Transfer*, **1**(2), pp. 131–138.
- [41] Lam, C., and Bremhorst, K., 1981, "Modified Form of k - ϵ Model for Predicting Wall Turbulence," *ASME J. Fluids Eng.*, **103**(3), pp. 456–460.
- [42] Menter, F., 1994, "Two-Equation Eddy-Viscosity Turbulence Models for Engineering Applications," *AIAA J.*, **32**(8), pp. 1589–1605.
- [43] Spalart, P., and Allmaras, S., 1992, "A One-Equation Turbulence Model for Aerodynamic Flows," *AIAA Paper No. 92-0439*.
- [44] Gross, A., and Fasel, H., 2007, "Characteristic Ghost-Cell Boundary Condition," *AIAA J.*, **45**(1), pp. 302–306.
- [45] Gross, A., and Fasel, H., 2002, "High-Order WENO Schemes Based on the Roe Approximate Riemann Solver," *AIAA Paper No. 2002-2735*.
- [46] Gross, A., and Fasel, H., 2008, "High-Order-Accurate Numerical Method for Complex Flows," *AIAA J.*, **46**(1), pp. 204–214.
- [47] Yee, H., 1987, "Upwind and Symmetric Shock-Capturing Schemes," NASA, Technical Memorandum No. 89464.
- [48] Menter, F., 1992, "Influence of Freestream Values on k - ω Turbulence Model Predictions," *AIAA J.*, **30**(6), pp. 1657–1659.
- [49] Volino, R., 2002, "Separated Flow Transition Under Simulated Low-Pressure Turbine Conditions—Part I: Mean Flow and Turbulence Statistics," *ASME J. Turbomach.*, **124**(4), pp. 645–655.
- [50] Simon, T., Qiu, S., and Yuan, K., 2000, "Measurements in a Transitional Boundary Layer Under Low-Pressure Turbine Airfoil Conditions," NASA, Contractor Report No. 209957.
- [51] Langtry, R., Menter, F., Likki, S., Suzen, Y., Huang, P., and Völker, S., 2006, "A Correlation-Based Transition Model Using Local Variables—Part II: Test Cases and Industrial Applications," *ASME J. Turbomach.*, **128**(3), pp. 423–434.
- [52] Hunt, J., Wray, A., and Moin, P., 1988, "Eddies, Stream, and Convergence Zones in Turbulent flows," Report No. CTR-S88.
- [53] Gross, A., and Fasel, H., 2005, "Numerical Investigation of Low-Pressure Turbine Blade Separation Control," *AIAA J.*, **43**(12), pp. 2514–2525.
- [54] Youngren, H., and Drela, M., 1991, "Viscous/Inviscid Method for Preliminary Design of Transonic Cascades," *AIAA Paper No. 1991-2364*.
- [55] Praisner, T., and Clark, J., 2007, "Predicting Transition in Turbomachinery—Part I: A Review and New Model Development," *ASME J. Turbomach.*, **129**(1), pp. 1–13.
- [56] Durbin, P., 1996, "On the K-3 Stagnation Point Anomaly," *Int. J. Heat Fluid Flow*, **17**(1), pp. 89–90.
- [57] Ho, C.-M., and Huerre, P., 1984, "Perturbed Free Shear Layers," *Annu. Rev. Fluid Mech.*, **16**, pp. 365–424.
- [58] Theolis, V., and Sherwin, S., 2004, "Instability and Control of Low-Pressure Turbine Flows," *Proceedings of the 2003 Minnowbrook IV Workshop on Transition and Unsteady Aspects of Turbomachinery Flows*, Blue Mountain Lake, NY, Aug. 17–20, J. LaGraff and D. Ashpis, eds., pp. 31–32, NASA Report No. TM-2004-212913.
- [59] Davis, R., Carter, J., and Reshotko, E., 1987, "Analysis of Transitional Separation Bubbles on Infinite Swept Wings," *AIAA J.*, **25**(3), pp. 421–428.

Laminar Non-Newtonian Fluid Flow in Noncircular Ducts and Microchannels

Y. S. Muzychka

Associate Professor
Mem. ASME

J. Edge

Graduate Research Assistant

Faculty of Engineering and Applied Science,
Memorial University of Newfoundland,
St. John's, NF, A1B 3X5, Canada

Non-Newtonian fluid flow in noncircular ducts and microchannels is examined. A simple model is proposed for power law fluids based on the Rabinowitsch–Mooney formulation. By means of a new characteristic length scale, the square root of the cross-sectional area, it is shown that dimensionless wall shear stress can be made a weak function of duct shape. The proposed model is based on the solution for the rectangular duct and has an accuracy of $\pm 10\%$ or better. The current model eliminates the need for tabulated data or equations for several common shapes found in handbooks, namely, circular tube, elliptic tube, parallel channel, rectangular duct, isosceles triangular duct, circular annulus, and polygonal ducts. [DOI: 10.1115/1.2979005]

Keywords: non-Newtonian flow, power law fluid, friction factor, noncircular ducts, laminar flow, microchannels

1 Introduction

The present work is concerned with the prediction of pressure drop in noncircular ducts for non-Newtonian power law fluids. Much work has been conducted in this area, and the most frequently cited solutions are found in the texts of Refs. [1,2]. Additional results are also available in a number of handbooks such as Ref. [3]. The flow of non-Newtonian power law fluids occurs frequently in the chemical process industries [2] and is also of interest in microfluidic applications [4,5]. Koo and Kleinstreuer [4] examined several issues related to the flow of liquids in microchannels. They considered simple power law fluids, and show that even with a small change in the power law flow index, the pressure drop can vary considerably. Recently, Azimain and Sefid [5] considered the effect of the power law flow index on heat transfer and pressure drop in microchannel heat sinks. For shear thinning fluids they found a considerable decrease in the pressure drop while realizing a significant increase in heat transfer.

Laminar flow of Newtonian fluids in a variety of cross sections such as circular tubes, parallel plates, and concentric annuli has been researched and documented by a number of sources [6]. Recently, Muzychka and Yovanovich [7] formulated a simple model for fundamental noncircular shapes using the solution for the rectangular duct and a new characteristic length scale, the square root of flow area. The proposed model predicted much of the laminar flow data within $\pm 10\%$ or better. A result not attainable with the hydraulic diameter as a length scale. Bharami et al. [8] further developed approximations for other noncircular ducts and microchannels for laminar flows. They also adopted the length scale advocated by Muzychka and Yovanovich [7]. They also showed that this length scale arises naturally when one non-dimensionalizes ducts and channels of noncircular shape without the a priori assumption of hydraulic diameter as a length scale.

The flow of non-Newtonian fluids in rectangular, elliptical, triangular, polygonal, and annular shaped ducts was also considered by Kozicki et al. [9] and Kozicki and Tiu [10,11]. Tiu and co-workers [9–11] developed an approximate two parameter model using the Rabinowitsch–Mooney formulations for the channel and duct. The advantage of this model was that the two parameters

were easily derived from the analytic solutions for laminar Newtonian flows. The disadvantage of this model is that these parameters vary with the shape and aspect ratio of the duct, and thus must be tabulated for each shape. This tabulation appears frequently in the open literature [2,3], albeit with some errors in the required constants.

The traditional method of relying on the use of tabulated and/or graphical data can be replaced with the use of a more robust model that is more effective, using one equation that is capable of predicting dimensionless mean wall shear stress for a variety of shapes within a small margin of error. This new model is based in part on the laminar Newtonian flow model of Muzychka and Yovanovich [7]. Given the current and potential uses of non-Newtonian fluids and the difficulty in obtaining solutions in more than one dimension, it is beneficial to develop a generalized model for ducts of any shape. This becomes more important in applications involving microchannels, where the fabrication process typically yields channels that are nearly rectangular in shape, having rounded sides or corners. In other cases, the process may yield channels of slightly trapezoidal shape. These issues pose no problem in the present analysis, as the model is most sensitive to changes in aspect ratio and not in shape.

2 Basic Equations

The present formulation utilizes the work of Kozicki et al. [9] who developed a simple generalization of the Rabinowitsch–Mooney equations for the circular duct and plane channel. Beginning first with the definition of an Otswald de Waele (power law) fluid,

$$\tau = K \left(-\frac{\partial u}{\partial \hat{n}} \right)^n \quad (1)$$

where K is the consistency index and n is the power law flow index [1,2]. Equation (1) is valid for one dimensional flow in a tube or annulus and plane channel. For two dimensional flows, such as in rectangular or elliptical ducts, constitutive relationships are much more complex, which make analytical solution difficult. Simple solutions to the momentum equation,

$$\nabla \tau = \frac{dp}{dz} \quad (2)$$

may be obtained for the tube, channel, and annulus [2].

Contributed by the Fluids Engineering Division of ASME for publication in the JOURNAL OF FLUIDS ENGINEERING. Manuscript received January 22, 2008; final manuscript received July 30, 2008; published online September 22, 2008. Assoc. Editor: Dennis Siginer.

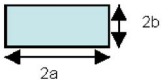
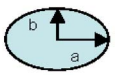
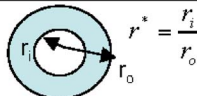
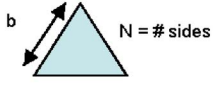
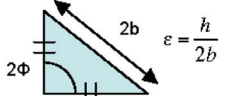
| Geometry | Shape | P/A |
|--------------------|---|---|
| Rectangle |  | $\frac{2(\varepsilon + 1)}{\sqrt{\varepsilon}}$ |
| Ellipse |  | $\frac{4E(\varepsilon')}{\sqrt{\pi\varepsilon}}$ |
| Annulus |  | $\frac{2\sqrt{\pi}(1+r^*)}{\sqrt{(1-r^*)}}$ |
| Polygons |  | $2\sqrt{N}\left(\tanh\left(\frac{\pi}{N}\right)\right)^{1/2}$ |
| Isosceles Triangle |  | $\frac{2/\cos\phi + 2\tan\phi}{\sqrt{\tan\phi}}$ |

Fig. 1 Shapes under consideration

The Rabinowitsch–Mooney equation was developed to calculate the rate of shear at the tube or channel wall [1] for non-Newtonian fluids. Using the Rabinowitsch–Mooney equations for the circular tube and parallel plate channel, Kozicki et al. [9] proposed that the rate of shear at the wall of a noncircular duct could be represented by a more general form

$$\left(-\frac{\partial u}{\partial \hat{n}}\right)_w = f(\bar{\tau}_w) = c_1 \bar{\tau}_w \frac{d\left(\frac{8U}{D_h}\right)}{d\bar{\tau}_w} + c_2 \left(\frac{8U}{D_h}\right) \quad (3)$$

where U is the bulk fluid velocity, $D_h = 4A/P$ is the hydraulic diameter, and c_1 and c_2 are constants, which depend on the duct shape and aspect ratio. The above equation can be re-arranged and integrated to give [2,7]

$$\left(\frac{8U}{D_h}\right) = \frac{1}{c_1} (\bar{\tau}_w)^{-c_2/c_1} \int_0^{\bar{\tau}_w} \tau^{c_2/c_1 - 1} f(\tau) d\tau \quad (4)$$

Now for a power law fluid we have

$$f(\tau) = \left(\frac{\tau}{K}\right)^{1/n} \quad (5)$$

Integration of Eq. (4) with Eq. (5) yields the following result:

$$\bar{\tau}_w = K \left[\frac{8U}{D_h} \left(c_2 + \frac{c_1}{n} \right) \right]^n \quad (6)$$

Finally, one can determine the pressure gradient from a simple force balance on the duct wall to obtain the relationship

$$\bar{\tau}_w = \frac{A}{P} \left(-\frac{\Delta p}{L} \right) \quad (7)$$

The advantage of Eq. (6) was that the constants c_1 and c_2 could be deduced from solutions for Newtonian fluid flows in noncircular ducts.

Frequently in literature a friction factor is defined having the form

$$f = \frac{\bar{\tau}_w}{\frac{1}{2}\rho U^2} \quad (8)$$

In the present work, we will propose a dimensionless mean wall shear stress to be used in conjunction with Eq. (7). The use of the

friction factor introduces the Reynolds number, which, for fully developed viscous flows, is not required or physically meaningful given the traditional interpretation of the Reynolds number. However, as a criterion for determining whether the flow is laminar or turbulent, the generalized Reynolds number, Re_g , will be defined [1,2] as

$$Re_g = \frac{\rho U^{2-n} D_h^n}{8^{n-1} K (c_2 + c_1/n)^n} \quad (9)$$

It is frequently assumed that the Dodge–Metzner criterion [1,2], $Re_g < 2100$, may be employed for predicting whether laminar flow prevails in the noncircular duct. In many texts [1,2], Eq. (8) after combining with Eq. (6) is often written as

$$f = \frac{16}{Re_g} \quad (10)$$

which when $n=1$, with $K=\mu$, gives $f=16/Re_{D_h}$, the solution for Newtonian flow in a tube.

Equations (9) and (10) are a convenient means of representing friction factors for non-Newtonian power law fluids. However, Eq. (9) is still beset with the problem of requiring tabulations for c_1 and c_2 for each geometry. Further, the constants c_1 and c_2 have only been deduced for a limited set of geometries [9]. Although they may be determined using appropriate numerical methods for other shapes, this additional effort is not required unless greater accuracy is desired. A new method will be proposed, which provides a convenient alternative, and may be applied to other geometries for which no solutions exist.

3 Fundamental Solutions

Seven fundamental shapes are given consideration in the published texts and handbooks [1–3]. These are the tube, channel, rectangular duct, annular duct, elliptical duct, polygonal ducts, and isosceles triangle ducts. The special cases of the tube and channel are also predicted from the solution for the circular annulus. The basic shapes under consideration are shown in Fig. 1.

These solutions are presented in tabular form in Refs. [2,3]. The two constants c_1 and c_2 are geometric parameters related to the cross section of the various shaped ducts. As pointed out by Kozicki et al. [9], they may be derived from the solutions for Newtonian flow in noncircular ducts. These two parameters have

Table 1 Summary of constants for polygonal ducts

| N | c_1 | c_2 |
|----------|--------|--------|
| 4 | 0.2121 | 0.6766 |
| 5 | 0.2245 | 0.6966 |
| 6 | 0.2316 | 0.7092 |
| 8 | 0.2391 | 0.7241 |
| ∞ | 0.2500 | 0.7500 |

the following values, which may be determined mathematically for each shape under consideration. For completeness, we review the following solutions.

For a circular tube,

$$c_1 = \frac{1}{4}, \quad c_2 = \frac{3}{4} \quad (11)$$

For a parallel plate channel,

$$c_1 = \frac{1}{2}, \quad c_2 = 1 \quad (12)$$

For a concentric annulus,

$$c_1 + c_2 = \frac{(1 - r^*)^2}{1 + r^{*2} - \frac{1 - r^{*2}}{\ln(1/r^*)}} \quad (13)$$

$$c_1 = \frac{(1 - r^*)^2}{4 \left\{ 1 - \frac{1 - r^{*2}}{2 \ln(1/r^*)} \left[1 - \ln \frac{1 - r^{*2}}{2 \ln(1/r^*)} \right] \right\}} \quad (14)$$

where $r^* = r_i / r_o$.

For an elliptic duct,

$$c_1 + c_2 = \frac{\pi^2}{8\mathbf{E}(\epsilon')^2}(\epsilon^2 + 1) \quad (15)$$

$$c_1 = \frac{\pi^2}{32\mathbf{E}(\epsilon')^2}(\epsilon^2 + 1) \quad (16)$$

where $\epsilon = b/a$ is the ratio of the minor to major axes and $\mathbf{E}(\epsilon')$ is a complete elliptic integral of the second kind of complementary modulus $\epsilon' = 1 - \epsilon^2$.

For a rectangular duct,

$$c_1 + c_2 = \frac{3}{2(1 + \epsilon)^2 \left[1 - \frac{192\epsilon}{\pi^5} \sum_{m=0}^{\infty} \frac{1}{(2m+1)^5} \tanh \frac{(2m+1)\pi}{2\epsilon} \right]} \quad (17)$$

$$c_1 = \frac{1}{2(1 + \epsilon)^2 \left[1 + 4 \sum_{m=0}^{\infty} \frac{(-1)^{m+1}}{\left(\frac{2m+1}{2}\pi\right)^3} \frac{1}{\cosh \frac{(2m+1)\pi}{2\epsilon}} \right]} \quad (18)$$

where $\epsilon = b/a$ is the ratio of the minor to major axes.

For regular polygons, their values are tabulated in Table 1.

For isosceles triangle ducts, their values are tabulated in Table 2. They are based on the work of Sparrow and co-workers [12,13].

4 Nondimensionalization and Modeling

In the present analysis, a simple model is proposed using two basic ideas, namely, the introduction of a *more appropriate characteristic length scale* and the definition of a *suitable duct aspect ratio* to provide a measure of slenderness.

Table 2 Summary of constants for isosceles triangle ducts

| 2ϕ (deg) | c_1 | c_2 |
|---------------|--------|--------|
| 10 | 0.1547 | 0.6278 |
| 20 | 0.1693 | 0.6332 |
| 40 | 0.1840 | 0.6422 |
| 60 | 0.1875 | 0.6462 |
| 80 | 0.1849 | 0.6438 |
| 90 | 0.1830 | 0.6395 |

4.1 Nondimensionalization. We begin first with the nondimensionalization of the theoretical results, by proposing a dimensionless mean wall shear stress, τ^* , defined as

$$\tau^* = \frac{\bar{\tau}_w \mathcal{L}^n}{KU^n} = \frac{A \left(-\frac{\Delta p}{L} \right) \mathcal{L}^n}{KU^n} \quad (19)$$

where \mathcal{L} is an arbitrary length scale related to the duct cross section. For Newtonian fluids, $n=1$ and τ^* reduces to the more familiar Poiseuille number $Po = \bar{\tau}_w \mathcal{L} / \mu U$ [14].

Using Eqs. (6) and (19) and the length scale $\mathcal{L} = D_h$, we obtain

$$\tau_{D_h}^* = 8^n \left(c_2 + \frac{c_1}{n} \right)^n \quad (20)$$

Equation (20) is a convenient form from which we perform our analysis. However, one drawback is the use of the hydraulic diameter as a length scale. With this choice of length scale there is no conformity in the results for different duct shapes. Further, Eq. (20) still requires the unique values of c_1 and c_2 for each particular case.

One issue addressed by Muzychka and Yovanovich [7] is the selection of an appropriate length scale for defining the dimensionless mean wall shear. It was found that the use of the hydraulic diameter in laminar flow situations yields greater scatter in results as compared with the use of $\mathcal{L} = \sqrt{A}$ as a characteristic length scale. When the latter length scale is used, the effect of duct shape becomes minimized, and much of the laminar Newtonian flow data can be predicted using a single expression based on the solution for the rectangular duct.

Redefining Eq. (20) using the length scale $\mathcal{L} = \sqrt{A}$ yields

$$\tau_{\sqrt{A}}^* = 2^n \left(c_2 + \frac{c_1}{n} \right)^n \left(\frac{P}{\sqrt{A}} \right)^n \quad (21)$$

The grouping P/\sqrt{A} has been shown by Muzychka and Yovanovich [7], Bharami et al. [8], and Bejan [15] to be an important geometric scaling factor.

In order to compare the various shapes the aspect ratio for each geometry needs to be defined. Referring to Table 3, the nominal aspect ratios for the shapes of interest are given [7].

The aspect ratio for the circular annulus was derived by Muzychka and Yovanovich [7]. This relationship may be obtained from two physical arguments. The first method is to solve for the ratio of the gap of the annulus, $r_o - r_i$, to the mean perimeter, while the second method is the ratio of the gap to the equivalent length if the duct area, $\pi(r_o^2 - r_i^2)$, is converted to the shape of a rectangle.

Table 3 Duct aspect ratio

| Geometry | Aspect ratio |
|--------------------|---------------------------------------|
| Regular polygon | $\epsilon = 1$ |
| Singly connected | $\epsilon = b/a$ |
| Circular annulus | $\epsilon = (1 - r^*) / \pi(1 + r^*)$ |
| Isosceles triangle | $\epsilon = 2b/h$ |

Table 4 Summary of coefficients in Eqs. (17) and (18)

| ϵ | $m=1$ | | $m=10$ | |
|------------|---------|---------|---------|---------|
| | c_1 | c_2 | c_1 | c_2 |
| 0.05 | 0.45351 | 0.95109 | 0.45351 | 0.95129 |
| 0.1 | 0.41322 | 0.90943 | 0.41322 | 0.90983 |
| 0.2 | 0.34750 | 0.84363 | 0.34750 | 0.84440 |
| 0.3 | 0.29914 | 0.79421 | 0.29914 | 0.79536 |
| 0.4 | 0.26591 | 0.75554 | 0.26591 | 0.75709 |
| 0.5 | 0.24394 | 0.72580 | 0.24393 | 0.72781 |
| 0.6 | 0.22971 | 0.70398 | 0.22971 | 0.70653 |
| 0.7 | 0.22079 | 0.68885 | 0.22077 | 0.69206 |
| 0.8 | 0.21557 | 0.67909 | 0.21550 | 0.68310 |
| 0.9 | 0.21298 | 0.67346 | 0.21285 | 0.67845 |
| 1 | 0.21233 | 0.67091 | 0.21209 | 0.67710 |

When the aspect ratio of the annulus is defined in this manner, it is limited to the range $0 < \epsilon < 1/\pi \approx 0.3183$ based on $0 < r^* < 1$. Similarly, in the isosceles triangle, the aspect ratio is simply a measure of slenderness, such that $0 < 2b/h, h/2b < 1$. In most cases, good agreement is achieved when the smallest angle $\theta > 15$ deg [7]. However, one can also define an aspect ratio using the equivalent rectangle approach when the smaller dimension is preserved and the equivalent areas are used to determine the larger dimension. This approach generally affords a small increase in accuracy.

4.2 General Model. Having chosen an appropriate length scale and measure of slenderness, it is now appropriate to propose a simple model. In Ref. [7], Muzychka and Yovanovich found that after choosing a more appropriate length scale and defining a suitable aspect ratio, most results fell within a narrow band that was very well approximated by the solution for a rectangular channel. More recently, Duan and Muzychka [16] also observed similar trends for slip flow of gases in microchannels. In both cases the model for the rectangular duct, which is normally defined in terms of an infinite series, could also be approximated well by the first term, without incurring a significant error.

Since the present work will utilize the rectangular duct solution for simplicity, one should examine the required number of terms in Eqs. (17) and (18). Table 4 presents the results for c_1 and c_2 for one and ten terms. Additionally, 100 terms were also considered, but the results were almost the same as those for the ten terms. Upon closer examination of the single term solution it is evident that as the number of terms in the summation series is increased to ten terms, the greatest error occurs when $\epsilon=1$, which gives an error of 0.12% higher for c_1 and 0.92% lower for c_2 , as compared with the single term solutions. It is therefore appropriate for the

rectangular duct to be approximated using a single term solution. The equations may then be simplified to the following format:

$$\bar{c}_1 = \frac{1}{2(1 + \epsilon)^2 \left(1 - \frac{32}{\pi^3 \cosh\left(\frac{\pi}{2\epsilon}\right)} \right)} \quad (22)$$

$$\bar{c}_2 = \frac{3}{2(1 + \epsilon)^2 \left(1 - \frac{192\epsilon \tanh\left(\frac{\pi}{2\epsilon}\right)}{\pi^5} \right)} - \bar{c}_1 \quad (23)$$

Using the \bar{c}_1 and \bar{c}_2 values defined by Eqs. (22) and (23) and the nondimensional equation, Eq. (21), with the appropriate value of P/\sqrt{A} from Fig. 1, the dimensionless shear stress for all shapes considered in the present work becomes

$$\tau_{\sqrt{A}}^* = 2^n \left(\bar{c}_2 + \frac{\bar{c}_1}{n} \right)^n \left(\frac{2(\epsilon + 1)}{\sqrt{\epsilon}} \right)^n \quad (24)$$

Finally, the Reynolds number criterion becomes

$$Re_g = \frac{\rho U^{2-n} (\sqrt{A})^n}{8^{n-1} K (\bar{c}_2 + \bar{c}_1/n)^n} \leq 2100 \left(\frac{\epsilon + 1}{2\sqrt{\epsilon}} \right)^n \quad (25)$$

5 Results and Discussion

The analysis of Eq. (24) was performed for shear thinning fluids $n=1/3, 1/2, 2/3, 3/4$, the Newtonian fluid $n=1$, and shear thickening fluids $n=5/4, 4/3, 3/2$. The results are given in Figs. 2 and 3 and Tables 4–7.

Beginning with Tables 5 and 6, we see that significant differences arise when the hydraulic diameter is used for nondimensionalizing the wall shear stress. Variances from the rectangular duct solution for other shapes such as the elliptic duct, annular duct, and isosceles triangle can be as large as 85% when $\mathcal{L}=D_h$ is used as a length scale. However, when $\mathcal{L}=\sqrt{A}$ is used, this variance is reduced to much less than 20%, and in most cases when re-entrant corners are not present, this variance is reduced to less than 10%. Turning to Table 7 for the regular polygons, it is clear that variances as much as 30% occur with $\mathcal{L}=D_h$ as a length scale, while for $\mathcal{L}=\sqrt{A}$, it is much less than 10%. If one excludes the triangular duct, then the variance is less than 1%.

Figures 2 and 3 show graphically the results summarized in Table 6 over the full range of aspect ratio. It is clear that when the length scale is based on the square root of the cross-sectional flow area, the rectangular duct may be used with reasonably good ac-

Table 5 $\tau_{D_h}^*$ (max/min) % difference

| | $n=1/3$ | $n=1/2$ | $n=2/3$ | $n=3/4$ | $n=1$ | $n=5/4$ | $n=4/3$ | $n=3/2$ |
|-----------|------------|------------|------------|-------------|------------|-------------|-------------|-------------|
| Rectangle | 0/0 | 0/0 | 0/0 | 0/0 | 0/0 | 0/0 | 0/0 | 0/0 |
| Ellipse | 7.69/0.28 | 10.16/0.20 | 11.91/0.82 | 12.67/-0.65 | 14.67/0.12 | 14.16/1.94 | 14.96/-1.75 | 16.55/-1.35 |
| Annulus | 8.34/0.011 | 11.43/0.02 | 14.20/0.02 | 15.51/0.021 | 19.18/0.03 | 22.57/0.033 | 23.66/0.035 | 25.76/0.039 |
| Isosceles | 21.22/3.45 | 29.95/4.70 | 23.76/6.02 | 42.80/6.41 | 55.97/8.04 | 45.26/11.30 | 74.62/10.16 | 84.55/11.21 |

Table 6 $\tau_{\sqrt{A}}^*$ (max/min) % difference

| | $n=1/3$ | $n=1/2$ | $n=2/3$ | $n=3/4$ | $n=1$ | $n=5/4$ | $n=4/3$ | $n=3/2$ |
|-----------|------------|------------|------------|------------|------------|------------|------------|-------------|
| Rectangle | 0/0 | 0/0 | 0/0 | 0/0 | 0/0 | 0/0 | 0/0 | 0/0 |
| Ellipse | 5.22/0.061 | 6.01/0.02 | 6.32/0.003 | 6.36/-0.19 | 6.19/0.030 | 5.74/-0.17 | 5.54/1.59 | 5.11/1.78 |
| Annulus | 1.97/0.006 | 2.25/0.007 | 2.48/0.009 | 3.18/0.010 | 5.45/0.01 | 7.92/0.013 | 8.78/0.014 | 10.54/0.015 |
| Isosceles | 10.68/0.36 | 13.39/0.18 | 15.48/0.27 | 16.39/0.99 | 18.75/0.42 | 20.76/0.23 | 21.39/5.02 | 22.59/4.84 |

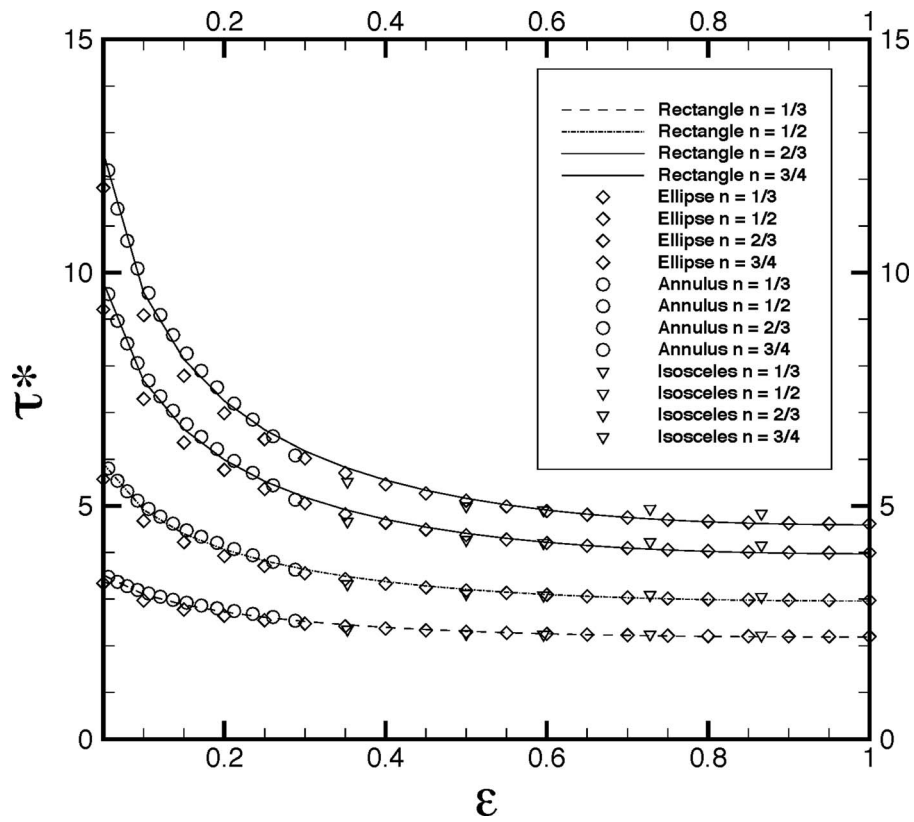


Fig. 2 $\tau^*_{\sqrt{A}}$ for noncircular ducts at $n < 1$

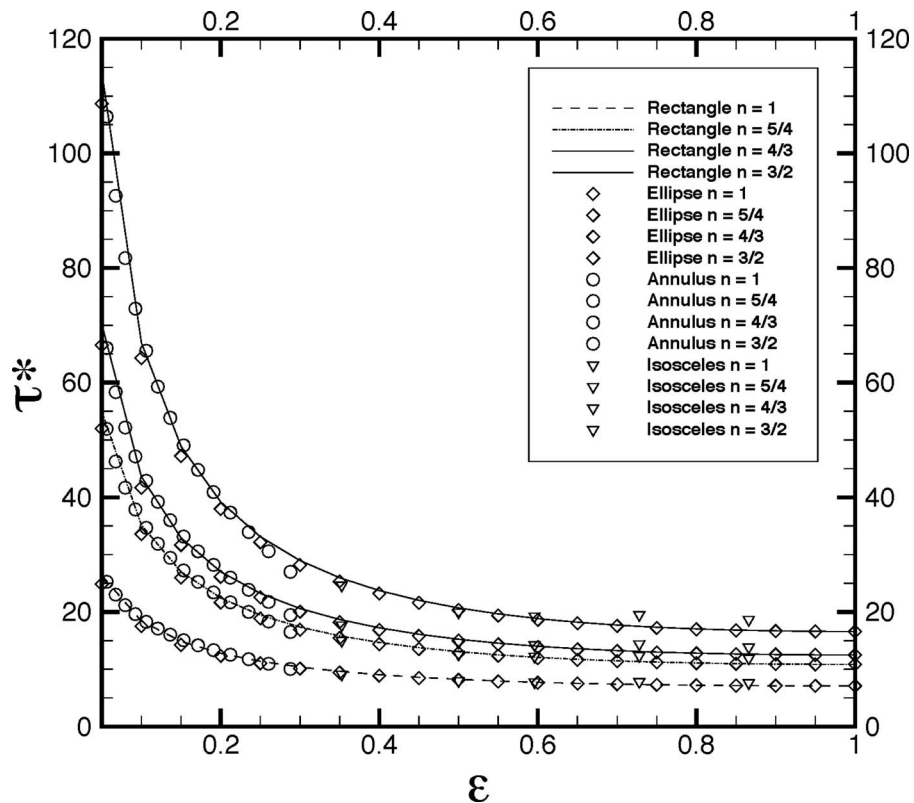


Fig. 3 $\tau^*_{\sqrt{A}}$ for noncircular ducts for $n \ge 1$

Table 7 Data for polygonal ducts

| N | n=1/3 | | n=1/2 | | n=2/3 | | n=3/4 | |
|----------------|----------------|---------------------|----------------|---------------------|----------------|---------------------|----------------|---------------------|
| | $\tau_{D_h}^*$ | $\tau_{\sqrt{A}}^*$ | $\tau_{D_h}^*$ | $\tau_{\sqrt{A}}^*$ | $\tau_{D_h}^*$ | $\tau_{\sqrt{A}}^*$ | $\tau_{D_h}^*$ | $\tau_{\sqrt{A}}^*$ |
| 3 | 2.130 | 2.225 | 2.858 | 3.051 | 3.804 | 4.151 | 4.382 | 4.833 |
| 4 | 2.190 | 2.190 | 2.968 | 2.968 | 3.987 | 3.987 | 4.613 | 4.613 |
| 5 | 2.221 | 2.186 | 3.027 | 2.955 | 4.088 | 3.959 | 4.742 | 4.574 |
| 6 | 2.240 | 2.187 | 3.063 | 2.954 | 4.149 | 3.955 | 4.821 | 4.568 |
| 8 | 2.259 | 2.189 | 3.101 | 2.959 | 4.218 | 3.961 | 4.909 | 4.575 |
| ∞ | 2.289 | 2.1991 | 3.162 | 2.977 | 4.327 | 3.992 | 5.051 | 4.614 |
| $N=\infty/N=3$ | 1.09 | 0.99 | 1.11 | 0.98 | 1.14 | 0.96 | 1.15 | 0.96 |

| N | n=1 | | n=5/4 | | n=4/3 | | n=3/2 | |
|----------------|----------------|---------------------|----------------|---------------------|----------------|---------------------|----------------|---------------------|
| | $\tau_{D_h}^*$ | $\tau_{\sqrt{A}}^*$ | $\tau_{D_h}^*$ | $\tau_{\sqrt{A}}^*$ | $\tau_{D_h}^*$ | $\tau_{\sqrt{A}}^*$ | $\tau_{D_h}^*$ | $\tau_{\sqrt{A}}^*$ |
| 3 | 6.669 | 7.602 | 10.119 | 11.917 | 11.622 | 13.837 | 15.325 | 18.647 |
| 4 | 7.114 | 7.114 | 10.929 | 10.929 | 12.604 | 12.604 | 16.756 | 16.756 |
| 5 | 7.369 | 7.022 | 11.406 | 10.739 | 13.186 | 12.366 | 17.616 | 16.388 |
| 6 | 7.526 | 7.004 | 11.704 | 10.698 | 13.552 | 12.313 | 18.160 | 16.302 |
| 8 | 7.706 | 7.014 | 12.047 | 10.710 | 13.974 | 12.326 | 18.791 | 16.317 |
| ∞ | 8.000 | 7.090 | 12.619 | 10.850 | 14.681 | 12.490 | 19.859 | 16.568 |
| $N=\infty/N=3$ | 1.20 | 0.93 | 1.25 | 0.91 | 1.26 | 0.90 | 1.30 | 0.89 |

curacy to approximate most shapes. In essence, $\mathcal{L}=\sqrt{A}$ achieves for laminar flows what $\mathcal{L}=D_h$ achieves for turbulent flows. In the case of non-Newtonian fluids, the degree of accuracy is quite good for shear thinning fluids $n < 1$ and shear thickening fluids $n > 1$, when ducts with small re-entrant corners are excluded, $\theta < 15$ deg. In general the results for most shear thinning fluids are quite good, due in part to the blunt velocity distributions, i.e., approaching plug flow. One can also see that for shear thinning fluids, the variances become smaller, even when $\mathcal{L}=D_h$ is used, which may offer insight to why the hydraulic diameter works so well for turbulent Newtonian fluid flows. Given the flatter profiles found in turbulent duct flows, and the marked decrease in variances in Table 5 for shear thinning fluids, it is hard to overlook the similarities.

Overall, the model defined by Eq. (24) is quite effective as a predictive scheme for non-Newtonian fluids. Equation (24) eliminates the need for complex tabulated solutions and may be used with a high degree of accuracy for most duct and microchannel shapes.

6 Summary and Conclusions

This paper examined the fully developed laminar flow in non-circular ducts for non-Newtonian power law fluids. A simple model was developed, which provides accuracy of better than 10% for ducts without re-entrant corners. In those cases, such as the isosceles triangle duct, the error increases to approximately 22%. This simple model is based on the solution for the rectangular duct when an appropriate characteristic length scale and measure of slenderness are chosen. In previous works, the length scale was chosen to be the square root of the duct rather than the hydraulic diameter. When the hydraulic diameter is used as a length scale, the aforementioned errors increase to 25% and 85%, respectively. With this new model it is now possible to predict the pressure drop in a number of ducts for which no solution exists. This is quite important in microchannel applications where micro-fabrication techniques often yield trapezoidal shaped ducts, semi-elliptical, or other variant of a rectangular channel. The analysis was conducted for a power law index in the range of $1/3 < n < 3/2$, which is much larger than most typical non-Newtonian fluids.

Acknowledgment

The authors acknowledge the financial support of the Natural Sciences and Engineering Research Council of Canada (NSERC) for support provided through the Discovery Grants program.

Nomenclature

- A = flow area, m²
- a, b = major and minor axes of ellipse or rectangle, m
- c₁, c₂ = Rabinowitsch–Mooney constants
- \bar{c}_1, \bar{c}_2 = generalized Rabinowitsch–Mooney constants
- D = diameter of circular duct, m
- D_h = hydraulic diameter, $\equiv 4A/P$
- E(ε') = complete elliptic integral of second kind
- f = friction factor $\equiv \tau/(\frac{1}{2}\rho U^2)$
- K = consistency index, Pa sⁿ
- n = power law flow index
- L = duct length, m
- ℒ = arbitrary length scale, m
- N = number of sides of polygon
- P = perimeter, m
- p = pressure, N/m²
- Po = Poiseuille number, $\equiv \bar{\tau}\mathcal{L}/\mu\bar{U}$
- r = radius, m
- Re = Reynolds number, $\equiv \rho U\mathcal{L}/\mu$
- U = average velocity, m/s

Greek Symbols

- ε = aspect ratio, $\equiv b/a$
- ε' = complementary modulus, $\sqrt{1-\epsilon^2}$
- μ = dynamic viscosity, N s/m²
- ν = kinematic viscosity, m²/s
- ρ = fluid density, kg/m³
- τ = shear stress, N/m²
- τ_w = wall shear stress, N/m²
- τ* = dimensionless wall shear stress, $\equiv \bar{\tau}_w\mathcal{L}^n/KU^n$

Subscripts

- \sqrt{A} = based on the square root of flow area
- D_h = based on the hydraulic diameter
- f = fluid

References

- [1] Skelland, A. H. P., 1967, *Non-Newtonian Flow and Heat Transfer*, Wiley, New York.
- [2] Chhabra, R. P., and Richardson, J. F., 1999, *Non-Newtonian Flow in the Process Industries*, Butterworth-Heinemann, Oxford.
- [3] Kakac, S., Shah, R. K., and Aung, W., 1987, *Handbook of Single Phase Convective Heat Transfer*, Wiley, New York.
- [4] Koo, J., and Kleinstreuer, C., 2003, "Liquid Flow in Microchannels: Experimental Observations and Computational Analyses of Microfluidic Effects," J.

- Micromech. Microeng., **13**, pp. 568–579.
- [5] Azimain, A. R., and Sefid, M., 2004, “Performance of Microchannel Heat Sinks With Newtonian and Non-Newtonian Fluids,” *Heat Transfer Eng.*, **25**(8), pp. 17–27.
- [6] Shah, R. K., and London, A. L., 1978, *Laminar Flow Forced Convection in Ducts*, Academic, New York.
- [7] Muzychka, Y. S., and Yovanovich, M. M., 2002, “Laminar Flow Friction and Heat Transfer in Non-Circular Ducts—Part I: Hydrodynamic Problem,” *Compact Heat Exchangers: A Festschrift on the 60th Birthday of Ramesh K. Shah*, G. P. Celata, B. Thonon, A. Bontemps, and S. Kandlikar, eds., Edizioni ETS, Italy, pp. 123–130.
- [8] Bharami, M., Yovanovich, M. M., and Culham, J. R., 2006, “Pressure Drop of Fully Developed Laminar Flow in Microchannels of Arbitrary Cross-Section,” *ASME J. Fluids Eng.*, **128**, pp. 1036–1044.
- [9] Koziicki, W., Chou, C. H., and Tiu, C., 1966, “Non-Newtonian Flow in Ducts of Arbitrary Cross-Sectional Shape,” *Chem. Eng. Sci.*, **21**, pp. 665–679.
- [10] Koziicki, W., and Tiu, C., 1968, “Geometric Parameters for Some Flow Channels,” *Can. J. Chem. Eng.*, **46**, pp. 389–393.
- [11] Koziicki, W., and Tiu, C., 1971, “Improved Parametric Characterization of Flow Geometries,” *Can. J. Chem. Eng.*, **49**, pp. 562–569.
- [12] Sparrow, E. M., 1962, “Laminar Flow in Isosceles Triangular Ducts,” *AIChE J.*, **8**, pp. 599–604.
- [13] Lundgren, T. S., Sparrow, E. M., and Starr, J. B., 1964, “Pressure Drop Due to the Entrance Region in Ducts of Arbitrary Cross Section,” *Trans. ASME*, **20**, pp. 620–626.
- [14] Churchill, S. W., 1987, *Viscous Flows: The Practical Use of Theory*, Butterworth-Heinemann, Boston, MA.
- [15] Bejan, A., 2000, *Shape and Structure: From Engineering to Nature*, Cambridge University Press, Cambridge, England.
- [16] Duan, Z. P., and Muzychka, Y. S., 2007, “Slip Flow in Non-Circular Micro-Channels,” *Microfluid. Nanofluid.*, **3**(4), pp. 473–484.

Nellyana Gonzalo Flores
Eric Goncalvès
Regiane Fortes Patella

LEGI-INP,
Grenoble, BP53,
38041 Grenoble, France

Julien Rolland
CNES,
Direction des Lanceurs,
Rond point de l'espace,
91023 Evry, France

Claude Rebattet
CREMHyG-INP,
Grenoble, BP95,
38402 Saint Martin d'Hères, France

Head Drop of a Spatial Turbopump Inducer

A computational fluid dynamics model for cavitation simulation was investigated and compared with experimental results in the case of a three-blade industrial inducer. The model is based on a homogeneous approach of the multiphase flow coupled with a barotropic state law for the cool water vapor/liquid mixture. The numerical results showed a good prediction of the head drop for three flow rates. The hydrodynamic mechanism of the head drop was investigated through a global and local study of the flow fields. The evolution of power, efficiency, and the blade loading during the head drop were analyzed and correlated with the visualizations of the vapor/liquid structures. The local flow analysis was made mainly by studying the relative helicity and the axial velocity fields. A first analysis of numerical results showed the high influence of the cavitation on the backflow structure. [DOI: 10.1115/1.2969272]

1 Introduction

Cavitation occurs frequently in the axial inducer stage of rocket engine turbopumps. It is initiated by a pressure decrease due to a high-speed local liquid velocity and can lead to a fatal failure in pump performance. In order to improve the design method and to evaluate the performance and application limits of inducers working under cavitating conditions, experimental and numerical works have been carried out by some research teams, as for example Refs. [1–8]. In complement to experimental observations, numerical approaches enable flow local analyses and the prediction of global performances.

Concerning three-dimensional (3D) numerical studies, cavitating flows in turbomachinery are generally modeled by a homogeneous fluid assumption through the one-fluid Reynolds-averaged Navier–Stokes equations (RANS). Different methods have been proposed to model the mixture and mass transfer between the liquid and vapor. We can cite the interface tracking method proposed by Hirschi et al. [9], the use of a state law to close the system [3,4,10,11], the introduction of an additional equation including source terms for vaporization, and the condensation processes applied by Medvitz et al. [12], Ait Bouziad et al. [5,6], Mejri et al. [2,13,14], or Athavale et al. [15].

Although the numerical modeling of such a phenomenon has received a great deal of attention, it is still a very difficult and challenging task to predict 3D complex cavitating flows with an acceptable accuracy. Physical and numerical calculations should be improved and validated. Methodologies enabling 3D flow analyses and design criteria should be proposed.

In this context, the aim of the present study is to endeavor to improve previous works [4,10,11,16] by

- (a) carrying out complementary observations and obtaining new experimental data in the case of a three-blade inducer,
- (b) applying and testing implemented physical and numerical models in the case of this inducer geometry running under different steady cavitating flow conditions, and

- (c) proposing an appropriate 3D analysis methodology.

The numerical simulation of cavitating flows in turbomachinery has been developed at the turbomachinery and cavitation team of Laboratoire des Ecoulements Géophysiques et Industriels (LEGI, Grenoble, France) in collaboration with the French space agency, Centre National d'Etudes Spatiales (CNES), and the rocket engine division of Snecma (Vernon, France), the civil and military aircraft manufacturer, a SAFRAN Group company. Studies are based on a homogeneous approach coupled with a barotropic state law to model the cavitation phenomenon [17]. The physical model has been previously integrated by the LEGI laboratory in the computational fluid dynamics (CFD) code FINETM/TURBO [11,18,19], developed and commercialized by Numeca International (Bruxelles, Belgium). Experimental works have been conducted at the Centre d'Essais de Machines Hydrauliques (CREMHyG) laboratory (Grenoble, France). This paper presents obtained results concerning the head drop, blade load, power, and hydraulic efficiency evolution in the case of a three-blade inducer. Local analyses of the cavitation influence on secondary flows and backflow are also developed.

2 Experimental Data

The present study refers to a three-blade industrial inducer, CREM1, illustrated in Fig. 1. It was designed with the goal to suppress the rotating cavitation instabilities [16]. It is worth noting that, for this geometry, the nominal flow rate is much smaller than the zero-incidence angle flow rate.

Water tests were performed at CREMHyG. The TM2 bench is devoted to the characterization of high-speed inducers. Time-averaged pressure measurements were performed at the shroud with two pressure taps, whose position is indicated in Fig. 2, connected to Druck 910-type pressure piezoresistive transducers with a relative accuracy of 0.2%. The volumetric flow rate is measured by an automatic oil tool (AOT)-type turbine flowmeter, with a relative accuracy of 0.3%. The rotational speed is measured with an HBM T32-type tachymeter with a relative accuracy of 0.1%. From these measurements, the pressure coefficient ψ and the cavitation parameter τ can be evaluated with an accuracy smaller than 0.4%.

The inducer is placed in a transparent liner housing to enable

Contributed by the Fluids Engineering Division of ASME for publication in the JOURNAL OF FLUIDS ENGINEERING. Manuscript received April 16, 2007; final manuscript received June 17, 2008; published online September 22, 2008. Assoc. Editor: Steven Ceccio.

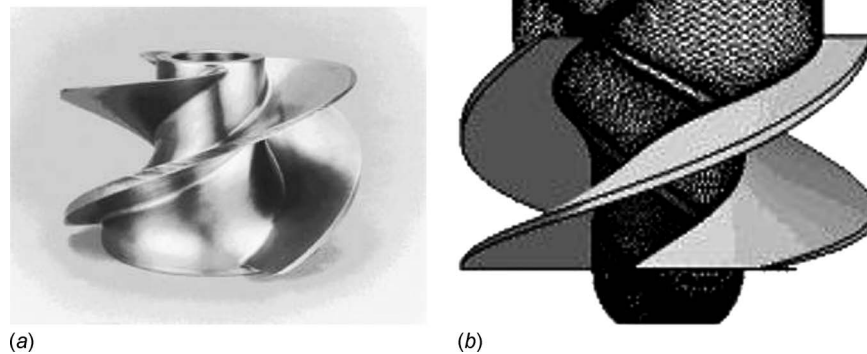


Fig. 1 Details of the inducer: (a) photograph of the inducer CREM1 and (b) a view of the inducer meshing

the observations of the cavitating flow. Photographs and video movies are taken with stroboscopic light synchronized with the rotating shaft. These are used to observe the topology of vapor structures. Details of procedure and results are presented in Ref. [16].

A large range of flow rates was investigated around the nominal point of operation in noncavitating and cavitating conditions. Noncavitating experiments consist of setting a high static pressure level, to avoid any apparition of vapor and then to vary the flow rate. In cavitating conditions, the flow rate is kept constant, and the static pressure is decreased slowly to enhance vapor development in the inducer and to reach the performance breakdown.

In Fig. 3, breakdown curves are presented for three flow rates. Parameter Ψ is evaluated from static pressures P_{inlet} and P_{outlet} measured at the shroud, as indicated in Fig. 2. τ^* is calculated as a function of the total pressure at the inlet level. The breakdown

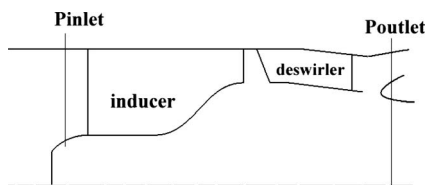


Fig. 2 Position of the pressure taps at the shroud used to measure pump performance (i.e., τ and Ψ pressure coefficients)

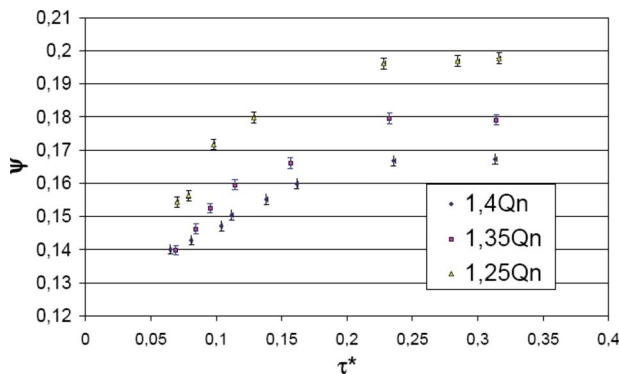


Fig. 3 Experimental head drop charts for the three different flow rates

curves appear very gradual for this inducer geometry. Head drops equivalent to $\sim 10\%$ of the noncavitating performance correspond to $\tau^* \sim 0.13$ (for $1.25Qn$), and to $\tau^* \sim 0.11$ (for $1.35Qn$ and $1.4Qn$). In the final drop zone, corresponding to about 20% of the head drop and $\tau^* \sim 0.07$, each point is stabilized with $\pm 1\%$ of the variation in the rate flow coefficient.

According to experimental observations [16], the cavitating zone is mainly located in a peripheral region and is fed by back-flow circulation. From the spectral analysis of inlet pressures, and of axial and radial forces on the shaft, axial instability is observed during breakdown. No rotating cavitation signature appears on spectral cascades of the CREM1 inducer.

3 Flow Model and Numerical Tool

3.1 Governing Equations and the Barotropic Model. The applied two-phase flow model is based on a mixture assumption (one-fluid model). The compressible RANS system, written in a rotating frame, associated with the $k-\epsilon$ turbulent model [20], has been solved. The barotropic model proposed by Delannoy and Kueny [17] is applied to model the cavitation phenomenon. In the model, ρ_l and ρ_v are, respectively, the density of the pure liquid (corresponding to $\alpha=0$) and pure vapor ($\alpha=1$). Both densities, corresponding to pure phases, are taken as constant. In the cavitation zone, the density of the vapor/liquid mixture is given as a function of the void ratio by the relation:

$$\rho = \alpha\rho_v + (1 - \alpha)\rho_l \quad (1)$$

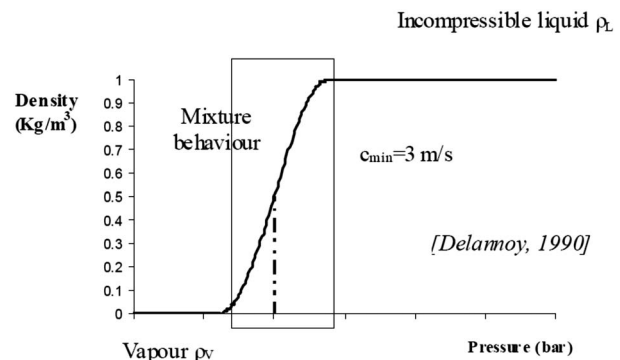


Fig. 4 The barotropic state law $\rho(p)$ for cold water

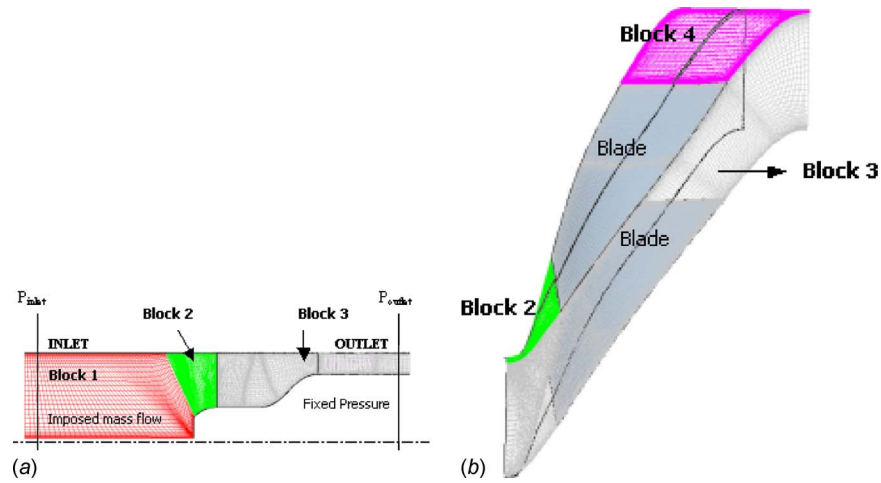


Fig. 5 Inducer views: (a) Inducer meridian view. Representation of mesh blocks and boundary conditions. (b) Representation of inducer blade-to-blade view mesh blocks.

This law is mainly controlled by its maximum slope, which is related to the minimum speed of sound c_{\min} in the mixture. In all computations presented in this paper, $c_{\min} \approx 3$ m/s (Fig. 4). The influence of the law state parameter c_{\min} on the behavior of the inducers has been evaluated in previous works [11,20].

The liquid density is set to 1000 kg/m^3 and the vapor density is fixed to its physical value of 0.02 kg/m^3 . Because of convergence difficulties in the case of the smallest cavitation numbers, some computations have been performed with a maximum value of $\rho_v = 15 \text{ kg/m}^3$.

3.2 Numerical Methods. Steady numerical simulations were carried out using the 3D CFD code FINETM/TURBO [19], developed by Numeca International in collaboration with the LEGI laboratory. The discretization is based on a cell-centered finite-volume approach for multidomain structured meshes. The convective numerical fluxes are computed with a second order central scheme stabilized by the artificial dissipation proposed by Jameson et al. [21]. An explicit four-stage Runge–Kutta time stepping procedure is used to advance the solution to the steady state. For incompressible areas, a low-speed preconditioner is introduced [18,23], enabling the reduction of the eigenvalue stiffness and the improvement of convergence.

The Yang–Shih $k-\epsilon$ turbulent model [22] with extended wall functions is used. The turbulence transport equations are integrated with a first order upwind scheme. The physical model and the numerical code are detailed in Refs. [11,23].

In the proposed cavitation model, thermal effects are neglected in the vaporization and condensation phenomena [24]. Complementary works are in progress to improve the cavitation model in order to take into account thermodynamic effects [25,26].

3.3 Grids and Boundary Conditions. Only one blade-to-blade channel is considered and periodicity conditions are applied to its frontiers in azimuthal directions to simulate the presence of the contiguous blades. The mesh is composed of four 3D blocks (Fig. 5): the upstream part of the bulb, the blade-to-blade channel, and two blocks, respectively, upstream from the blade leading edge and downstream from its trailing edge. The whole mesh contains around 700,000 nodes for the first considered grid V1 (Fig. 1(b)). The tip leakage is not taken into account in the present study.

The y^+ values from the center of the adjacent cells to walls vary from 0.8 to 100, for all computations, and the largest y^+ values are mainly placed in the leading edge near the shroud of the inducer.

The calculations are performed with water flow conditions. The mass flow is imposed at the inlet, and the static pressure is imposed at the outlet. The hub and the blades are rotating, the shroud is immobile. Wall functions are imposed along solid boundaries.

In order to develop the phenomenon of cavitation in the numerical simulations and to obtain different values of τ^* during head breakdown, the imposed vapor pressure is increased progressively. The calculated inlet pressure is used to evaluate the numerical cavitation parameter τ^* . Parameter ψ is calculated by the difference between the outlet and inlet static pressures, as indicated in Fig. 5.

In order to evaluate the grid influence, two additional grids (V2 and V3) have been tested. The grid specifications are shown in Table 1. Steady numerical simulations have been performed in cavitating conditions at $1.4Q_n$ flow rate with the same conditions applied in the reference grid (V1). Numerical head drop charts are

Table 1 Tested meshes

| | Reference grid V1 | V2 | V3 |
|------------------------------|-------------------|--------|--------|
| Totals numbers of grid point | 697564 | 838672 | 962844 |
| y^+_{\max} | 97.6 | 87.2 | 78.3 |
| y^+_{\min} | 0.81 | 0.65 | 0.61 |

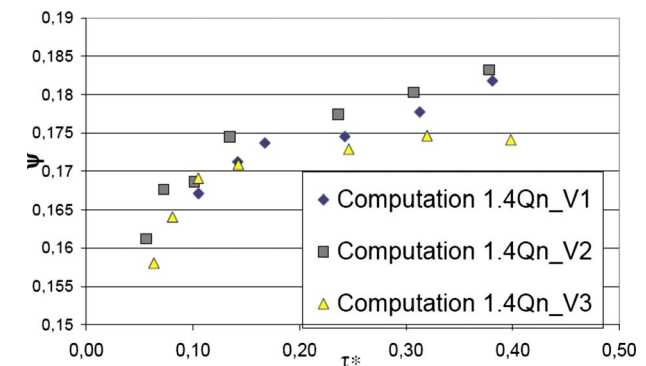


Fig. 6 Cavitation head drop curves obtained with three different grids at $1.4Q_n$ flow rate

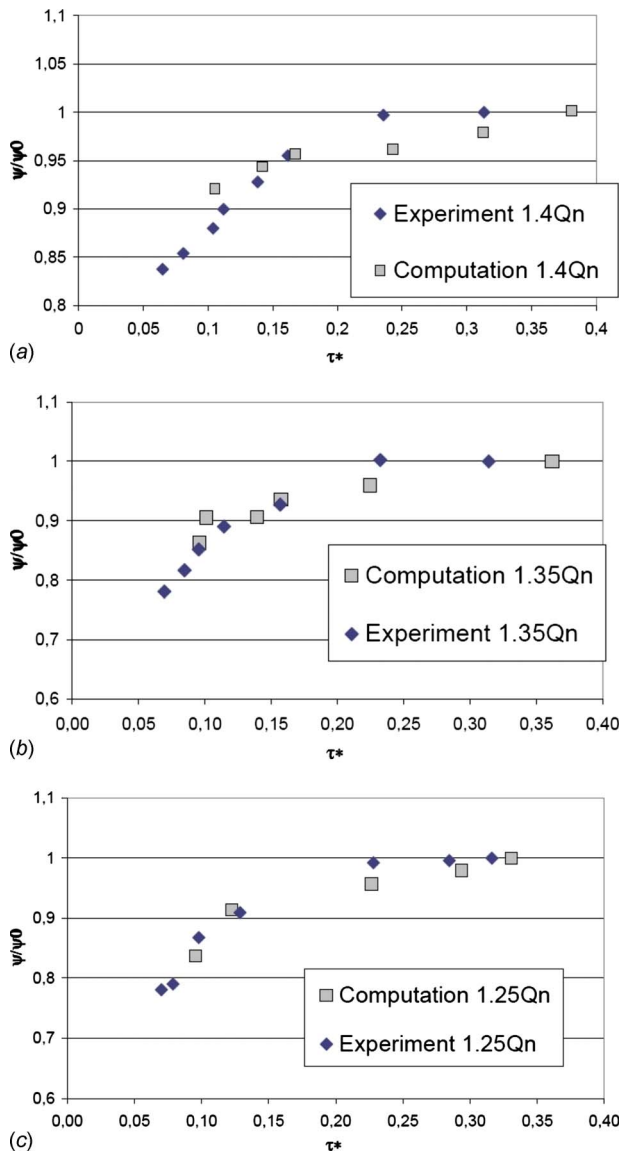


Fig. 7 Experimental and numerical head drop charts. (a) $1.4Q_n$, (b) $1.35Q_n$, and (c) $1.25Q_n$.

presented in Fig. 6. It is worth noting that each calculated steady state solution was carefully converged.

The relative differences between noncavitating pump heads cal-

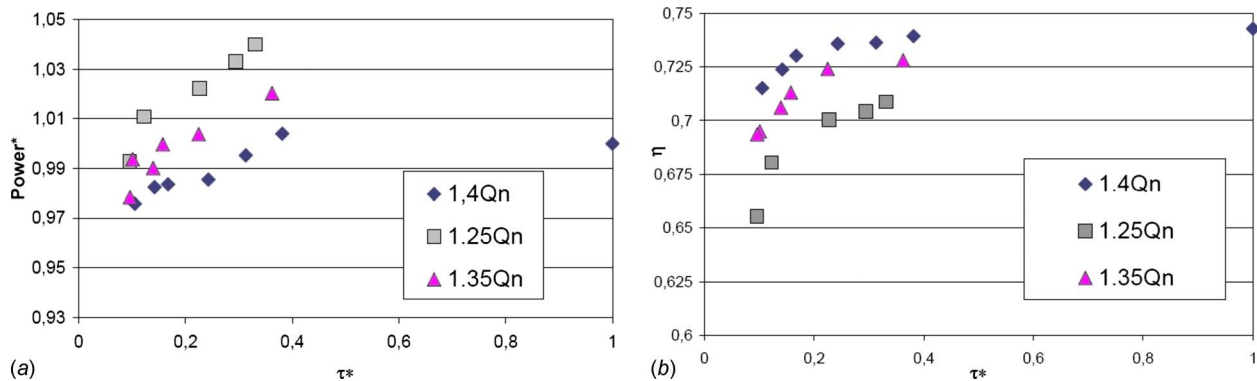


Fig. 8 Evolution of (a) the computational dimensionless available power as a function of the cavitation parameter τ^* and (b) the hydraulic efficiency as a function of the cavitation parameter τ^*

culated with the three meshes are smaller than 5%. Concerning τ^* equivalent to a 10% head drop, the maximum relative error between calculated values is about 30%, which corresponds to a $\Delta\tau^* \sim 0.02$.

Numerical results have been analyzed in order to improve knowledge about head drop mechanisms, local flow characteristics, and secondary flows in the inducer. The development of cavitation structures (Sec. 4.4) calculated with these grids are quite similar, and the analyses of secondary flows, presented in Sec. 4.5, appear almost independent to the applied mesh.

The aim was also to propose a methodology of 3D calculations and analyses of complex cavitating flows. In relation to prior works presented in Ref. [11] concerning the inducer geometry, meaningful numerical work has been performed by Pouffary et al. [4], Numeca International, and Rolland [26] to improve the preconditioner and the stability of the numerical code for calculations of cavitating flows. It is worth noting that these numerical modifications led to major improvements in the accuracy and numerical stability in comparison to our previous computations [10].

4 Numerical Results and Discussion

Steady numerical simulations of the inducer have been performed with grid VI in cavitating conditions at a given rotational speed and three flow rates: $1.4Q_n$, $1.35Q_n$, and $1.25Q_n$. First, we present a quantitative analysis by comparing the experimental and numerical results of head drop charts.

The power and efficiency evolutions obtained by numerical simulations are illustrated for the three flow rates. Some qualitative results, concerning the blade load and visualizations of vapor/liquid structures are also presented for several τ^* values. Finally, a study of secondary flows during the τ^* decrease is proposed.

4.1 Head Drop. Numerical head drop charts are compared with experimental ones for three flow rates in Fig. 7. The absolute comparisons between the experimental and numerical parameters ψ are not possible because outlet pressure values are not taken at the same points (see Figs. 2 and 5). The head drop $\psi/\psi_0(\tau^*)$ is shown in relation to the maximal values (ψ_0) obtained for each case (experimental and numerical) and for the different flow rates.

For $1.4Q_n$ and the flow rate, the numerical prediction at the 10% head drop were found for values of τ^* close to 0.1. For $1.35Q_n$ and $1.25Q_n$ flow rates, it is close to ~ 0.11 , these estimations correspond well to experimental observations. The most important differences between the numerical and experimental values of ψ/ψ_0 (around $\sim 4\%$) are observed in the range of $0.2 < \tau^* < 0.4$.

We underline that for lower flow rates, the angle of attack of the flow at the blade leading edge is higher than for $1.4Q_n$; the cavity

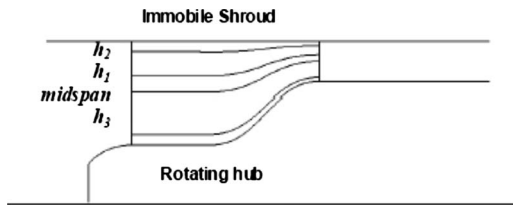


Fig. 9 Planes h_3 , h_2 , and h_1 and the midspan represented in the meridian view considered for the blade load analysis

thickness increases and sometimes it is difficult to obtain a good level of convergence.

Globally, the simulated head drops are gradual, and numerical results show a good correlation with the experimental ones for the three studied cases. The breakdown is clearly associated with a decrease in the torque and the hydraulic efficiency, as illustrated below.

4.2 Power and Efficiency Evolution. As illustrated in Fig. 8, the computed power and efficiency of the inducer are calculated at considered flow rates. The power is done from the calculated numerical torque and the fixed rotational speed. The torque is computed by the integration of the pressure and the stress tensor along the blade surface. The $Power^*$ represents the ratio of calculated power to reference power corresponding to the noncavitating condition for $1.4Qn$. The efficiency is defined as the ratio of the provided power to the available power.

The maximal values of $Power^*$ are observed for τ^* around 0.38, higher than the value in the noncavitating condition. This may be attributed to the change in the flow incidence angle due to the appearance of cavitation attached to the blade that induced a better blade load, mainly near the hub (see Sec. 4.3). For smaller τ^* values, the computed power decreases, this is attributed to the development of cavitation structures and a lower blade load.

The efficiency decreases with the cavitation parameter reduction. The efficiency variation is about 3% for $1.4Qn$, 4% for $1.35Qn$, and more than 5% for $1.25Qn$ in the range of analyzed τ^* . We conclude that the head drop is associated with both the decrease in torque and the hydraulic efficiency.

4.3 Static Pressure Distributions Around a Blade Section.

Figure 9 shows the different sections considered for the study of the static pressure distributions around the blade: midspan plane, two planes placed between the midspan and shroud, and one plane placed near the hub.

The blade load at midspan and three additional planes (h_1 , h_2 , and h_3) at $1.4Qn$ flow rate are drawn in Fig. 10 during the τ^* decrease. For these studied planes and analyzed τ^* values, it can be observed that the blades are loaded mainly near the leading edge. In the cavitating regime, the development of the sheet cavity from the leading edge of the suction side modifies progressively the blade load and, consequently, the inducer head decreases gradually, as illustrated in Fig. 7(a).

The blade load is slightly modified for $\tau^*=0.38$. For the smallest τ^* value, the figures show clearly a short sheet cavity attached from the leading edge of the suction side of the blades. For the considered conditions, the appearance of the cavitation does not influence the pressure side load. We do not observe the strong influence of the cavitation on the trailing edge pressure distribution because the cavity attached is not developed toward the interior of the blade-to-blade channels for the considered τ^* values.

The pressure values for plane h_2 (near the shroud) at the pressure side are higher than the ones evaluated for the other planes. Moreover, the blade load seems to be more important at the shroud.

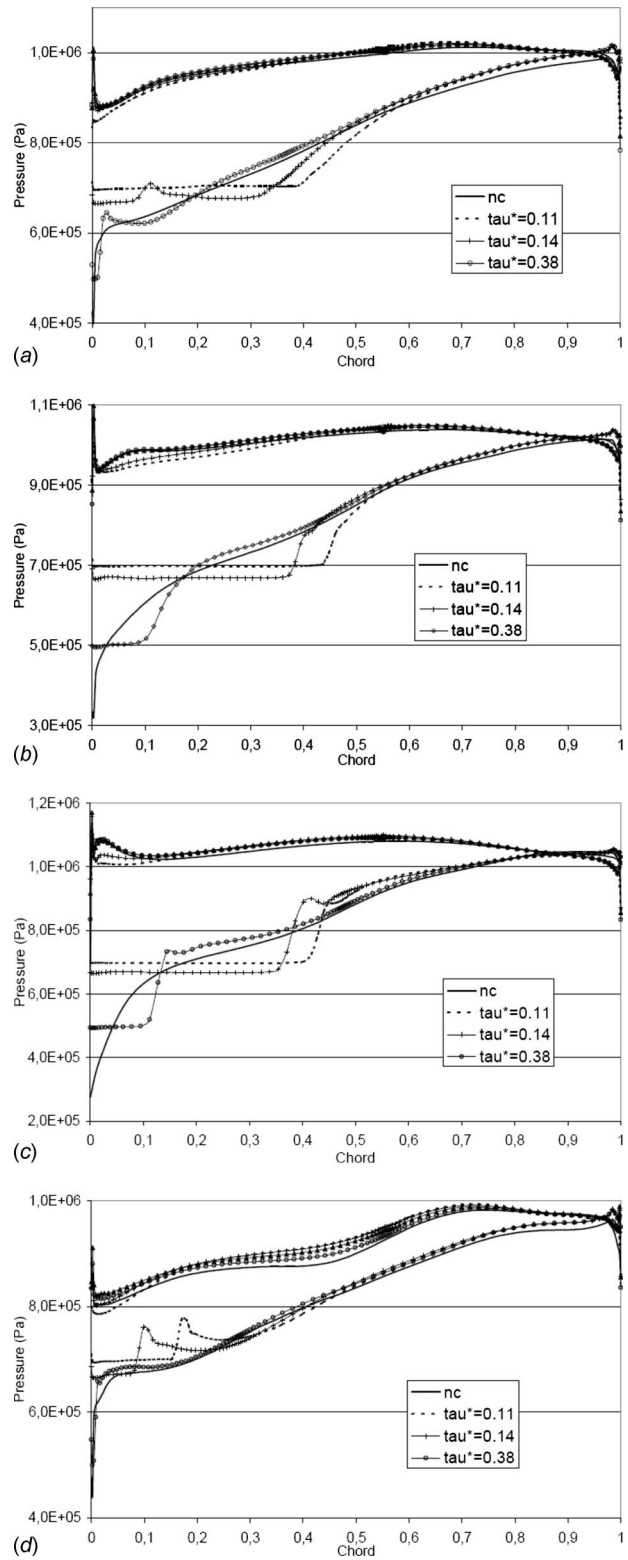


Fig. 10 Pressure distributions around the blade for decreasing τ^* at the $1.4Qn$ flow rate in four locations: (a) midspan, (b) h_1 , (c) h_2 , and (d) h_3

To improve the analyses during the τ^* decrease, the evolution of the blade load at additional plane h_3 near the hub (Fig. 10(d)) has been studied. For this plane, a better blade load for $\tau^*=0.38$ was observed, if compared with the noncavitating condition; the appearance of the cavitation influences the pressure side load and

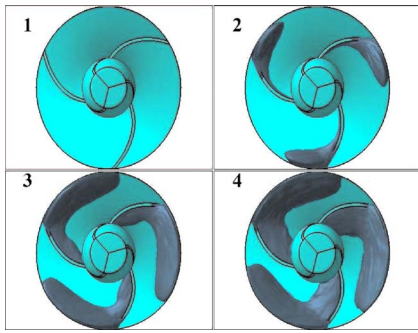


Fig. 11 Isolines of density ($\rho=950 \text{ kg/m}^3$) during the τ^* decrease at $1.4Qn$; 1 is no cavitation, 2 is $\tau^*=0.31$, 3 is $\tau^*=0.14$, and 4 is $\tau^*=0.11$

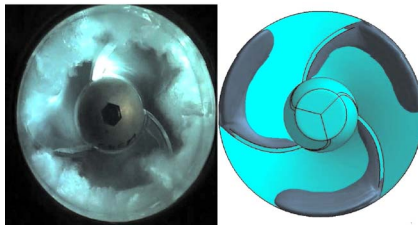


Fig. 12 Frontal view of the experimental and numerical results with an isoline of density $\rho=950 \text{ kg/m}^3$ for $\tau^*=0.17$ at $1.4Qn$

modifies the trailing edge pressure distribution slightly. This behavior, observed near the hub, seems to explain the augmentation of the torque and the power (Fig. 8) for the $\tau^*=0.38$ value in comparison to the noncavitating case ($1.4Qn$).

4.4 Visualizations of the Vapor/Liquid Structures. The computed mixture vapor/liquid structures are presented in Fig. 11, during the τ^* decrease for the $1.4Qn$ flow rate. The development of the cavitation structures are pronounced at the inducer periphery, and a large backflow structure in front of the blades is observed in Figs. 12 and 13.

The attached cavitation sheet slightly increases from the hub to the shroud and merges with the cavitating backflow structures. Head drop occurs progressively with the increase in vapor structures near the shroud. It is worth noting that at $\tau^* \sim 0.1$, the vapor structures do not reach the throat and do not enter into the blade-to-blade channel.

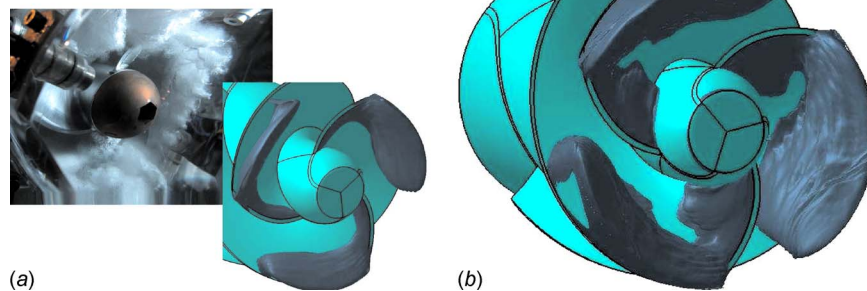


Fig. 13 Lateral view of (a) the experimental and numerical results with an isoline of density ($\rho=950 \text{ kg/m}^3$) for $\tau^*=0.17$ at $1.4Qn$ and (b) the numerical result with an isoline of density ($\rho=950 \text{ kg/m}^3$) for $\tau^*=0.08$ at $1.25Qn$

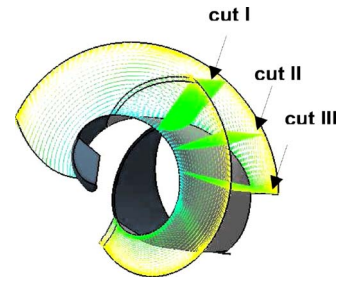


Fig. 14 Location of the analyzed flow sections in the inducer

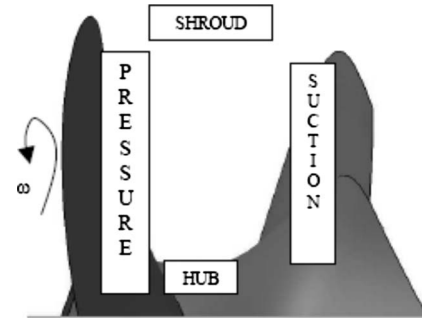


Fig. 15 Section representation for the local analysis of the secondary flow

The cavitation behavior obtained by numerical simulations presents a very good qualitative agreement with experimental visualizations (Figs. 12 and 13). We can observe that a consequence of the CREM1 design is the development of the ringed vapor structure at the shroud, which limits the development of the cavitation sheet on the blades.

Calculations performed with grids V2 and V3 lead to similar vapor/liquid structures.

4.5 Local Flow Analyses. An analysis of the flow within the inducer has been performed in three different sections in the blade-to-blade channel (Fig. 14). The local analysis of the influence of cavitation on the flow structure in the different sections has been made using the convention in Fig. 15.

4.5.1 Helicity. In the present paper, the analysis of the secondary flows is first based on the dimensionless relative helicity.

Secondary flows can be characterized by the dimensionless relative helicity, which is defined as

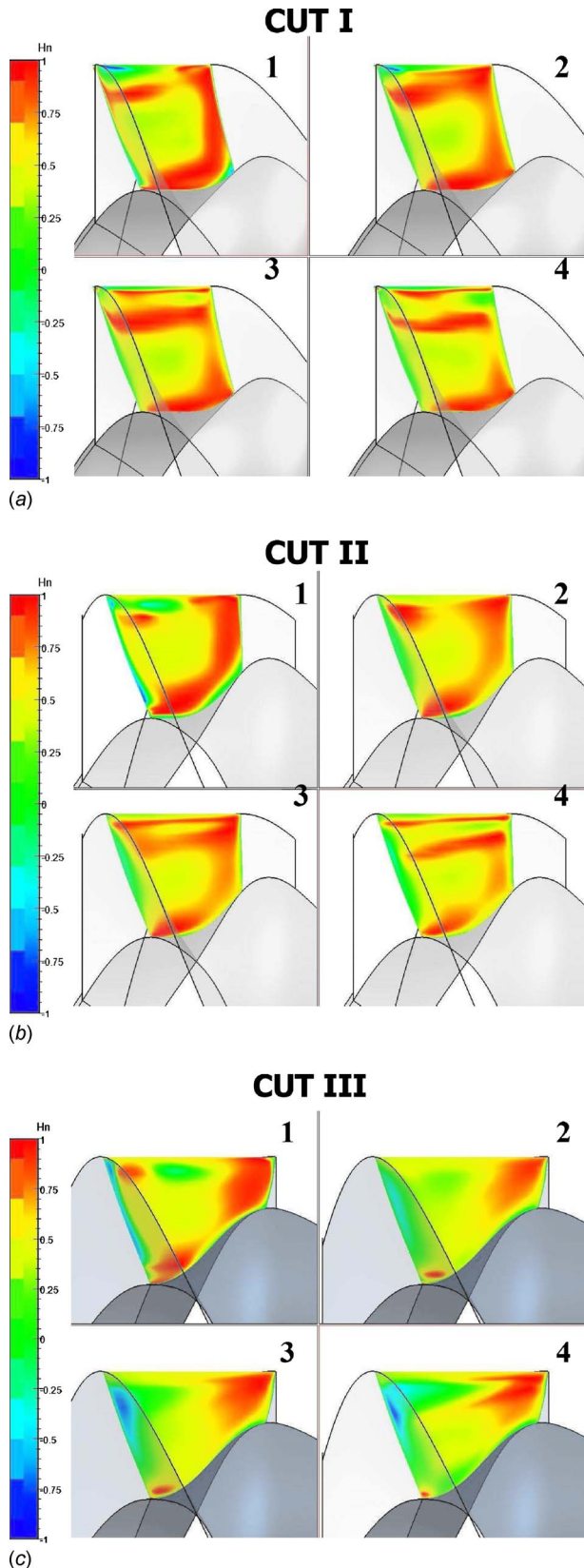


Fig. 16 Secondary flows: dimensionless relative helicity representation at three locations in the blade-to-blade channel: (a) Sec. 1, (b) Sec. 2, and (c) Sec. 3. Blue represents the maximum anticlockwise vorticity zone and red the maximum clockwise vorticity zone. The results are shown for the noncavitating condition (1) and typical cavitating regimes: $\tau^* = 0.31$, $\tau^* = 0.14$, and $\tau^* = 0.11$ (2, 3, and 4).

$$H = \frac{\mathbf{W} \cdot \text{rot}(\mathbf{W})}{|\mathbf{W}| \times |\text{rot}(\mathbf{W})|} \quad (2)$$

The normalized relative helicity indicates the value of the cosine of the angle between the velocity vector and the swirl vector. Consequently, the swirling centers will be associated with values +1 and -1, the sign determining the direction of the rotation of the swirl. This quantity is drawn in Fig. 16 for the three defined sections during the breakdown, for the $1.4Q_n$ flow rate. The black color represents anticlockwise vorticity and yellow to white indicate clockwise vorticity.

In Sec. 1, the secondary flow in the rotating frame develops mainly along the blade suction side (white color), especially in the noncavitating condition. With the cavitation coefficient decrease, the clockwise vorticity on the suction side tends to be less important. A clockwise vorticity structure of low intensity is located on the pressure side. This behavior is due to the development of the boundary layer, which is less important on the pressure side than on the suction side because of the leading edge proximity on the pressure side. It is also observed that the flow is disturbed in the zone near the hub; the flow displays a high clockwise vorticity.

It is important to recall that tip leakage was not considered in the numerical simulations (which explains the absence of zones with a strong vorticity near the shroud).

In the noncavitating regime in Sec. 2 (Fig. 16(b)), we observe a clockwise vorticity (white color) on the suction side. For the cavitating conditions the secondary flows are similar to the structures observed in Sec. 1.

Finally, in Sec. 3 (Fig. 16(c)), in the noncavitating regime, the clockwise vorticity is located on the suction side and some regions of the anticlockwise vorticity appear close to the shroud on the pressure side. The vorticity effects are less important near the hub for this section due to the meridian curvature of this inducer.

In the analyzed sections in cavitating conditions, we observed some vorticity structures (white color) located near the shroud, which seem to be associated with the ringed vapor structure at the shroud (Figs. 11 and 12). Boundary layers are developed in the zones close to solid surfaces of the blades in the pressure side and suction side for the three different sections.

Figure 17 shows the distribution of the radial velocity in the three sections. For noncavitating conditions we observe a strong centrifugation of the boundary layers, mainly at the suction side (radial velocity is around 12 m/s), which is associated to the secondary structures observed from helicity analyses.

It is worth noting that comparisons between results obtained from grids V1, V2, and V3 indicate slight modifications on calculated secondary flows, as illustrated in Fig. 18.

4.5.2 Axial Velocity. In order to analyze the flow rate distribution in the inducer, results obtained for the $1.4Q_n$ flow rate concerning the axial velocity in the three sections previously defined (Fig. 14) are illustrated in Fig. 19. Results correspond to different τ^* values.

In Sec. 1 (Fig. 19(a)), a backflow zone near the shroud, characterized by negative axial velocities can mainly be observed. This zone is clearly observed in the meridian view by the analysis of the streamlines (Fig. 20). An anticlockwise vorticity (Fig. 16(a)) can also be observed in this zone (Sec. 1, noncavitating condition).

The figures corresponding to Sec. 2 (Fig. 19(b)) show that the zones of the negative axial velocity are mainly near the hub. For the smallest values of the cavitation parameter, the appearance of zones of low velocities close to the shroud can be observed. For Sec. 3 (Fig. 19(c)), the negative axial velocity area is placed in the pressure side near the hub and it seems to be related to the high meridian curvature of the hub.

In a general overview, it can be noticed that the flow rate is not uniformly distributed in the channel and that axial velocities are more important at the blade suction side.

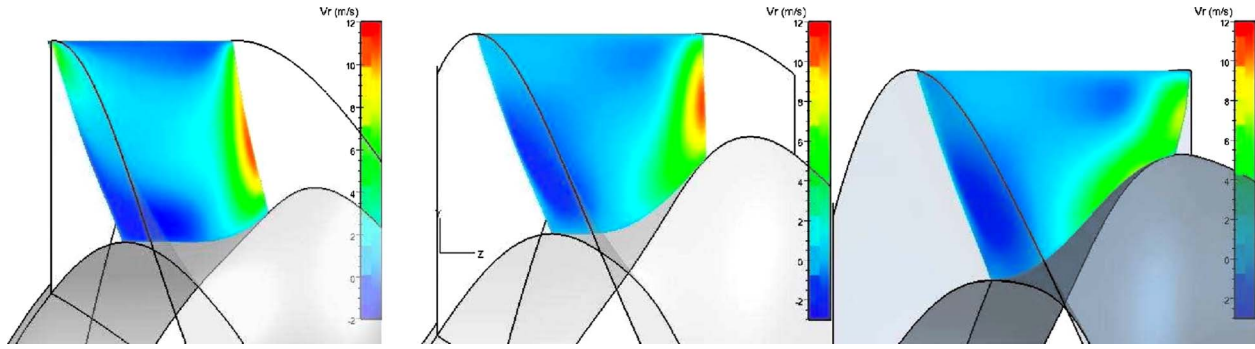


Fig. 17 Secondary flows: radial velocity evolution in the noncavitating regime in Secs. 1–3 for $1.4Qn$

By analyzing results presented in Fig. 20, we observe that the backflow zone near the shroud tends to decrease during breakdown; the appearance of cavitation structures and the reduction of pressure gradients between the suction and pressure sides lead to a decrease in the thickness of the backflow area (in the meridian plane). The width (Fig. 19(a)) and the length (Fig. 20) of this zone are also modified by cavitation structures.

5 Conclusion

In the present work, 3D steady RANS computations were performed and compared with experiments concerning water cavitating flows in a three-blade inducer at different flow rates. In complement to prior works [4,10,11], the main targets of the present study were to pursue model validation and to improve analyses of complex 3D cavitating flows in rocket engine turbopump inducers.

The qualitative development of the cavitation in the inducer was simulated and the extension of vapor near the shroud was favorably compared with experimental results. Experimental and numerical performance charts concerning three different flow rates were also compared. Thanks to recent numerical improvements, predictions of the inducer breakdown were adequate and much better than the ones presented in previous works [11].

Analyses of the numerical results provided interesting information about the power, blade load, and hydraulic efficiency evolution during head breakdown. Secondary flows were analyzed from dimensionless relative helicity maps corresponding to three different sections in the blade-to-blade channel. Moreover, local analyses of axial velocity fields enabled the determination of backflow zones and of the flow rate distribution in the inducer channels. For the considered cavitation number range, the study pointed out a relevant influence of the cavitation structures on the flow fields around the leading edge, near the shroud zone.

The methodology of analysis proposed in this paper showed that numerical simulations can provide useful information for the design of turbomachinery, and more particularly for inducers. Based on the experimental and numerical results obtained, the inducer geometry was improved. A new inducer was designed and is being tested for future works concerning mainly instable cavitation analyses and prediction.

Complementary works are also in progress, mainly

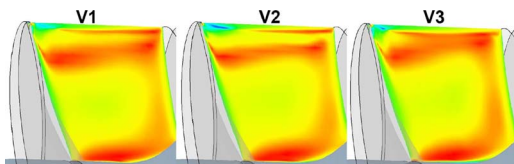


Fig. 18 Secondary flows: dimensionless relative helicity (Cut I) at $1.4Qn$ at $\tau^* = 0.24$. Representation of numerical results in Grids V1, V2, and V3.

- to improve the cavitation model to take into account thermodynamic effects, mainly in the case of cryogenic propellants [25,26] and
- to implement and to apply a multigrid strategy to accelerate the convergence of cavitating flow calculations in inducer geometries. This work is very important for carrying out 3D unsteady calculations and for analyzing cavitation instabilities [8,20,27].

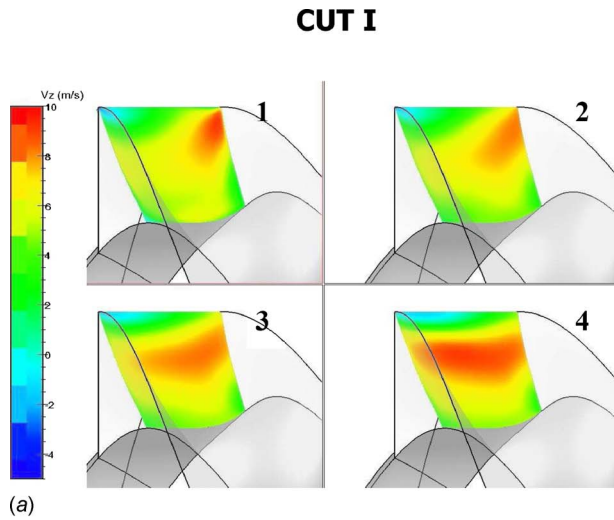
It is worth underlining that further local and global experimental studies are also required in order to validate and calibrate the physical models applied in an improved way.

Acknowledgment

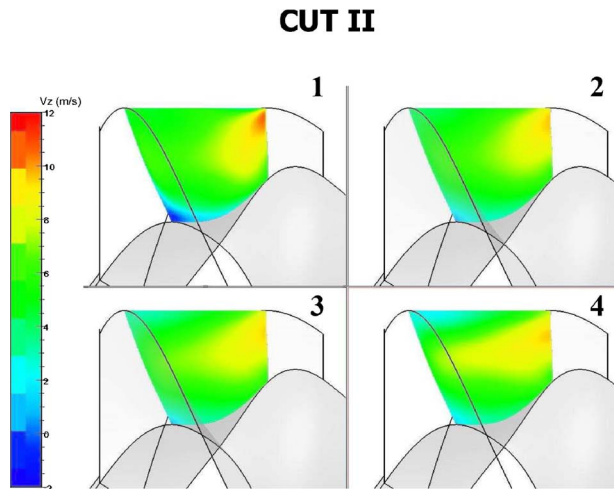
The authors wish to express their gratitude to French space agency CNES, to Snecma for their continuous support, and to Numeca International for their cooperation in the development of the numerical code. This research was also supported by a doctoral grant from the Los Andes University, Venezuela.

Nomenclature

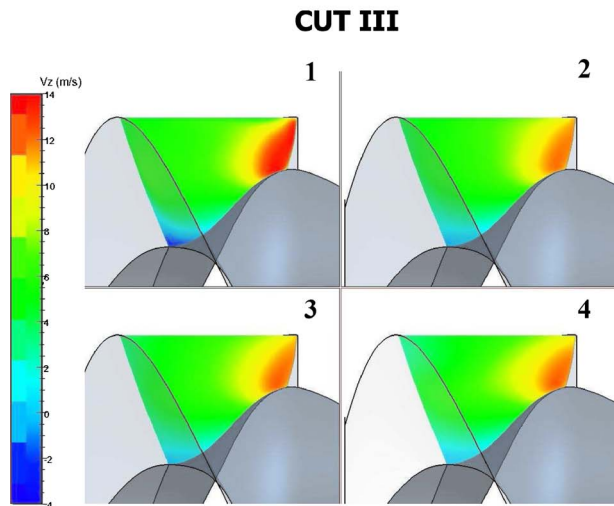
- c_{\min} = minimum speed of sound in the vapor/liquid mixture (m/s)
 L_{ref} = geometry reference length (m)
 P = local static pressure (Pa)
 $P_{\text{tot}} = P + (\rho V^2 / 2)$ local total pressure (Pa)
 P_{vap} = vapor pressure (Pa)
 $\text{power} = T\omega$ (W)
 $\text{power}^* = \text{power} / \text{power}_{\text{noncavitating}}$ dimensionless power
 Q = flow rate (m^3/s)
 Qn = nominal flow rate (m^3/s)
 T = torque (N m)
 V = flow velocity (m/s)
 V_{ref} = reference velocity: tangential tip velocity (m/s)
 W = relative flow velocity (m/s)
 $\Delta P_{\text{tot}} = P_{\text{tot downstream}} - P_{\text{tot upstream}}$ total pressure variation in inducer (Pa)
 $\Psi = (P_{\text{static outlet}} - P_{\text{static inlet}}) / (\rho \cdot V_{\text{ref}}^2)$ shroud elevation coefficient
 Ψ_0 = shroud elevation coefficient for the noncavitating condition
 ρ = fluid density (kg/m^3)
 ρ_l, ρ_v = liquid/vapor density (kg/m^3)
 $a = (\rho - \rho_l) / (\rho_v - \rho_l)$ void ratio
 $\eta = \Delta P_{\text{tot}} Q / T\omega$ hydraulic efficiency
 $\tau = (P_{\text{tot inlet}} - P_{\text{vap}}) / (\rho \cdot V_{\text{ref}}^2)$ cavitation parameter
 $\tau^* = (\tau / \text{const})$ dimensionless cavitation parameter
 w = angular velocity (rad/s)
 y^+ = dimensionless distance to the wall



(a)



(b)



(c)

Fig. 19 Secondary flows: axial velocity distribution in the blade-to-blade channel: (a) Sec. 1, (b) Sec. 2, and (c) Sec. 3. The results are presented for the noncavitating regime (1) and cavitating regimes $\tau^* = 0.31$, $\tau^* = 0.14$, and $\tau^* = 0.11$ (2, 3, and 4).

References

- [1] Bakir, F., Kouidri, S., Noguera, R., and Rey, R., 2003, "Experimental Analysis

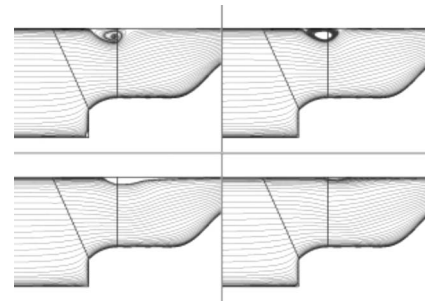


Fig. 20 Streamlines in the meridian plane: (a) noncavitating regime, (b) cavitating regime corresponding to $\tau^* = 0.31$, (c) cavitating regime corresponding to $\tau^* = 0.14$, and (d) cavitating regime corresponding to $\tau^* = 0.11$

of an Axial Inducer Influence of the Shape of the Blade Leading Edge on the Performances in Cavitating Regime," *ASME J. Fluids Eng.*, **125**(2), pp. 293–301.

- [2] Mejri, I., Bakir, F., Rey, R., and Belamri, T., 2006, "Comparison of Computational Results Obtained From a Homogeneous Cavitation Model With Experimental Investigations of Three Inducers," *ASME J. Fluids Eng.*, **128**(6), pp. 1308–1322.
- [3] Pascarella, C., Ciucci, A., Salvatore, V., and d'Agostino, L., 2000, "A Numerical Tool for the Investigation of Cavitating Flows in Turbopump Inducers," Proceedings of the 36th AIAA Joint Propulsion Conference and Exhibit, Huntsville, AL, Jul. 20–23.
- [4] Pouffary, B., Fortes-Patella, R., and Reboud, J. L., 2008, 2008, "Numerical Simulation of 3D Cavitating Flows: Analysis of Cavitation Head Drop in Turbomachinery," *ASME J. Fluids Eng.*, **130**(4), to be published.
- [5] Ait Bouziad, Y., Farhat, M., Guennoun, F., Kueny, J. L., and Avellan, F., 2003, "Physical Modelling and Simulation of Leading Edge Cavitation, Application to an Industrial Inducer," Proceedings of the Fifth International Symposium on Cavitation, Osaka, Japan, Nov. 1–4.
- [6] Ait Bouziad, Y., Farhat, M., Kueny, J. L., Avellan, F., and Miyagawa, K., 2004, "Experimental and Numerical Cavitation Flow Analysis of an Industrial Inducer," Proceedings of the 22nd IARH Symposium on Hydraulic Machinery and Systems, Stockholm, Sweden, Jun. 29–Jul. 2.
- [7] Hosagandi, A., and Ahuja, V., 2006, "Numerical Study of a Flat Plate Inducer: Comparison of Performance in Liquid Hydrogen and Water," Proceedings of the Symposium CAV 2006, Wageningen, The Netherlands, Sep. 11–15.
- [8] Tsujimoto, Y., Kamijo, K., and Yoshida, Y., 1993, "A Theoretical Analysis of Rotating Cavitation Inducers," *ASME J. Fluids Eng.*, **115**, pp. 135–141.
- [9] Hirschi, R., Dupont, F., and Avellan, F., 1998, "Centrifugal Pump Performance Drop Due to Leading Edge Cavitation: Numerical Predictions Compared With Model Tests," *ASME J. Fluids Eng.*, **120**, pp. 705–711.
- [10] Coutier-Delgosha, O., Fortes-Patella, R., Reboud, J. L., Hofmann, M., and Stoffel, B., 2003, "Experimental and Numerical Studies in a Centrifugal Pump With 2D-Curved Blades in Cavitating Conditions," *ASME J. Fluids Eng.*, **125**(6), pp. 970–978.
- [11] Coutier-Delgosha, O., Fortes-Patella, R., Reboud, J. L., Hakimi, N., and Hirsch, C., 2005, "Numerical Simulation of Cavitating Flow in 2D and 3D Inducer Geometries," *Int. J. Numer. Methods Fluids*, **48**(2), pp. 135–167.
- [12] Medvitz, R. B., Kunz, R. F., Boger, D. A., Lindau, J. W., Yocum, A. M., and Pauley, L. L., 2001, "Performance Analysis of Cavitating Flow in Centrifugal Pumps Using Multiphase CFD," Proceedings of the ASME Fluids Engineering Division Summer Meeting, New Orleans, LA, May 29–Jun. 1.
- [13] Mejri, I., Bakir, F., Rey, R., and Belamri, T., 2005, "Comparison of Computational Results Obtained From a VOF Cavitation Model With Experimental Investigations of Three Inducers: Part I: Experimental Investigations," Proceedings of the ASME Fluids Engineering Division Summer Meeting and Exhibition, Houston, TX, Jun. 19–23.
- [14] Mejri, I., Bakir, F., Rey, R., and Belamri, T., 2005, "Comparison of Computational Results Obtained From a VOF Cavitation Model With Experimental Investigations of Three Inducers: Part II: Numerical Approach," Proceedings of the ASME Fluids Engineering Division Summer Meeting and Exhibition, Houston, TX, Jun. 19–23.
- [15] Athavale, M. M., Li, H. Y., Jiang, Y., and Singhal, A. K., 2002, "Application of the Full Cavitation Model to Pumps and Inducers," *Int. J. Rotating Mach.*, **8**(1), pp. 45–56.
- [16] Rebattet, C., Wegner, M., Morel, P., and Bonhomme, C., 2001, "Inducer Design That Avoids Rotating Cavitation," Proceedings of the AFI Conference, Sandai, Japan, Oct. 4–5.
- [17] Delannoy, Y., and Kueny, J. L., 1990, "Two Phase Flow Approach in Unsteady Cavitation Modelling," Cavitation and Multiphase Flow Forum, FED (Am. Soc. Mech. Eng.), **98**, pp. 153–158.
- [18] Hakimi, N., 1998, "Preconditioning Methods for Time Dependent Navier-Stokes Equations," Ph.D. thesis, Vrije University, Brussels.
- [19] FineTM/Turbo, 2003, Numerical Mechanics Applications, Software Package, Version 4.0-1, Numeca International.
- [20] Fortes-Patella, R., Coutier-Delgosha, O., Perrin, J., and Reboud, J. L., 2007,

- "Numerical Model to Predict Unsteady Cavitating Flow Behaviour in Inducer Blade Cascades," *ASME J. Fluids Eng.*, **129**(2), pp. 128–135.
- [21] Jameson, A., Schmidt, W., and Turkel, E., 1981, "Numerical Solution of the Euler Equations by Finite-Volume Methods Using Runge–Kutta Time Stepping Schemes," AIAA Paper No. 81–1259.
- [22] Yang, Z., and Shih, T. H., 1993, "A k-e Model for Turbulence and Transitional Boundary Layer," *Near-Wall Turbulent Flows*, R. M. C. So, C. G. Speziale, and B. E. Launder, eds., Elsevier, New York, pp. 165–175.
- [23] Coutier-Delgosha O., Fortes-Patella R., Reboud J. L., Hakimi N., and Hirsch C., 2005, "Stability of Preconditioned Navier–Stokes Equations Associated With a Cavitation Model," *Comput. Fluids*, **34**(3), pp. 319–349.
- [24] Pouffary B., Fortes-Patella R., Reboud J. L., and Lambert P. A., 2008, "Numerical Analysis of Cavitation Instabilities in Inducer Blade Cascade," *ASME J. Fluids Eng.*, **130**(4), to be published.
- [25] Rolland, J., Boitel, G., Barre, S., Goncalves, E., and Fortes Patella, R., 2006, "Inducer Experiments and Modelling of Cavitating Flows in Venturi: Part I: Stable Cavitation," *Proceedings of the Symposium CAV2006*, Wageningen, The Netherlands, Sep. 11–15.
- [26] Rolland, J., 2008, "Modélisation Des Écoulements Cavitants Dans les Inducteurs de Turbopompes: Prise en Compte des Effets Thermodynamiques," Ph.D. thesis, Institut National Polytechnique de Grenoble, France.
- [27] Horiguchi, H., Watanabe, S., Tsujimoto, Y., and Aoki, M., 2000, "A Theoretical Analysis of Alternate Blade Cavitation in Inducers," *ASME J. Fluids Eng.*, **122**(2), pp. 156–163.

Kengo Kikuta

e-mail: kikuta.kengo@jaxa.jp

Yoshiki Yoshida

e-mail: yoshida.yoshiki@jaxa.jp

Mitsuo Watanabe

Tomoyuki Hashimoto

Japan Aerospace Exploration Agency,
Kakuda Space Center,
Koganezawa 1, Kimigaya, Kakuda,
Miyagi 981-1525, Japan

Katsuji Nagaura

Foundation for Promotion of Japanese Aerospace
Technology,
Koganezawa 1, Kimigaya, Kakuda,
Miyagi 981-1525, Japan

Katsuhide Ohira

Institute of Fluid Science,
Tohoku University,
Katahira 2-1-1, Aoba, Sendai,
Miyagi 980-8577, Japan

Thermodynamic Effect on Cavitation Performances and Cavitation Instabilities in an Inducer

Based on the length of the tip cavitation as an indication of cavitation, we focused on the effect of thermodynamics on cavitation performances and cavitation instabilities in an inducer. Comparison of the tip cavity length in liquid nitrogen (76 K and 80 K) as working fluid with that in cold water (296 K) allowed us to estimate the strength of the thermodynamic effect on the cavitations. The degree of thermodynamic effect was found to increase with an increase of the cavity length, particularly when the cavity length extended over the throat of the blade passage. In addition, cavitation instabilities occurred both in liquid nitrogen and in cold water when the cavity length increased. Sub-synchronous rotating cavitation appeared both in liquid nitrogen and in cold water. In the experiment using liquid nitrogen, the temperature difference between 76 K and 80 K affected the range in which the subsynchronous rotating cavitation occurred. In contrast, deep cavitation surge appeared only in cold water at lower cavitation numbers. From these experimental results, it was concluded that when the cavity length extends over the throat, the thermodynamic effect also affects the cavitation instabilities as a "thermal damping" through the unsteady cavitation characteristics. [DOI: 10.1115/1.2969426]

Keywords: thermodynamic effect, cavitating inducer, cavitation instability, cavity length

Introduction

For the rocket engine turbopump, an inducer is installed upstream of the main impeller to obtain high suction performance. This inducer, however, suffers due to serious cavitating conditions, which often leads to the development of flow instabilities that degrade the performance of the turbopump or even cause its failure.

The propellants of Japanese rocket engines are liquid hydrogen (20 K ($T^*=(T-T_c)/(T_c-T_i)=0.33$), where T_c is the temperature at the critical point and T_i is the temperature at the triple point) and liquid oxygen (90 K ($T^*=0.36$)). These cryogenic fluids are employed at a temperature that is considerable near that of the critical point, although water is employed at a temperature far from the critical point. The vapor density near the critical point is much greater than that far from the critical point. Thus, the mass rate of evaporation for the same volume growth rate of the bubble is also much larger, and consequently, the heat that must be transferred from the liquid bulk to the bubble through the interface is much larger. This causes the temperature inside the bubble (T_c) to fall well below that of the liquid bulk (T_∞). In turn, the vapor pressure ($p_v(T_c)$) within the bubble is also less than that ($p_v(T_\infty)$) in the liquid bulk. Consequently, the pressure imbalance ($p_v(T_c)-p_{ref}$) between the bubble and the reference point at infinity decreases less than the pressure imbalance ($p_v(T_\infty)-p_{ref}$). Thus, it can be understood that the growth of the bubble with the thermodynamic effect is less than that without the thermodynamic effect, even under the same cavitation number (σ) at the reference point at infinity.

A pioneer study of the thermodynamic effect in pumps was

conducted by Stahl et al. [1], who investigated the thermodynamic effect with regard to the reduction of pump performance (i.e., the measurable cavitation effect of $\Delta H/H=3\%$) as an indication of cavitation. Franc et al. [2] recently investigated the thermodynamic effect in a four-bladed inducer based on direct optical observations of the development of leading edge cavitation using refrigerant R114 as working fluid. They examined the thermodynamic effect and the onset of cavitation instabilities (i.e., alternate blade cavitation and supersynchronous rotating cavitation) based on comparison of the cavity length in R114 (temperature varying between 293 K and 313 K) with that in cold water. Cervone et al. [3] have examined a three-bladed inducer operating with cold water at 293 K and hot water at 343 K to investigate the thermodynamic effect on cavitation instabilities (i.e., rotating cavitation and cavitation surge).

In our previous study (Yoshida et al. [4]), the relation between the degree of the thermodynamic effect and the cavity length of the tip cavitation was examined by using liquid nitrogen (80 K ($T^*=0.27$)) as working fluid. The cavity length of the tip cavitation in the liquid nitrogen was estimated from measurements of the unsteady pressure on the casing wall without direct optical observation (Yoshida et al. [5]). It was found that (1) the degree of thermodynamic effect was a function of the cavity length, (2) the estimated temperature depression due to vaporization was small when the cavity length was short, (3) the temperature depression increased considerably when the cavity extended over the throat of the blade passage, and (4) the estimated temperature inside the bubble nearly reached the temperature of the triple point when the pump performance deteriorated.

In the present study, we also adopted cavity length of the tip cavitation as a cavitation indication since it is obvious that tip cavitation plays an important role in cavitation performance as well as in cavitation instabilities in inducers. Examinations of the relation of the cavity length to cavitation performance and the onset of cavitation instabilities (i.e., subsynchronous rotating cavi-

Contributed by the Fluids Engineering Division of ASME for publication in the JOURNAL OF FLUIDS ENGINEERING. Manuscript received May 25, 2007; final manuscript received July 2, 2008; published online September 22, 2008. Review conducted by Joseph Katz.

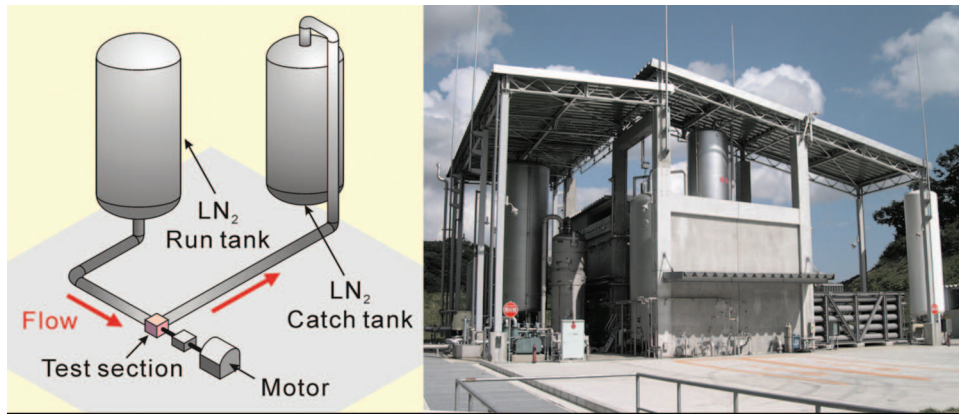


Fig. 1 Cryogenic inducer test facility of JAXA

tation and cavitation surge) were conducted by comparison of results in liquid nitrogen set at different temperatures, 76 K ($T^*=0.20$) and 80 K ($T^*=0.27$), with those in cold water at 296 K ($T^*=0.06$).

Experimental Facility

Experiments in Water and Liquid Nitrogen. In the present study, we carried out two types of experiments, experiments in water, in which the thermodynamic effect can be disregarded, and experiments in liquid nitrogen, in which the thermodynamic effect appears distinctly. Both experiments were conducted at the Kakuda Space Center (KSC) of the Japan Aerospace Exploration Agency (JAXA).

Experiments in water were conducted in a closed-loop tunnel

cavitation tunnel (Shimagaki et al. [6]). The working fluid was cold water at room temperature, 296 K ($T^*=0.06$), after degassing. The inducer casing was made of transparent acrylic resin to permit direct optical visualization of cavitation by use of a video camera. The rotational speed was 6000 rpm and the flow rate was $Q/Q_d=1.06$ (Q_d : design flow rate). The Reynolds number of the inducer, $Re=UD/\nu$ (D =diameter of inducer; U =peripheral speed of inducer tip), was $Re=9.1 \times 10^6$.

Experiments in liquid nitrogen were conducted at the Cryogenic Inducer Test Facility (CITF) (Yoshida et al. [7]) shown in Fig. 1. This facility is a blowdown cavitation tunnel, in which the working fluid is flushed from the run tank to the catch tank through the inducer test section. The temperature of the liquid nitrogen in the run tank can be controlled at different temperatures by regulating the pressure to investigate the characteristic of the thermodynamic properties. Thanks to this capability, the temperatures of liquid nitrogen as a working fluid were set at 76 K ($T^*=0.20$) and 80 K ($T^*=0.27$) in the present experiments. Figure 2 shows a schematic of the inducer drive unit. The inducer is driven by an inverter controlled motor with an epicyclic gear at a rotational speed of 18,300 rpm, which is equal to that of an actual turbopump. Inducer shaft torque is measured by a noncontact high-speed torque sensor. The flow rate is $Q/Q_d=1.05$, and the Reynolds number of the inducer is $Re=1.1 \times 10^8$. Figure 3 shows the inducer test section for the experiment in liquid nitrogen. The inducer used in the liquid nitrogen experiment has the same dimensions and geometric configurations as that in cold water. It has three blades with

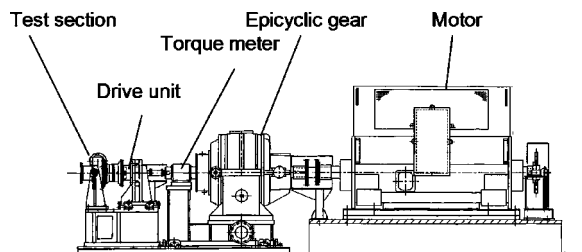


Fig. 2 Schematic diagram of the drive unit

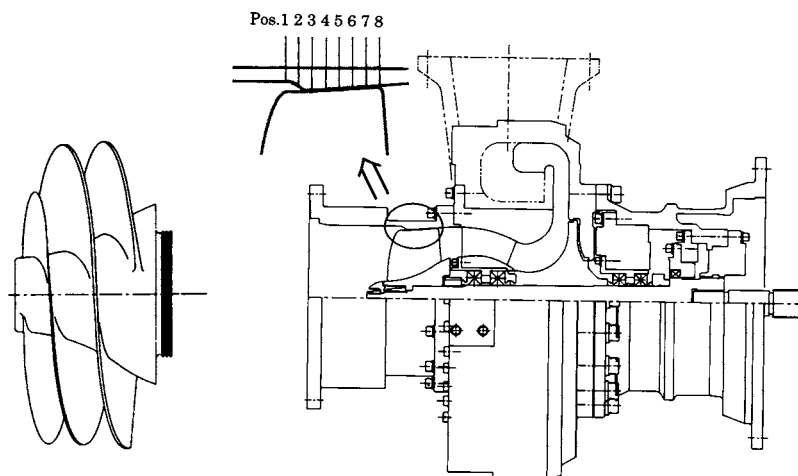


Fig. 3 Section of the test inducer in liquid nitrogen, showing the location of pressure sensors

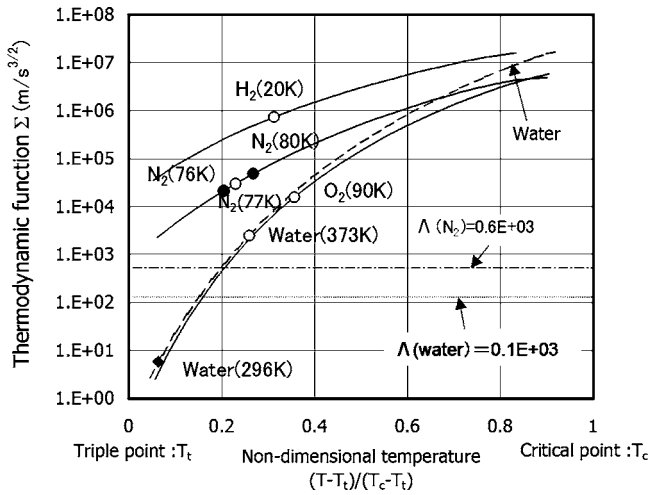


Fig. 4 Variation of the thermodynamic function $\Sigma(T)$ of hydrogen, nitrogen, oxygen, and water

sweep cutback at the leading edge, and its solidity is about 1.9, as shown in Fig. 3. The inducer casing for the experiment in liquid nitrogen is made of stainless steel, and thus optical visualization of the cavitating inducer is not possible.

Thermodynamic Function $\Sigma(T)$. Brennen [8] proposed the thermodynamic function $\Sigma(T) (= (\rho_v / \rho_l)^2 \cdot (L^2 / C_{pL} T \alpha_l^{1/2})) (m/s^{3/2})$ and the dynamic fluid parameter $\Lambda (= (U^3 \sigma / C)^{1/2} (m/s^{3/2}))$ that show the degree of the thermodynamic effect on the growth of a simple spherical cavity in the flow. Comparing the magnitude of both parameters, $\Sigma(T)/\Lambda$ is nondimensional thermodynamic parameter of thermodynamic effect. Similar nondimensional thermodynamic parameters, $\Sigma(T) \cdot (D/V^3)^{1/2}$, were also derived by Kato [9], Franc et al. [2], and Watanabe et al. [10]. Figure 4 shows the variation of the thermodynamic function $\Sigma(T)$ for hydrogen, nitrogen, oxygen, and water as the function of nondimensional temperature $T^* = (T - T_t) / (T_c - T_t)$ (T_c is the temperature at the critical point and T_t is the temperature at the triple point). Moreover, Λ ($\Lambda(\text{nitrogen}) = 0.6 \times 10^{+03}$, $\Lambda(\text{water}) = 0.1 \times 10^{+03}$) in the cases of the present nitrogen and water test at $\sigma = 0.04$ are also shown in Fig. 4. In the test condition of nitrogen, nondimensional thermodynamic parameter $\Sigma(T)/\Lambda$ is about $1.0 \times 10^{+02}$. Thus, the thermodynamic effect is expected to appear hugely. In contrast, in the test condition of water, nondimensional thermodynamic parameter $\Sigma(T)/\Lambda$ is about 1.0×10^{-01} . Thus, the thermodynamic effect cannot be disregarded at all.

When the temperature decreases, the thermodynamic function $\Sigma(T)$ becomes lower, i.e., the strength of the thermodynamic effect decreases. The thermodynamic function $\Sigma(T)$ of nitrogen at 75 K ($T^* = 0.19$) is almost the same as that of oxygen at 90 K ($T^* = 0.36$). This is one of the reasons why we set the temperature

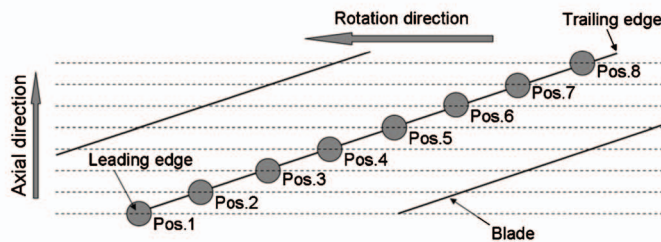
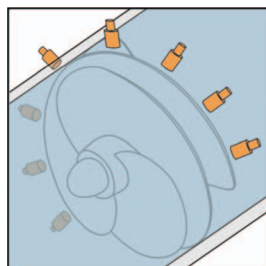


Fig. 6 Location of pressure taps along the blade

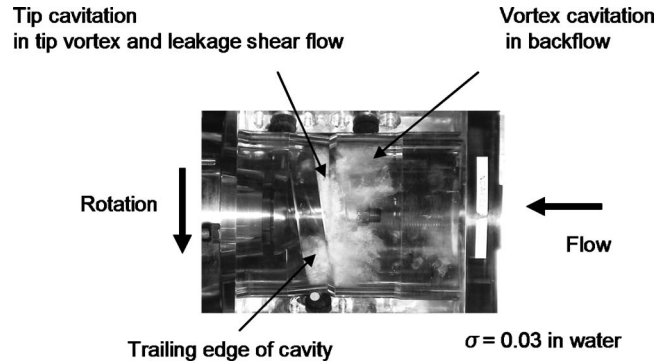


Fig. 5 Typical optical visualization of cavitating inducer in cold water

of nitrogen at 76 K ($T^* = 0.20$). However, the temperature of the triple point of nitrogen is 63.1 K ($T^* = 0.0$). The margin between 76 K ($T^* = 0.20$) and 63.1 K is less than the margin between 80 K ($T^* = 0.27$) and 63.1 K. Thus, it is estimated that nitrogen of 76 K has a low margin for the critical limit with the triple point for thermodynamic properties, although oxygen at 90 K ($T^* = 0.36$) has a high margin due to the distance from the triple point of 54.4 K ($T^* = 0.0$).

Observation of Cavitation

Optical Visualization in Cold Water. Figure 5 shows a typical cavitating inducer (at $\sigma = 0.03$) with direct optical visualization in cold water. Several kinds of cavitation patterns are observed. Tip leakage vortex cavitation, cavitation in the shear layer between the tip leakage flow and the main flow, cavitation in the backflow upstream of the inducer, and sheet cavitation generated from the leading edge of the blade can be distinguished. In the experiment in cold water, the length of the tip cavity along the blade was measured from the leading edge of the blade to the trailing edge of the cavity with the visual images.

Indirect Visualization in Liquid Nitrogen. As direct optical visualization could not be done in liquid nitrogen, unsteady pressure sensors were installed on the casing to estimate the cavitation region. Figures 3 and 6 show the location of the pressure taps (Pos. 1–8). There are eight sensors located from the leading edge to the trailing edge along the blade. The pressure sensors detect the unsteady pressure caused by the tip cavitation, which includes the tip leakage vortex cavitation, cavitation in the shear layer, and a part of the attached cavitation on the blade surface. However, the pressure sensor could not detect the cavitation in the backflow. Also, as the sensor is a charge mode pressure sensor and cannot detect the dc component of unsteady pressure, the value of the vapor pressure cannot be measured. Thus, the vapor pressure was estimated based on the unsteady pressure wave forms as follows.

When cavitation develops on the suction side of the blade at the

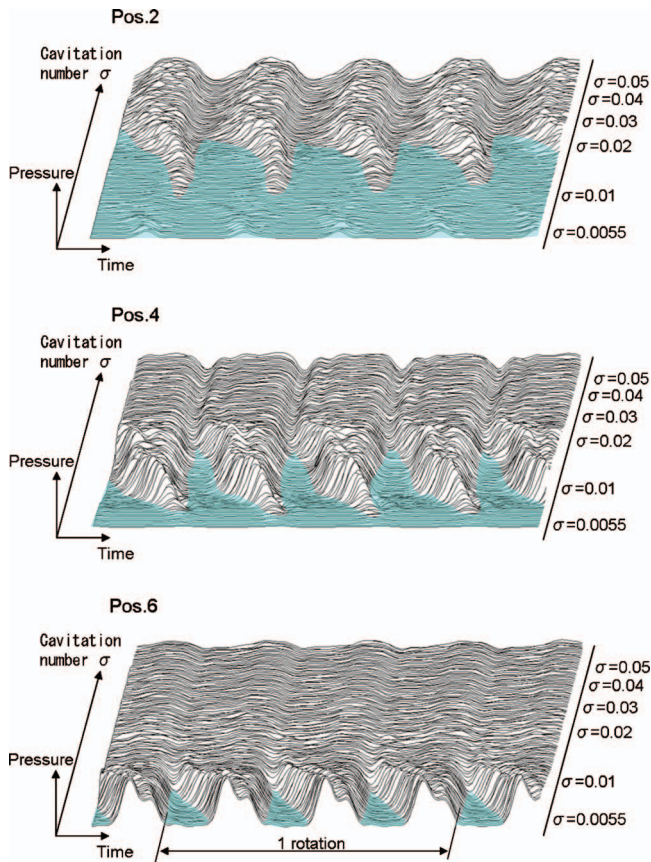


Fig. 7 Waterfalls of unsteady pressure wave form at Pos. 2, 4, and 6 (uncertainty in $\sigma=0.001$)

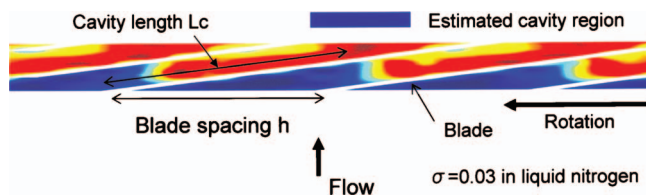


Fig. 8 Typical unsteady pressure distribution showing the estimated cavity region in liquid nitrogen

tip, the pressure sensor shows a particular wave form. Figure 7 shows the waterfalls of typical wave forms measured at Pos. 2, 4, and 6, respectively. Wave forms of 50 rotations are averaged using the trigger signal of a rotation. When the cavitation number becomes smaller, a flat region (light blue) appears at the bottom of the wave form and extends from the suction side to the pressure side within the interblade. The pressure of this region can be considered to be the vapor pressure of the cavitation. Thus, we judged this domain to be the region of cavitation, as shown in Fig. 8. The estimated cavitation region (colored blue) develops along the blade from the leading edge to the blade passage. From this figure, it was found that the cavitating region could be estimated indirectly by examination of the unsteady pressure wave form. In a previous work (Yoshida et al. [4]), we confirmed that this indirect observation results using the pressure sensor agrees with the direct optical observation in the water experiment.

In addition, focusing on blade loading based on the wave forms in Fig. 8, it was observed that the leading edge loading (at Pos. 2 and 4) is higher than the channel loading (at Pos. 6) at higher cavitation numbers. When the cavitation number decreases, the channel loading (at Pos. 6) becomes higher than the leading edge loading (at Pos. 2 and 4). From these results, it was concluded that the distribution of the blade loading transfers from the leading edge to the trailing edge due to the development of the cavity.

Experimental Results

Cavitation Performance. Figures 9 and 10 show comparisons of the cavitation performances in cold water (296 K (○) in Fig. 9) with those in liquid nitrogen (76 K (Δ) and 80 K (○) in Fig. 10). The horizontal axis is the cavitation number (σ), and the vertical axis is the normalized head coefficient (ψ/ψ_0). The inducer heads in liquid nitrogen are maintained until the cavitation number is smaller than that in water. The cavitation performances are greatly improved due to the thermodynamic effect in liquid nitrogen.

Regarding the pressure performance in liquid nitrogen, the inducer head tends to increase gradually as the cavitation number decreases; i.e., the pump gain is negative ($d\psi/d\sigma < 0$) in Fig. 10. However, the torque characteristic is flat ($d\tau/d\sigma = 0$) in liquid nitrogen. Unfortunately, shaft torque was not measured in the water experiment. The distribution of inducer blade loading moves from the leading edge to the trailing edge as described above, as the cavitation number decreases. Thus, it was found that the hydraulic efficiency increases depending on the distribution of the blade loading as the cavitation number decreases. This is the origin of the negative pump gain ($d\psi/d\sigma < 0$) in liquid nitrogen. Contrary

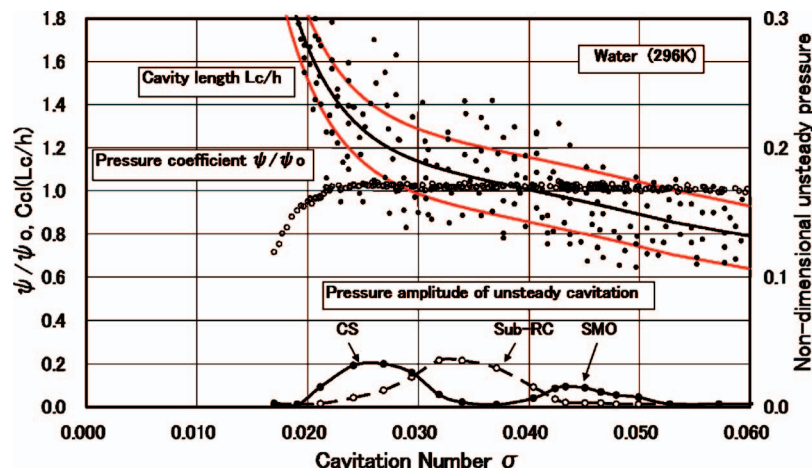


Fig. 9 Cavitation performance, cavity length, and pressure amplitude of cavitation instabilities in cold water (296 K) (uncertainty in $\sigma=0.001$, $\psi/\psi_0=0.01$, $C_{ci}=0.05$)

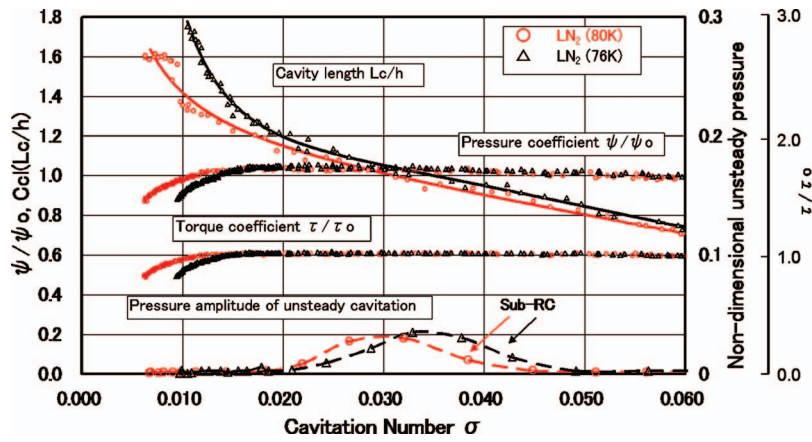


Fig. 10 Cavitation performance, cavity length, torque, and pressure amplitude of cavitation instabilities in liquid nitrogen (76 K and 80 K) (uncertainty in $\sigma = 0.001$, $\psi/\psi_0=0.01$, $C_{cl}=0.03$)

to the result in liquid nitrogen, the pump gain in water in Fig. 9 is smaller than that in liquid nitrogen. It is almost flat ($d\psi/d\sigma=0$). Thus, it is inferred that the thermodynamic effect affects the cavity shape, i.e., length, thickness, and void fraction, which in turn affects the slope of the pressure performance, i.e., the pump gain ($d\psi/d\sigma$) through the hydraulic efficiency.

Cavity Length. Figures 9 and 10 also show comparisons of the cavity length C_{cl} (L_c/h , cavity length along the blade from the leading edge of the blade to the trailing edge of the cavity/blade spacing) versus the cavitation number σ . The closed black circles (●) in Fig. 9 indicate the cavity lengths in cold water from the direct visualization shown in Fig. 5. One symbol shows a reading from one picture. There is a large scatter caused by cavitation unsteadiness (i.e., subsynchronous rotating cavitation and cavitation surge described in the following section). The standard deviation $S(C_{cl})$ of those plots is 0.15. The best-fit curve (black line) obtained by the least squares method and the best-fit curve \pm standard deviation $S(C_{cl})=0.15$ (red line) are also shown in the figure.

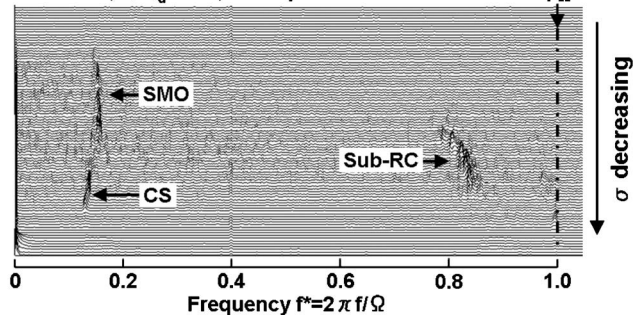
The cavity lengths in liquid nitrogen (at 76 K (Δ) and 80 K (\circ)) based on the estimated pressure distribution shown in Fig. 8 are presented in Fig. 10. There is almost no scatter since one symbol shows the averaged value of 50 rotations. Best-fit curves (76 K (black line) and 80 K (red line)) are also shown in the figure. From comparison of the best-fit curves, the cavity length in nitrogen was found to be shorter than that in cold water at the given cavitation number. Therefore, it can be concluded that the thermodynamic effect suppressed the growth of the cavity. The difference between the cavity length in cold water and that in liquid nitrogen was smaller when C_{cl} was less than 1.0. However, the difference increased considerably when C_{cl} was larger than about 1.2. Similar characteristics were observed in the experiments of liquid nitrogen between at 76 K and 80 K. In other words, the degree of the thermodynamic effect decreases at lower temperature of liquid nitrogen.

Occurrence of Cavitation Instability. Occurrences of cavitation instability were confirmed by the fast Fourier transform (FFT) analysis of the pressure fluctuations. Figure 11 shows the comparisons of FFT analysis in the experiment of water at 296 K (Fig. 11, upper) with that of liquid nitrogen at 80 K (Fig. 11, lower). In cold water, several kinds of cavitation instabilities appear, i.e., surge mode oscillation (SMO) at higher cavitation numbers, subsynchronous rotating cavitation (Sub-RC) at middle cavitation numbers, and deep cavitation surge (CS) at lower cavitation numbers. The nondimensional pressure amplitudes of the compo-

nent of each cavitation instability are shown in Figs. 9 and 10, and the nondimensional frequencies $f^* (=2\pi f/\Omega)$ of the pressure fluctuations are shown in Table 1.

Subsynchronous rotating cavitation appeared both in liquid nitrogen and in cold water. The nondimensional frequency of subsynchronous rotating cavitation was almost the same for water and for liquid nitrogen. The temperature difference between 76 K and 80 K in liquid nitrogen affected only the range in which the subsynchronous rotating cavitation appeared. The range of subsynchronous rotating cavitation at 80 K shifted to a lower cavitation number compared with that at 76 K in Fig. 10. The degree of this shift was the same as that of the cavity length. From these results, it was concluded that subsynchronous rotating cavitation is one type of the cavitation instability mainly depending on the cavity length. It is caused only by the critical growth of the cavity

Water 296 K, $Q/Q_d=1.06$, 7500 rpm



Liquid nitrogen 80 K, $Q/Q_d=1.05$, 18300 rpm

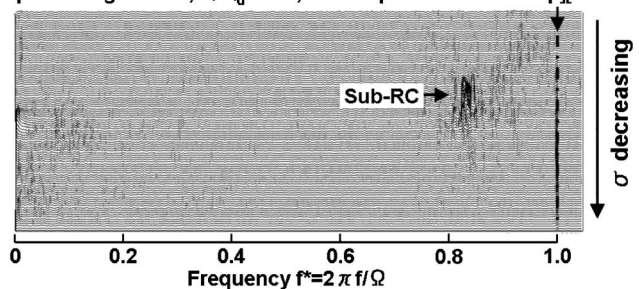


Fig. 11 FFT analyses of unsteady pressure fluctuation at Pos. 4 (upper: in water (296 K); lower: in liquid nitrogen (80 K)) (uncertainty in $f^*=2\pi f/\Omega=0.005$)

Table 1 Nondimensional frequency f^* of cavitation instability in liquid nitrogen and cold water

| Test conditions | Cavitation instability | Nondimensional frequency $f^* = 2\pi f / \Omega$ |
|-----------------------------------|------------------------|--|
| Nitrogen, 76 K $Q/Q_d = 1.05$ | Sub-RC ^b | 0.82–0.85 |
| Nitrogen, 80 K, $Q/Q_d = 1.05$ | Sub-RC | 0.82–0.84 |
| Water, 296 K, $Q/Q_d = 1.06$ | SMO ^a | 0.16 |
| | Sub-RC | 0.79–0.84 |
| | CS ^c | 0.12–0.14 |

^aSMO: Surge mode oscillation

^bSub-RC: Sub-synchronous rotating cavitation

^cCS: Cavitation surge

length as a type of flow instability.

To the contrary, slight surge mode oscillation at higher cavitation numbers and deep cavitation surge at lower cavitation numbers appeared only in cold water. Cavitation surge is a kind of system instability that depends on the pump gain and unsteady characteristics of cavitation, i.e., mass flow gain factor and cavitation compliance. The thermodynamic effect on cavitation instability will be discussed in the next chapter.

Discussions

Thermodynamic Effect. In this section, to examine the degree of the thermodynamic effect, i.e., the temperature depression $\Delta T (=T_\infty - T_c)$ between the liquid at infinity and the cavity bubble was estimated using the classical scaling rules by the same method employed in Franc's work [2].

First, the cavitation number σ is calculated from the vapor pressure at the liquid temperature at infinity T_∞ :

$$\sigma = \frac{p_{\text{ref}} - p_v(T_\infty)}{\frac{1}{2}\rho_l U^2} \quad (1)$$

Second, the cavitation number σ_c is calculated from the actual cavity pressure p_c equal to the vapor pressure at the actual temperature of the cavity T_c :

$$\sigma_c = \frac{p_{\text{ref}} - p_c}{\frac{1}{2}\rho_l U^2} = \frac{p_{\text{ref}} - p_v(T_c)}{\frac{1}{2}\rho_l U^2} \quad (2)$$

The temperature depression ΔT caused by the thermodynamic effect is obtained by Eqs. (1) and (2):

$$\frac{1}{2}\rho_l U^2(\sigma_c - \sigma) = \int_{T_c}^{T_\infty} \frac{dp_v}{dT} dT, \quad \Delta T = T_\infty - T_c \quad (3)$$

From Eq. (3), the temperature depression ΔT can be calculated from the difference of the cavitation numbers, $\sigma_c - \sigma$, of two corresponding conditions. The value σ_c is obtained from the experimental result without the thermodynamic effect (i.e., in cold water), while the value σ is obtained from the experimental result with the thermodynamic effect (i.e., in liquid nitrogen). In the present study, we assumed that the cavity length is a function of only cavitation number σ_c regardless of the type of fluid and focused on the cavity length of the tip cavitation as an indication of cavitation.

Figure 12 shows a comparison of the temperature depression ΔT in the cases of 76 K and 80 K versus the cavity length C_{cl} calculated by Eq. (3). In the calculation, the difference of the cavitation number of $\sigma - \sigma_c$ was calculated based on a given cavity length using the best-fit curves in Figs. 9 (in water) and 10 (in

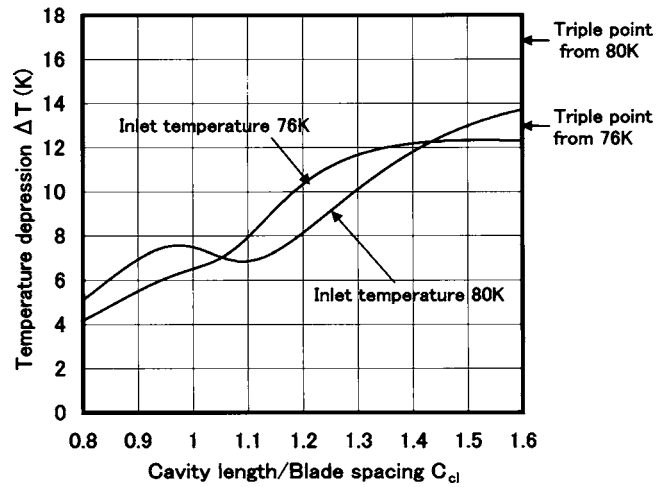


Fig. 12 Estimated temperature depression ΔT as a function of the cavity length C_{cl} (uncertainty in $C_{cl} = 0.03$)

liquid nitrogen). It is interesting that the temperature depression changes with the cavity length. The temperature depression is smaller when the cavity length C_{cl} is less than 1.0. The increase of the temperature depression stagnates at $C_{cl} \approx 1.0$, in particular, in the case of 80 K. When the cavity develops over the throat ($C_{cl} > 1.1$), the temperature depression increases again. After that ($C_{cl} > 1.3$), the slope of the temperature depression decreases gradually in the case of 76 K, and the temperature depression finally reaches a limit of 12 K. In this case, the estimated temperature in the cavity T_c is 64 K ($=T_\infty(76 \text{ K}) - \Delta T(12 \text{ K})$, i.e., $T^* = 0.01$), a value near the temperature of the triple point of nitrogen T_t (63.1 K, i.e., $T^* = 0.0$). On the contrary, the temperature depression increases gradually without limit in the case of 80 K with the increase of the cavity. The temperature depression is about 14 K at $C_{cl} = 1.6$. In this case, the estimated temperature in the cavity T_c is 66 K ($=T_\infty(80 \text{ K}) - \Delta T(14 \text{ K})$, i.e., $T^* = 0.05$). This value shows the margin between the temperature and the triple point of nitrogen T_t (63.1 K). From these results, it is concluded that the temperature of working fluid leads to this difference of the tendency of the temperature depression. The margin between the temperature of the fluid and that of the triple point in the case of 76 K is relatively smaller than that in the case of 80 K. This is the reason why the temperature depression in the case of 76 K is limited.

This result seems to be important with regard to the limitation of the thermodynamic effect for cryogenic fluid. Not only thermodynamic properties such as $\Sigma(T)$ and Λ but also the margin between the temperature of the fluid and that at the triple point need to be considered. Watanabe et al. [11] also came to the same conclusion based on the results of their theoretical analysis using the nonlinear effect of saturation characteristics.

Cavitation Instability. In this section, we discuss the thermodynamic effect on cavitation instability based on the measurements of cavity length. Figure 13 shows the range in which cavitation instability occurs by comparing the results in cold water (296 K) with those in liquid nitrogen (76 K and 80 K). One difference was the appearance of surge-type instability, which occurred only in cold water without the thermodynamic effect.

Regarding surge mode oscillation at higher cavitation numbers in water, the nondimensional frequency $f^* (=2\pi f / \Omega)$ was almost constant at $f^* = 0.16$. On the other hand, the nondimensional frequency of distinct subsynchronous rotating cavitation was about $f^* = 0.84$ both in water and in liquid nitrogen. The relation of these values in nondimensional frequency f^* is as follows:

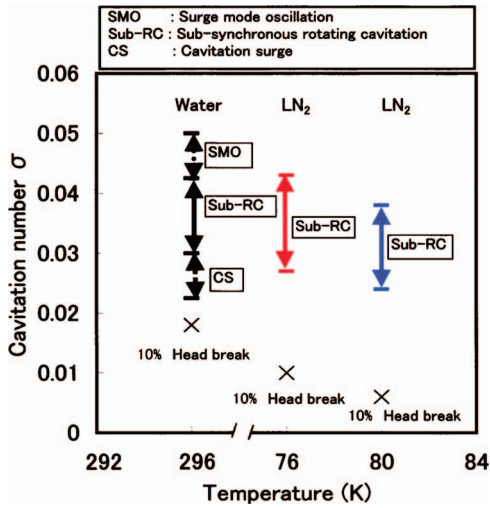


Fig. 13 Range of occurrence of cavitation instability in water (296 K) and liquid nitrogen (76 K and 80 K) (uncertainty in $\sigma = 0.001$)

$$0.16 \text{ (surge mode oscillation)} \\ + 0.84 \text{ (subsynchronous rotating cavitation)} \\ = 1.0 \text{ (rotation)} \quad (4)$$

In addition, based on his sophisticated analysis, Brennen [12] recently reported that there is an implied potential for instability involving the coupling of a basic mode with a frequency around $f^* = 0.9$ and a low frequency complementary mode of about $f^* = 0.1$. This relation is similar to above relation of Eq. (4). From these results, it seems that surge mode oscillation is instability similar to subsynchronous rotating cavitation (Yoshida et al. [13]). The nondimensional oscillating frequency of the cavity on a blade on the rotating coordinate was found to be $f^* = 0.16$ in both instabilities by FFT analysis of the pressure fluctuation. In the case of surge mode oscillation, there is no phase difference of cavity oscillation on the three blades. Thus, this oscillation is recognized as “surge mode” oscillation. In other words, it can be regarded as slight cavitation surge in the interblade. However, there is a phase difference of $-2\pi/3$ on each blade in subsynchronous rotating cavitation. Thus, this instability is recognized as “rotating” cavitation on the absolute coordinate, the propagating speed of which is slower than that of the shaft rotation. The difference between surge mode oscillation and subsynchronous rotating cavitation is estimated to be small except for the phase difference on each blade. Thus, “surge mode oscillation” and “subsynchronous rotating cavitation” are similar types of “fluid dynamic instability” with little dependence on the thermodynamic effect.

On the contrary, deep cavitation surge appeared at lower cavitation numbers ($\sigma = 0.022 - 0.030$) only in cold water, the oscillating frequency of which became smaller as the cavitation number decreased. Cavitation surge, well known as one type of cavitation instability, is expected to depend on the unsteady cavitation char-

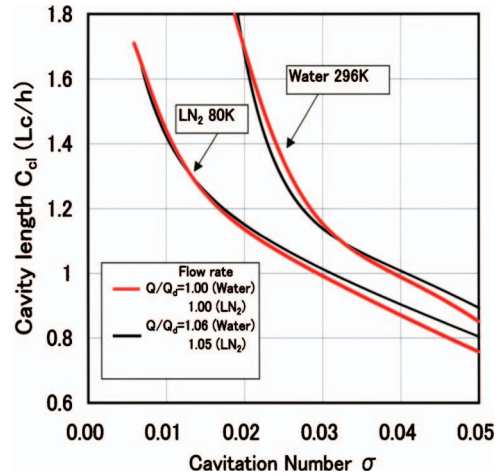


Fig. 15 Comparison of cavity lengths in liquid nitrogen (80 K, $Q/Q_d = 1.00, 1.05$) with those in water (296 K, $Q/Q_d = 1.00$ and 1.06) (uncertainty in $\sigma = 0.001$, $C_{cl} = 0.03$ (nitrogen), $C_{cl} = 0.03$ (water))

acteristics caused by the thermodynamic effect. Figure 14 shows the visualization within one period under the condition of the deep cavitation surge in cold water. Oscillation of the length of tip leakage cavitation is closely correlated with the oscillation of the vortex cavitation in backflow upstream of the inducer. Thus, the oscillation of the cavity length (L_c) can be recognized as an indication of the oscillation of total cavity volume (V_c). Figure 15 shows a comparison of the growth of the cavity length in cold water (296 K) with that in liquid nitrogen (80 K), both at flow rate $Q/Q_d = 1.00$ (from Yoshida et al. [4]) and 1.06 (1.05). In liquid nitrogen, the property of the cavity growth at flow rate $Q/Q_d = 1.00$ is almost the same as that at flow rate $Q/Q_d = 1.05$ except at higher cavitation numbers. In cold water, however, the cavity length at flow rate $Q/Q_d = 1.00$ is longer than that at flow rate $Q/Q_d = 1.06$ within a limited range of cavitation numbers $\sigma = 0.02 - 0.03$, in which the deep cavitation surge shown in Fig. 14 occurs only in cold water. From those tendencies, we can estimate that the quasisteady mass flow gain factor $M_q (= -\Delta V_c / \Delta Q)$ is positive, at least $\sigma = 0.020 - 0.030$, in cold water. The positive mass flow gain factor facilitates the onset of cavitation surge (Tsujiimoto et al. [14]). This is one of the reasons why a deep cavitation surge appears only in cold water. It is concluded that the thermodynamic effect has a strong influence on unsteady cavitation characteristics at lower cavitation numbers. In the present experiment, it was inferred that the thermodynamic effect decreased the mass flow gain factor in liquid nitrogen and suppressed the deep cavitation surge at lower cavitation numbers.

In addition, Watanabe et al. [15] analyzed the thermodynamic effect on unsteady cavitation characteristics of inducers, such as cavitation compliance and mass flow gain factor. They found that the growth rate of cavitation compliance and mass flow gain factor against the reduction of cavitation number decreases rapidly

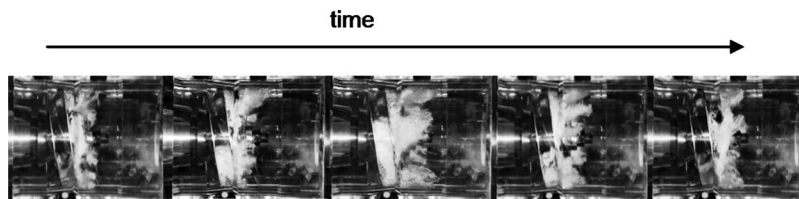


Fig. 14 Photograph under the condition of deep cavitation surge at lower cavitation numbers in cold water (296 K)

under the strong thermodynamic effect. In addition, the thermodynamic effect on unsteady cavitation characteristics becomes significant when the cavity extends over the throat of the blade passage. This analysis well explains the experimental tendencies of the “thermal damping effect” on deep cavitation surge, which we observed.

Conclusions

To obtain a fundamental understanding of the thermodynamic effect with regard to cavitation performance and cavitation instabilities, the cavity length of the tip cavitation as a cavitation indicator was examined in cold water (296 K) and liquid nitrogen at two temperatures (76 K and 80 K). The following points were clarified.

- (1) It was found that the thermodynamic effect depends on the cavity length. The temperature depression due to vaporization is considerably small when the cavity length is before the throat of the blade passage.
- (2) When the cavity extends over the throat of the blade passage, the temperature depression increases considerably. The temperature depression, however, is limited when the temperature in the cavity nearly reaches the temperature of the triple point in liquid nitrogen. It was inferred that the small margin between the temperature and that of the triple point in the cryogenic fluid, i.e., like liquid nitrogen, results in a limitation of the degree of the thermodynamic effect.
- (3) Deep cavitation surge occurred at lower cavitation numbers only in cold water, in which case the thermodynamic effect can be disregarded.
- (4) From the examination of cavity length, the estimated quasisteady mass flow gain factor, one of the unsteady cavitation characteristics, was positive in a narrow range of cavitation numbers at which deep cavitation surge appeared in water. In contrast, the estimated quasisteady mass flow gain factor in liquid nitrogen was not positive in the same range of cavity length.
- (5) It was inferred that the thermodynamic effect decreases the mass flow gain factor at lower cavitation numbers when the cavity extends over the throat and that its influence suppresses deep cavitation surge as a thermal damping effect in liquid nitrogen.

Acknowledgment

The authors would like to thank Mr. Yoshinobu YASUTOMI of IHI Corporation, who made many valuable suggestions to the test inducer.

Nomenclature

| | |
|-----------|---|
| C | = chord of blade |
| C_{cl} | = cavity length/blade spacing= L_c/h |
| C_{pl} | = liquid heat capacity |
| D | = characteristics diameter of inducer or characteristics length |
| f | = oscillating frequency |
| f^* | = nondimensional oscillating frequency= $2\pi f/\Omega$ |
| h | = blade spacing |
| L | = latent heat of vaporization |
| L_c | = cavity length |
| M_q | = quasisteady mass flow gain factor= $-\Delta V_c/\Delta Q$ |
| p_c | = cavity pressure |
| p_{ref} | = reference pressure |
| p_v | = vapor pressure |
| Q | = flow rate |

| | |
|-------------|---|
| Q_d | = design flow rate |
| Re | = Reynolds number= UD/ν |
| $S(C_{cl})$ | = standard deviation |
| T_c | = cavity temperature or temperature of critical point |
| T_l | = temperature of triple point |
| T_∞ | = temperature at infinity |
| ΔT | = temperature depression |
| T^* | = nondimensional temperature= $(T-T_l)/(T_c-T_l)$ |
| U | = peripheral speed of inducer tip or main flow velocity |
| V | = main flow velocity |
| V_c | = cavity volume |
| V_l | = volume flow rate of liquid |
| V_v | = volume flow rate of vapor |
| α_l | = thermal diffusivity of liquid |
| ν | = kinematic viscosity |
| ρ_l | = liquid density |
| ρ_v | = vapor density |
| Λ | = dynamic fluid parameter |
| $\Sigma(T)$ | = thermodynamic function |
| σ | = cavitation number |
| τ | = torque |
| τ_o | = normal torque |
| ψ | = inducer head coefficient |
| ψ_o | = normal inducer head coefficient |
| Ω | = shaft rotational angular speed |

References

- [1] Stahl, H. A., and Stepanoff, A. J., 1956, “Thermodynamic Aspects of Cavitation in Centrifugal Pumps,” *ASME J. Basic Eng.*, **78**, pp. 1691–1693.
- [2] Franc, J. P., Rebattet, C., and Coulon, A., 2004, “An Experimental Investigation of Thermal Effect in a Cavitating Inducer,” *ASME J. Fluids Eng.*, **126**, pp. 716–723.
- [3] Cervone, A., Testa, R., and d’Agostino, L., 2005, “Thermal Effects on Cavitation Instabilities in Helical Inducers,” *J. Propul. Power*, **21**, pp. 893–899.
- [4] Yoshida, Y., Kikuta, K., Hasegawa, S., Shimagaki, M., and Tokumasu, T., 2007, “Thermodynamic Effect on a Cavitating Inducer in Liquid Nitrogen,” *ASME J. Fluids Eng.*, **129**, pp. 273–278.
- [5] Yoshida, Y., Tsujimoto, Y., Kamijo, K., and Maekawa, Y., 1997, “Unsteady Interblade Pressure Distributions and Fluid Forces Under Rotating Cavitation,” *Proceeding of the Fifth Asian International Conference on Fluid Machinery*, Seoul, Korea, Oct. 6–8, pp. 457–464.
- [6] Shimagaki, M., Watanabe, M., Hashimoto, T., Hasegawa, S., Yoshida, Y., and Nakumara, N., 2005, “Effect of the Casing Configurations on the Internal Flow in Rocket Pump Inducer,” *42nd Joint Propulsion Conference and Exhibit*, Jul. 9–12, Sacramento, CA AIAA-2006-5071.
- [7] Yoshida, Y., Watanabe, M., Hashimoto, H., Shimagaki, M., Yamada, H., and Shimura, T., 2005, “Cryogenic Inducer Test Facility in JAXA,” *Turbomachinery (in Japanese)*, **33**, pp. 468–475.
- [8] Brennen, C. E., 1973, “The Dynamic Behavior and Compliance of a Stream of Cavitating Bubbles,” *ASME J. Fluids Eng.*, **95**, pp. 533–541.
- [9] Kato, H., 1984, “Thermodynamic Effect on Incipient and Development of Sheet Cavitation,” *Proceedings of International Symposium on Cavitation Inception*, New Orleans, LA, Dec. 9–14, ASME FED. 16, pp. 127–136.
- [10] Watanabe, S., Hidaka, T., Horiguchi, H., Furukawa, A., and Tsujimoto, Y., 2007, “Steady Analysis of Thermodynamic Effect of Partial Cavitation Using The Singularity Method,” *ASME J. Fluids Eng.*, **129**, pp. 121–127.
- [11] Watanabe, S., Furukawa, A., and Yoshida, Y., 2008, “Theoretical Analysis of Thermodynamic Effect of Cavitation in Cryogenic Inducer Using Singular Method,” *Proceedings of the 12th International Symposium on Transport Phenomena and Dynamics of Rotating Machinery*, Honolulu, Hawaii, Feb. 17–22, ISROMAC12-2008-20251.
- [12] Brennen, C. E., 2006, “Multifrequency Instability of Cavitating Inducers,” *ASME J. Fluids Eng.*, **129**, pp. 731–736.
- [13] Yoshida, Y., Hashimoto, T., Shimagaki, M., and Watanabe, S., 2006, “An Overview of Sub-Synchronous Rotating Cavitation,” *Turbomachinery (in Japanese)*, **34**, pp. 168–180.
- [14] Tsujimoto, Y., Kamijo, K., and Brennen, C. E., 2001, “Unified Treatment of Flow Instabilities of Turbomachines,” *J. Propul. Power*, **17**, pp. 893–899.
- [15] Watanabe, S., Furukawa, A., and Yoshida, Y., 2006, “Theoretical Analysis of Thermodynamic Effect on Cavitation Characteristics of Inducer,” *Proceedings JSME Fluids Engineering Conference*, Kawagoe, Japan, Oct., Paper No. G703.

On the Preliminary Design and Noncavitating Performance Prediction of Tapered Axial Inducers

Luca d'Agostino

Professor
Department of Aerospace Engineering,
University of Pisa,
Via G. Caruso,
56100 Pisa, Italy
e-mail: luca.dagostino@ing.unipi.it

Lucio Torre

Project Manager
e-mail: l.torre@alta-space.com

Angelo Pasini

Ph.D. Student
e-mail: a.pasini@alta-space.com

Angelo Cervone

Senior Engineer
e-mail: a.cervone@alta-space.com

Alta S.p.A.,
Via Gherardesca 5,
56121 Pisa, Italy

A reduced order model for preliminary design and noncavitating performance prediction of tapered axial inducers is illustrated. In the incompressible, inviscid, irrotational flow approximation, the model expresses the 3D flow field in the blade channels by superposing a 2D cross-sectional vorticity correction to a fully guided axisymmetric flow with radially uniform axial velocity. Suitable redefinition of the diffusion factor for bladings with non-negligible radial flow allows for the control of the blade loading and the estimate of the boundary layer blockage at the specified design flow coefficient, providing a simple criterion for matching the hub profile to the axial variation of the blade pitch angle. Carter's rule is employed to account for flow deviation at the inducer trailing edge. Mass continuity, angular momentum conservation, and Euler's equation are used to derive a simple second order boundary value problem, whose numerical solution describes the far-field axisymmetric flow at the inducer discharge. A closed form approximate solution is also provided, which proved to yield equivalently accurate results in the prediction of the inducer performance. Finally, the noncavitating pumping characteristic is obtained by introducing suitably adapted correlations of pressure losses and flow deviation effects. The model has been verified to closely approximate the geometry and noncavitating performance of two space inducers tested in Alta's Cavitating Pump Rotordynamic Test Facility, as well as the measured pumping characteristics of a number of tapered-hub inducers documented in the literature. [DOI: 10.1115/1.2979007]

1 Introduction

Current rocket propellant feed turbopumps often employ an inducer upstream of the centrifugal stage in order to avoid unacceptable cavitation, improve the suction performance, and reduce the propellant tank pressure and weight. The main purpose of inducers consists in sufficiently pressurizing the flow for the main pump to operate satisfactorily. Compared with centrifugal pump impellers, typical inducers have fewer blades (usually 3 or 4), lower flow coefficients (from 0.05 to 0.1), larger stagger angles (70–85 deg), and significantly higher blade solidities (between 1.5 and 2.5). Long blades with small angles of attack provide ample time and room for the collapse of the cavitation bubbles and for the gradual exchange of energy with the flow. The resulting configuration, even though beneficial from the standpoint of cavitation performance, results in relatively low values of the inducer efficiency due to the highly viscous, turbulent, and dissipative flow inside the blade passages.

The development of three-dimensional (3D) theoretical models capable of rapidly predicting the performance of axial inducers in order to provide indications for the preliminary design of the machine is of particular interest to rocket engineers. However, not many such models have been proposed so far, probably due to the difficulty of adequately describing the 3D flow field inside the inducer blades. Therefore, designers often refer to simple “rules of thumb” or to the general indications of design manuals, such as the one published by NASA [1]. In the past decades, numerical simulation of the complex 3D features of inducer flows has

emerged has a promising tool for design validation and refinement (see, for example, Refs. [2,3]), but its use in the early stages of design still remains impractical.

A number of two-dimensional (2D) reduced order models for the prediction of the noncavitating flow in turbopump inducers are illustrated by Brennen [4,5]. These models are based on linear and radial cascade analyses with semi-empirical inclusion of flow deviation and viscous effects. Three-dimensional corrections for inlet flow prerotation, tip leakage, and discharge flow are also indicated.

A second class of models has been aimed at the prediction of the effects of cavitation on inducer performance [6–8]. These models are essentially two dimensional, where cavitation is assimilated to a vapor layer on the blade or a mixture of bubbles and liquid. Early studies opened the way to a number of more recent analyses capable of better understanding and predicting the major flow instabilities affecting cavitating inducers [9–14].

Some earlier analyses of single and two phase flows in inducers have been carried out, among others, by Cooper [15]. More recently, Lakshminarayana [16] addressed the problem of performance prediction of noncavitating inducers by the combined use of a simplified radial equilibrium analysis and the Euler equation. Viscous effects are taken into account through an empirical loss coefficient deduced from the reported performance of inducers documented in the literature. Indications on the effects of solidity and number of blades are also provided.

In 2007, Bramanti et al. [17] developed at Alta S.p.A. a simplified model based on the traditional throughflow theory approximations with empirical corrections for incidence, friction, and deviation losses of the flow through the inducer blades. The model proved to be in good agreement with the reported performance of several inducers tested in different facilities worldwide and represented the basis for the development of the work illustrated in this paper.

Contributed by the Fluids Engineering Division of ASME for publication in the JOURNAL OF FLUIDS ENGINEERING. Manuscript received February 5, 2008; final manuscript received July 10, 2008; published online September 23, 2008. Assoc. Editor: Chunill Hah.

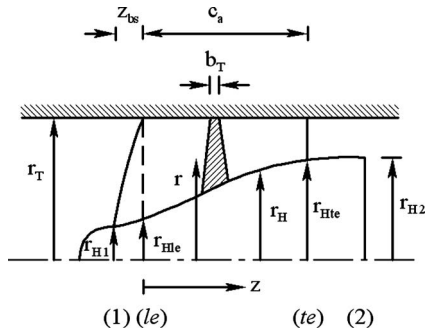


Fig. 1 Inducer schematic and nomenclature

The present model is based on the incompressible, inviscid, irrotational flow approximation, where the 3D velocity field inside the blade channels is expressed as the superposition of a fully guided axisymmetric flow with radially uniform axial velocity and a 2D cross-sectional vorticity correction. Boundary layer blockage is estimated by means of a suitable redefinition of the diffusion factor for bladings with non-negligible radial flow and Carter's rule is used to account for flow deviation at the inducer trailing edge. Performance losses are evaluated by adding suitably adapted correlations of turbulent duct losses to the inlet flow incidence losses. Model validation has been carried out against the experimental data obtained from two space inducers tested in the Cavitating Pump Rotodynamic Test Facility at Alta S.p.A., as well as from a number of inducers documented in the open literature.

2 Inducer Flow and Geometry

2.1 Flow Velocity. The incompressible, inviscid, irrotational flow through a helical inducer with N radial blades, rotational speed Ω , constant tip radius r_T , tapered-hub radius r_H , variable axial pitch P , and blade angle γ (as schematically shown in Fig. 1) is held by the equations

$$\nabla \cdot \mathbf{u} = 0$$

$$\nabla \times \mathbf{u} = 0$$

The relatively large value of the blade solidity typical of inducers designed for controlling cavitation in highly loaded turbopumps suggests that near design conditions ($\Phi \cong \Phi_D$), the 3D velocity \mathbf{u} in the blade channels can be approximated by the superposition of a fully guided axisymmetric flow $\hat{\mathbf{u}}$ with radially uniform axial velocity component \hat{w} and a 2D cross-sectional slip velocity correction $\tilde{\mathbf{u}}$ (Fig. 2):

$$\mathbf{u} = \hat{\mathbf{u}} + \tilde{\mathbf{u}}$$

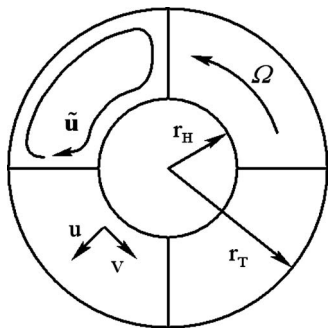


Fig. 2 Schematic of the 2D cross-sectional slip velocity correction in the inducer blade channels

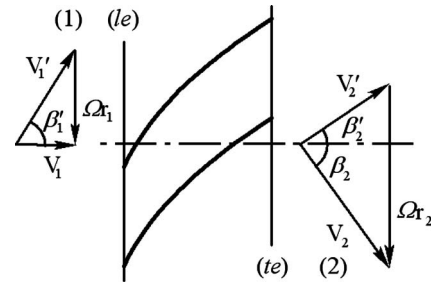


Fig. 3 Velocity triangles

With reference to the velocity triangles of Fig. 3, for radial helical blades,

$$\tan \gamma = \frac{2\pi r}{P} \Rightarrow \begin{cases} \hat{v} = \Omega r - \hat{w} \tan \gamma = \Omega r - 2\pi r \frac{\hat{w}}{P} \\ \hat{w} = \frac{\dot{m}}{\rho \pi (r_T^2 - r_H^2) B} = \frac{\Phi \Omega r_T^3}{(r_T^2 - r_H^2) B} \end{cases}$$

where $0 \leq B \leq 1$ is the average cross-sectional blockage due to the boundary layer displacement effects and, if significant, to blade thickness. The 2D slip velocity components are most synthetically expressed and solved for in terms of a scalar stream function $\psi(r', \vartheta')$ in the rotating cylindrical coordinates $r' = r$, $\vartheta' = \vartheta - \Omega t$, and $z' = z$:

$$\tilde{u} = \frac{1}{r'} \frac{\partial \psi}{\partial \vartheta'} \quad \text{and} \quad \tilde{v} = -\frac{\partial \psi}{\partial r'}$$

2.2 Inducer Tip and Hub Radius. Substitution of the assumed velocity field in the expressions of the incompressibility and irrotationality conditions in cylindrical coordinates r, ϑ, z yields

$$\frac{\partial(r\hat{u})}{\partial r} = -r \frac{d\hat{w}}{dz}$$

$$\frac{d}{dz} \left(\frac{\hat{w}}{P} \right) = 0$$

$$\frac{d^2 \hat{w}}{dz^2} = 0$$

$$\frac{1}{r} \frac{\partial}{\partial r} \left(r \frac{\partial \psi}{\partial r} \right) + \frac{1}{r^2} \frac{\partial^2 \psi}{\partial \vartheta'^2} = 2\Omega - 4\pi \frac{\hat{w}}{P}$$

Integration of $d^2 \hat{w} / dz^2 = 0$ with the boundary conditions $\hat{w}(0) = \hat{w}_{le}$ and $\hat{w}(c_a) = \hat{w}_{te}$ at the axial locations bounding the full-height portion of the blades (indices le and te) yields

$$\frac{d\hat{w}}{dz} = \frac{\hat{w}_{te} - \hat{w}_{le}}{c_a} \equiv \text{const}$$

and the following expression for the axial velocity:

$$\hat{w} = \hat{w}_{le} + (\hat{w}_{te} - \hat{w}_{le}) \frac{z}{c_a}$$

Similarly, by integrating the continuity equation with the impermeability condition $\hat{u}(r_T) = 0$ at the tip radius, the following expression for the radial velocity is obtained:

$$\hat{u} = \frac{1}{2} \frac{d\hat{w}}{dz} \left(\frac{r_T^2}{r} - r \right)$$

Finally, by evaluating \hat{w} at design conditions (index D) by means of the continuity equation and integrating $d(\hat{w}/P)/dz = 0$

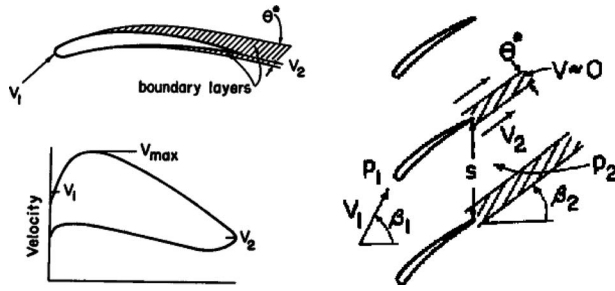


Fig. 4 Nomenclature for blade boundary layer (left) and linear cascade (right)

with $P(w_{leD}) = P_{Tlc}$ at $z=0$, the following expressions for matching the axial changes of the hub radius r_H and blade pitch P are obtained:

$$\frac{1}{(r_T^2 - r_H^2)B} = \frac{1}{(r_T^2 - r_{Hlc}^2)B_{lc}} + \left[\frac{1}{(r_T^2 - r_{Hlc}^2)B_{lc}} - \frac{1}{(r_T^2 - r_{Hle}^2)B_{lc}} \right] \frac{z}{c_a}$$

$$P = P_{Tlc} \frac{\hat{w}_D}{\hat{w}_{leD}} = P_{Tlc} + P'z$$

where

$$P' = \left[\frac{(r_T^2 - r_{Hlc}^2)B_{lc}}{(r_T^2 - r_{Hle}^2)B_{lc}} - 1 \right] \frac{P_{Tlc}}{c_a}$$

and a linear axial variation of the blockage

$$B = B_{lc} + (B_{te} - B_{lc}) \frac{z}{c_a}$$

can be approximately assumed inside the blade passages from the leading edge station (le), where $B=B_{lc} \cong 1$, to the trailing edge (te), where $B=B_{te}$. The assumption of no leading edge blockage implies zero blade thickness, no leading edge separation, and zero initial boundary layer thickness. Given the relative magnitudes of blade and boundary layer thicknesses and the level of accuracy of the present model, these effects can be considered of second order and therefore have not been taken into account.

2.3 Slip Flow. Finally, on each channel cross section, Poisson's equation for the stream function can be conformally mapped in a rectangular domain and integrated by standard methods [18] with the condition $\psi=0$ on the boundary to

$$\psi = - \sum_{m=1}^{+\infty} \sum_{n=1}^{+\infty} C_{m,n} \sin \left[m\pi \frac{\ln(r/r_H)}{\ln(r_T/r_H)} \right] \sin \frac{(2n-1)N\theta'}{2}$$

where

$$C_{m,n} = \frac{A_{m,n}}{m^2 \pi^2 / \ln^2(r_T/r_H) + (n - \frac{1}{2})^2 N^2}$$

$$A_{m,n} = Kr_H^2 \frac{m(n - \frac{1}{2}) \ln^2(r_T/r_H)}{1 + m^2 \pi^2 / 4 \ln^2(r_T/r_H)} \left[1 - (-1)^m \frac{r_T^2}{r_H^2} \right]$$

and

$$K = 2\Omega - 4\pi \frac{\hat{w}}{P} = 2\Omega \left[1 - \frac{2\pi \Phi r_T^3}{P(r_T^2 - r_H^2)} \right]$$

from which the radial and tangential slip velocity components \tilde{u} and \tilde{v} are readily computed.

2.4 Blade Loading and Boundary Layer Blockage. With reference to Fig. 4, suitable redefinition of the diffusion factor for axial bladings [19]

$$D = \frac{V_1' - V_2'}{V_1'} + \frac{|v_2 - v_1|}{2\sigma V_1'} \cong \frac{p_2 - p_1}{\frac{1}{2}\rho V_1'(V_1' + V_2')} + \frac{P_{r2} - P_{r1}}{\sigma \rho \Omega (r_1 + r_2) V_1'}$$

to the case of tapered inducers with non-negligible radial flow allows for the control of the blade loading (a crucial design aspect under cavitating conditions) and the estimate of the boundary layer blockage at nominal flow conditions.

By evaluating

$$p_2 - p_1 = \frac{1}{2}\rho(V_1'^2 - V_2'^2) - \frac{1}{2}\rho\Omega^2(r_1^2 - r_2^2)$$

$$P_{r2} - P_{r1} = \rho\Omega(r_2 v_2 - r_1 v_1)$$

with Bernoulli's and Euler's equations for mixed-flow bladings and substituting in the above expression for D obtains

$$D \cong \frac{V_1' - V_2'}{V_1'} - \frac{\Omega^2(r_1^2 - r_2^2)}{V_1'(V_1' + V_2')} + \frac{r_2 v_2 - r_1 v_1}{\sigma(r_1 + r_2)V_1'}$$

Here all relevant properties including the solidity $\sigma=c/s$ are evaluated on the mean streamline:

$$r = r_M = \sqrt{\frac{r_T^2 + r_H^2}{2}}$$

and, for flow with no inlet prerotation and fully guided at the inducer outlet ($v_1 \cong 0$ and $v_2' \cong w_{te} \tan \gamma_{te}$), the relative velocities are expressed by

$$v_1' = \sqrt{w_1^2 + V_1'^2} = \sqrt{\left(\frac{\Phi_D \Omega r_T^3}{r_T^2 - r_{Hlc}^2} \right)^2 + \Omega^2 r^2}$$

$$v_2' = \sqrt{w_2^2 + V_2'^2} \cong \frac{\Phi_D \Omega r_T^3}{(r_T^2 - r_{H2}^2) \cos \gamma_{te}}$$

As illustrated in Fig. 5, in turbulent boundary layers over blade

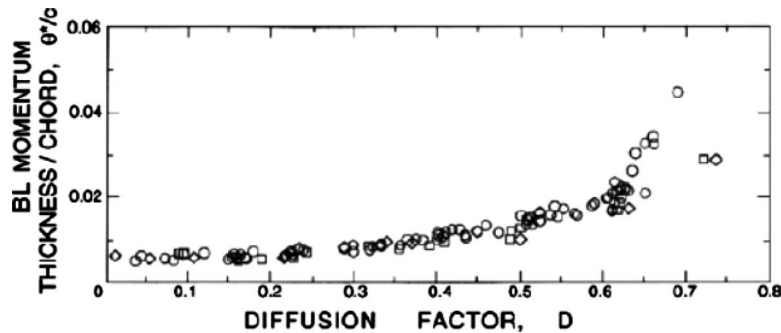


Fig. 5 Ratio of the momentum thickness θ' of the blade boundary layer to the chord c as a function of the diffusion factor D , for axial cascades with three different profiles (adapted from Brennen [4]).

cascades, the diffusion factor is directly correlated with the momentum thickness θ^* [20,4]:

$$\frac{\theta^*}{c} = f(D)$$

Furthermore, by using the Prandtl equations for the turbulent boundary layer velocity profile on a flat plate [24], it is possible to show that the displacement thickness is given by $\delta^* \cong 9/7\theta^* \cong 1.3\theta^*$. With these results, the blade boundary layer blockage at the inducer trailing edge is computed as

$$B_{te} = 1 - \frac{2\delta^*}{s_{te} \cos \gamma_{te}}$$

(Fig. 4), where the blade spacing $s_{te} = 2\pi r_{te}/N$ is evaluated at the mean radius.

2.5 Mean Radius, Chord, and Solidity. On a relative streamline of the fully guided flow,

$$\frac{dr}{u'} = \frac{rd\vartheta'}{\hat{v}'} = \frac{dz}{\hat{w}'}$$

where from earlier results,

$$\hat{u}' = \hat{u} = \frac{1}{2}P' \frac{\hat{w}_{te}}{P_{Te}} \left(\frac{r_T^2}{r} - r \right)$$

$$\hat{v}' = \Omega r - \hat{v} = 2\pi r \frac{\hat{w}_{te}}{P_{Te}}$$

$$\hat{w}' = \hat{w} = \frac{\hat{w}_{te}}{P_{Te}} (P_{Te} + P'z)$$

Hence, integrating with initial conditions $r_{Mle}, \vartheta'_{Mle}, z_{Mle}$, the equations of the mean streamline are

$$r_M = \sqrt{r_T^2 - (r_T^2 - r_{le}^2) \frac{P_{Te} + P'z_{Mle}}{P_{Te} + P'z_M}}$$

$$\vartheta'_M = \vartheta'_{Mle} + \frac{2\pi}{P'} \ln \frac{P_{Te} + P'z_M}{P_{Te} + P'z_{Mle}}$$

The mean values of the blade chord and solidity are then evaluated as

$$c = \int_{z_{Mle}}^{c_a} dz_M \sqrt{\left(\frac{\partial r_M}{\partial z_M} \right)^2 + \left(r_M \frac{\partial \vartheta'_M}{\partial z_M} \right)^2 + 1}$$

$$\sigma = \int_{z_{Mle}}^{c_a} \frac{dc}{s_M} = \int_0^{c_a} \frac{dz_M}{2\pi r_M/N} \sqrt{\left(\frac{\partial r_M}{\partial z_M} \right)^2 + \left(r_M \frac{\partial \vartheta'_M}{\partial z_M} \right)^2 + 1}$$

2.6 Flow Pressure in the Blade Channels. The pressure of the (absolutely) irrotational flow in the blade channels can readily be obtained by straightforward integration of steady Bernoulli's equation in the reference frame r, ϑ', z rotating with the inducer:

$$\nabla \left(\frac{p}{\rho} + \frac{1}{2} \mathbf{u}' \cdot \mathbf{u}' - \frac{1}{2} \Omega^2 \mathbf{r} \cdot \mathbf{r} \right) = \mathbf{u}' \times (\nabla \times \mathbf{u}') = 0$$

where the same integration constant

$$C = p_1 + \frac{1}{2} \rho w_1^2$$

applies over the entire flow field, and the velocity \mathbf{u}' is expressed by

$$\mathbf{u}' = \mathbf{u} - \Omega \times \mathbf{r} = \mathbf{u} - \Omega r e_\vartheta$$

Therefore, with earlier notations,

$$\mathbf{u}' \cdot \mathbf{u}' = (\hat{u} + \tilde{u})^2 + (\hat{v} + \tilde{v} - \Omega r)^2 + \hat{w}^2$$

and, solving for the flow pressure at the generic location in the blade channels,

$$p = p_1 + \frac{1}{2} \rho [w_1^2 - (\hat{u} + \tilde{u})^2 - (\hat{v} + \tilde{v})^2 + 2(\hat{v} + \tilde{v})\Omega r - \hat{w}^2]$$

3 Inducer Performance Modeling

3.1 Discharge Flow. No inlet flow prerotation is assumed, thus implicitly referring for the application of Euler equation to a control volume extending in the upstream direction down to the region of unswirled flow in the inducer suction line. This approach only neglects the torque of shear forces on the inner surfaces of the inlet line and therefore in the present inviscid flow approximation correctly estimates the power exerted by the inducer on the flow.

In the assumption of uniform inlet flow to the inducer with no prerotation ($v_1=0$), radial differentiation of the incompressible isentropic Euler equation

$$\frac{p_2}{\rho} + \frac{1}{2}(v_2^2 + w_2^2) - \frac{p_1}{\rho} - \frac{1}{2}(v_1^2 + w_1^2) = \Omega(r_2 v_2 - r_1 v_1)$$

for the axisymmetric flow at sections (1) and (2) of Fig. 1 and elimination of the pressure by means of the radial equilibrium condition

$$\frac{v^2}{r} = \frac{1}{\rho} \frac{\partial p}{\partial r}$$

yield the following ordinary differential equation (ODE) for the axial and tangential velocity profiles $w_2(r_2)$ and $v_2(r_2)$ at the inducer discharge section

$$\frac{1}{2} \frac{dw_2^2}{dr_2} + \left(\frac{v_2}{r_2} - \Omega \right) \frac{d(r_2 v_2)}{dr_2} = 0$$

In order to solve the above equation for the axial velocity profile, it is necessary to establish a correlation between w_2 and the azimuthal velocity v_2 . To this purpose, the fully guided flow with uniform axial velocity and slip vorticity correction at the inducer trailing edge (station te)

$$u_{te} = \tilde{u}_{te}$$

$$v_{te} = \Omega r_{te} - w_{te} \frac{r_{te}}{r_T} \tan \gamma_{Te} + \tilde{v}_{te}$$

$$w_{te} = \frac{\Phi \Omega r_T^3}{r_T^2 - r_{He}^2}$$

is assumed to mix into an axisymmetric swirled axial flow with velocities v_2 and w_2 at the discharge section (station 2), while satisfying mass continuity and, in the absence of wall friction, conserving the axial component of angular momentum:

$$2\pi w_2 r_2 dr_2 = 2\pi w_{te} r_{te} dr_{te}$$

$$2\pi w_2 v_2 r_2^2 dr_2 = w_{te} r_{te}^2 dr_{te} \int_0^{2\pi} v_{te} d\vartheta'$$

Integration of the second equation with earlier expressions of v_{te} and \tilde{v}_{te} yields

$$v_2 = \frac{r_{te}}{r_2} \left[\Omega r_{te} - w_{te} \frac{r_{te}}{r_T} \tan \gamma_{Te} + \tilde{v}_s(r_{te}) \right]$$

where

$$\tilde{v}_s(r_{te}) = \frac{1}{r_{te}} \sum_{m=1}^{+\infty} \sum_{n=1}^{+\infty} \frac{mC_{m,n}}{(n-\frac{1}{2})\ln(r_T/r_H)} \cos \left[m\pi \frac{\ln(r_{te}/r_{Hte})}{\ln(r_T/r_H)} \right]$$

Finally, substitution in the ODE for the axial velocity profile, where from the mass balance,

$$\frac{d}{dr_2} = \frac{dr_{te}}{dr_2} \frac{d}{dr_{te}} = \frac{w_2 r_2}{w_{te} r_{te}} \frac{d}{dr_{te}} \quad \text{and} \quad \frac{dr_{te}^2}{dr_2^2} = \frac{w_2}{w_{te}}$$

results in the following boundary value problem (BVP) for w_2 and r_{te} as functions of r_2^2 :

$$\begin{aligned} \frac{dw_2}{dr_2^2} &= \frac{1}{2w_{te}} \left[\Omega - \left(\Omega - \frac{w_{te}}{r_T} \tan \gamma_{Tte} + \frac{\tilde{v}_s(r_{te})}{r_{te}} \right) \frac{r_{te}^2}{r_2^2} \right] \\ &\times \left\{ 2\Omega - 2 \frac{w_{te}}{r_T} \tan \gamma_{Tte} + \frac{1}{r_{te}} \frac{d}{dr_{te}} [r_{te} \tilde{v}_s(r_{te})] \right\} \\ \frac{dr_{te}^2}{dr_2^2} &= \frac{w_2}{w_{te}} \end{aligned}$$

The above problem can then be solved by numerical shooting from r_{H2}^2 to r_T^2 with initial conditions:

$$w_2(r_{H2}^2) = w_{H2} \quad \text{and} \quad r_{te}^2(r_{H2}^2) = r_{Hte}^2$$

iterating on the assumed value of w_{H2} until the final boundary condition $r_{te}^2(r_T^2) = r_T^2$ is satisfied.

A closed form approximation of the axial velocity profile $w_2(r_2)$ can also be obtained by assuming $r_{te} \cong r_2$ in the expression of v_2 and neglecting \tilde{v}_s in

$$\frac{v_2}{r_2} - \Omega = - \frac{w_2}{r_T} \tan \gamma_{T2} + \frac{\tilde{v}_s}{r_2} \cong - \frac{w_2}{r_T} \tan \gamma_{T2}$$

Then the ODE for the axial velocity profile becomes

$$\frac{dw_2}{dr_2} - \frac{1}{r_T} \tan \gamma_{T2} \frac{d(r_2 v_2)}{dr_2} = 0$$

whose closed form solution (MOD) is

$$w_2(r_2) = \frac{[\Omega r_2 + \tilde{v}_s(r_2)](r_2/r_T) \tan \gamma_{T2} + c}{1 + (r_2^2/r_T^2) \tan^2 \gamma_{T2}}$$

with the integration constant c determined by the mass balance between the inlet and discharge cross sections:

$$\int_{r_{H2}}^{r_T} w_2 2\pi r_2 dr_2 = \int_{r_{H1}}^{r_T} w_1 2\pi r_1 dr_1$$

3.2 Flow Losses. The assumptions of inviscid flow fully guided at the inducer trailing edge are not accurately satisfied in practice. In order to better approximate the actual pumping characteristic of noncavitating inducers, the main sources of performance degradation (flow incidence, friction, and deviation) have to be accounted for.

Friction losses in the blade channels are evaluated by means of standard correlations for turbulent duct flows:

$$\Delta p_{\text{friction}} = f \frac{L_{\text{ch}}}{D_{\text{ch}}} \frac{1}{2} \rho V_1'^2$$

where the friction factor f depends on the Reynolds number based on the hydraulic diameter D_{ch} of the blade channels, L_{ch} is the effective channel length evaluated along the mean streamline, and V_1' is the relative flow velocity at the mean inlet radius.

Incidence losses due to the sudden change of the flow direction at the leading edge of the inducer blades are expressed in terms of a nondimensional equivalent length $L_{\text{eq}}/D_{\text{ch}}$, function of the incidence angle evaluated on the mean streamline. Hence, the overall pressure losses can be written as follows:

$$\Delta p_{\text{loss}} = f \left(\frac{L_{\text{ch}}}{D_{\text{ch}}} + \frac{L_{\text{eq}}}{D_{\text{ch}}} \right) \frac{1}{2} \rho V_1'^2$$

3.3 Flow Deviation. The mean value of the exit flow deviation is evaluated at the mean radius using Carter's correlation

$$\delta^\circ \cong \frac{m_C}{\sqrt{\sigma}} (\gamma_{te} - \gamma_{te})$$

and applied to correct the discharge flow direction at all radii in the inducer annulus. In order to better match the experimental data, the standard correlation for the coefficient m_C has been slightly modified according to the equation

$$m_C \cong 1.22 \left[0.23 \left(\frac{2a}{c} \right)^2 + 0.1 \left(\frac{\gamma_{te}}{50 \text{ deg}} \right) \right]$$

where $a \cong c/2$ is the relative position of the maximum camber point from the blade leading edge. Hence, the azimuthal flow velocity at the inducer discharge section (2) with flow deviation corrections becomes

$$v_{2\delta^\circ} = \Omega r - w_2 \tan(\beta_2' + \delta^\circ)$$

where

$$\beta_2' = \tan^{-1} \left(\frac{\Omega r - v_2}{w_2} \right)$$

3.4 Pumping Performance. With the above results, the pumping performance is readily evaluated from the Euler equation

$$\frac{p_2 - p_1}{\rho} = \frac{p_2 - p_1}{\rho} + \frac{v_{2\delta^\circ}^2 + w_2^2 - w_1^2}{2} = \Omega r_2 v_{2\delta^\circ} - \frac{\Delta p_{\text{loss}}}{\rho}$$

Hence, by mass averaging the pressure changes, the total and static head coefficients are expressed by

$$\Psi_t = \frac{1}{\Omega^2 r_T^2 \dot{m}} \int_{r_{H2}}^{r_T} (p_{t2} - p_{t1}) w_2 2\pi r_2 dr_2$$

$$\Psi = \frac{1}{\Omega^2 r_T^2 \dot{m}} \int_{r_{H2}}^{r_T} (p_2 - p_1) w_2 2\pi r_2 dr_2$$

4 Model Discussion and Validation

With reference to the definition of the inducer geometry, in the stated assumptions and approximations, the standard requirement for radially uniform axial velocity in the blade channels at design conditions determines the correlation between the axial schedules of the hub radius and the blade pitch angle of helical inducers. If, in particular, the hub-to-tip radius ratio is known at the leading and trailing edge sections and the design flow coefficient and leading edge blade angle are assigned, then all of the main geometric features of tapered-hub helical inducers can be derived, including the trailing edge pitch angle. Comparison with the geometry of the MK1 and FAST2 space inducers, produced by Avio S.p.A. and tested in Alta's Cavitating Pump Rotordynamic Test Facility, confirms that all of the main design characteristics and the relation between the hub geometry and the blade pitch are almost perfectly predicted by the proposed model.

As an example, Fig. 6 shows a three-dimensional drawing of a four-bladed inducer designed by using the model. The inducer tip radius is 90.9 mm, the hub radius is 57 mm at the inlet and 73 mm at the outlet, the tip blade angle is 8.9 deg at the inlet and 20.54 deg at the outlet, the tip solidity is 1.97, and the design flow coefficient is 0.060.

With reference to the inducer performance evaluation, it is first worth noting that the numerical solution of the BVP for the discharge velocity profiles and the corresponding closed form approximation lead to essentially equivalent results, as illustrated by

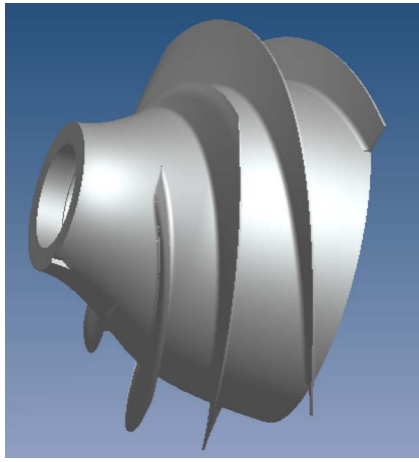


Fig. 6 3D rendering of a four-bladed, tapered-hub, variable-pitch inducer designed according to the proposed model

the comparison of the noncavitating pumping characteristics shown Fig. 7. Only for significantly low values of the flow coefficient ($\Phi < 0.02$), when the slip velocity becomes comparable to the axial velocity, a small difference between the two curves can be observed.

The model has been validated against the experimental performance of six different tapered-hub inducers, whose main characteristics are summarized in Table 1. Information on inducers A, B, C, and D comes from the open Japanese literature. The experimental data concerning inducers A and B have been taken from Hashimoto et al. [21] and refer to two different LOX pumps. The tests of inducer C are documented in Ref. [22]. Finally, inducer D is used in the LE-7A HTP and its experimental performance is reported in Ref. [23].

Figures 8–11 compare the experimental noncavitating characteristics of the MK1, FAST2, A, and B inducers with the respective predictions of the simplified closed form solution. The head coefficients based on the static and total pressures, with and with-

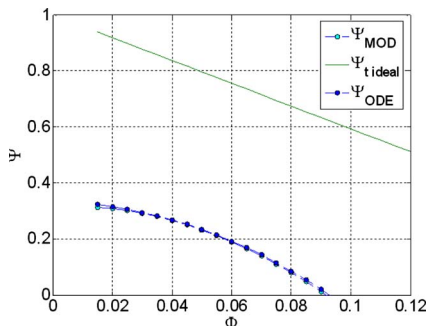


Fig. 7 Comparison between the numerical solution (ODE) and the corresponding closed form approximation (MOD) for the noncavitating performance prediction of tapered inducers

Table 1 Geometrical characteristics of the inducers used for validation of the proposed model

| | MK1 | FAST2 | Inducer A | Inducer B | Inducer C | Inducer D |
|-----------------------------|-------------|--------------|-----------|-----------|-----------|-----------|
| Number of blades | 4 | 2 | 3 | 4 | 3 | 3 |
| Tip diameter (mm) | 168.0 | 82.2 | 127.4 | 127.4 | 149.8 | 174.0 |
| Inlet tip blade angle (deg) | 82.36 | 82.62 | 82.75 | 82.75 | 82.5 | 83.6 |
| Outlet blade angle (deg) | 73.4 medium | 68.76 medium | 80.75 tip | 80.75 tip | 81.0 tip | 78.9 tip |
| Hub/tip at inlet | 0.428 | 0.365 | 0.300 | 0.300 | 0.250 | 0.287 |
| Hub/tip at outlet | 0.690 | 0.685 | 0.500 | 0.500 | 0.500 | 0.460 |
| Solidity at tip | 2.1 | 1.59 | 2.7 | 3.0 | 1.91 | 2.1 |

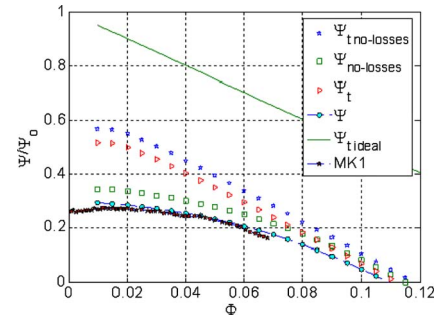


Fig. 8 Comparison between the experimental noncavitating performance of the MK1 inducer (dark stars) and the predictions of the analytical model

out losses, are reported, together with the “ideal” pumping performance for perfectly guided flow in the absence of pressure losses and deviation effects. For all of these inducers, the static head rise predicted by the model closely agrees with the experimental results.

For better assessment of these results, it is worth noting that the pressure tap used for the measurement of the static head rise developed by the MK1, FAST2, A, and B inducers was located more than two diameters downstream of the blade trailing edge. At this location, the flow closely approximates the fully settled axisymmetric conditions necessary for correct comparison of the experimental data with the model predictions.

Conversely, Figs. 12 and 13 show that the noncavitating performance of inducers C and D is evaluated with lower accuracy. Most likely, this situation is related to the different position of the downstream pressure tap, which in this case was located very close to the blade trailing edge. This is clearly inconsistent with the intrinsic nature of the proposed model, whose predictions are specifically derived from consideration of the axisymmetric far-field flow downstream of the inducer. The consequent deviation of the tangential velocity profile from the radial equilibrium introduces a systematic error in the evaluation of the centrifugal effects and, therefore, of the static pressure downstream of the inducer. This is confirmed by the almost linear nature of the measured pumping characteristics of inducers C and D, which is consistent with the expected behavior for nearly uniform distribution of the axial flow velocity at the inducer trailing edge before the establishment of radial equilibrium conditions [24].

The proposed model can also be applied for predicting the performance of helical inducers of more general hub and blade shapes. However, it is obviously expected to deliver best results when used for geometries more closely consistent with the assumptions used for its derivation, as confirmed by the results for the MK1 and FAST2 inducers.

5 Conclusions

Based on the available evidence, the present theoretical model proved to represent a useful tool for preliminary design and performance analyses of turbopump inducers. More specifically, the

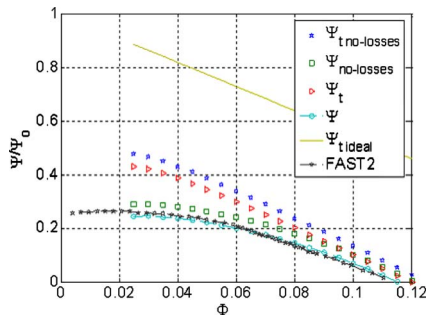


Fig. 9 Comparison between the experimental noncavitating performance of the FAST2 inducer (white stars) and the prediction of the analytical model

model is able to provide accurate quantitative indications for geometry definition, 3D flow field description, characterization and control of the blade loading, and prediction of the noncavitating pumping characteristics of helical inducers with tapered hub and variable blade pitch angle.

In this context, the model can be effectively used in two ways:

- for the preliminary definition of the geometry of tapered inducers, with particular reference to the hub and blade shape in order to minimize secondary flow losses and attain adequate cavitation performance;
- for the preliminary evaluation of the noncavitating performance of an inducer of given shape, or for defining the main geometric characteristics of an inducer, starting from the desired noncavitating pumping characteristic

More generally, the model provides inducer designers with a comprehensive interpretative framework where the main—often

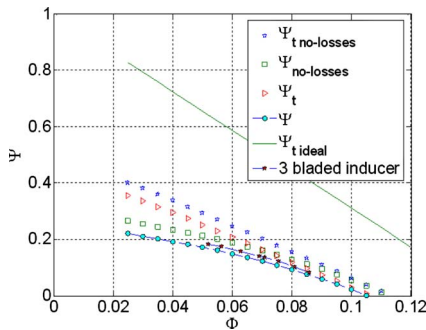


Fig. 10 Comparison between the experimental noncavitating performance of the inducer A (dark stars) and the predictions of the analytical model

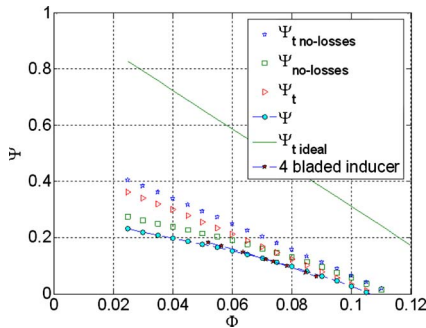


Fig. 11 Comparison between the experimental noncavitating performance of the inducer B (dark stars) and the predictions of the analytical model

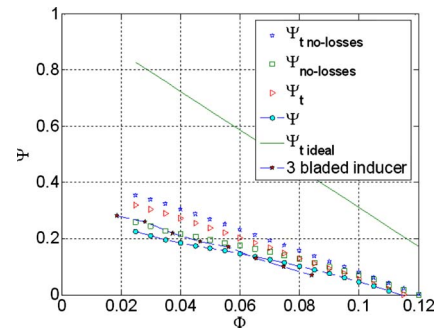


Fig. 12 Comparison between the experimental noncavitating performance of the inducer C (dark stars) and the predictions of the analytical model

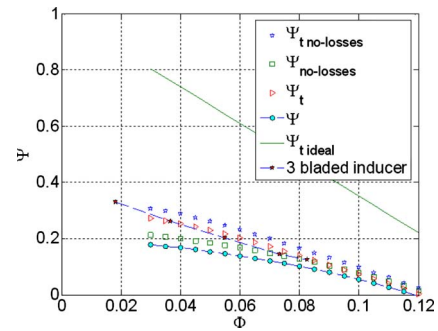


Fig. 13 Comparison between the experimental noncavitating performance of the inducer D (dark stars) and the predictions of the analytical model

conflicting—aspects of inducer design and their mutual implications can be assessed, quantified, and balanced in view of the attainment of the desired requirements and performance.

The limitations of the model are mostly related to the simplifying assumptions and approximations introduced in order to attain a practical solution. In particular, improvements in the description of the flow, control of the blade load, and accuracy of the inducer performance prediction are expected to be gained by a more refined treatment of viscous effects, capable to account for the axisymmetric nature of the blade boundary layers and the radial changes of their thickness across the inducer annulus.

Acknowledgment

The present activity has been funded by the European Space Agency under Contract No. 20081/06/NL/IA, whose support is gratefully acknowledged. The authors would like to express their gratitude to Professors Mariano Andreucci, Renzo Lazeretti, and Fabrizio Paganucci of the Dipartimento di Ingegneria Aerospaziale, Università di Pisa, Pisa, Italy, for their constant and friendly encouragement.

Nomenclature

- a = distance of the leading edge from the maximum camber point
- B = flow blockage
- c = blade chord
- c_a = full-blade axial length
- D = diameter, diffusion factor
- D_{ch} = hydraulic diameter of blade channels
- e_θ = azimuthal direction vector in coordinate frame
- f = friction coefficient
- h = specific enthalpy

L_{ch} = effective length of blade channels
 L_{eq} = equivalent duct length
 m_C = Carter's rule coefficient
 \dot{m} = mass flow rate
 N = number of blades
 p, p_t = static and total pressures
 P = (local) blade pitch
 \mathbf{r} = position vector
 r = radial coordinate
 r_H = inducer hub radius
 r_M = inducer mean radius
 r_T = inducer tip radius
 s = azimuthal blade spacing
 T = flow temperature
 \mathbf{u} = flow velocity
 u = radial flow velocity
 U = freestream boundary layer velocity
 v = azimuthal flow velocity
 V = absolute value of the flow velocity
 w = axial flow velocity
 z = axial coordinate
 β'_2 = relative discharge flow angle without deviation
 γ = blade angle from axial direction
 δ = boundary layer thickness
 δ^* = boundary layer displacement thickness
 δ° = discharge flow deviation angle
 ϑ = azimuthal coordinate
 θ^* = boundary layer momentum thickness
 ρ = flow density
 σ = blade solidity
 Φ = flow coefficient
 ψ = slip velocity stream function
 Ψ, Ψ_r = static and total head coefficients
 Ω = inducer rotational speed
 $\boldsymbol{\Omega}$ = inducer rotational speed (vector)

Superscripts

q' = value of q in the rotating frame
 \bar{q} = mean value of q
 $\hat{\mathbf{u}}$ = fully guided flow velocity
 $\tilde{\mathbf{u}}$ = slip flow velocity

Subscripts

D = design conditions
 T = tip radius
 H = hub radius
 Le = blade leading edge
 Te = blade trailing edge
 δ° = flow deviation angle
 1 = upstream station (1)
 2 = downstream station (2)

References

[1] Jakobsen, J. K., 1971, "Liquid Rocket Engine Turbopump Inducers," Space

- Vehicle Design Criteria Manuals, NASA Report No. SP-8052.
- [2] Ashihara, K., Goto, A., Kamijo, K., Yamada, H., and Uchiyumi, M., 2002, "Improvements of Inducer Inlet Backflow Characteristics Using 3D Inverse Design Method," *Proceedings of the 38th AIAA/ASME/SAE/ASEE Joint Propulsion Conference*, Indianapolis, Jul. 7–10.
 - [3] Kang, D., Cervone, A., Yonezawa, K., Horiguchi, H., Kawata, Y., and Tsujimoto, Y., 2007, "Effect of Blade Geometry on Tip Leakage Vortex of Inducer," *Proceedings of the Ninth Asian International Conference on Fluid Machinery*, Jeju, South Korea, Oct. 16–19.
 - [4] Brennen, C. E., 1994, *Hydrodynamics of Pumps*, Concepts ETI, Norwich/Oxford University Press, Oxford, England.
 - [5] Brennen, C. E., 1995, *Cavitation and Bubble Dynamics*, Oxford University Press, Oxford, England.
 - [6] Stripling, L. B., and Acosta, A. J., 1962, "Cavitation in Turbopumps: Part I," *ASME J. Basic Eng.*, **84**, pp. 326–338.
 - [7] Brennen, C. E., and Acosta, A. J., 1973, "Theoretical, Quasi-Static Analysis of Cavitation Compliance in Turbopumps," *J. Spacecr. Rockets*, **10**(3), pp. 175–179.
 - [8] Brennen, C. E., 1978, "Bubbly Flow Model for the Dynamic Characteristics of Cavitating Pumps," *J. Fluid Mech.*, **89**, pp. 223–240.
 - [9] Tsujimoto, Y., Kamijo, K., and Yoshida, Y., 1993, "A Theoretical Analysis of Rotating Cavitation in Inducers," *ASME J. Fluids Eng.*, **115**, pp. 135–141.
 - [10] Tsujimoto, Y., Watanabe, S., and Horiguchi, H., 1998, "Linear Analyses of Cavitation Instabilities of Hydrofoils and Cascades," *Proceedings of the US-Japan Seminar: Abnormal Flow Phenomena in Turbomachinery*, Osaka, Japan, Nov. 1–6.
 - [11] Watanabe, S., Yokota, K., Tsujimoto, Y., and Kamijo, K., 1999, "Three-Dimensional Linear Analysis of Rotating Cavitation in Inducers Using an Annular Cascade Model," *ASME J. Fluids Eng.*, **121**, pp. 866–871.
 - [12] d'Agostino, L., and Venturini-Autieri, M. R., 2002, "Three-Dimensional Analysis of Rotordynamic Fluid Forces on Whirling and Cavitating Finite-Length Inducers," *Proceedings of the Ninth International Symposium on Transport Phenomena and Dynamics of Rotating Machinery (ISROMAC-9)*, Honolulu, Feb. 10–14.
 - [13] d'Agostino, L., and Venturini-Autieri, M. R., 2003, "Rotordynamic Fluid Forces on Whirling and Cavitating Radial Impellers," *Proceedings of the Fifth International Symposium on Cavitation (CAV 2003)*, Osaka, Japan, Nov. 1–4.
 - [14] Semenov, Y. A., Fujii, A., and Tsujimoto, Y., 2004, "Rotating Choke in Cavitating Turbopump Inducer," *ASME J. Fluids Eng.*, **126**, pp. 87–93.
 - [15] Cooper P., 1967, "Analysis of Single- and Two-Phase Flows in Turbopump Inducers," *ASME J. Eng. Power*, **89**, pp. 577–588.
 - [16] Lakshminarayana, B., 1982, "Fluid Dynamics of Inducers: A Review," *ASME J. Fluids Eng.*, **104**, pp. 411–427.
 - [17] Bramanti, C., Cervone, A., and d'Agostino, L., 2007, "A Simplified Analytical Model for Evaluating the Noncavitating Performance of Axial Inducers," *Proceedings of the 43rd AIAA/ASME/SAE/ASEE Joint Propulsion Conference*, Cincinnati, Jul. 8–11.
 - [18] Hildebrand, F. B., 1976, *Advanced Calculus for Applications*, 2nd ed., Prentice-Hall, Saddle River, NJ.
 - [19] Lieblein S., Schwenk F. C., and Broderick R. L., 1953, "Diffusion Factor for Estimating Losses and Limiting Blade Loadings in Axial Flow Compressor Blade Elements," NACA Report No. RM E53D01.
 - [20] Lieblein, S., 1965, "Experimental Flow in Two-Dimensional Cascades," Aerodynamic Design of Axial Flow Compressors, NASA Report No. SP-36.
 - [21] Hashimoto, T., Yamada, H., Funatsu, S., Ishimoto, J., Kamijo, K., and Tsujimoto, Y., 1997, "Rotating Cavitation in Three and Four-Bladed Inducers," *Proceedings of the 33rd AIAA/ASME/SAE/ASEE Joint Propulsion Conference*, Seattle, Jul. 6–9.
 - [22] Fujii, A., Azuma, S., Yoshida, Y., Tsujimoto, Y., Horiguchi, H., and Watanabe, S., 2002, "Higher Order Rotating Cavitation in an Inducer," *Proceedings of the Ninth International Symposium on Transport Phenomena and Dynamics of Rotating Machinery (ISROMAC-9)*, Honolulu, Feb. 10–14.
 - [23] Fujii, A., Mizuno, S., Horiguchi, H., and Tsujimoto, Y., 2005, "Suppression of Cavitation Instabilities by Jet Injection at Inducer Inlet," *Proceedings of the ASME Fluid Engineering Division Summer Meeting and Exhibition (FEDSM2005)*, Houston, Jun. 19–23.
 - [24] Prandtl, L., and Tietjens, O. G., 1934, *Applied Hydro- and Aeromechanics*, McGraw-Hill, New York.

C. C. Gutiérrez-Torres

SEPI-ESIME-Zacatenco,
Departamento de Ingeniería Mecánica,
Instituto Politécnico Nacional,
U.P. Adolfo López Mateos Edif. 5 3er. Piso,
LABINTHAP,
Mexico,
Distrito Federal 07738,
Mexico
e-mail: cgutierrez@ipn.mx

Y. A. Hassan

Department of Nuclear Engineering,
Texas A&M University,
3133 TAMU,
College Station, TX 77843-3133
e-mail: y-hassan@tamu.edu

J. A. Jimenez-Bernal

SEPI-ESIME-Zacatenco,
Departamento de Ingeniería Mecánica,
Instituto Politécnico Nacional,
U.P. Adolfo López Mateos Edif. 5 3er. Piso,
LABINTHAP,
Mexico,
Distrito Federal 07738,
Mexico
e-mail: jjimenezb@ipn.mx

Turbulence Structure Modification and Drag Reduction by Microbubble Injections in a Boundary Layer Channel Flow

Turbulent boundary layer modification in a channel flow using injection of microbubbles as a means to achieve drag reduction was studied. The physical mechanism of this phenomenon is not yet fully understood. To obtain some information related to this phenomenon, single-phase (pure water) flow and two-phase (water and microbubbles) channel flow measurements are taken. The void fraction conditions were varied while maintaining a Reynolds number of 5128 based on the half channel height. The study indicates that the presence of microbubbles within the boundary layer modifies the turbulence structure such that variations in time and space turbulent scales are observed, as well as ejection and sweep phenomena. [DOI: 10.1115/1.2969444]

Keywords: drag reduction, microbubbles, PIV, channel flow

1 Introduction

Injection of microbubbles into the boundary layer as a method of drag reduction has been an active area of study in recent years due to its energy saving potential and environmental friendly characteristics. The work of McCormick and Bhattacharyya [1] first reported the use of electrolysis to produce hydrogen microbubbles on the hull of a submersible axisymmetric body. Drag reduction values as high as 30% were observed, such that a decrease in the Reynolds stresses was obtained.

Madavan et al. [2] carried out a numerical investigation of the phenomenon in an effort to clarify the effect of changes of physical properties (density and viscosity) of the fluid in the boundary layer due to the presence of the microbubbles. This work concluded that the microbubbles present in the boundary layer affect the turbulent structure by altering the local effective viscosity and density of the fluid. They can also affect the turbulence directly. A strong dependence on the magnitude of the drag reduction, the volumetric concentration of the bubbles, and their location was found. It was also stated that the bubbles are most effective when they are in the buffer layer.

Results presented by Merkle and Dutsch [3] showed that up to 80% drag reduction can be obtained by injecting microbubbles in the boundary layer. It was observed that microbubble injection became ineffective for very low-speed conditions due to buoyancy. The strong relationship between the drag reduction, microbubbles concentration, and location was again experimentally confirmed. A new parameter, namely, the diameter of the bubbles, was introduced to the discussion. The role of the size of the bubbles with regard to their trajectories, their location, and concentration in the boundary layer was stated as the source of im-

portance for this parameter. In a study of turbulence control, Kodama [4] pointed out that the effect of bubbles in turbulent flows depends on bubble size. In short, small bubbles dampen turbulence and large bubbles enhance turbulence. His conclusion reinforces the idea of the use of microbubbles to reduce drag.

The marker-density-function (MDF) method was developed by Kanai and Miyata [5] to conduct direct numerical simulation (DNS) for bubbly flows. The method was applied to a turbulent bubbly channel flow to elucidate the interaction between bubbles and wall turbulence. Their results indicate that the interaction between the bubbles and the wall turbulence near the wall contributes to the reduction of turbulent energy. Here, the necessity of bubble concentration near the wall, specifically inside the buffer layer, for drag reduction was elucidated. The drag reduction effect was attributed to the prevention of spanwise vorticity sheetlike structure formation near the wall due to the presence of bubbles. The streamwise vorticity, which is considered to be created from the spanwise vorticity detaching from the wall, was weakened, depressing the bursting phenomenon. Accordingly, the low-speed streaks below the detachment position of the spanwise vorticity disappeared, reducing the turbulent energy and attaining the drag reduction.

In 2002, Xu et al. [6] presented the results of a numerical simulation of turbulent drag reduction using microbubbles. It was found that the strongest reduction in drag was achieved using small bubbles ($a^+ = 13.5$, where a^+ is the radius in wall units). These results also suggest the existence of at least three mechanisms involved in the drag reduction process: one linked to the initial seeding of the bubbles and another associated with density effects, where the bubbles reduce the momentum transfer and the third governed by specific correlations between the bubbles and the turbulence.

Lu et al. [7] used DNS to find that bubbles of a size comparable to the buffer layer in a low Reynolds number turbulent flow can

Contributed by the Fluids Engineering Division of ASME for publication in the JOURNAL OF FLUIDS ENGINEERING. Manuscript received September 2, 2007; final manuscript received May 26, 2008; published online September 23, 2008. Assoc. Editor: Steven Ceccio.

generate significant drag reduction. It was also found that the deformability of the bubbles plays a major role in the way that bubbles affect the turbulence.

Shen et al. [8] suggested that the drag reduction by microbubble injection is more dependent on the effective gas phase volumetric rate than the microbubble size.

Kawashima et al. [9] demonstrated that drag reduction is increased and sustained for a longer time when microbubbles are kept in place by attaching end plates to a 50×1 m flat plate. The presence of the end plates prevents air bubbles from getting lost from the sides of the flat plate, which allows concentration to increase and subsequently reduce drag. It was also found that there is not a relationship between reduction of drag and the method of bubble production.

In this paper, particle image velocimetry (PIV) is used to obtain statistical properties of turbulence within a streamwise near-wall region perpendicular to the wall surface. Measurements of single-phase flow (pure water) and two-phase flow (water and microbubbles) are carried out. The differences between the two cases and the influence of the local void fraction values in the turbulence structure are discussed.

2 Experimental Facility

The experiments were conducted in a rectangular acrylic channel with dimensions of 4.8 m length, 20.6 cm width, and 5.6 cm height. Water flowed through the channel by gravity from a tank, which was located 2.02 m above the channel level. Then, water flowed to a lower tank, where it was pumped to the upper tank forming a closed loop. The upper tank's water level was maintained constant through the experiment so as to maintain constant flow rate through the channel.

The velocity field in the x - y plane was obtained by PIV at 3.15 m downstream from the channel inlet. A Nd:YAG (yttrium aluminum garnet) laser with a wavelength of 532 nm (green light) and power of 350 mJ per pulse was utilized. The polystyrene particles used for seeding had a diameter of 6–9 μm with a specific gravity almost identical to water's specific gravity.

The laser light scattered from the seeding particles was recorded using a charge coupled device (CCD) Kodak Megaplug camera, Model ES 1.0, with a resolution of 1008×1018 pixels. The viewing area was 1.28 cm^2 and was located close to the channel wall. The system recorded 30 velocity fields per second. Each velocity field was obtained from a pair of consecutive images capturing the second image of the pair 1 ms after the first one. Images were recorded for a time span of approximately 3.3 s.

The pressure gradient in the test section was measured with pressure taps located on the top wall of the channel. A Validyne pressure transducer (Model DP103) was used.

The hydrogen microbubbles used to achieve drag reduction were produced by electrolysis at 10 cm upstream of the test zone. Platinum wire with a diameter of 76 μm was used as electrodes. To produce hydrogen microbubbles of 30 μm , a current of 25 mA was conducted through the electrodes. The small size of the microbubbles was intentionally chosen to reduce buoyancy effects, in hopes of keeping them in the buffer layer within the boundary layer. The negative electrode (cathode) produced hydrogen microbubbles, whereas the positive one (anode) produced oxygen microbubbles. A schematic of the channel apparatus is shown in Fig. 1.

3 Results and Discussion

All the experiments were carried out at constant volumetric flow. The Reynolds number that was calculated using half height of the channel, the bulk velocity, and the viscosity of water was $Re \approx 5128$. Characterization of turbulence parameters such as Reynolds Stresses, turbulent intensities, and average vorticity for this facility were presented in a previous work [10]. In this work, the results were compared to other available studies in the litera-

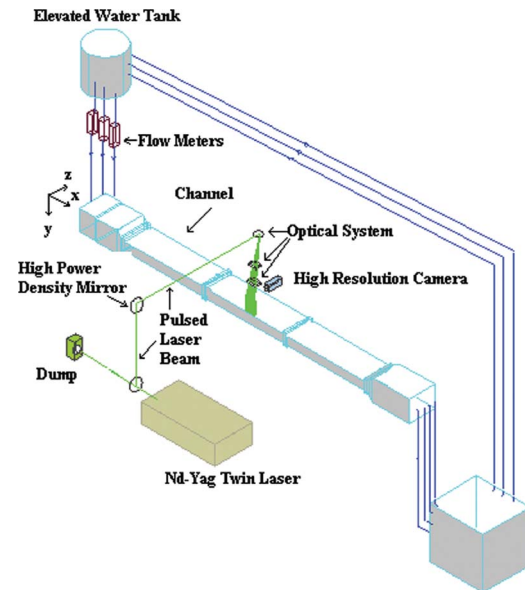


Fig. 1 Channel setup

ture. Figure 2 presents the nondimensional streamwise velocity U^+ ($U^+ = U/u_\tau$), versus the nondimensional y -location, y^+ ($y^+ = yu_\tau/\nu$), for single-phase flow, and a comparison with data obtained by Warholic [11] in a fully developed channel flow for water at $Re_H = 5100$.

For $y^+ < 5$, the streamwise nondimensional velocity agrees with the law of the wall. The solid line passing through the data represents the log law. A good agreement between the theoretical model and the measured data is observed for $y^+ > 30$.

For two-phase flow (water and microbubbles), different void fraction values were used. The void fraction was calculated using

$$\alpha = \frac{V_g}{V_g + V_l} \quad (1)$$

where V_g is the volume of the gas bubble in the viewing volume with a thickness of about 1 mm and V_l is the volume of the liquid water in the viewing volume. Conditions of various void fraction test cases for Re of 5128 are summarized in Table 1. The void fraction was calculated based on the gas bubble concentration in the viewing area only. Consequently, the values are drastically larger than the global void fraction. The results of Table 1 (where the conditions of the cases presented in this paper are summarized) confirm that drag reduction has a strong dependence on the local void fraction values. In the table, the diameter d of the bubble is presented in the wall units; i.e., $d^+ = du_\tau/\mu$, and the

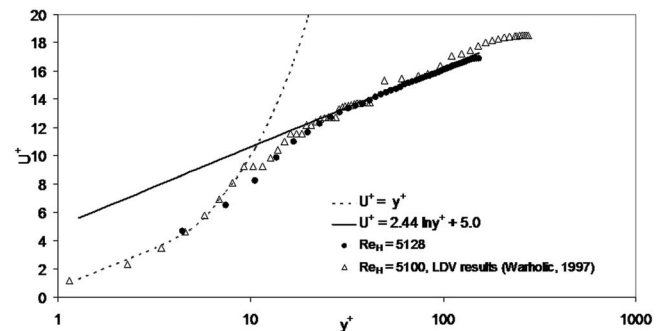


Fig. 2 Nondimensional streamwise velocity, U^+ , versus the nondimensional distance from the wall, y^+ , for single-phase flow

Table 1 Summary of two-phase flow cases studied

| Void fraction (α) | 2.4% | 3.4% | 4.4% | 4.9% |
|----------------------------|--------|--------|--------|--------|
| u_τ (m/s) | 0.0108 | 0.0106 | 0.0097 | 0.0091 |
| d^+ | 0.32 | 0.31 | 0.29 | 0.27 |
| Drag reduction (DR) | 12% | 16.6% | 29.8% | 38.4% |

changes shown for d^+ are caused by changes of u_τ values not because of changes of microbubbles diameter.

The resolution of the PIV measurements in single-phase flow is approximately 2.7 wall units in both x and y directions. The highest concentration of microbubbles can be found within the buffer layer, where they seem to be more effective. The concentration of microbubbles expressed in percentage across the normal direction from the wall for different drag reduction percentages is shown in Fig. 3.

Measurements of the average velocity in the normal direction are presented in Fig. 4. An increase in the values of the mean vertical velocity V can be observed when microbubbles are present. This agrees with the results presented by Ferrante and Elghobashi [12] for the vertical component of the velocity using DNS.

3.1 Quadrant Analysis. The quadrant analysis of the Reynolds shear stress is used to obtain detailed information on the contribution of events occurring in the flows in turbulence production (Lu and Willmarth [13], Wallace et al. [14]). This method classifies the Reynolds stress production using four categories organized according to the signs of the fluctuating velocity components (u' and v'). The Q1 events ($u' > 0$ and $v' > 0$) represent the outward motion of high-speed fluid; the Q2 events ($u' < 0$ and $v' > 0$) represent the outward motion of high-speed fluid, also known as “ejections” or “bursts.” The Q3 events ($u' < 0$ and $v' < 0$) represent the inward motion of low-speed fluid; the Q4 ($u' > 0$ and $v' < 0$) events represent inrushes of high-speed fluid, also known as “sweeps.” Both Q2 events (ejections) and Q4 events (sweeps) occur intermittently through the boundary layer and are the main contributors to the production of Reynolds shear stress $-u'v'$. Sweeps are the main contributors to the Reynolds stress production near the wall while ejections dominate in the region beyond $y^+ \approx 12$ [15]. The sweeps are considered to contribute significantly to the generation of turbulent wall skin friction [16]. Figure 5 shows a representation of these events in a channel flow.

Traditionally, measurements of the velocity fluctuations have been performed using methods that are capable of capturing a single-point of the velocity variations in time at a fixed point location. Alternatively, the PIV method has the advantage of mea-

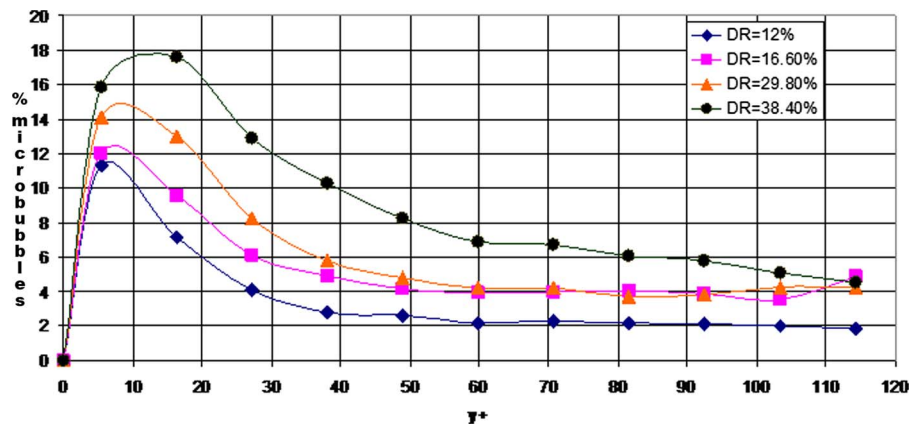


Fig. 3 Microbubble distribution along the normal direction

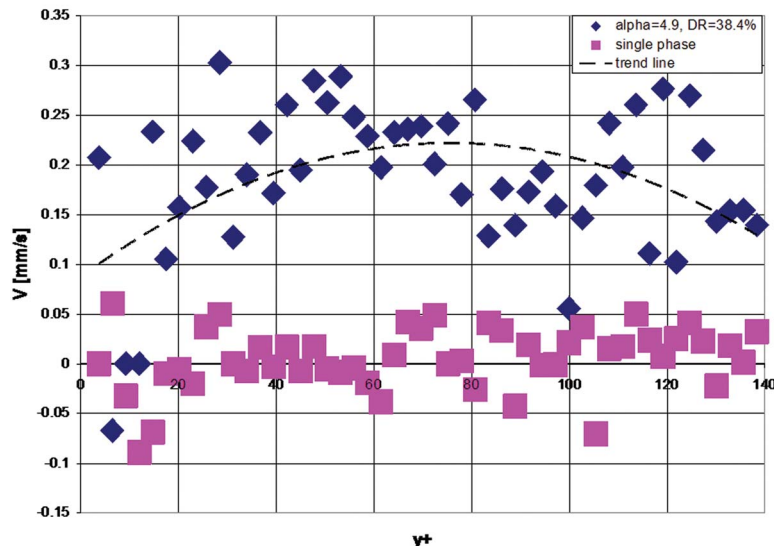


Fig. 4 Normal mean velocity profile

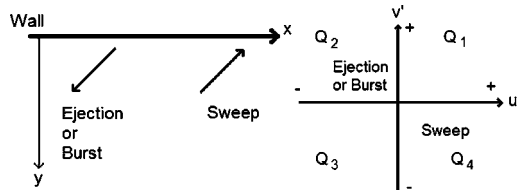


Fig. 5 Quadrant analysis events classification

suring full-field velocity components within a viewing area with time. Figure 6 shows an instantaneous velocity field where contributions from the four different quadrants can be observed for single-phase flow.

For two-phase flow, an instantaneous fluctuating velocity field is shown in Fig. 7, for a void fraction of 4.9%. The positions of the microbubbles are represented in white; however, they are not to scale. Here, a decrease in the Q4 events or sweeps is noted when microbubbles are present.

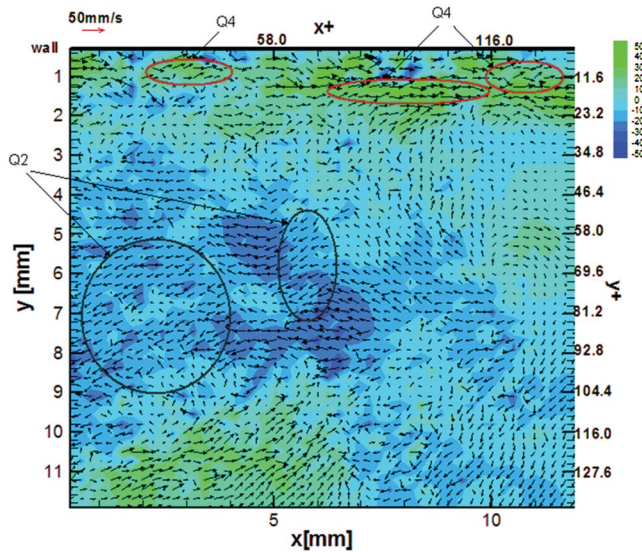


Fig. 6 Instantaneous fluctuating velocity field for single-phase flow

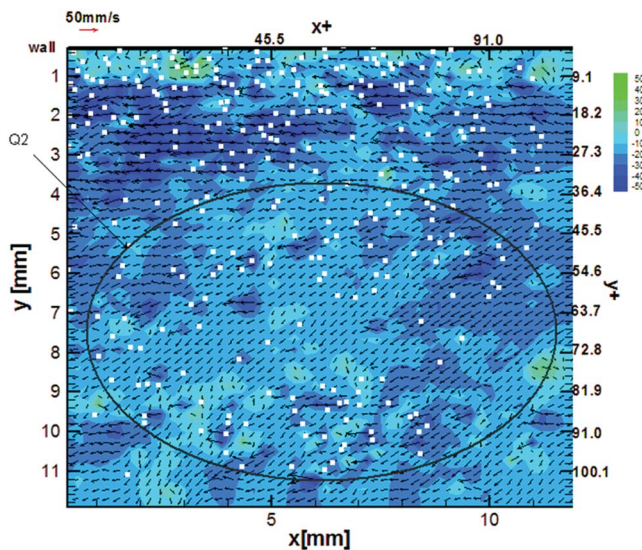


Fig. 7 Instantaneous fluctuating velocity field for two-phase flow ($\alpha=4.9\%$, $DR=38.4\%$)

Table 2 Total contribution from each quadrant to the production of Reynolds shear stresses

| | S_1 (%) | S_2 (%) | S_3 (%) | S_4 (%) |
|------------------------------|-----------|-----------|-----------|-----------|
| Single-phase flow | 22.04 | 29.63 | 22.1 | 26.22 |
| $\alpha=4.9\%$, $DR=38.4\%$ | 23.62 | 28.2 | 23.2 | 24.8 |

3.1.1 Conventional One-Point Measurement Analysis. Traditionally, in one-point velocity measurements, the evaluation of the quadrant fractional contribution to the Reynolds shear stress is obtained using the following function:

$$I(t) = \begin{cases} 1 & \text{if the point } (u', v') \text{ is in the } Q_{th} \\ 0 & \text{otherwise} \end{cases} \quad (2)$$

where $I(t)$ is a function depending on time that registers the existence of the events in the Q_{th} quadrant and Q indicates the quadrant where the event takes place (1, 2, 3, or 4).

The quadrant analysis technique has been traditionally used for velocity measurements using hot wire/hot film anemometry and laser Doppler velocimetry (LDV). These techniques measure the flow and velocity at a stationary point in space.

The contributions from each quadrant for single- and two-phase flow over the time span of time (3.3 s) were measured for each velocity field in the entire domain using PIV. Contributions from Quadrants 1 and 3 are considered negative for the production of actual Reynolds shear stresses.

To quantify the percentage of the contributions from each quadrant over the whole period of time in the entire PIV viewing area, Eq. (3) was used.

$$S_Q = \frac{1}{T} \int_0^T I(t)_Q dt, \quad Q = 1, 2, 3, \text{ and } 4 \quad (3)$$

where $I(t)_Q$ is the contribution for quadrant Q from all velocity points of the viewing area at instant t .

The percentage of contribution from each quadrant can be obtained from

$$S_Q \% = \frac{S_Q}{S_1 + S_2 + S_3 + S_4} \times 100 \quad (4)$$

A comparison of the total contribution of each quadrant to the production of Reynolds shear stresses for single-phase and two-phase flow is presented in Table 2.

3.1.2 Full-field velocity measurement analysis. The PIV measurements provide a full-field velocity in 2D or 3D dimensions (field measurements). A modification of the traditional methods implemented for quadrant analysis was attempted. Such method is based on "dominant event" detection for PIV. In this method, the fluctuating components of the velocity are discriminated using the traditional quadrant analysis. However, the dominant event, i.e., the event that has the strongest impact within a determined area, is recorded for the final statistics, while the weak ones are ignored. This approach is applied to present the dominant event observed within the PIV viewing area. In other words, although there might be contributions from the four quadrants in a velocity field, only the largest one is taken into account in the final statistics. This can be expressed as

$$S_Q = \frac{1}{T} \int_0^T (DE)_Q^{\Delta A = \Delta x \Delta y = 1.28 \text{ cm}^2} dt \\ = \frac{1}{N} \sum_1^N (DE)_Q \Big|_{\Delta A = 1.28 \text{ cm}^2}, \quad Q = 1, 2, 3, \text{ and } 4 \quad (5)$$

where DE indicates the largest event registered in the measure-

Table 3 Total contribution from each quadrant to the production of Reynolds shear stresses considering the dominant event only

| | S_1 (%) | S_2 (%) | S_3 (%) | S_4 (%) |
|---------------------------|-----------|-----------|-----------|-----------|
| Single-phase flow | 15.72 | 41.65 | 9.33 | 33.29 |
| $\alpha=4.9\%$, DR=38.4% | 22.88 | 29.17 | 21.14 | 26.8 |

ment area. ΔA indicates the measurement area, Δx is the width of the measurement area, Δy is the height of the measurement area, and N is the number of velocity fields used.

Again, the events were measured over the time span of the 3.3 s. A comparison between the single- and two-phase flow results is presented in Table 3.

The results obtained with the proposed method show, in a more evident way, that there is indeed a change in the production of Reynolds stresses with the injection of microbubbles. A reduction in the Q2 and Q4 (Reynold stress producing events) is delineated. It is clear that both of these events demonstrate the results of the mechanism responsible for the reduction of drag.

3.2 Two Point Correlations. The computation of a two-dimensional correlation coefficient offers a significant advantage since it allows the correlations to be measured in any arbitrary direction on the measurement plane. The two-dimensional correlation function is shown below.

$$R_{ij}(\Delta x, \Delta y) = \frac{u'_i(x, y)u'_j(x + \Delta x, y + \Delta y)}{u'_{rms_i}(x, y)u'_{rms_j}(x + \Delta x, y + \Delta y)} \quad (6)$$

Figures 8 and 9 present the cross correlations of the axial velocity R_{uu} , for the single- and two-phase flows, respectively, for locations $y^+=14.7$ and $x^+=69.7$. The variation of the streamwise (Δx) and normal (Δy) length scales, which in this case are associated with the maximum widths (along the x - and y -directions, respectively) of the contour $R_{uu}=0.3$, is obtained from the measurement plane. This R_{uu} level was chosen as a reasonable value to focus on the large-scale events with sufficient accuracy.

From the results of $R_{uu}(\Delta x, \Delta y)$, the values of length scales are calculated using the dimensions of the regions where the correlation coefficient has a value of at least 0.3. These results are shown

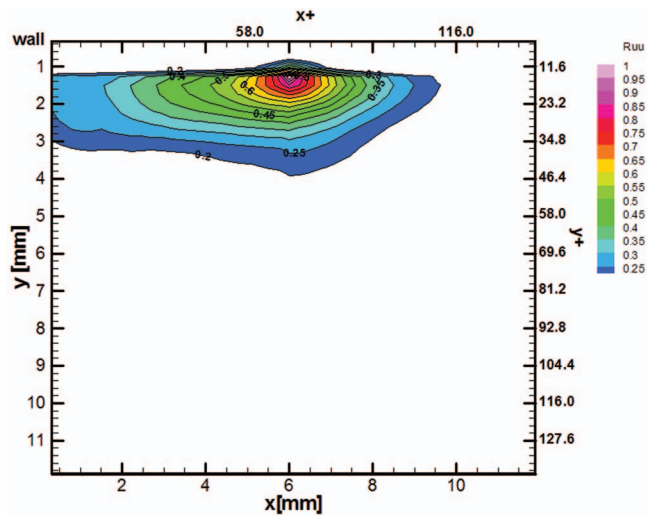


Fig. 8 Two-dimensional two-point correlation coefficient at $x^+=69.7$, $y^+=14.7$ for streamwise fluctuating velocity for single-phase

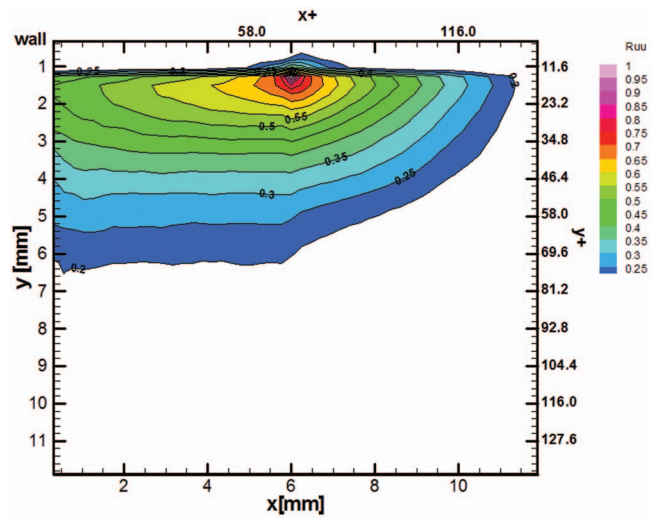


Fig. 9 Two-dimensional two-point correlation coefficient at $x^+=69.7$, $y^+=14.7$ for streamwise fluctuating velocity for $\alpha=4.9\%$, DR=38.4%

in Table 4.

Figures 10 and 11 show the correlation coefficient patterns for single-phase flow and two-phase flow at $y^+=14.7$ and $x^+=69.7$ for the normal component of the fluctuating velocities.

From the results of $R_{vv}(\Delta x, \Delta y)$, the values of length scales are also computed using the dimensions of the regions where the correlation coefficient has a value of at least 0.3. These results are shown in Table 5.

The length scale obtained from these measurements indicates that the presence of microbubbles increases the correlation for the streamwise velocity in both the longitudinal and the normal directions. However, the correlation coefficient values, R_{vv} , obtained

Table 4 Length scale obtained from R_{uu}

| | L_x (mm) | L_y (mm) |
|---------------------------|------------|------------|
| Single-phase | 6.8332 | 1.6584 |
| $\alpha=4.9\%$, DR=38.4% | 9.71245 | 3.0798 |

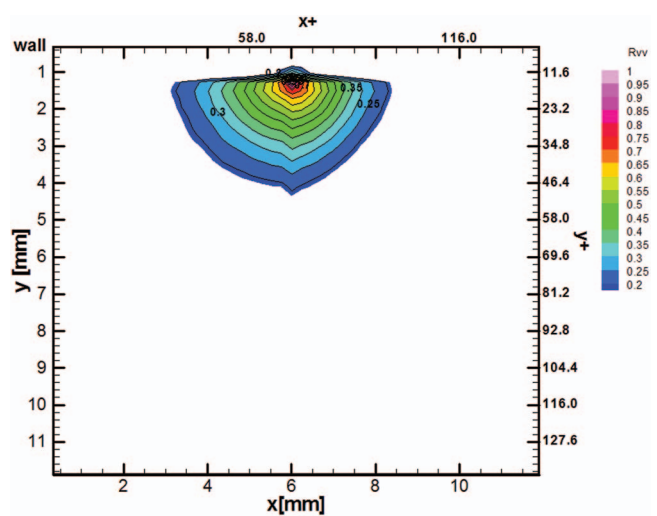


Fig. 10 Two-dimensional two-point correlation coefficient at $x^+=69.7$, $y^+=14.7$ for normal fluctuating velocity for single-phase

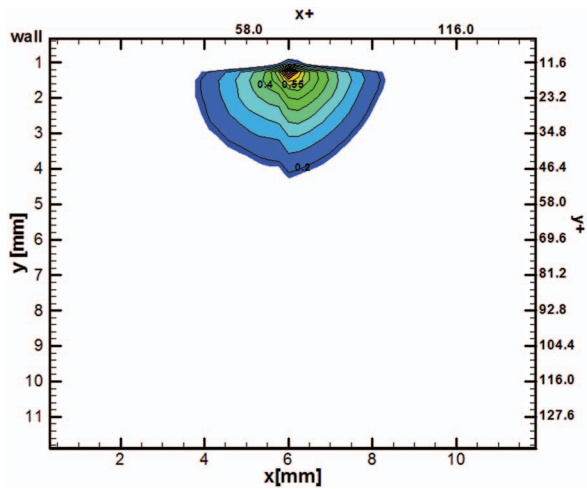


Fig. 11 Two-dimensional two-point correlation coefficient at $x^+=69.7$, $y^+=14.7$ for normal fluctuating velocity for $\alpha=4.9\%$, $DR=38.4\%$

from the normal velocity components show an opposite behavior, i.e., they decrease in the presence of microbubbles. This opposite behavior for the length scales obtained from R_{vv} suggests a decorrelation between the normal velocity components due to the presence of microbubbles.

3.3 Vortex Identification. To elucidate the changes that microbubbles inside the boundary layer cause, two different methods were used to identify vortex cores. The first one was proposed by Chong et al. [17], where eigenvalues of the velocity gradient tensor (∇u) are used to classify the local streamline pattern around any point in a flow in a reference frame moving with the velocity of that point. It was suggested that a vortex core is a region with complex eigenvalues of ∇u . Complex eigenvalues imply that the local streamline pattern is closed or spiral in a reference frame moving with a point. Since this method is inherently three dimensional (in three dimensions, the local velocity gradient tensor will have one real eigenvalue and a pair of complex conjugate eigenvalues when the discriminant of its characteristic equation is positive), Adrian et al. [18] proposed the use of an equivalent two-dimensional velocity gradient tensor for PIV two-dimensional measurements. In this case, the two-dimensional tensor will either have two real eigenvalues or a pair of complex conjugate eigenvalues. The vortices can then be identified by plotting isoregions of a positive imaginary component of the complex conjugate eigenvalues. Results for the vortex core identification for single and two-phase flow are shown in Figs. 12 and 13.

As seen in the figures, there is an evident decrease in vortices near the wall and in the buffer layer when comparing the two-phase flow to the single-phase flow.

To verify that the variation of vortex presence within the buffer layer was due to the microbubbles and not to the identification method, a second method was utilized. This method was proposed by Jeong and Hussain [19]. They define λ_2 as the second largest eigenvalue of the tensor $S_{ij}S_{jk} + \Omega_{ij}\Omega_{jk}$, where $S_{ij} \equiv (\partial_j U_i + \partial_i U_j)/2$ is the strain rate tensor and $\Omega_{ij} \equiv (\partial_j U_i - \partial_i U_j)/2$ is the rotation rate tensor. The connected flow regions of negative values

Table 5 Length scale obtained from R_{vv}

| | L_x (mm) | L_y (mm) |
|--------------------------------|------------|------------|
| Single-phase | 3.7907 | 1.8953 |
| $\alpha=4.9\%$, $DR=38.4\%$. | 2.3690 | 1.6584 |

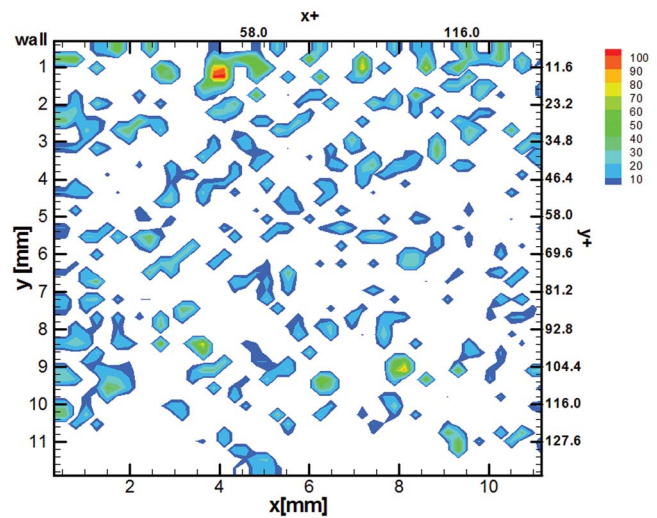


Fig. 12 Instantaneous vortex field for a single-phase flow (method of Chong et al.)

of λ_2 are used to identify cores of vertical structures.

The results obtained from the Jeong and Hussain method for single-phase flow and two-phase flow are shown in Figs. 14 and 15.

The Jeong and Hussain method echoed the results obtained by the method of Chong et al., showing a decrease in vortices in the boundary layer in the bubbly flow. This indicates that both methods are capable of identifying vortex patterns; however, there is a difference in the strength of identified vortices using the Jeong and Hussain method. Nevertheless, a decrease in the strength and the presence of vortical structure are found for two-phase flow using both methods.

4 Conclusions

Changes in the boundary layer were produced by the injection of microbubbles for drag reduction purposes. A modification of the normal average velocity profile was found after the injection of microbubbles. An increase in the local void fraction causes the normal mean velocity to depart from the normally zero value for

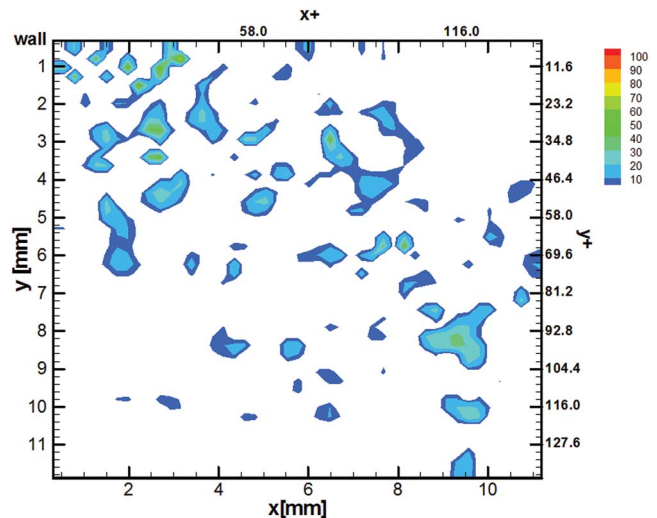


Fig. 13 Instantaneous vortex field for $\alpha=4.9\%$, $DR=38.4\%$ (method of Chong et al.)

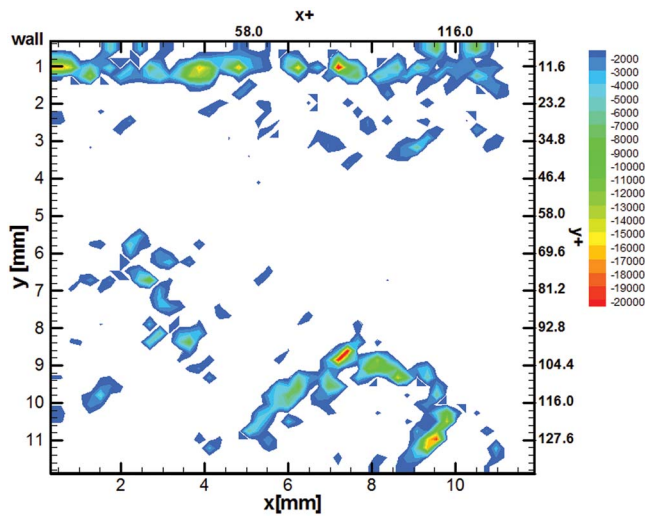


Fig. 14 Instantaneous vortex field for a single-phase flow (Jeong and Hussain method)

channel flow. This result is similar to the observations reported by Ferrante and Elghobashi [12] for DNS in a microbubble laden channel flow.

Bursts and sweeps, responsible for frictional drag along a near-wall vortical structure, were identified in an x - y plane close to the channel upper wall. A very slight decrease in burst and sweep events was observed when microbubbles are injected within the buffer layer. Furthermore, using the dominant event criterion, the differences between the single- and two-phase flows are more noticeable, showing that this new criterion can be useful for flow analysis using PIV.

Length scale evaluations using two-point two-dimensional correlation coefficient calculations were carried out. It was observed that the correlation increases for the streamwise velocity when microbubbles are present. However, for the normal component of the velocity, a noticeable decrease in the correlation coefficients is observed.

Two different methods for vortex identification were used for both single- and two-phase flows. In both cases, a decrease in the presence of vortex was found when microbubbles are present as opposed to single-phase flow.

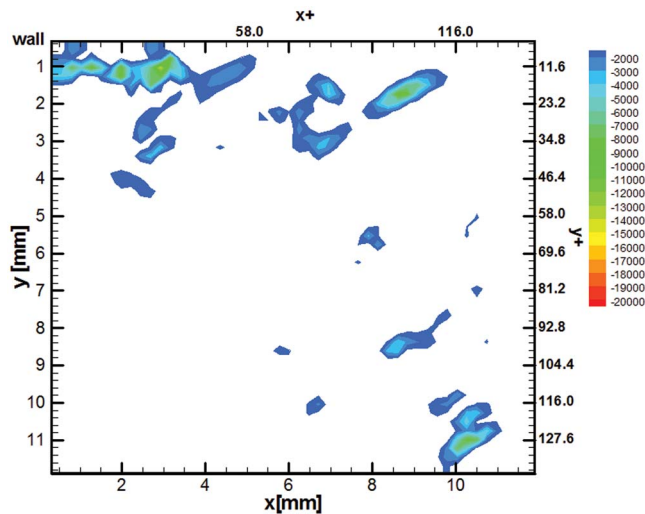


Fig. 15 Instantaneous vortex field for $\alpha=4.9\%$, $DR=38.4\%$ (Jeong and Hussain method)

Microbubbles within the boundary layer seem to disrupt near-wall vortical structures and also dampen the occurrence of sweeps, modifying the turbulence structure (integral length scale changes).

All of these may suggest an interruption of the autonomous cycle of near-wall turbulence (Jimenez and Pinelli [20]) and therefore a decrease in the turbulent nature of the flow resulting in drag reduction.

The relationship between the bubble size and the different scales of the turbulent flows has to be investigated carefully to further our understanding of the drag reduction phenomena by injection of microbubbles.

Nomenclature

- L = length scale (mm)
- N = number of velocity fields
- Q = quadrant events
- R = correlation coefficient
- Re = Reynolds number
- Re_H = Reynolds number based on half channel height
- S = percentage of contribution for quadrant events
- S_{ij} = strain rate tensor
- T = total time of measurement (s)
- U = average streamwise velocity (m/s)
- U^+ = average streamwise velocity in wall units
- V = normal velocity (m/s)
- V_g = gas volume (m^3)
- V_l = liquid volume (m^3)
- a^+ = bubble radius in wall units
- d = bubble diameter (m)
- d^+ = bubble diameter in wall units
- u_τ = friction velocity (m/s)
- x^+ = x position in wall units
- y = y position (mm)
- y^+ = y position in wall units

Greek Letters

- α = void fraction
- μ = dynamic viscosity (kg/m s)
- ∇ = gradient
- ν = kinematic viscosity (m^2/s)
- ρ = density (kg/m^3)
- Ω_{ij} = rotation tensor
- λ = eigenvalue

Subscripts

- i = streamwise direction
- j = normal direction
- rms = rms average quantity

Superscripts

- $-$ = time averaged quantity
- $'$ = fluctuating value

References

- [1] McCormick, M. E., and Bhattacharyya, R., 1973, "Drag Reduction of a Submersible Hull by Electrolysis," *Nav. Eng. J.*, **85**(2), pp. 11–16.
- [2] Madavan, N. K., Merkle, C. L., and Deutsch, S., 1985, "Numerical Investigations Into the Mechanisms of Microbubble Drag Reduction," *ASME J. Fluids Eng.*, **107**(3), pp. 370–377.
- [3] Merkle, C. L., and Deutsch, S., 1989, "Microbubble Drag Reduction," *Frontiers in Experimental Fluid Mechanics (Lecture Notes in Engineering)*, Springer-Verlag, Berlin, Vol. 46, pp. 291–335.
- [4] Kodama, Y., 1999, "Turbulence Control by Functionalization Fluids," *Proceedings of Symposium on Smart Control of Turbulence*, Tokyo, Japan, Dec. 2–3.
- [5] Kanai, A., and Miyata, H., 2001, "Direct Numerical Simulation of Wall Turbulent Flows With Microbubbles," *Int. J. Numer. Methods Fluids*, **35**(5), pp. 593–615.
- [6] Xu, L., Maxey, M. R., and Karniadakis, G. E., 2002, "Numerical Simulation of Turbulent Drag Reduction Using Microbubbles," *J. Fluid Mech.*, **468**, pp. 271–281.

- [7] Lu, J., Fernandez, A., and Tryggvason, G., 2005, "The Effects of Bubbles in the Wall Drag in a Turbulent Channel Flow," *Phys. Fluids*, **17**(9), 095102.
- [8] Shen, X., Ceccio, S. L., and Perlin, M., 2006, "Influence of Bubble Size on Micro-Bubble Drag Reduction," *Exp. Fluids*, **41**(3), pp. 415–424.
- [9] Kawashima, H., Kodama, Y., Hinatso, M., Hori, T., Makino, M., Ohnawa, M., Jakeshi, H., Sakoda, M., and Matsuno, F., 2007, "A Research Project on Application of Air Bubble Injection to a Full Scale Ship for Drag Reduction," *Proceedings of FEDSM 2007*, San Diego, CA, July 30–Aug. 2, ASME, San Diego, CA, FEDSM 2007-37079.
- [10] Hassan, Y. A., and Gutierrez-Torres, C. C., 2006, "Investigation of the Drag Reduction Mechanism by Microbubble Injection Within a Channel Boundary Layer Using PIV," *Nuc. Eng. Technol., J. Korean Nucl. Soc.*, **38**, pp. 763–778.
- [11] Warholic, M. D., 1997, "Modification of Turbulent Channel Flow by Passive and Additive Devices," Ph.D. thesis, University of Illinois, Urbana, IL.
- [12] Ferrante, A., and Elghobashi, S., 2004, "On the Physical Mechanisms of Drag Reduction in a Spatially Developing Turbulent Boundary Layer Laden With Microbubbles," *J. Fluid Mech.*, **503**, pp. 345–355.
- [13] Lu, S. S., and Willmarth, W. W., 1973, "Measurements of the Structure of the Reynolds Stress in a Turbulent Boundary Layer," *J. Fluid Mech.*, **60**, pp. 481–512.
- [14] Wallace, J. M., Eckelmann, H., and Brodkey, R. S., 1972, "The Wall Region in Turbulent Shear Flow," *J. Fluid Mech.*, **54**, pp. 39–48.
- [15] Robinson, S. K., 1991, "Coherent Motion in the Turbulent Boundary Layer," *Annu. Rev. Fluid Mech.*, **23**, pp. 601–639.
- [16] Kawahara, G., Ayukawa, K., Ochi, J., and Ono, F., 1998, "Bursting Phenomena in a Turbulent Square-Duct Flow," *JSME Int. J., Ser. B*, **41**, pp. 245–253.
- [17] Chong, M. S., Perry, A. E., and Cantwell, B. J., 1990, "A General Classification of Three-Dimensional Flow Fields," *Phys. Fluids A*, **2**, pp. 765–777.
- [18] Adrian, R. J., Christensen, K. T., and Liu, Z. C., 2000, "Analysis and Interpretation of Instantaneous Turbulent Velocity Fields," *Exp. Fluids*, **29**, pp. 275–290.
- [19] Jeong, J., and Hussain, F., 1995, "On the Identification of a Vortex," *J. Fluid Mech.*, **285**, pp. 69–94.
- [20] Jimenez, J., and Pinelli, A., 1999, "The Autonomous Cycle of Near-Wall Turbulence," *J. Fluid Mech.*, **389**, pp. 335–359.

PIV Study of Adverse and Favorable Pressure Gradient Turbulent Flows Over Transverse Ribs

M. Agelinchaab

M. F. Tachie

Department of Mechanical and Manufacturing
Engineering,
University of Manitoba,
Winnipeg, MB, R3T 5V6, Canada

This paper reports an experimental study of the combined effects of rib roughness and pressure gradient on turbulent flows produced in asymmetric converging and diverging channels. Transverse square ribs with pitch-to-height ratio of 4 were attached to the bottom wall of the channel to produce the rib roughness. A particle image velocimetry technique was used to conduct measurements at several streamwise-transverse planes located upstream, within, and downstream of the converging and diverging sections of the channel. From these measurements, the mean velocities and turbulent statistics at the top plane of the ribs and across the channel were obtained. The data revealed non-negligible wall-normal motion and interaction between the cavities and overlying boundary layers. The different drag characteristics of the rough bottom wall and the smooth top wall produced asymmetric distributions of mean velocity and turbulent statistics across the channel. The asymmetry of these profiles is most extreme in the presence of adverse pressure gradient. Because of the manner in which pressure gradient modifies the mean flow and turbulence production, it was found that the streamwise turbulence intensity and Reynolds shear stress in the vicinity of the ribs are lower in the adverse pressure gradient than in the favorable pressure gradient channel. The results show also that the combined effects of rib roughness and adverse pressure gradient on the turbulent intensity statistics are significantly higher than when roughness and adverse pressure gradient are applied in isolation. [DOI: 10.1115/1.2969448]

1 Introduction

Pressure gradient turbulent flows are found in many fluid engineering applications. Prior research demonstrates that adverse pressure gradient (APG) considerably slows the mean flow close to the wall and thereby thickens the boundary layer. APG also increases the turbulence intensities and Reynolds shear stress compared with values reported in zero pressure gradient (ZPG) turbulent boundary layers. On the other hand, favorable pressure gradient (FPG) tends to decrease the relative turbulent intensities and Reynolds stresses compared to ZPG values [1]. The FPG boundary layer studies performed prior to 1972 were reviewed by Narasimha and Sreenivasan [2]. Subsequently, Ichimiya et al. [3] studied the behavior of turbulent boundary layer during relaminarization under a favorable pressure gradient. The development of mild APG turbulent boundary layers was studied by Aubertine and Eaton [4]. It was found that the displacement thickness, momentum thickness, and the Reynolds number based on momentum thickness increased in the diverging section. Skåre and Krogstad [5] conducted measurements in equilibrium boundary layer in a strong APG and found that although the Reynolds stress distribution across the boundary layer is different from ZPG turbulent boundary layers, the stress ratios were nearly independent of pressure gradient. A vivid review of previous APG studies can be found in Ref. [6] and in a recent work by Angele and Mohammad-Klingman [7].

Many surfaces of engineering systems are aerodynamically or hydraulically rough. It is generally acknowledged that wall roughness increases the drag, transport of momentum, and heat transfer

characteristics. In addition to three-dimensional roughness elements such as sand grains, gravels, and spheres, two-dimensional transverse ribs have also been used to study roughness effects on turbulent flows. Although transverse ribs are also used to augment heat transfer performance in heat exchangers and gas turbines, they are used to model wall roughness in the present study. Because of the geometrical simplicity of transverse ribs and advances in computational resources in recent years, it has been possible to apply large eddy simulation (LES) and direct numerical simulation (DNS) to study such flow fields. For example, Cui et al. [8] employed LES to study turbulent flows over transverse square ribs in a fully developed channel while DNS studies of similar flow geometries have been reported by Nagano et al. [9], Ikeda and Durbin [10], Lee and Sung [11], Ashrafian et al. [12], and Leonardi et al. [13]. Following earlier experimental results [14], transverse ribs are classified into d -type (for pitch-to-height ratio, $p/k < 4$) and k -type ($p/k > 4$). Previous experimental studies include measurements over d -type, intermediate-, and k -type ribs in a ZPG turbulent boundary layer [15] and hot-wire measurements in a two-dimensional channel with both the top and bottom walls roughened by k -type ribs [16]. Open channel turbulent flows over different types of rib roughness have been studied by Agelinchaab and Tachie [17] and Tachie and Adane [18]. A more complete review of previous rib roughness studies can be found in Ref. [16].

Although pressure gradient turbulent flows over rough surfaces are found in many engineering applications such as draft tube of hydroelectric turbines, turbine blades, and reentry vehicles, the combined effects of pressure gradient and surface rough on the turbulence structure have received little research attention. Perry et al. [19] studied APG turbulent boundary layers over d -type ribs using a Pitot tube. Favorable pressure gradient open channel turbulent flows over square ribs with $p/k=2, 4$, and 8 have also been studied [20]. The FPG was produced by linearly converging each

Contributed by the Fluids Engineering Division of ASME for publication in the JOURNAL OF FLUIDS ENGINEERING. Manuscript received September 28, 2007; final manuscript received June 12, 2008; published online September 23, 2008. Assoc. Editor Juergen Kompenhans. Paper presented at the 37th AIAA Fluid Dynamics Conference And Exhibit, 2007.

of the open channel side walls at $\alpha=1$ deg and 2 deg and the measurements were conducted using a particle image velocimetry (PIV) technique. More recently, measurements were conducted in asymmetric APG turbulent boundary layers over square ribs with $p/k=3, 6,$ and 8 [21]. The results show that APG and rib roughness enhanced the drag and levels of the Reynolds stresses compared with a smooth-wall ZPG turbulent boundary layer. One of the complicating features of turbulent flows over rough walls is that the flow field close to the roughness elements is spatially inhomogeneous. In such cases, an individual vertical profile of the mean velocity and turbulent statistics is not exactly representative of the boundary layer so that spatial averaging is necessary [22,23]. Such spatial averaging has been performed in a number of numerical simulations [8] and PIV experiments performed over transverse ribs [21].

The above summary review shows that turbulent flows over rib roughness in a fully developed channel have been studied experimentally and numerically using LES or DNS. To the knowledge of the authors, no DNS study of pressure gradient turbulent flow over rib roughness has been reported. Although limited experimental studies of adverse and favorable pressure gradient turbulent flows over rib roughness have also been reported, additional comprehensive research is needed to better understand the characteristics of these relatively complex flow fields. The benchmark data sets obtained in such studies will be very useful for validating numerical results for pressure gradient turbulent flows over rough surfaces. The goal of the present work is to investigate the combined effects of rib roughness and APG or FPG turbulent flows on the mean velocity and turbulent statistics using a PIV technique.

2 Experimental Setup and Measurement Procedure

2.1 Test Facility.

The experiments were performed in a recirculation water tunnel. The test section of the water tunnel was 2500 mm long, 200 mm wide, and 200 mm deep. Closed test sections designed to produce favorable and adverse pressure gradients were inserted inside the water tunnel. The inserted test sections were made of 3 mm thick acrylic sheets. Figure 1 shows the schematic side views of the test section, the local test section heights, h , the measurement planes, P , as well as the ribs. The width of the test section was $w=194$ mm. Figures 1(a) and 1(b) show the diverging and converging sections, which were used to produce the APG and FPG flows, respectively. They will also be referred to as APG and FPG channels. The x coordinate is aligned with the streamwise direction, while the y and z coordinates are, respectively, in the transverse and spanwise directions; $x=0$ is at the start of the converging or diverging section (O), $y=0$ is on the cavity floor (Fig. 1(c)), and $z=0$ is at the midspan of the channel. In both figures, the first and last 750 mm (AO and PB) have straight parallel walls. For the APG channel, the middle section (OP) of 1000 mm length diverges nonlinearly from a height of $h=60$ mm to 90 mm as follows: $h(x)=60.00-7.39 \times 10^{-4}x+5.73 \times 10^{-5}x^2-3.12 \times 10^{-9}x^3-5.09 \times 10^{-11}x^4+2.78 \times 10^{-14}x^5$. Similarly, the middle section of the FPG channel converges nonlinearly from a height of $h=90$ mm to 60 mm as follows: $h(x)=90.00-4.01 \times 10^{-2}x+2.09 \times 10^{-5}x^2-7.17 \times 10^{-8}x^3+8.83 \times 10^{-11}x^4-2.78 \times 10^{-14}x^5$. In the above expressions, x is measured relative to O in millimeters and the equations are valid for $0 \leq x \leq 1000$. The FPG and APG channels described above have been employed previously by Tachie [21] and Shah and Tachie [24]. As explained in those studies, the choice of the above channel distribution ($h(x)$) was partly constrained by the test section of the existing main water channel and the need to obtain two-dimensional mean flow at the midplane of the converging and diverging channels. A number of distributions were tried and the pressure gradient along the channel was analytically calculated assuming inviscid flow. The distributions described above were chosen because they produced pressure gradients that were not too

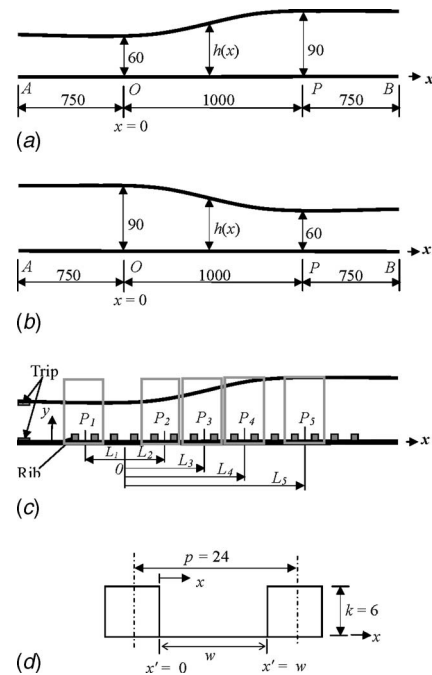


Fig. 1 Experimental setup: schematic side views of the adverse pressure gradient (a) and favorable pressure gradient (b) test sections; measurement planes (c). P_1 – P_5 denote x - y planes in which PIV measurements were made, L_1 – L_5 correspond to locations where detailed data analysis was performed; and (d) pitch and top plane of adjacent ribs. All units are in millimeters.

severe to cause flow separation in the APG channel or relaminarization in the FPG channel, yet high enough to noticeably modify the flow field compared with that in a channel with parallel walls.

Two-dimensional transverse square ribs of size $k=6$ mm were glued onto a 4.5 mm thick acrylic sheet and screwed to the bottom wall of the test section. Note that the 4.5 mm acrylic sheet reduced the original height of the test section. In the x -direction, the ribs span a total distance of 1650 mm leaving margins of about 425 mm at both ends. As indicated in Fig. 1(d), the pitch and height of the ribs are denoted by p and k , respectively. A pitch-to-height ratio, $p/k=4$, was used. In this paper, mean velocities will be denoted by upper cases (e.g., U and V) while fluctuating quantities will be denoted by lower case letters (e.g., u , v , $-uw$, etc.). The location where the maximum streamwise mean velocity (U_{\max}) occurs will be denoted as y_{\max} . The flow region extending from the lower channel wall to y_{\max} will be referred to as the lower boundary layer whereas the region from the upper wall to y_{\max} will be referred to as the upper boundary layer. The boundary layer thickness is defined as the y -location where $U/U_{\max}=0.99$.

2.2 Measurement System.

A PIV technique was used to conduct the velocity measurements. The flow was seeded with 5 μm polyamide seeding particles and a Nd: YAG (yttrium aluminum garnet), 120 mJ pulse laser of 532 nm wavelength was used to illuminate the flow field. The laser sheet was located at the midplane of the channel. A 60 mm diameter Nikkor lens was fitted to a 12 bit high-resolution digital camera (Dantec Dynamic HiSense 4M camera) that uses a digital camera with a charge-coupled device (CCD) of 2048 pixels \times 2048 pixels and a 7.4 μm pixel pitch. The camera field of view was 95 \times 95 mm². During the image acquisition, it was ensured that the maximum particle displacement was less than quarter of the interrogation window (IW) size. The average number of particles in an IW varied from 7 (32 pixel \times 16 pixel IW) to 14 (32 pixel \times 32 pixel IW). The images were processed using the adaptive correlation option of a

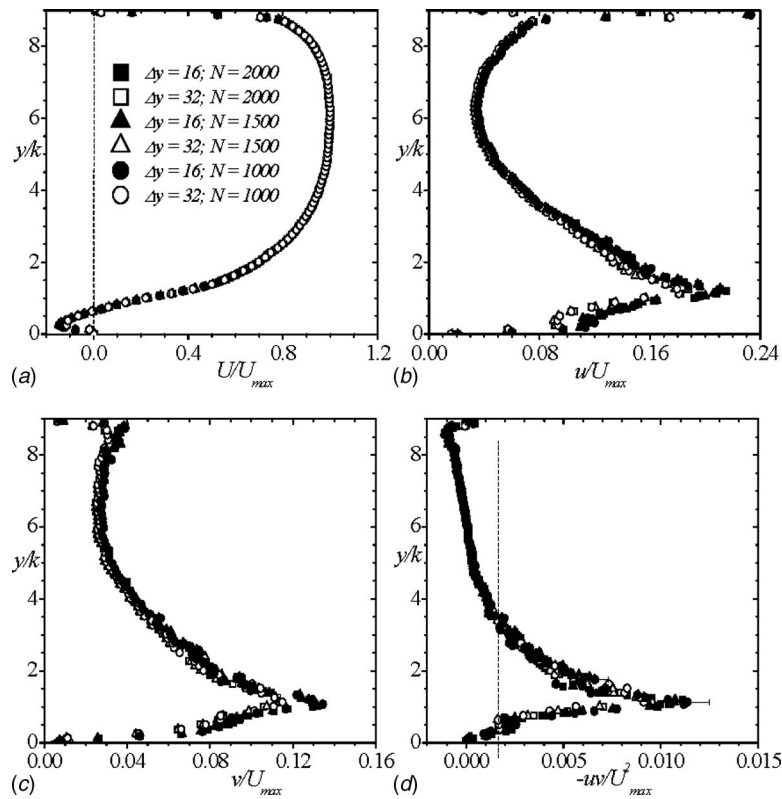


Fig. 2 Profiles of the mean velocity and turbulent quantities at the cavity center for two interrogation window sizes and three sample sizes. (a) Mean velocity, U , (b) streamwise, u , and (c) transverse, v , turbulent intensities, and (d) Reynolds shear stress, $-uv$. The symbols in (b), (c), and (d) as in (a).

commercial software (FLOWMANAGER 4.50.17) developed by Dantec Dynamics. A three-point Gaussian curve fit was used to determine particle displacement with subpixel accuracy. The particle diameter was $d_p = 2.1$ pixels, which is close to the recommended optimum value of $d_p \approx 2$ pixels required to minimize peak locking [25]. In fact, the histograms of the raw velocity vectors confirmed that there was no observable peak locking. In order to study the effect of IW size and sample size (N) on the mean velocity and turbulent quantities, these quantities were computed using $N = 1000, 1500$, and 2000 instantaneous images and both $32 \text{ pixels} \times 16 \text{ pixels}$ and $32 \text{ pixels} \times 32 \text{ pixels}$ IWs with 50% overlap. Figure 2 shows that typical profiles of the mean velocity, turbulent intensities, and Reynolds shear stress obtained from the two IWs and three sample sizes at the cavity center are nearly indistinguishable. This implies that the IWs and sample sizes used provide adequate spatial resolution and statistical convergence, respectively, for these quantities. The data presented subsequently were those obtained from 2000 images and processed using a $32 \text{ pixels} \times 16 \text{ pixels}$ IW with 50% overlap. The corresponding physical spacing between velocity vectors, taking the 50% overlap into account, is $\Delta x \times \Delta y = 0.74 \times 0.37 \text{ mm}^2$. Based on the friction velocity obtained in the approach flow at the upstream section of the APG channel, the space between vectors was $\Delta y^+ = 9.1$. The effects of PIV spatial resolution on the mean velocities as well as the second, third, and fourth order moments in turbulent flows over a smooth wall, a transitionally rough wire mesh, and a fully rough surface that was composed of transverse square ribs with $p/k = 8$ were studied recently by Shah et al. [26]. Based on those results, it was concluded that the spatial resolution used in the present study is sufficient for the mean and turbulent quantities reported subsequently.

Detailed analyses of bias and precision errors inherent in PIV measurements have been reported by Prasad et al. [27] and Forliti

et al. [28]. Based on those studies and the measurement uncertainty analysis procedure explained by Coleman and Steele [29], it was estimated that the uncertainties in the mean velocities, turbulent intensities, and Reynolds shear stress at 95% confidence level are $\pm 2\%$, $\pm 5\%$, and $\pm 10\%$, respectively. Close to the ribs, uncertainties in the mean velocities and Reynolds stresses are estimated to be $\pm 2.5\%$ and $\pm 12.5\%$, respectively. Error bars are used to indicate measurement uncertainty at 95% confidence level in subsequent graphs.

2.3 Test Conditions. A 42 mm wide trip made of four 6 mm square ribs and spaced at 6 mm apart was placed at the entrance of the channel (Fig. 1(c)) to enhance rapid development of the flow. In addition to the rib roughness, measurements were also obtained over a 4.5 mm acrylic plate (without the ribs), which was screwed onto the bottom wall of the channel. These measurements were performed at $x \approx -100 \text{ mm}$ upstream of the converging section and $x \approx -40 \text{ mm}$ upstream of the diverging section. These data sets will be referred to as smooth and will be used as the basis for discussing the effects of rib roughness on the flow characteristics. For the rib experiments, measurements were made in five x - y planes: one plane upstream of the convergence/divergence (P_1), three planes within the convergence/divergence sections (P_2, P_3 , and P_4), and one plane downstream of convergence/divergence sections (P_5). In each plane, there were four ribs; however, data sets were extracted between the centers of two adjacent ribs. The distance from O to the middle of the adjacent ribs of interest in a particular plane is denoted by L . For example, L_1 corresponds to data extracted from plane P_1 , and L_2, L_3, L_4 , and L_5 correspond to data extracted from planes P_2, P_3, P_4 , and P_5 , respectively. In many cases, the profiles were spatially averaged. The spatial averaging was performed in the x -direction over a pitch. A spatial averaged profile typically corresponds to the av-

Table 1 Test conditions and pertinent parameters

| Test | L | x (mm) | h (mm) | U_{\max} (m/s) | dU_{\max}/dx (s^{-1}) | $K \times 10^6$ | Re_{θ_L} | Re_{θ_U} |
|------|-------|----------|----------|------------------|-----------------------------|-----------------|-----------------|-----------------|
| FPG | SM | -100 | 84.0 | 0.460 | 0.04 | 0.20 | 750 | 1630 |
| | L_1 | -70 | 85.9 | 0.460 | 0.28 | 1.32 | 1700 | 430 |
| | L_2 | 290 | 75.2 | 0.540 | 0.37 | 1.27 | 1690 | 440 |
| | L_3 | 592 | 63.7 | 0.651 | 0.41 | 0.97 | 1830 | 490 |
| | L_4 | 807 | 57.8 | 0.739 | 0.46 | 0.84 | 2120 | 580 |
| | L_5 | 1371 | 55.9 | 0.807 | 0.32 | 0.49 | 2820 | 720 |
| APG | SM | -40 | 54.0 | 0.461 | 0.02 | 0.09 | 550 | 740 |
| | L_1 | -55 | 55.8 | 0.549 | 0.26 | 0.86 | 2450 | 1380 |
| | L_2 | 372 | 62.6 | 0.520 | -0.23 | -0.85 | 3690 | 780 |
| | L_3 | 717 | 75.6 | 0.402 | -0.55 | -3.40 | 4000 | 360 |
| | L_4 | 913 | 82.8 | 0.364 | -0.26 | -1.96 | 4110 | 350 |
| | L_5 | 1212 | 85.9 | 0.334 | 0.02 | 0.18 | 3510 | 370 |

erage of 32 individual vector lines or profiles. The specific x -locations corresponding to the various L values and the local test section heights, h , are presented in Table 1. The test conditions are Test APG and Test FPG representing tests in the APG and FPG channels, respectively. It should be noted that if the 4.5 mm thick acrylic sheet that was screwed onto the bottom wall of the test section is taken into account, the design values of h at the upstream section of the FPG and APG channels without the ribs (FPG-SM and Test APG SM) should be $h=85.5$ mm and 55.5 mm, respectively. The 1.5 mm difference between those design values and the values reported in Table 1 is likely due to nonuniformity in the thickness of the acrylic sheets used to fabricate the bottom and top walls of the channel as well as the 4.5 mm insert. Table 1 also includes the maximum velocities, U_{\max} , the velocity gradients, dU_{\max}/dx , accelerating/decelerating parameters, $K=(\nu/U_{\max}^2)(dU_{\max}/dx)$, and the Reynolds numbers based on the lower and upper boundary layer momentum thicknesses, $Re_{\theta_L}=U_{\max}\theta_L/\nu$ and $Re_{\theta_U}=U_{\max}\theta_U/\nu$, respectively. The dU_{\max}/dx value for each plane was estimated as the slope of the least square linear fit to U_{\max} versus x shown in Fig. 3(a). Note that the subscripts L and U in this table and in subsequent sections denote the lower and upper boundary layer parameters, respectively.

3 Results and Discussions

3.1 Boundary Layer Characteristics. The local values of U_{\max} were obtained at five selected x -locations in each of the planes P_1-P_5 over the ribs. For clarity, only three of these five values of U_{\max} normalized by the upstream smooth-wall value of $U_{\max,SM}=0.460$ m/s (i.e., $U_{\max}^*=U_{\max}/U_{\max,SM}$) are plotted in Fig. 3(a). It should be noted that x^* is the value of x normalized by 1000 mm, which is the distance between the start (O) and end (P) of the variable section of the channels (Fig. 1). As noted in Sec. 2.1, Shah and Tachie [24] conducted velocity measurements in the APG and FPG channels but without ribs on the channel floor. In Fig. 3(a), their data at approach velocities identical to those studied in the present study are denoted as SM-FPG and SM-APG for the favorable and adverse pressure gradients, respectively. The solid and dash lines in the figure represent the distributions of U_{\max}^* that would be obtained along the APG and FPG channels, respectively, if the flow were inviscid. As expected, U_{\max}^* increases and decreases monotonically with x^* in the converging and diverging sections of the channels ($0 < x^* < 1$), respectively. There is no significant difference between the inviscid distribution and measured smooth-wall values. In both channels, however, the ribs increased U_{\max}^* values by up to 20% compared with the corresponding smooth-wall values. This increase is partly due to blockage produced by the ribs as well as the higher flow

resistance and growth of the boundary layer over the ribs. Table 1 also shows that K values decreased consistently from L_1 to L_5 for the FPG but for the APG, it decreased from L_1 to L_3 and then increased.

Figure 3(b) depicts the variation of y_{\max} with x^* under the influence of FPG and APG. Upstream of the converging and diverging sections (L_1), $y_{\max}/h=0.50$ and 0.73 for the FPG and APG flows, respectively. The higher value for the APG is likely due to higher blockage ($k/h=0.11$) than that in the FPG ($k/h=0.07$). In

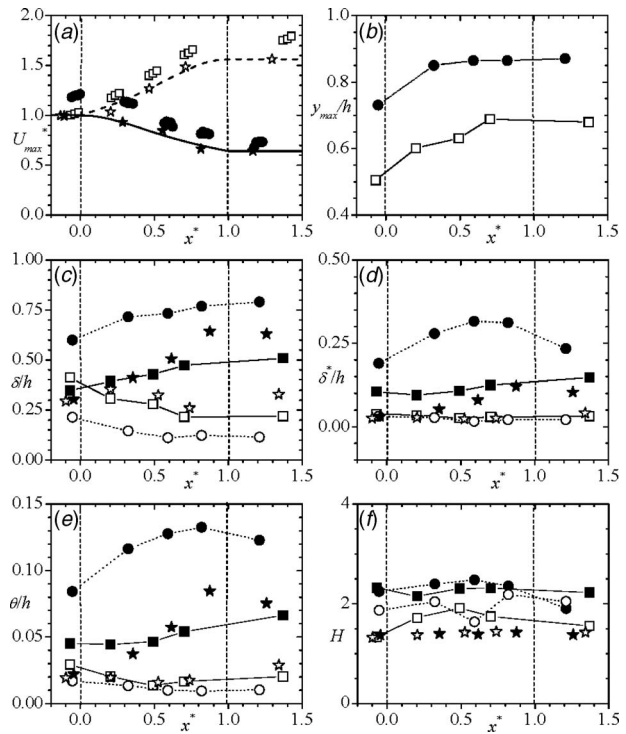


Fig. 3 Variation of boundary layer (BL) parameters with x -locations. $x^*=x/1000$. (a) Local maximum velocity, U_{\max} . U_{\max}^* is U_{\max} normalized by the maximum velocity at location L_1 , (b) y -location of the maximum velocity, y_{\max} , (c) BL thickness, δ , (d) BL displacement thickness, δ^* , (e) BL momentum thickness, θ , and (f) the shape factor, H . The vertical dash lines indicate the start and end of the converging/diverging sections. Note. y_{\max} , δ , δ^* , and θ are normalized by the local channel height, h . Symbols in (a): inviscid flow in APG (---), inviscid flow in FPG (—), APG (●), FPG (□), SM-FPG (☆), and SM-APG (★). Symbols in the rest of the figure: (---□---) FPG upper, (---●---) FPG lower, (---○---) APG upper, and (---●---) APG lower.

the LES study by Cui et al. [8] over transverse square ribs with $p/k=5$ and $k/h=0.2$, a value of $y_{\max}/h=0.83$ was reported. The effects of rib roughness and pressure gradient produced in asymmetric FPG and APG channels are to skew the mean velocity distribution and shift the location of the maximum velocity toward the upper curved wall. As will be shown later, APG skewed the mean profiles more than the FPG did. For example, $y_{\max}/h=0.86$ and 0.68 , respectively, at the last measurement locations (L_4) within the converging ($x^*=0.807$) and diverging ($x^*=0.913$) sections.

The local values of the boundary layer, displacement, and momentum thicknesses normalized by the corresponding local value of h (i.e., δ/h , δ^*/h , and θ/h) are shown in Figs. 3(c)–3(e), respectively. These parameters were calculated using the spatially averaged mean velocity profiles. Note that δ_U and δ_L , respectively, denote upper and lower boundary layer thicknesses. As will be shown in Fig. 6(a), the spatially averaged mean velocity profiles have a narrow region of weak flow reversal or negative velocities. The boundary layer parameters for the lower boundary layer (δ_L , δ_L^* , and θ_L) were computed with and without the negative velocities. The average percentage differences between the values computed using the profiles with and without the negative velocities were 10%, 20%, and 1.2% for the APG section and 17%, 45%, and 5% for the FPG section. It should be noted that the parameters for the lower boundary layer plotted in Fig. 3 are those obtained without the negative velocities. The shape factor ($H=\delta^*/\theta$), which is a measure of the effectiveness of turbulent flow and surface condition to enhance mass deficit in comparison to momentum deficit, is plotted in Fig. 3(f). In the absence of ribs on the channel walls, the data reported by Shah and Tachie [24] revealed that APG increased the values of δ/h , δ^*/h , and θ/h compared with those obtained in the FPG channel but the shape parameter is independent of pressure gradient. Aubertine and Eaton [4] also reported an increase in δ^* and θ in their diverging section. Because of enhanced mass and momentum flux deficits associated with rib roughness, the values of δ^* and θ at the upstream parallel section are significantly larger for the lower boundary layer than those for the upper boundary layer. Within the diverging section of the APG channel ($0 < x^* < 1$), rib roughness and APG increased δ_L^*/h and θ_L/h by 66% and 50%, respectively, compared with the corresponding upstream values. For the FPG channel, the values of δ_L^*/h and θ_L/h over the ribs in the converging section are not significantly different from the corresponding upstream values. Furthermore, the values of δ_L^*/h and θ_L/h in the diverging section are approximately 200% and 150%, respectively, higher than those obtained in the converging section. Irrespective of the pressure gradient, the rib roughness enhanced the values of H compared to the values obtained over a smooth wall.

3.2 Streamlines and Isocontour of Mean Vorticity In and Just Above the Cavity.

The streamlines and mean vorticity isocontours were obtained to reveal some of the qualitative features of the mean flow pattern. Because of space consideration, these quantities are plotted for only three measurement planes: an upstream plane (Test FPG- L_1) and typical planes within the diverging section (Test APG- L_3) and converging section (Test FPG- L_3). The streamlines shown in Figs. 4(a), 4(c), and 4(e) reveal stable clockwise rotating vortices inside the cavities. The primary vortices filled most of the cavities and prevented the outer flow from reattaching onto the cavity floor. Smaller secondary corner counter-rotating vortices are also formed between the upstream ribs and the primary vortices. The streamlines are nearly parallel close to the top plane of the ribs. This observation is consistent with the LES results of Cui et al. [8] over square ribs. Because $\partial U/\partial y > \partial V/\partial x$ close to the ribs, the values of the mean vorticity ($\Omega = \partial V/\partial x - \partial U/\partial y$) are negative. Figures 4(b), 4(d), and 4(f) re-

veal regions of intense shear layer in the vicinity of the ribs. Close to the ribs, the dimensionless values of Ω are higher for the FPG than for the APG.

3.3 Mean Velocities, Turbulent Intensities, and Momentum Fluxes at Interface.

The mean streamwise velocity (U), mean momentum flux ($-UV$), streamwise turbulent intensity (u), and turbulent moment flux ($-uv$) at the top plane of the ribs ($y=k$) are shown in Fig. 5. Data are plotted at L_2 and L_5 for both APG and FPG. In each case, the corresponding upstream profiles (at L_1) are included for comparison. In each plot, the data are plotted on the scale: $0 \leq x'/w \leq 1$. As shown in Fig. 1(d), $x'/w=0$ and $x'/w=1$, respectively, correspond to the downstream corner of the upstream rib and the upstream corner of the downstream rib. Since the top plane corresponds to the interface between the cavities and the overlying boundary layer, these data sets provide insight into the interaction between flow within the cavities and the overlying boundary layer. Figure 5(a) shows that the flow accelerates ($\partial U/\partial x > 0$) in the region $x'/w < 0.60$ and decelerates ($\partial U/\partial x < 0$) in the region $x'/w > 0.68$. As a result, the normal production term $-u^2 \partial U/\partial x$ in the turbulent kinetic energy transport equation will be negative close to the upstream rib ($x'/w=0$) and positive adjacent to the downstream rib ($x'/w=1$). Therefore, the normal production term will augment turbulence production close to the downstream ribs but will attenuate production close to the upstream ribs. The combined effect of APG and rib roughness is to reduce the mean velocity along the interface compared with the data obtained for a similar rib roughness with no pressure gradient or rib roughness with FPG.

The mean momentum fluxes ($-UV$) at the interface are related to momentum transport between the cavities and the overlying boundary layer. Figure 5(b) shows negative values close to the region where the flow accelerates and positive close to where the flow decelerates. Therefore, unlike smooth-wall fully developed channel flows, the dynamic role of $-UV$ in momentum transport cannot be neglected close to the ribs. There is no significant difference in the negative peaks; however, the positive peaks are generally higher for the FPG (0.8%) than for the APG (0.4%).

The turbulent intensity (Fig. 5(c)) increases immediately downstream of the upstream ribs to a maximum value of $u/U_{\max} \approx 17\%$ for the FPG and 14% for the APG and then decrease to the no-slip value on the downstream rib. In general, v -profiles (not shown) are similar to the u -profiles but with a lower peak value of 13%. The peaks of turbulent momentum fluxes ($-uv$) in Fig. 5(d) are higher for the FPG (1.2%) than for the APG (0.6%). The nonzero values of $-uv$ are indicative of momentum exchange between the cavities and the overlying boundary layer. The mean and turbulent momentum fluxes are of opposite sign in the region where the mean flow accelerates ($x'/w < 0.60$). In this region, the absolute values of turbulent momentum fluxes are larger than the corresponding values of the mean momentum fluxes. On the other hand, the mean and turbulent momentum fluxes are both positive and have similar value in the region where the mean decelerates ($x'/w > 0.68$). As will be explained subsequently, the low values of u and $-uv$ observed for the APG are due to relatively lower mean velocity gradient ($\partial U/\partial y$) and reduced production of u^2 and $-uv$ close to the ribs.

4 Development of Profiles of the Mean and Turbulent Quantities

The profiles of the mean streamwise velocity, turbulent intensities, and Reynolds shear stress are shown in Fig. 6. At each plotting station, four profiles representing the upstream (L_1) and each specific location (L_2 , L_3 , and L_5) for both FPG and APG are plotted. The smooth-wall profile at the upstream section of the FPG channel is also plotted for comparison. For that particular test condition, both the top and bottom channel walls are smooth and parallel to each other. As a result, the flow resistance is similar on

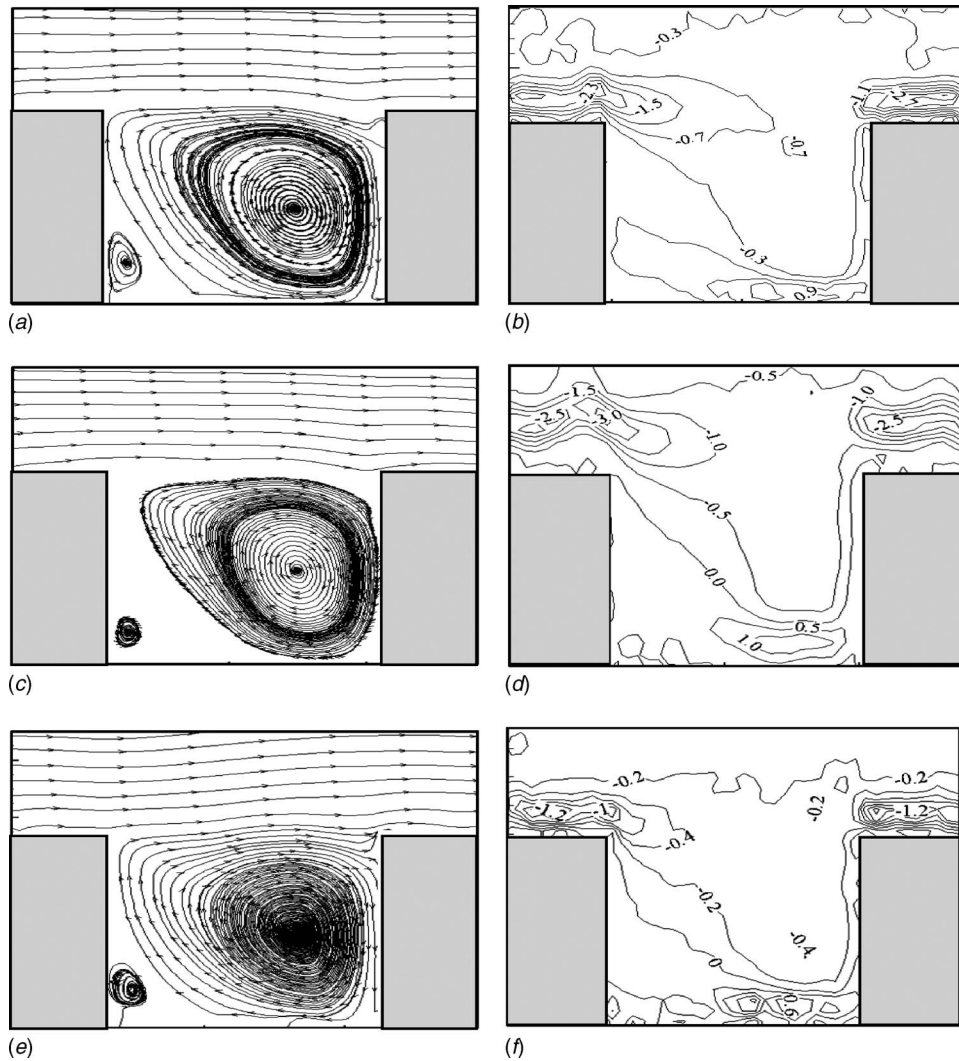


Fig. 4 Streamlines and their corresponding isocontours of the mean vorticities for selected locations. The vorticities are normalized by local maximum velocity, U_{\max} , and rib height, k . ((a) and (b)) Location L_1 without a pressure gradient, ((c) and (d)) location L_3 in a favorable pressure gradient, and ((e) and (f)) location L_3 in an adverse pressure gradient.

both walls and the mean profile is more symmetric with respect to the channel centerline than when ribs are installed on the bottom wall (i.e., L_1 for the APG and FPG channels). Similar to previous rough-wall measurements and LES data over ribs, the higher drag characteristics of the lower rib-roughened wall reduced the mean velocity substantially compared with the data obtained if the lower wall were smooth. When the flow is subjected to pressure gradient, the velocity distribution becomes even more complicated.

The combined effects of APG and rib roughness, for example, are to further reduce the mean velocity in the lower boundary layer and increase the asymmetry of the mean profile compared with the profile obtained over the ribs in the upstream section of the APG channel. This observation is consistent with the data reported by Tachie [21] in APG turbulent flow over transverse ribs. The FPG, on the other hand, has little effects on the mean velocity profiles (L_2 and L_3). It should be noted that the mean flow distortion produced by the combined effects of rib roughness and APG is more significant than the data obtained in the APG channel without rib roughness [24]. Perhaps a more important observation from Fig. 6(a) is that the variation of U with y in the lower boundary layer is more gradual for APG compared with FPG and the upstream profiles. Since $\partial U / \partial y$ plays an important role in the

production of turbulent kinetic energy and Reynolds stresses, one would expect substantial pressure gradient effects on turbulence production.

The profiles of u and v obtained over the smooth wall and upstream ribs show two distinct peaks: one close to the lower wall and the other near the upper wall (Figs. 6(b) and 6(c)). Similar to previous experimental as well as LES and DNS studies, wall or rib roughness enhanced the turbulence levels. One of the salient features of the FPG profiles is that they decay very rapidly from their peak values. Similar to the mean velocity profiles, the effects of the FPG on the turbulent intensities in the presence of rib roughness are not significant although the turbulence levels reported in Figs. 6(b) and 6(c) close to the ribs are higher than when the flow is subjected to FPG in the absence of rib roughness [24]. The turbulent intensities measured in the APG flow over the rib roughness are significantly higher than would be obtained for a smooth-wall APG flow. Figure 6 shows that, in the immediate vicinity of the ribs, APG reduced the values of v/U_{\max} and u/U_{\max} substantially but beyond $y'/h > 0.4$, their values become significantly higher than those in the FPG. The Reynolds shear stress plotted in Fig. 6(d) show qualitative features similar to those observed for the turbulent intensities. For example, profiles for the FPG are higher close to the ribs but decay dramatically and

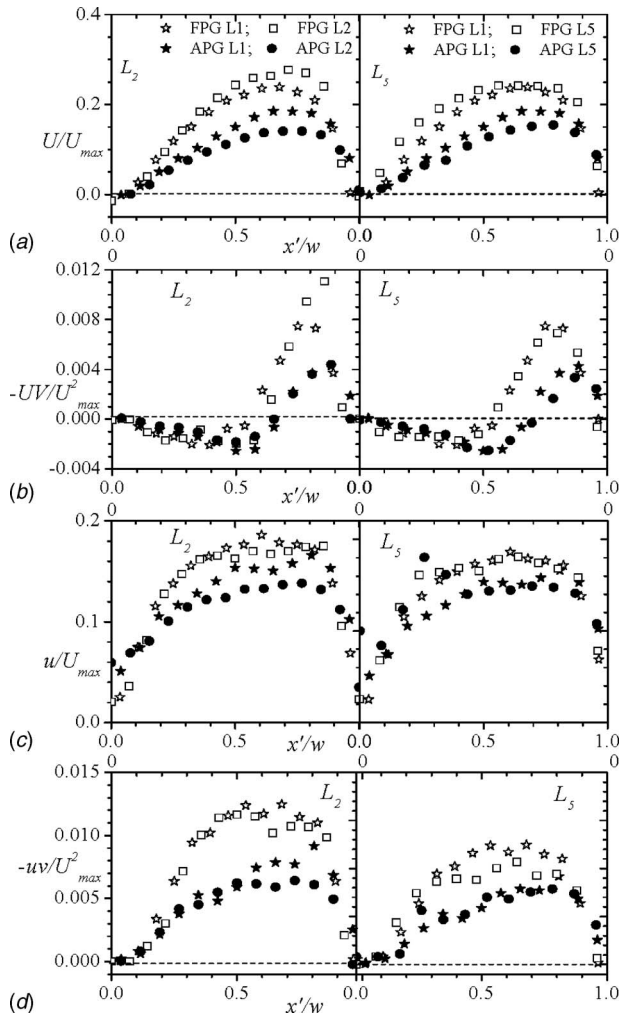


Fig. 5 Mean velocities, turbulent intensities, and momentum fluxes at the interface, $y=0$, for selected test conditions. (a) Streamwise velocity, (b) mean momentum flux, (c) streamwise turbulent intensity, and (d) turbulent momentum flux.

become lower than the values measured in the APG. The magnitude of the lower peaks of $-uv$ is significantly higher than the corresponding values in the upper boundary layer.

The general trends observed for the spatially averaged profiles of the turbulent intensities and Reynolds shear stress above can be explained by the turbulence production terms. In two-dimensional turbulent flows, the production terms in the transport equations for the normal stress (u^2), Reynolds shear stress ($-uv$), and turbulent kinetic energy (k) are, respectively, given by $P_{uu} = [-u^2 \partial U / \partial x - uv \partial U / \partial y]$, $P_{-uv} = [u^2 \partial V / \partial x + v^2 \partial U / \partial y - uv(\partial U / \partial x + \partial V / \partial y)]$, and $P_k = [-uv(\partial U / \partial y + \partial V / \partial x)] - [(u^2 \partial U / \partial x + v^2 \partial V / \partial y)]$. The present data show that the dominant mean strain is $\partial U / \partial y$. Meanwhile, $\partial U / \partial x = -\partial V / \partial y$ due to mass conservation and $u^2 \partial V / \partial x \ll v^2 \partial U / \partial y$ so that $P_{uu} \approx -uv \partial U / \partial y$, $P_{-uv} \approx v^2 \partial U / \partial y$, and $P_k \approx -uv \partial U / \partial y$. Typical profiles of $-uv \partial U / \partial y$ and $v^2 \partial U / \partial y$ for FPG and APG are compared with the upstream profile in Figs. 7(a) and 7(b). While the production terms for the FPG are much larger than those obtained for the APG close to the ribs, the FPG profiles decayed and became nearly zero in the region $y/h > 0.25$. For the APG, on the other hand, nonzero values of $-uv \partial U / \partial y$ and $v^2 \partial U / \partial y$ are evident across most of the channel. The significant turbulence production observed outside the immediate vicinity of the ribs in the APG channel is attributed to nonzero values of

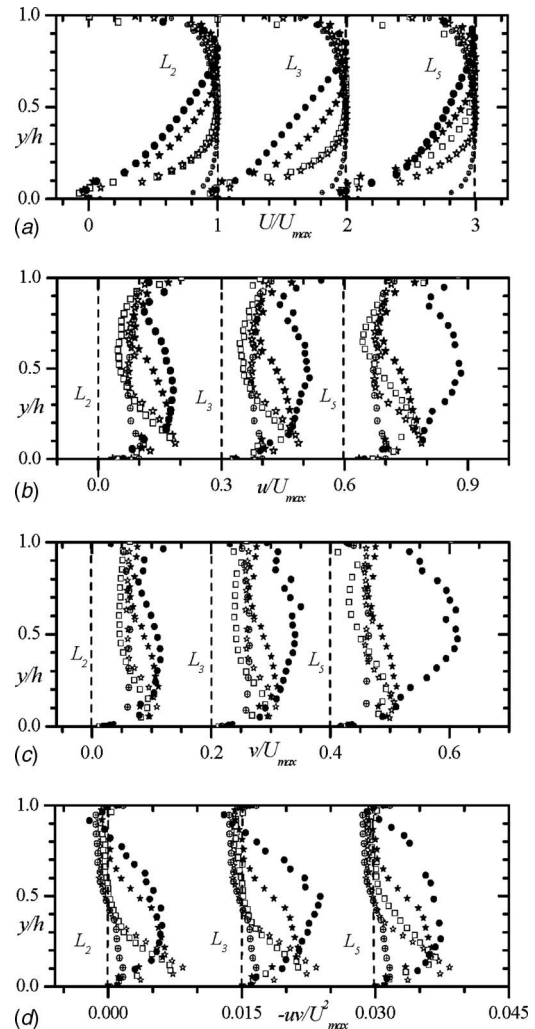


Fig. 6 Development of spatially averaged mean and turbulent quantities. (a) Streamwise mean velocity, (b) streamwise turbulent intensity, and (c) Reynolds shear stress. The symbols are as follows: smooth wall (\oplus), upstream of the converging section (\star), within the converging section (\square), upstream of the diverging section (\star), and within the diverging section (\bullet).

$\partial U / \partial y$ observed in Fig. 6(a) in that region. It is believed that the lower values of u , v , and $-uv$ close to the ribs in the APG channel (compared with those in the FPG channel) are due to the reduced turbulence production observed in Figs. 7(a) and 7(b). Meanwhile, the non-negligible values of u , v , and $-uv$ in the central domain of the APG channel are due to the higher turbulence production in that region.

It has been suggested that the Reynolds stress ratios may be used to provide a rough guide to the large-scale anisotropy [30]. With regard to the normal stresses, the flow becomes more isotropic if v^2/u^2 tends to unity. Since surface roughness or APG tends to increase the levels of the Reynolds stresses, the flow would become more isotropic if roughness or APG enhanced v^2 more significantly than u^2 is increased. For the FPG on the other hand, a tendency toward isotropy would imply that u^2 is attenuated faster than v^2 . In the measurements conducted in the present APG and FPG channels but without the ribs on the channel floor [24], it was reported that the stress ratio, $-uv/u^2$, shows increasing and decreasing trends, respectively, away from the walls in the APG and FPG channels. This was attributed to a greater rate of increase of $-uv$ compared to u^2 for APG whereas in the FPG channel, u^2 decays faster than $-uv$. The data showed no systematic pressure

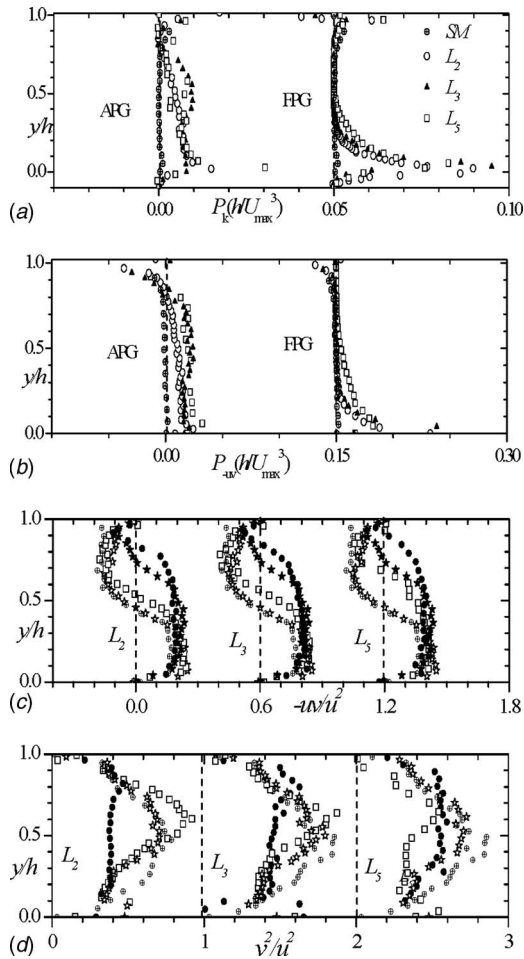


Fig. 7 Profiles of spatially averaged turbulence production terms and stress ratios at selected locations. (a) $P_k = -uv\partial U/\partial y$, (b) $P_{uv} = v^2\partial U/\partial y$, (c) stress ratio, $-uv/u^2$, and (d) stress ratio, v^2/u^2 . P_k and P_{uv} are normalized by local maximum velocity, U_{max} and height, h . Symbols in (b) as in (a) and in (c) and (d) as in Fig. 6.

gradient effects on v^2/u^2 close to a smooth wall. Away from the wall, however, v^2/u^2 was reduced within the APG channel but increased in the FPG channel. In contrast, measurements in an equilibrium APG boundary layer by Skåre and Krogstad [5] revealed that the distribution of v^2/u^2 is independent of the pressure gradient.

Notwithstanding the significant differences between the turbulent intensities and Reynolds shear stress in the rib-roughened FPG and APG channels (Fig. 6), profiles of $-uv/u^2$ (Fig. 7(c)) are nearly independent of pressure gradient. The only difference is that the y -location where $-uv/u^2$ changes sign varies with location and also with pressure gradient. This implies that unlike the smooth-wall results [24], rib roughness and pressure gradient (both APG and FPG) increase the levels of $-uv$ and u^2 proportionately. The v^2/u^2 profiles (Fig. 7(d)) show collapse of the smooth-wall and upstream (L_1) values. Therefore, notwithstanding the enhanced turbulence levels over the ribs, rib roughness (in the absence of pressure gradient) does not promote a tendency toward local isotropy. This observation is consistent with the DNS results reported by Krogstad et al. [30] over smooth and rib-roughened walls in a channel. It also implies that although the production of turbulent kinetic energy depends on wall roughness (Fig. 8), once the energy is transferred to the u^2 -component, the mechanism by which it is redistributed into the various components of the normal stresses is independent of surface roughness.

When the flow over the ribs is subjected to APG, the peak values increased from $v^2/u^2=0.25$ at L_2 to 0.6 at L_5 . Favorable pressure gradient, on the other hand, decreased the peak values from $v^2/u^2=0.90$ at L_2 to 0.5 at L_5 . It appears that a more severe APG tend to make the flow over the rib roughness more isotropic while the increasing FPG has the opposite effects.

5 Profiles of Mean Velocity and Turbulent Quantities in the Lower Boundary Layers

5.1 Mean Velocity in Outer Coordinates. The profiles of the mean velocities in the lower boundary layer are shown in Figs. 8(a) and 8(b). The U and y are normalized by the local maximum velocity, U_{max} , and the boundary layer thickness, δ_L , respectively. Figures 8(a) and 8(b) show that profiles on the ribs are “less full” compared to SM. The profiles at the various measurement locations nearly collapsed for the FPG. For the APG, however, the profiles increasingly become less full from L_1 to L_3 but the profile at L_5 tends toward the upstream and smooth-wall profiles.

5.2 Mean Velocity in Inner Coordinates. The log law. The log law for a rough wall may be written as $U^+ = \kappa^{-1} \ln y^+ + B - \Delta B^+$, where κ and B are the log law constants (with $\kappa=0.41$ and $B=5.0$) and ΔB^+ is the roughness shift ($\Delta B^+=0$ for a smooth wall). In rough-wall experiments, it is customary to define y as the distance from the top plane of the roughness elements y^* plus a virtual origin d_0 (i.e., $y=y^*+d_0$). The log law has been applied in APG turbulent flows over a smooth surface. Kader and Yaglom [31] suggested that the inner region of the mean velocity profile for APG turbulent flow over a rough surface can also be described by the log law. Experience from prior rough-wall experiments shows that U_τ values determined from the log law are susceptible to uncertainty because d_0 and ΔB^+ are not known a priori. In this study, the log law was fitted to the measured mean velocity data and d_0 and U_τ were adjusted to ensure a reasonable agreement between the measured data and the log law. Based on the DNS results by Leonardi et al. [13] over square ribs initial guess values of $d_0/k=0.15$, and the values of d_0 and U_τ were then optimized. The measurement uncertainties were estimated to be $\pm 5\%$ and $\pm 10\%$, respectively, for the smooth wall and ribs. As shown in Table 2, U_τ values decrease along the channel for the APG but increase for the FPG. The values of skin friction coefficient $C_f = 2(U_\tau/U_e)^2$ are nearly constant for the APG whereas the C_f slightly decreases for the FPG.

The mean velocity profiles in the inner coordinates are shown in Figs. 8(c) and 8(d). As expected the APG increased the wake component of the velocity profile compared to the upstream location. The wake parameter, $\Pi = \Delta U_{max}^+ \kappa/2$, increased from 0.18 at L_1 to 0.34 at L_4 in the APG and from 0.06 at L_1 to 0.16 at L_4 in the FPG. The values of ΔB^+ estimated from Figs. 8(c) and 8(d), and k_s^+ determined from the following relation proposed by Ligrani and Moffat [32]: $\Delta B^+ = \kappa^{-1} \ln(k_s^+) + B - D$ (where $D=8.5$) are also summarized in Table 2. The values of ΔB^+ (11.4 and 11.8) at the upstream parallel section are similar to those reported in the DNS by Leonardi et al. [13] at $p/k=4$ but lower than $\Delta B^+=13.2$ in the LES study by Cui et al. [8] at $p/k=5$. The FPG decreased the values of ΔB^+ slightly to 10.1 while the APG increased ΔB^+ to 14.6. Following the roughness classification proposed by Schlichting [33] all the rib surfaces studied in this work are in the fully rough regime. Table 2 also shows that in order to produce the amount of flow resistance over the ribs at the upstream (i.e., L_1) of APG or FPG using monodispersed equivalent sand grains, sand grains whose diameter is about $2k$ will be required. This value is also smaller than $k_s/k=3.2$ reported by Cui et al. [8]. At the last measurement location within the variable section (L_4) in the APG and FPG, $k_s=9k$ and $0.8k$, respectively, are required.

The power law. One of the difficulties in applying the log law to rough-wall turbulent flows is the large number of unknowns. It

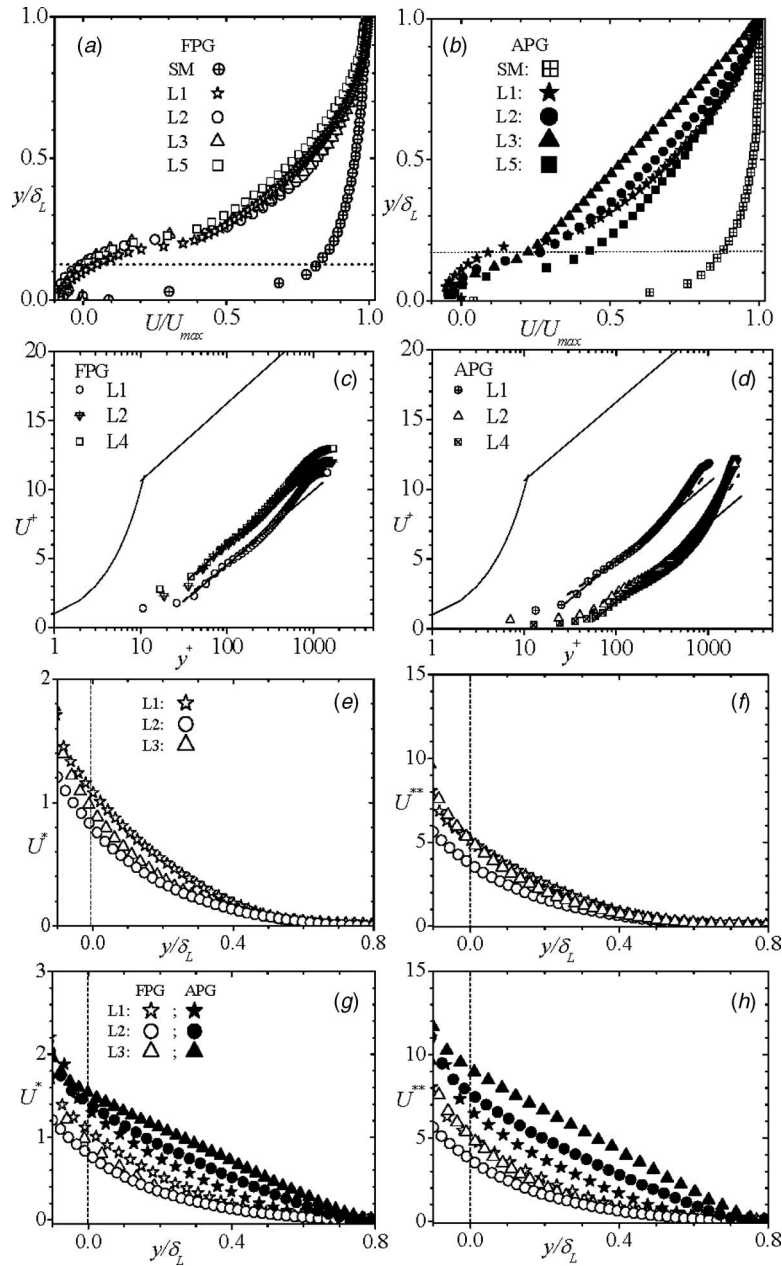


Fig. 8 Spatially averaged mean velocity and mean velocity defect profiles in the lower boundary layer. Outer coordinates. (a) favorable pressure gradient (FPG) and (b) adverse pressure gradient (APG). Inner coordinates. (c) FPG and (d) APG. Defect profiles for the FPG normalized by (e) $U_{\max} \delta^* / \delta$ and (f) U_{τ} , and for both FPG and APG normalized by (g) $U_{\max} \delta^* / \delta$ and (h) U_{τ} . The solid lines in (c) and (d) are as follows. $U^+ = 2.44 \ln y^+ + 5$ and $U^+ = 2.44 \ln y^+ + 5 - \Delta B^+$. The Dash lines are $U^+ = C_i [(y^+ + a^+)]^\gamma$. Symbols in (f) as in (e) and in (h) as in (g). Note. $U^* = (U_{\max} - U) / U_{\max} \delta^* / \delta$; $U^{**} = (U_{\max} / U) / U_{\tau}$.

can be seen from Fig. 8(d), for example, that the region over which the measured data and the log law overlap is fairly narrow. This is partly due to the relatively low Reynolds numbers and the APG, both of which tend to reduce the overlap region. A variety of power laws have been proposed as an alternate formulation to model the mean velocity profile of near-wall turbulent flows. Buschmann and Gad-el-Hak [34] provided a summary of the various power law formulations. In the present study the power law proposed by George and Castillo [35] is also used to model the mean velocity profile and to determine the friction velocity and the results are compared with those obtained from the log law.

The power laws in the outer and inner coordinates are given, respectively, by

$$U/U_e = C_o [(y+a)/\delta]^\gamma \quad (1)$$

$$U^+ = C_i [(y^+ + a^+)]^\gamma \quad (2)$$

where the power law constants C_o , C_i , and γ are weak functions of Reynolds number ($\delta^+ = \delta U_{\tau} / \nu$) and ($a^+ = -16$) represents a shift in origin for measuring y associated with growth of the mesolayer

Table 2 Summary of log law and power law parameters

| Test | L | Log law | | | | | Power law | | | | | | |
|------|-------|----------------|--------|--------------|---------|---------|-----------|-------|----------|-------|----------------|---------------------|--|
| | | U_τ (m/s) | C_f | ΔB^+ | k_s^+ | k_s/k | C_o | C_i | γ | a^+ | U_τ (m/s) | ΔU_τ (%) | |
| FPG | L_1 | 0.041 | 0.0159 | 11.4 | 449 | 1.8 | 1.1 | 0.99 | 0.35 | -25 | 0.0413 | 0.03 | |
| | L_2 | 0.046 | 0.0145 | 10.1 | 263 | 1.0 | 1.1 | 2.12 | 0.25 | -30 | 0.0457 | -0.03 | |
| | L_3 | 0.052 | 0.0128 | 10.1 | 263 | 0.8 | | | | | | | |
| | L_4 | 0.058 | 0.0123 | 10.1 | 263 | 0.8 | 1.1 | 2.37 | 0.25 | -30 | 0.0578 | -0.02 | |
| APG | L_1 | 0.046 | 0.0140 | 11.8 | 529 | 1.9 | 1.1 | 0.97 | 0.35 | -20 | 0.0455 | -0.05 | |
| | L_2 | 0.044 | 0.0143 | 14.6 | 1666 | 6.3 | 1.0 | 0.52 | 0.40 | -45 | 0.0452 | 0.12 | |
| | L_3 | 0.034 | 0.0144 | 14.6 | 1666 | 8.2 | | | | | | | |
| | L_4 | 0.031 | 0.0145 | 14.6 | 1666 | 9.0 | 1.0 | 0.26 | 0.50 | -50 | 0.0315 | 0.05 | |

region. They showed that the friction law is also a power law given by

$$U/U_e = (C_o/C_i)^{1/(1+\gamma)} [(U_e \delta/\nu)]^{-\gamma/(1+\gamma)} \quad (3)$$

The above power law has been used extensively to model low Reynolds number in open channel turbulent flows over diverse roughness elements [36], in ZPG turbulent boundary layers over smooth and rough surfaces [37] and in APG over ribs [21]. Because the power law in the outer coordinates does not contain U_τ , Eq. (1) was first fitted to the measured data to determine C_o and γ . With the values of C_o and γ , Eqs. (2) and (3) were used iteratively to determine C_i and U_τ . Figures 8(c) and 8(d) show the power law fits (dash lines) in the inner coordinates. During the fitting process, it was found that different values of a^+ were needed for the various ribs and location to achieve good agreement between the lower portions of the measured data and the power law. It should be noted that the exact value of a^+ used for a particular profile did not significantly change the values of C_o , C_i , and γ (and U_τ); it only affects the quality of agreement between the measured data and the power law close to the ribs. The values of a^+ as well as the power law constants and friction velocities used to obtain the fits shown in Figs. 8(c) and 8(d) are summarized in Table 2. The values of a^+ are different from $a^+ = -16$ proposed in the original formulation for a smooth surface. It is also important to note that the magnitude of a^+ values is higher in the converging and diverging sections than at the upstream locations, and the APG values are generally higher than the FPG values. These results demonstrate that as the mean velocity profile becomes less full, so does the magnitude of a^+ . The values of C_i decreased and those of γ increased for the APG whereas C_i increased and those of γ decreased for the FPG. Similar to prior studies [37,21], it is observed that the power law describes a wider region of the measured data compared to the log law. At L_4 in both FPG and APG, for example, the log law described the measured data up to $y^+ = 320$ and 1050, respectively, while the power law described the data up to $y^+ = 1050$ and 1550, respectively. As shown in Table 2, the differences between the U_τ values obtained from the log law and those obtained from the power law are within the measurement uncertainty.

5.3 Mean Velocity Defect Profiles. The outer region of the mean velocity is often studied using the mean velocity defect profiles. Although the friction velocity, U_τ , remains the most widely used characteristic velocity scale for the outer layer, Zagarola and Smits [38] proposed that the mixed scaling, $U_{max} \delta^* / \delta$, is the appropriate characteristic velocity for the mean defect profile. Tachie et al. [20] showed that over a particular rib type, the mixed scaling collapses the upstream profile and those obtained in the converging sections. Figures 8(e) and 8(f) show the FPG defect profiles normalized by the mixed scaling and the friction velocity, respectively, whereas Figs. 8(g) and 8(h) are the defect profiles for both FPG and APG normalized by the mixed scaling and the

friction velocity, respectively. Figures 8(e) and 8(f) show that FPG profiles collapse very well in the region $y/\delta_L > 0.4$. The profiles in Figs. 8(g) and 8(h) show that neither the mixed nor the friction velocity scaling collapsed the profiles in the APG channel. The figures also shows that the defect profiles obtained in the APG fall less rapidly compared to the FPG profiles.

5.4 Turbulent Intensities and Reynolds Stresses in Inner Coordinates. The profiles of the turbulent intensities and Reynolds shear stress at the lower boundary layer in the inner coordinates are shown in Fig. 9. In the immediate vicinity of the ribs,

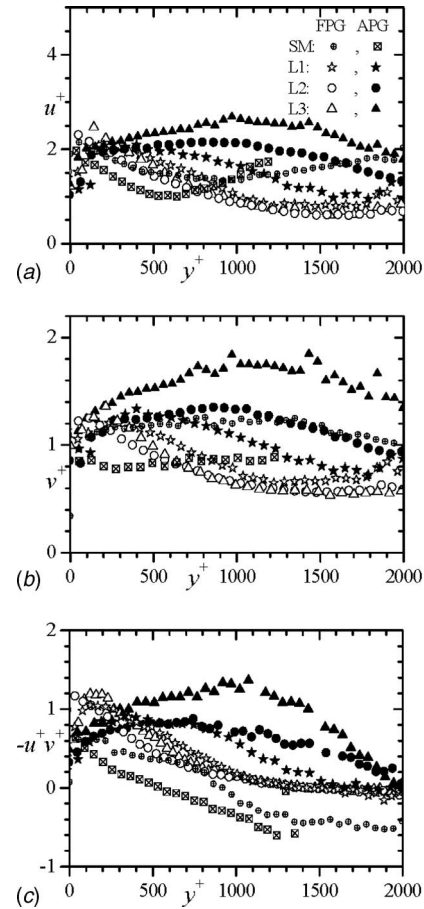


Fig. 9 Spatially averaged turbulent intensities and Reynolds shear stresses in the lower boundary layer in the inner coordinates. (a) Streamwise turbulent intensity, (b) transverse turbulent intensity, and (c) Reynolds shear stress. All symbols are as in (a).

values of u^+ , v^+ , and $-u^+v^+$ for APG are lower than those measured in the FPG and at the upstream section (L_1). However, the FPG profiles decay rapidly from their peak values so that the profiles for the APG are significantly higher across the outer 80% of the boundary layer. The distributions of the turbulent intensities and Reynolds shear stress are more insensitive to changes in the FPG as evident in the reasonable collapse among the profiles obtained upstream and within the converging section. On the other hand, as the flow decelerated through the diverging section, the values of u^+ , v^+ , and $-u^+v^+$ increased consistently. The profiles of v^+ appear to be the most affected by the APG.

6 Summary and Conclusions

This paper reported a comprehensive PIV study of favorable and adverse pressure gradient turbulent flow over two-dimensional square ribs. The results obtained in this study show that the presence of ribs on the straight bottom wall shifts the location of the maximum velocity toward the upper walls. As a result, the boundary layer that develops on the smooth upper wall becomes thin with characteristic low Reynolds numbers. The degree of shift is highest for the adverse pressure gradient. The boundary layer thicknesses are significantly larger for the rib-roughened lower boundary layer than the corresponding values obtained in the smooth-wall upper boundary layers. The boundary layer parameters (and, therefore, mass and momentum deficit) in the lower boundary layer are significantly higher for the adverse pressure gradient than for the favorable pressure gradient; however, no significant effect of pressure gradient was in the upper boundary layer.

The data obtained at the top plane of the ribs demonstrate non-negligible vertical motion and interaction between the cavities and overlying boundary layers. The values of the mean momentum flux are quite high and comparable to the Reynolds shear stress at some locations. Because of the manner in which pressure gradient modifies the mean velocity and turbulence production, it was found that the streamwise turbulence intensity and Reynolds shear stress are generally lower in the diverging section than in the converging section.

In the lower boundary layer, rib roughness and adverse pressure gradient act to reduce the mean velocity considerably in comparison to the rib-roughened profile without a pressure gradient or an adverse pressure gradient profile over a smooth surface. Similarly, the combined effects of rib roughness and adverse pressure gradient on the turbulent intensities and Reynolds shear stress are significantly higher than when these effects are applied in isolation. Although favorable pressure gradient and rib roughness modified the mean and turbulent quantities than would be obtained over a smooth wall (with or without a favorable pressure gradient), the mean flow and turbulent quantities over rib roughness are independent of a favorable pressure gradient. Another salient observation was that the profiles of turbulence production revealed two peaks in the lower boundary layer for the adverse pressure gradient in comparison to a single peak in the favorable pressure gradient and upstream profiles. The mechanism responsible for redistributing turbulent kinetic energy into the various components of the normal stresses is independent of rib roughness. Significant changes are observed, however, when the flow over rib roughness is subject to the adverse or favorable pressure gradient.

Acknowledgment

The support of this work by the Natural Sciences and Engineering Research Council of Canada and The Canada Foundation for Innovation is gratefully acknowledged.

References

- [1] Blackwelder, R. F., and Kovaszny, L. S. G., 1972, "Large-Scale Motion of a Turbulent Boundary Layer During Relaminarization," *J. Fluid Mech.*, **53**, pp. 61–83.
- [2] Narasimha, R., and Sreenivasan, K. R., 1973, "Relaminarization in Highly

- Accelerated Turbulent Boundary Layers," *J. Fluid Mech.*, **61**, pp. 417–447.
- [3] Ichimiya, M., Makamura, I., and Yamashita, S., 1998, "Properties of a Relaminarizing Turbulent Boundary Layer Under a Favorable Pressure Gradient," *Exp. Therm. Fluid Sci.*, **17**, pp. 37–48.
- [4] Aubertine, C. D., and Eaton, J. K., 2005, "Turbulence Development in a Non-Equilibrium Turbulent Boundary Layer With Mild Adverse Pressure Gradient," *J. Fluid Mech.*, **532**, pp. 345–364.
- [5] Skåre, P. E., and Krogstad, P.-Å., 1994, "A Turbulent Equilibrium Boundary Layer Near Separation," *J. Fluid Mech.*, **272**, pp. 319–348.
- [6] Dengel, P., and Fernholz, H. H., 1990, "An Experimental Investigation of an Incompressible Turbulent Boundary Layer in the Vicinity of Separation," *J. Fluid Mech.*, **212**, pp. 615–636.
- [7] Angele, K. P., and Muhammad-Klingmann, B., 2006, "PIV Measurements in a Weakly Separating and Reattaching Turbulent Boundary Layer," *Eur. J. Mech. B/Fluids*, **25**, pp. 204–222.
- [8] Cui, J., Patel, V. C., and Lin, C.-L., 2003, "Large-Eddy Simulation of Turbulent Flow in a Channel With Rib Roughness," *Int. J. Heat Fluid Flow*, **24**, pp. 372–388.
- [9] Nagano, Y., Hattori, H., Yasui, S., and Houra, T., 2004, "DNS of Velocity and Thermal Fields in Turbulent Channel Flow With Transverse-Rib Roughness," *Int. J. Heat Fluid Flow*, **25**, pp. 393–403.
- [10] Ikeda, T., and Durbin, P. A., 2007, "Direct Simulation of a Rough-Wall Channel Flow," *J. Fluid Mech.*, **571**, pp. 235–263.
- [11] Lee, S.-H., and Sung, H. J., 2007, "Direct Numerical Simulation of the Turbulent Boundary Layer Over a Rod-Roughened Wall," *J. Fluid Mech.*, **584**, pp. 125–146.
- [12] Ashrafian, A., Andersson, H. I., and Manhart, M., 2004, "DNS of Turbulent Flow in a Rod-Roughened Channel," *Int. J. Heat Fluid Flow*, **25**, pp. 373–383.
- [13] Leonardi, S., Orlandi, P., Smalley, R. J., Djenidi, L., and Antonia, R. A., 2003, "Direct Numerical Simulations of Turbulent Channel Flow With Transverse Square Bars on One Wall," *J. Fluid Mech.*, **491**, pp. 229–238.
- [14] Tani, I., 1987, "Equilibrium, or Non-Equilibrium, of Turbulent Boundary Layer Flows," *Proc. Jpn. Acad., Ser. B: Phys. Biol. Sci.*, **63**, pp. 96–100.
- [15] Kameda, T., Mochizuki, S., and Osaka, H., 2004, "LDA Measurement in Roughness Sublayer Beneath Turbulent Boundary Layer Developed Over Two-dimensional Square Rough Surface," *12th International Symposium on Applications of Laser Techniques to Fluid Mechanics*, Lisbon, Portugal, July 12–15.
- [16] Bakken, O. M., Krogstad, P.-Å., Ashrafian, A., and Andersson, H. I., 2005, "Reynolds Number Effects in the Outer Layer of the Turbulent Flow in a Channel With Rough Walls," *Phys. Fluids*, **17**, pp. 065101.
- [17] Agelintchaab, M., and Tachie, M. F., 2006, "Open Channel Turbulent Flow Over Hemispherical Ribs," *Int. J. Heat Fluid Flow*, **27**, pp. 1010–1027.
- [18] Tachie, M. F., and Adane, K. K., 2007, "PIV Study of Shallow Open Channel Flow Over d - and k -Type Transverse Ribs," *ASME J. Fluids Eng.*, **129**, pp. 1058–1072.
- [19] Perry, A. E., Schofield, W. H., and Joubert, P. N., 1969, "Rough Wall Turbulent Boundary Layers," *J. Fluid Mech.*, **37**, pp. 383–413.
- [20] Tachie, M. F., Agelintchaab, M., and Shah, M. K., 2007, "Turbulent Flow Over Transverse Ribs in Open Channel With Converging Side Walls," *Int. J. Heat Fluid Flow*, **28**, pp. 683–707.
- [21] Tachie, M. F., 2007, "PIV Study of Turbulent Flow Over Transverse Square Ribs in Asymmetric Diffuser," *Phys. Fluids*, **19**, pp. 065106.
- [22] Raupach, M. R., Antonia, R. A., and Rajagopalan, S., 1991, "Rough-Wall Turbulent Boundary Layers" *Appl. Mech. Rev.*, **44**(1), pp. 1–25.
- [23] Castro, I. P., 2007, "Rough-Wall Boundary Layers: Mean Flow Universality," *J. Fluid Mech.*, **585**, pp. 469–485.
- [24] Shah, M. K., and Tachie, M. F., 2008, "PIV Study of Turbulent Flow in Asymmetric Converging and Diverging Channels," *ASME J. Fluids Eng.*, **130**, p. 011204.
- [25] Raffel, M., Willert, C. E., and Kompenhaus, J., 1998, *Particle Image Velocimetry: A Practical Guide*, Springer, New York.
- [26] Shah, M. K., Agelintchaab, M., and Tachie, M. F., 2008, "Influence of PIV Interrogation Area on Turbulent Statistics Up to 4th Order Moments in Smooth and Rough Wall Turbulent Flows," *Exp. Therm. Fluid Sci.*, **32**, pp. 725–747.
- [27] Prasad, A. K., Adrian, R. J., Landreth, C. C., and Offutt, P. W., 1992, "Effect of Resolution on the Speed and Accuracy of Particle Image Velocimetry Interrogation," *Exp. Fluids*, **13**, pp. 105–116.
- [28] Forliti, D. J., Strykowski, P. J., and Debatin, K., 2000, "Bias and Precision Errors of Digital Particle Image Velocimetry," *Exp. Fluids*, **28**, pp. 436–447.
- [29] Coleman, H. W., and Steele, W. G., 1995, "Engineering Application of Experimental Uncertainty Analysis," *AIAA J.*, **33**, pp. 1888–1896.
- [30] Krogstad, P.-Å., Andersson, H. I., Bakken, O. M., Ashrafian, A., 2005, "An Experimental and Numerical Study of Channel Flow With Rough Walls," *J. Fluid Mech.*, **530**, pp. 327–352.
- [31] Kader, B. A., and Yaglom, A. M., 1978, "Similarity Treatment of Moving-Equilibrium Turbulent Boundary Layers in Adverse Pressure Gradients," *J. Fluid Mech.*, **89**, pp. 305–342.
- [32] Ligriani, P. M., and Moffat, R. J., 1986, "Structure of Transitionally Rough and Fully Rough Turbulent Boundary Layers," *J. Fluid Mech.*, **162**, pp. 69–98.
- [33] Schlichting, H., 1979, "Boundary-Layer Theory," McGraw-Hill, New York.
- [34] Buschmann, M. H., and Gad-el-Hak, M., 2003, "Debate concerning the Mean-Velocity Profile of a Turbulent Boundary Layer," *AIAA J.*, **41**(4), pp. 565–572.
- [35] George, W. K., and Castillo, L., 1997, "Zero Pressure Gradient Turbulent

Boundary Layer," *Appl. Mech. Rev.*, **50**(11), pp. 689–729.

- [36] Bergstrom, D. J., Tachie, M. F., and Balachandar, R., 2001, "Application of Power Laws to Low Reynolds Number Boundary Layers on Smooth and Rough Surfaces," *Phys. Fluids*, **13**, pp. 3277–3284.
- [37] Kotey, N. A., Bergstrom, D. J., and Tachie, M. F., 2003, "Power Laws for Rough Wall Turbulent Boundary Layers," *Phys. Fluids*, **15**(6), pp. 1396–1404.
- [38] Zagarola, M. V., and Smits, A. J., 1998, "Mean-Flow Scaling of Turbulent Pipe Flow," *J. Fluid Mech.*, **373**, pp. 33–79.

Aloke Kumar

School of Mechanical Engineering,
and Birck Nanotechnology Center,
Purdue University,
West Lafayette, IN 47907

Venu M. Gorti¹

School of Mechanical Engineering,
Purdue University,
West Lafayette, IN 47907

Hao Shang²

School of Chemical and Biomedical Engineering,
Purdue University,
West Lafayette, IN 47907

Gil U. Lee

School of Chemical and Biomedical Engineering,
and Birck Nanotechnology Center,
Purdue University,
West Lafayette, IN 47907

Nung Kwan Yip

Department of Mathematics,
Purdue University,
West Lafayette, IN 47907

Steve T. Wereley³

School of Mechanical Engineering,
and Birck Nanotechnology Center,
Purdue University,
West Lafayette, IN 47907
e-mail: wereley@purdue.edu

Optical Diffusometry Techniques and Applications in Biological Agent Detection

Optical diffusometry is a technique used for measuring diffusion. This work explores the possibility of directly measuring diffusion coefficients of submicron particles for pathogen detection. The diffusion coefficient of these particles is a function of the drag coefficient of the particle at constant temperatures. Particles introduced into a sample containing an analyte bind with the analyte if functionalized with the appropriate antibodies. This leads to an increase in the hydrodynamic drag of the particles and hence a decrease in their diffusion coefficient. This study uses the above principle to effectively measure the diffusion coefficient of the particles using two different experimental approaches. The measured reduction in the diffusion coefficient can be correlated to the amount of analyte present and thus forms the basis of biological agent detection. Sensitivity to experimental conditions is analyzed. It is observed that alternative techniques such as optical trapping hold promise: the diffusive behavior of particles in optical traps is found to be quantitatively different from that of a free particle. Hence preconditions are identified to make optical trapping appropriate for agent detection. [DOI: 10.1115/1.2969430]

Introduction

The early work of Einstein [1], Smoluchowski [2], and Langevin [3] established the much needed theoretical framework required to understand Brownian motion. The strange jiggling motion of the pollen grains was first documented by Brown, but it took an intuitive leap when Einstein [1] explained the underlying physical mechanism behind the phenomenon. Based on the molecular kinetic theory of heat and the fluctuation-dissipation theorem, Einstein deduced that the diffusion coefficient (D) of the particle is related to the viscous frictional resistance (ξ) in the following form:

$$D = \frac{kT}{\xi} \quad (1)$$

where k is the Boltzmann constant and T is the temperature. See also Ref. [4] for a contemporary treatment.

For spherical particles with radius r and low Reynolds number flow, ξ is well approximated by Stokes' law [5],

$$\xi = 6\pi\mu r \quad (2)$$

where μ is the viscosity of water.

From the above formula, the diffusion coefficient of submicron particles can be used to measure the temperature of the fluid at small length scales, the local fluid viscosity, and also the particle size. Recently, several researchers [6–9] studied the Brownian motion of submicron sized particles suspended in a fluid using digital video microscopy. Crocker [6] made use of optical traps to study the hydrodynamic correction to Brownian motion for the case of two spheres in close proximity. They demonstrated with carefully designed experiments that the diffusion coefficient can be experimentally measured to an accuracy of $\pm 1\%$. Nakroshis et al. [10] measured the Boltzmann constant, whereas Salmon et al. [9] measured Avogadro's number by studying the Brownian motion of submicron sized particles.

The present work explores the process of measuring the mean diffusion coefficient of a population of nearly identical virus-tagged rigid spherical particles. It is motivated by the idea that the binding of viruses on antibody functionalized particles should result in a measurable change in the diffusion coefficient. Such a decrease can be measured by the observation of particles, which are freely moving or are held in a region by an optical trap. Thus the objective is to establish optical diffusometry as a viable technique for biosensing, which is the name given to a host of technologies designed to detect the presence of biological analytes in a solution. These technologies use recognition elements such as antibodies, DNA, receptor proteins, and biomimetic elements for the above stated purpose. These methods include, but are not limited to, immunoassays [11], enzyme-catalyzed reactions [12], surface plasmon resonance technique [13], and impedimetric methods [14,15]. Optical methods for biosensing were explored by Anderson et al. [11] who developed a portable and automated

¹Present address: Hindustan Unilever Limited, Mumbai, India.

²Present address: MagSense Life Sciences Inc., USA.

³Corresponding author.

Contributed by the Fluids Engineering Division of ASME for publication in the JOURNAL OF FLUIDS ENGINEERING. Manuscript received June 22, 2007; final manuscript received June 11, 2008; published online September 22, 2008. Assoc. Editor: Juergen Kompenhans.

optical biosensor called RAPTOR to perform immunoassays. Fluorescence intensity was used to quantify the presence of antigens in a sample. Cui et al. [16] showed that binding of an analyte to the surface of a silicon nanowire leads to an observable change in the electrical conductivity of a medium. Such methods provide a basis for sensitive sensors to detect chemical and biological species. Typically, affinity biosensors use sandwich assays for detection and measurement. One drawback of sandwich assays is the difficulty in producing two antibodies that each bind to different sites of an antigen. Also, the probability of two binding events on a single antigen is less than that of a single binding event.

Most of the prevalent biological agent detection methods suffer from the disadvantage of being an indirect method. The present work explores different optical diffusometry techniques and establishes these as direct means of pathogen detection. The principles underlying all of them are discussed in detail, and the advantages and disadvantages of each are examined.

Experimental Techniques for Optical Diffusometry

This section discusses two experimental techniques—particle tracking and micron resolution particle image velocimetry (μ PIV).

Particle Tracking. Einstein, in his pioneering work [1], defined the diffusion coefficient in terms of a measurable property of Brownian motion—the mean square displacement of particles. These quantities are related by

$$\langle \Delta x^2 \rangle = 2nD\Delta t \quad (3)$$

where Δx is the displacement of the Brownian particle over a period of time Δt , the brackets $\langle \cdot \rangle$ refer to the statistical average of the contained quantity, and n is the number of degrees of translational freedom.

In particle tracking the motion of individual particles as a function of time is measured, and then Eq. (3) is applied to find the diffusion coefficient [7,17]. The accuracy and practicability of using diffusometry as a means of biological agent detection strongly depends on how the mean square displacement $\langle \Delta x^2 \rangle$ is determined. For this a discrete approach to position detection is undertaken by analyzing a sequence of images.

Particle position detection requires a position acquisition system, usually a video microscopy system. The particles undergoing Brownian motion are imaged at a fixed time interval using a video camera or a charge coupled device (CCD) camera attached to a microscope. Particle tracking can be done for a single or for multiple particles. The former, as the name suggests, involves tracking a single particle. The more advanced multiple particle tracking method tracks multiple particles simultaneously and recovers track data for each particle.

An accurate calculation of diffusion coefficient relies directly on the ability to track and identify particles. Einstein's original formulation assumes negligible boundary effects on the random motion of particles. To achieve such a condition experimentally, the focal plane of objective lens was adjusted so that each imaged particle is several particle diameters away from the wall. The particles were imaged using fluorescence microscopy, and a CCD camera (CoolSnap HQ, Photometrics, Tuscon, AZ) was used to acquire images at specified intervals. The camera has a 1392×1040 element CCD at $6.45 \times 6.45 \mu\text{m}^2$ pixel pitch. Image acquisition was controlled using the METAMORPH software package (Universal Imaging Corp., PA). The exposure time was set at 10 ms, and the time between images was 300 ms. The images were filtered using wavelet transformation to improve the signal-to-noise ratio. These images were then processed to yield the location of particle centers. Local maxima were first found with pixel level accuracy and the centers were located with subpixel accuracy using Gaussian curve fitting. Selecting only those maxima, which were above a certain threshold level, ensured that

the particles being selected were in the vicinity of the focal plane of the objective lens.

The objective lens had a magnification of $20\times$, and the resulting field of view had 10–20 particles per image. The center locations of the particles in the images were analyzed using a MATLAB[®] adaptation of the IDL particle tracking software developed by Grier, Crocker, and Weeks. The adaptation by Blair and Dufresne is freely available for public use [18].

Referring to Eq. (3), we see that the equation is statistical in nature and that the accuracy in the computation of diffusion coefficient is limited by the accuracy of the measured value of displacement values. Pixelation of data is the foremost source of error in the above discussed methodology. However, with Gaussian curve fitting, an accuracy of a tenth of a pixel can be achieved for particles of this size. The accuracy of subpixel location is directly correlated to the original size of the object being located. It is simply a biasing of the brightest portion of the feature of interest, weighed by the location of neighboring bright areas. In addition Eq. (3) ideally requires an infinite sample size, but this is clearly not possible. In accordance with statistical theory, the error reduces with an increase in sample size. Hence care should be taken to ensure that an adequate number of images are processed in order to arrive at an accurate value of the diffusion coefficient.

μ -PIV. μ -PIV uses instantaneous and ensemble-averaged flow fields in micron-scale fluidic devices. μ -PIV is now an established nonintrusive technique to obtain accurate velocity data with high spatial resolution and is widely used as a design tool for microfluidic devices. Like the setup of Santiago et al. [19], epifluorescent microscopy with micron sized (~ 700 nm) seed particles was used, and a CCD camera was used to record high-resolution particle-image fields. Although μ -PIV is primarily used to measure velocity fields, for small seed particles ($< 1 \mu\text{m}$) and low speed flow ($< 10 \mu\text{m/s}$), information regarding temperature and Brownian motion behavior can be extracted from the flow field. The basis for such extraction was laid out by the work of Olsen and Adrian [20] who showed that at such small scales errors from Brownian motion were significant enough to contribute to errors in the μ -PIV velocity measurements. It was later shown [21] that the broadening of the signal peak in the cross-correlation function is the key to measuring temperature using PIV. Olsen and Adrian [20], using theoretical considerations, derived equations describing the shape and height of the cross-correlation function in the presence of Brownian motion for both light-sheet illumination and volume illumination, which is used in μ -PIV. A minor manipulation of those equations (Eqs. (11) and (12) of Ref. [21]) shows that the diffusion coefficient can be related to the signal width by

$$2D\Delta t = \frac{\Delta s_{o,c}^2 - \Delta s_{o,a}^2}{8M^2} \quad (4)$$

where $\Delta s_{o,c}^2$ is the width of the correlation peak with Brownian motion, $\Delta s_{o,a}^2$ is the width of the correlation peak without Brownian motion, and M is the magnification of the objective lens. It should be noted that in any experiment, even where Brownian motion is significant, a computation of the autocorrelation function of one of the PIV image pairs yields $\Delta s_{o,a}^2$.

Assessment of Optical Traps for Diffusometry Measurements

Both the previous methods use a population of particles. Biosensing, based on diffusion differential, can be made more precise if such a differential could be established for single particles. Such a method can even allow for the identification of a single virus-tagged particle in a population of bare particles. A proposed solution is to trap a bead and hence confine them to a given spatial domain. Such a technique enables also the acquisition of a large amount of data in a single experiment. On the other hand, the

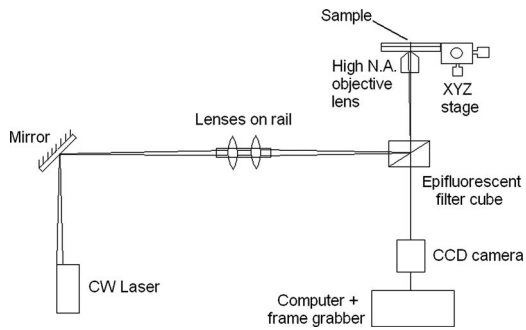


Fig. 1 Experimental setup for optical trapping. The lenses on the rail expand the beam, while the objective lens focuses the beam onto a diffraction limited spot. Epifluorescent imaging enhances the image quality.

forementioned two methods suffer from the disadvantage that particles often escape out of the field of view, thus leading to loss of efficiency and also to errors.

Optical trapping appeared as a revolutionary technique for manipulating microscale particles around 1970 in a series of path-breaking experiments conducted by Ashkin in Bell Laboratories [22]. Although Ashkin originally used both single and dual light beams to guide and confine particles, the former soon grew in popularity and is now commonly referred to by the name “optical tweezers.” Since their invention, optical tweezers have proven themselves to be a very powerful interdisciplinary tool. For instance, they have found extensive use in biophysics, as they serve as unique tools to manipulate and study single molecules of DNA [22–24]. Optically trapped beads have been successfully utilized to study cellular mechanics and structures [25,26]. Ashkin [27] provided an overview of the diverse uses of optical traps as a significant tool in various important areas of research.

Figure 1 shows the setup for the optical tweezers. Like other typical designs, it uses a laser beam that is suitably expanded, shaped, and focused through a high numerical aperture (NA) microscope objective lens. The laser has a TEM₀₀ (transverse electric magnetic) mode, which eliminates inefficiency due to excessive laser modes. The laser beam is focused by an optical train to a diffraction limited spot where stable three dimensional trapping can be achieved. The size of the diffraction limited spot is mainly a function of the wavelength of trapping light used and the NA of the objective lens used [28]. The optical path consists of lenses, directing mirrors, and a filter cube, which is set up to specifically enable fluorescent imaging. The various practical and theoretical aspects involved in setting up a laser trap are discussed by Smith et al. [28] and Bechhoefer and Wilson [29]. The sample is held on an XYZ translational stage that serves primarily to focus the sample and also to laterally displace the sample. The functionalized microparticles are basically dielectric particles with sub-micron dimensions, hence in an intermediate range between Rayleigh and geometric optics regimes. The forces from the optical trap in this case arise from (i) the scattering (or radiative) force originated by momentum changes of light due to scattering and (ii) the gradient (or dipole) force caused by the Lorentz force acting on the induced dipole [22,27]. The scattering force is proportional to the laser intensity, and its effect is to push the particle along the axis of laser beam propagation while the gradient force moves the particle along the gradient of the optical field. An optical trap for the purpose of the present work can be considered to be akin to a potential well with a constant stiffness. Such characterization of a trap is useful for both the Rayleigh and Mie regimes [30,31]. Diffusion measurements for particles in a trap were done using an IEEE 1394 digital camera (Foculus, NET USA, Inc.).

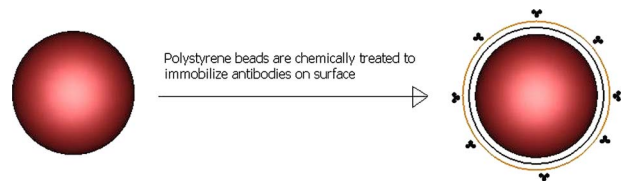


Fig. 2 Polystyrene beads are made to undergo a series of chemical processes so that a monolayer of poly(ethylene glycol) (PEG) is formed, and subsequently antibodies are immobilized on the PEG monolayer. The viruses bind onto the antibodies, thus leading to functionalized particles.

Optical Diffusometry and Biological Agent Detection

As indicated earlier, pathogen detection is achieved by virus tagging bare polystyrene beads. Such tagging is achieved by first coating the bead with appropriate antibodies (Fig. 2). These antibodies contain functional groups, which allow them to bind with certain proteins on the surface of the bead and hence make binding possible. In this work the M13 phage virus was used, and antibodies against the pVIII surface protein of the M13 phage virus were used. The M13 phage virus is filamentous in nature, with an approximate diameter of 6.5 nm and a length of 930 nm [32]. The detailed chemistry of functionalization of beads has been provided elsewhere [33].

Green fluorescent microspheres (diameter of 0.71 μm , excitation maximum of 468 nm, and emission maximum of 508 nm) and red fluorescent microspheres (diameter of 0.69 μm , excitation maximum of 542 nm, and emission maximum of 612 nm) were acquired from Duke Scientific Co. (Palo Alto, CA). Both types of particles were made of polystyrene latex, which has a density of 1.05 g/cm³. The M13 phage was obtained from New England BioLabs Inc. (Beverly, MA), and the antibodies against the pVIII protein of the M13 phage were obtained from Pharmacia (Piscataway, NJ).

Results

The viability of the proposed technique was tested by incubating known concentrations of virus with known densities of particles and by subsequently measuring the change in the diffusion coefficient of the particles. The green particles were used in unmodified form, while the red ones were coated with an anti-pVIII antibody. The antibody-coated red beads were incubated with the M13 virus at ratios of 2:1, 6:1, 8:1, and 10:1 viruses per particle. At the end of the incubation reaction, the unmodified green particles were added to the solution of red particles. The diffusion coefficients of the mixture of antibody functionalized red particles and unmodified green particles were measured as a function of M13 concentration. This methodology was followed to ensure that both bead populations are subjected to identical external conditions.

As mentioned earlier the particles were imaged using fluorescence microscopy, which affords the user selective imaging of red or green particles by simply interchanging filter cubes. In Fig. 3(a) the particles in and near the focal plane are the ones sharpest in feature, and diffuse images represent particles considerably removed from the focal plane. Subsequently these images are filtered to improve the signal-to-noise ratio (Fig. 3(b)). From an ensemble of such images, the position values are processed to yield track information about individual particles. It should be pointed out that particles often leave the field of view or migrate away from the plane of focus, leading to loss of efficiency. Brownian motion is often stated as the random walk motion of small particles suspended in a fluid due to bombardment by molecules obeying a Maxwellian velocity distribution. The tracks appear to demonstrate the random walk behavior that the particles are expected to show (Fig. 4).

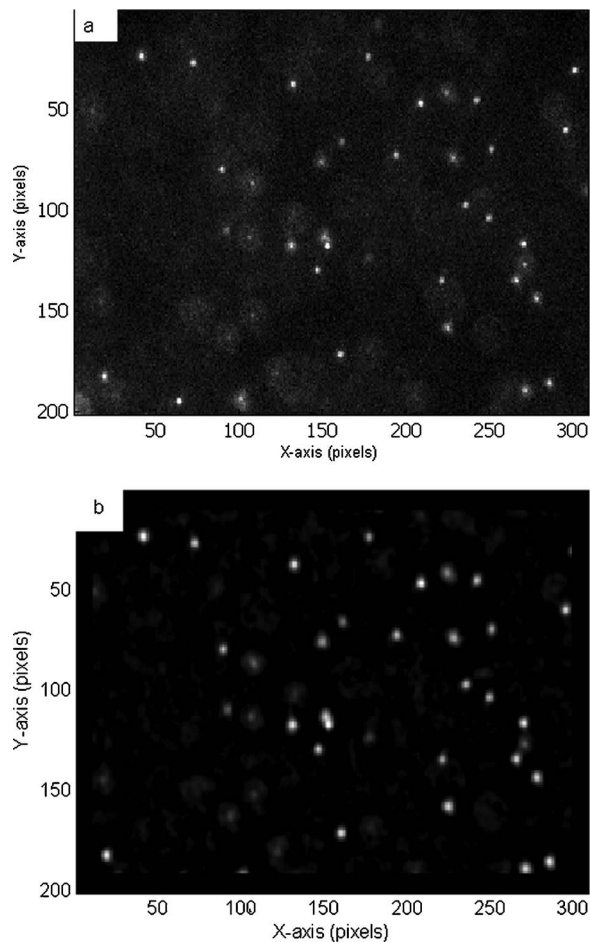


Fig. 3 Red microparticles ($0.69 \mu\text{m}$) functionalized with viruses are visualized using fluorescent microscopy. Note that fluorescent particles of only one type can be imaged at a time. (a) Fluorescent red particles can be seen as white dots on a black background. (b) The same image is filtered to enhance image quality. For particle tracking only, particles with intensity above a certain threshold are taken into account.

Figure 5 presents the diffusion coefficients measured for the particles without anti-pVIII antibodies and with antibodies in the

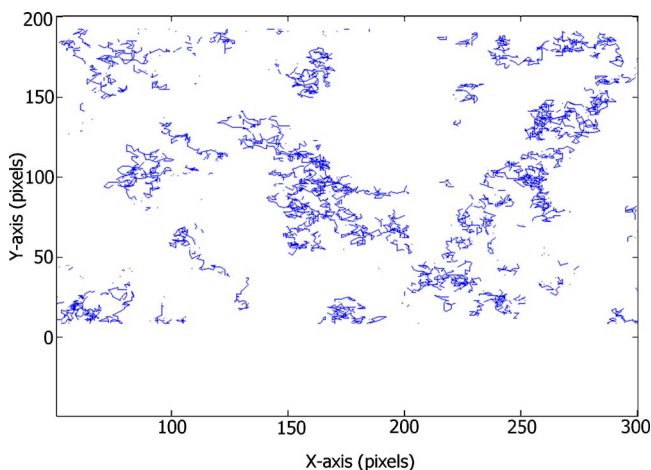


Fig. 4 A large number of images are processed to yield particle tracks. The terminated paths indicate loss of particle from the viewing volume.

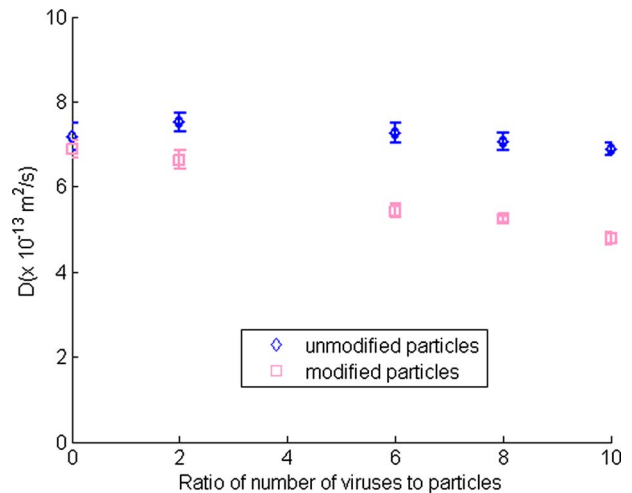


Fig. 5 Diffusion coefficients of antibody functionalized particles and unmodified particles as a function of virus concentration

presence of increasing virus concentrations. The significance of changes in the diffusion coefficients of the two populations was tested using analysis of variance (ANOVA). Both interpopulation and intrapopulation variances were tested, and it was found that for green particles, the variation in diffusion coefficient is not significant ($p\text{-value}=8.6 \times 10^{-8}$). However for red particles the variation in diffusion coefficient is found to be significant ($p\text{-value}=0.087$). The analysis indicates that virus tagging of red particles is the principal factor leading to a change in diffusion behavior. The diffusion coefficient values plotted here were obtained from a particle tracking analysis and were confirmed using $\mu\text{-PIV}$.

A first order model for diffusion of $0.69 \mu\text{m}$ particles functionalized with antibodies and incubated with M13 viruses is constructed based on experimental findings. We assume in this simplified model that the virus tagging results in an increase in drag and that this increase is linear in nature. Specifically, the model assumes that the diffusion coefficient of tagged particles is given by

$$D = \frac{kT}{\xi_{\text{virus}} + \xi_{\text{sphere}}} \quad (5)$$

where ξ_{virus} increases linearly with an increase in virus concentration.

A least squares fit yields the following correlation

$$\xi_{\text{total}} = \xi_{\text{sphere}} + \xi_{\text{virus}} = (0.2705n_{\text{virus}} + 5.863) \times 10^{-9} \text{ N s/m} \quad (6)$$

The variable n_{virus} represents viruses per particle and assumes a value from the set $\{2, 6, 8, 10\}$. The goodness of the fit is characterized by the R^2 value, and its high value of 0.98 for the above fit suggests the adequacy of the linear model.

One of the primary sources of systematic error that results from the use of images is pixelation. An estimate of error due to digitization (pixelation in the case of video microscopy) loss can be gauged from Fig. 6. The figure depicts experimental error in the calculation of diffusion coefficient with respect to the number of data points. These errors were calculated from simulated images of particles exhibiting Brownian motion. Simulations of this experimental error reveal a decreasing trend with the number of data points. It will be shown (Appendix) that the error in the calculation of diffusion coefficient, resulting from pixelation, is bound by

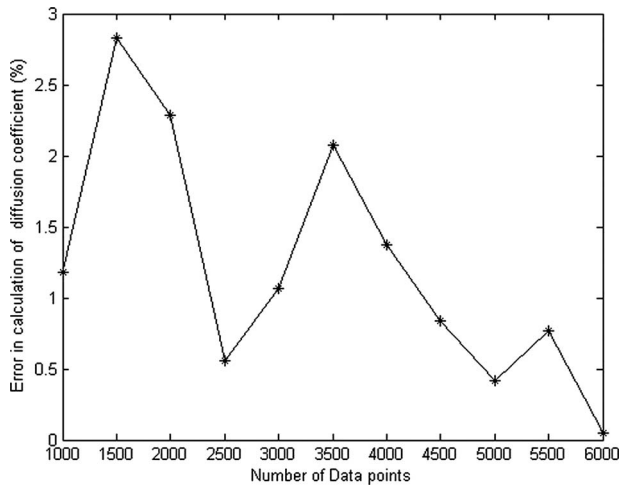


Fig. 6 Experimental error in the calculation of diffusion coefficient versus number of data points. These errors were calculated from simulated images of particles exhibiting Brownian motion.

$$\text{Error} \leq O\left(\frac{\delta}{\sqrt{t}}\right) \quad (7)$$

where δ is an upper bound for the error in locating the particle centers. Eq. (7) reveals that this error can be reduced by making long time measurements.

Microparticles were successfully trapped in the optical trap, which appears in Fig. 7 as a bright spot approximately in the middle of the image. That the optical traps were effective in trapping the particles was confirmed by artificially inducing a flow and observing the movement of the trapped beads. The images provide positional data of the trapped beads. The higher the laser power used, the higher the trap strength and the lesser the observable Brownian motion.

Simulation runs (Fig. 8) show that the particle in an optical trap still exhibits a random walk behavior, which, however, is modified due to the presence of the potential well. Figure 9 shows the typical response of a particle in a trap. This response was captured using a frame rate of 155 frames/s.

Discussion

Advantages of Optical Diffusometry. The results show that binding of an analyte to an antibody functionalized particle can produce a significant decrease in its diffusion coefficient. Although the experiment used $0.69 \mu\text{m}$ particles, the method applies to particles as small as 40 nm [34]. Smaller particles undergo

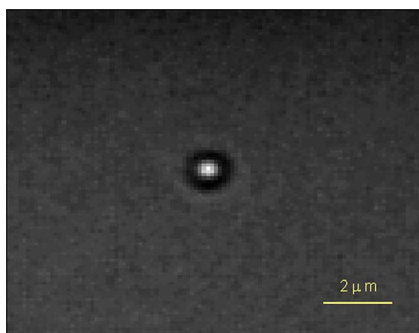


Fig. 7 A $0.69 \mu\text{m}$ particle (center) in an optical trap

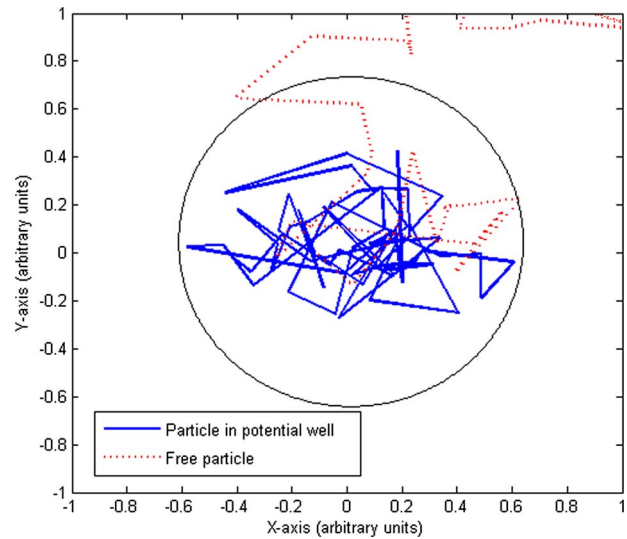


Fig. 8 Simulation runs of particles with and without a trap. The particle in a potential well exhibits a modified Brownian motion.

enhanced alteration in the diffusion coefficient, enabling detection of even smaller analytes.

The proposed technique offers four distinct advantages over affinity biosensors, which typically use sandwich assays for detection and measurement. Optical diffusometry uses a single antibody, which significantly reduces the reagent cost and enables virus detection with limited epitopes. Another advantage is the use of a label free detection mechanism. Sandwich assays usually involve an enzyme used as a signal reporter, which is limited by the availability of the detection conjugate. The proposed technique uses fluorescent particles, which serve the dual role of capturing and detecting. This combination simplifies the detection procedure. Thirdly optical diffusometry is much faster than sandwich assay. Typically this requires 30 min for virus binding and 15 min for optical detection and analysis. The assay can be finished within 1 h, whereas typical sandwich assays take 3–5 h [35]. Lastly, optical diffusometry can be multiplexed to detect multiple pathogens simultaneously. In order to multiplex the assay, par-

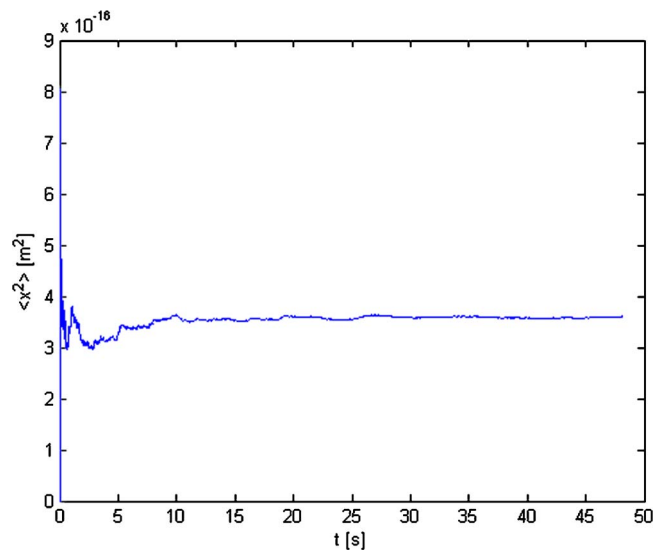


Fig. 9 Typical response of a bead confined to a small spatial volume by an optical trap

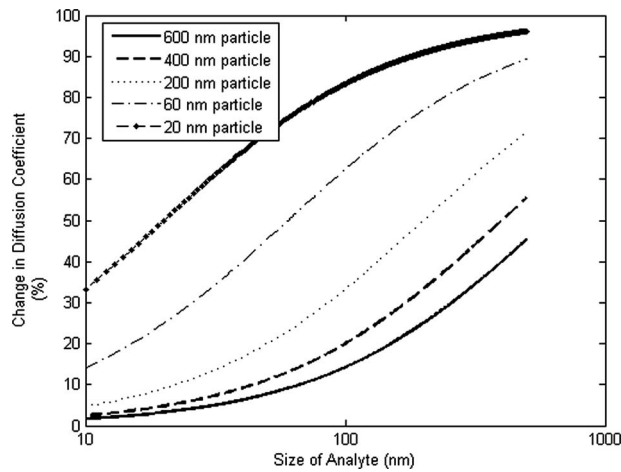


Fig. 10 Percentage change in the diffusion coefficient of virus-tagged beads as a function of the hydrodynamic radius of the pathogen

ticles with different colors can be coated with antibodies against different pathogens, and a mixture of particles can be used to detect multiple pathogens in a single assay.

Particle Tracking and μ -PIV. The particle tracking methodology applied here relies on a strong contrast between the background and the particle image. Fluorescent imaging usually provides such high contrast, but other methods like phase contrast microscopy may also be applied. μ -PIV, however, does not have such requirements [36]. In an optical trap since only a single particle is investigated, particle tracking is a natural choice. A particle in an optical trap is confined to a small spatial dimension. Hence one can use subpixel imaging, which enables the user to use a higher frame rate. A small dimension of 104×100 pixels only was imaged (Fig. 7), enabling the use of a higher frame rate of 155 frames/s.

Both Eqs. (3) and (4) are statistical in nature. For particle tracking Gaussian curve fitting can usually achieve good subpixel accuracy [7]. However, as will be shown in the Appendix, for particle tracking the calculation of D becomes more and more accurate by using longer time measurements irrelevant of the error in locating particle centers. This is confirmed by simulation results, as shown in Fig. 6. Error analysis for Eq. (4) is straightforward, and the peak width can typically be calculated with subpixel accuracy [37].

Sensitivity Analysis. The selection of bead diameter should be such that binding of the analyte has an appreciable change in its diffusion coefficient. We use for sensitivity analysis the same first order model that was used for correlation analysis. Assuming that the analytes can be characterized by a hydrodynamic radius, we get

$$\Delta D \% = \frac{r_{\text{virus}}}{r_{\text{virus}} + r_{\text{particle}}} \times 100 \quad (8)$$

The percentage change in diffusion coefficient is inversely proportional to the size of the particles used. Compared to a large particle, a smaller particle will undergo a more significant change in diffusion for a similar sized pathogen and hence can be used to detect smaller analytes. Figure 10 characterizes the change in diffusion coefficient as a function of this hydrodynamic radius. The model is simplistic in that it assumes that a virus can be characterized by a unique hydrodynamic radius, but it can give a good first guess. It should also be noted that the effective hydrodynamic radius of the virus need not coincide with its physical size. For viruses like the M13 phage virus, one way of calculating the corresponding hydrodynamic radius would be to correlate the in-

crease in hydrodynamic drag (Eq. (5)) to the change in radius required to cause the variation (Eq. (8)). For example at a virus to bead ratio of 6:1, the calculated increase in hydrodynamic radius is 186 nm with a corresponding uncertainty of $\sim 5\%$.

Influence of Environmental Variables on the Resolution of Optical Diffusometry. Measurement of diffusion coefficient can be influenced by the variations of numerous factors, such as temperature, viscosity, and particle size. If the changes in these parameters are small, then a simple calculation shows that the influence of these changes can be expressed as

$$\frac{\delta D}{D} = \left(1 - \frac{T}{\mu} \frac{\partial \mu}{\partial T}\right) \frac{\delta T}{T} - \frac{\delta \mu}{\mu} - \frac{\delta r}{r} \quad (9)$$

Note that in the above equation it is assumed that the viscosity depends on temperature ($\partial \mu / \partial T$) and on other factors as well ($\delta \mu$). Variations in temperature can occur in each experiment due to radiation and absorption from the illumination source. A change of 0.1 K in absolute temperature changes the diffusion coefficient of particles by approximately 0.2%. Hence in controlled environments, temperature has a limited influence on diffusometry. Viscosity might independently change due to the presence of free viruses. The presence of particles in a medium changes the viscosity by [1]

$$\mu = \mu(1 + 2.5\phi) \quad (10)$$

where ϕ is the volume fraction of particles and viruses. Since in our case $\phi \ll 1$, the effect of particles on viscosity is small. The volume fraction of viruses is even smaller. Thus it appears that the variation in viscosity due to the presence of analytes and microparticles is quite small. By using multicolor beads of the same size, one can subject modified and unmodified particles to similar experimental conditions, thus minimizing errors due to such changes. Variations in microparticle size are unavoidable when using a population of particles.

Optical Trapping as a Multiplexing Tool and Its Role in Biosensing. Both the methods, particle tracking and μ -PIV, rely heavily on the necessity to extract a large number of images. It can be shown that the diffusion of trapped particles is quantitatively different from that of a freely diffusing particle. The diffusive behavior in the presence of such harmonic forces has been studied in detail. The statistics of such a particle becomes stationary in the long time, and it was established in Ref. [38] that

$$\lim_{t \rightarrow \infty} \langle \Delta x^2 \rangle = \frac{kT}{m\omega^2} \quad (11)$$

where ω is the angular frequency associated with the optical trap.

Equation (6) implies that the diffusion coefficient for a particle is zero irrespective of the strength of the trap or the variation in other parameters. Thus diffusive differential cannot be established by a study of the long time behavior. One alternative would be to establish a potential well with a "flat bed" and "steep walls." The walls would prevent the particle from escaping a given spatial domain, thus forming a cage. However, this requires the use of holographic optical traps, which has not yet been pursued in this work.

Another alternative is to study the diffusive behavior in the ballistic regime [39]. Although the long term behavior of a particle is independent of the particle drag, response on smaller time scales can also provide an insight. Figure 11 demonstrates the behavior of a particle in a trap, where two distinct regimes (linear and axiomatic convergences) are clearly depicted. The linear region can be used for the diffusion and drag differential study. In these small time scales, it is shown [39] that

$$\langle \Delta x^2(t) \rangle \approx 2Dt \quad (12)$$

Hence particle tracking can be done to establish drag differential between virus-tagged polystyrene beads. As can be seen in Fig. 9,

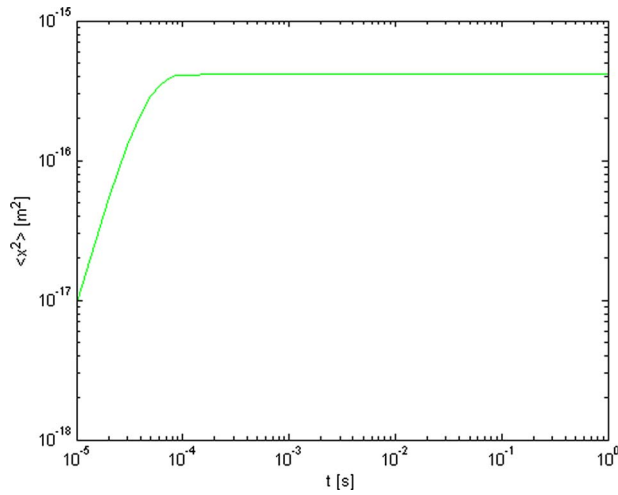


Fig. 11 A particle in a trap exhibits a linear trend on small time scales. This linear trend can be used for diffusion based differentiation. Note the extremely small time scales involved.

the response of the bead at low data acquisition rates does not reveal any information about the drag. For pathogen detection, high-speed cameras or other techniques, such as quadrant photodiode position detection, appear to be necessary.

Conclusion

This research demonstrates that binding of viruses on antibody functionalized particles results in a significant decrease in diffusion coefficients, which can be measured by particle tracking algorithms or μ -PIV techniques. Analytes, as small as 1 nm, can be detected by measuring the change in diffusion of antibody functionalized 40 nm particles. This method offers several advantages such as high spatial resolution, multianalyte detection capability, avoidance of sandwich assays, less preparation time, and quicker results. It is a more direct approach to biosensing compared to many other contemporary methods. The diffusion coefficient is measured from a population of particles. It was demonstrated that the experimental error due to pixelation depends not only on positional accuracy but also on the total data points used. This error decreases to zero with longer time measurements. This technology will be more powerful if accurate diffusion coefficients of single particles are measured. Optical traps offer such a technique, which is useful, even when the particles exhibit a modified Brownian motion. Optical traps make it feasible to locally constrain the particle in question for long time intervals, which then allows for extraction of a large amount of data. Static optical traps suffer from the shortcoming of having to require small time scale measurement techniques.

Appendix: Estimate of Error Due to Pixelation

According to the procedure outlined in the previous section, images of particles are acquired to yield the particle trajectories, which in turn are used to estimate the diffusion coefficient of particles. However, the trajectories suffer from discretization due to pixelation. The following analysis provides an estimate of this error.

Let $X(t)$ denote the n -dimensional Brownian motion process (where n can range from 1 to 3). Its probability density function (pdf) is given by $e^{-|x|^2/4Dt}/(4\pi Dt)^{n/2}$. The diffusion coefficient D and the mean square displacement is related by

$$D = \frac{\langle |X(t)|^2 \rangle}{2nt} \quad (\text{A1})$$

where $\langle \cdot \rangle$ denotes statistical averaging.

Now let δ be half the pixel size. The measured diffusion coefficient denoted by D_δ is calculated as

$$D_\delta = \frac{\langle |X_\delta(t)|^2 \rangle}{2nt} \quad (\text{A2})$$

where $X_\delta(t)$ is the experimentally obtained positional data. Note that $|X(t) - X_\delta(t)| \leq \delta$. The error in estimating the diffusion coefficient is thus

$$\begin{aligned} |D - D_\delta| &\leq \frac{1}{2nt} \int ||x|^2 - |x_\delta|^2| \frac{e^{-|x|^2/4Dt}}{(4\pi Dt)^{n/2}} d^n x \\ &\leq \frac{1}{2nt} \int ||x|^2 - |x \pm \delta|^2| \frac{e^{-|x|^2/4Dt}}{(4\pi Dt)^{n/2}} d^n x \\ &\leq \frac{1}{2nt} \int |2\delta|x| + \delta^2| \frac{e^{-|x|^2/4Dt}}{(4\pi Dt)^{n/2}} d^n x \\ &\leq O\left(\frac{\delta}{\sqrt{t}}\right) + O\left(\frac{\delta^2}{t}\right) \leq O\left(\frac{\delta}{\sqrt{t}}\right) \end{aligned} \quad (\text{A3})$$

which indicates that the error goes to zero as $t \rightarrow \infty$. It should be noted that only the error due to pixelation is taken into account here.

References

- [1] Einstein, A., 1956, *Investigations on the Theory of the Brownian Movement*, Dover, New York, p. 119.
- [2] Langevin, P., 1908, "The Theory of Brownian Movement," *C. R. Hebd. Seances Acad. Sci.*, **146**, pp. 530–533.
- [3] Smoluchowski, M., 1906, "Zur Kinetischen Theorie der Brownschen Molekularbewegung und der Suspension," *Ann. Phys.(Leipzig)*, **326**, pp. 756–780.
- [4] Nelson, E., 1967, *Dynamical Theories of Brownian Motion*, Princeton University Press, Princeton, NJ, p. 142.
- [5] White, F. M., 2006, *Viscous Fluid Flow*, McGraw-Hill Series in Mechanical Engineering, 3rd ed., McGraw-Hill, New York, p. 629.
- [6] Crocker, J. C., 1997, "Measurement of the Hydrodynamic Corrections to the Brownian Motion of Two Colloidal Spheres," *J. Chem. Phys.*, **106**(7), pp. 2837–2840.
- [7] Crocker, J. C., and Grier, D. G., 1996, "Methods of Digital Video Microscopy for Colloidal Studies," *J. Colloid Interface Sci.*, **179**(1), pp. 298–310.
- [8] Park, J. S., Choi, C. K., and Kihm, K. D., 2005, "Temperature Measurement for a Nanoparticle Suspension by Detecting the Brownian Motion Using Optical Serial Sectioning Microscopy (OSSM)," *Meas. Sci. Technol.*, **16**(7), pp. 1418–1429.
- [9] Salmon, R., Robbins, C., and Forinash, K., 2002, "Brownian Motion Using Video Capture," *Eur. J. Phys.*, **23**(3), pp. 249–253.
- [10] Nakroshis, P., Amoroso, M., Legere, J., and Smith, C., 2003, "Measuring Boltzmann's Constant Using Video Microscopy of Brownian Motion," *Am. J. Phys.*, **71**(6), pp. 568–573.
- [11] Anderson, G. P., King, K. D., Gaffney, K. L., and Johnson, L. H., 2000, "Multi-Analyte Interrogation Using the Fiber Optic Biosensor," *Biosens. Bioelectron.*, **14**(10–11), pp. 771–777.
- [12] Eu, J. Y., Wang, C. Y., and Andrade, J., 1999, "Homogeneous Bioluminescence Assay for Galactosuria: Interference and Kinetic Analysis," *Anal. Biochem.*, **271**(2), pp. 168–176.
- [13] Liedberg, B., Nylander, C., and Lundstrom, I., 1983, "Surface-Plasmon Resonance for Gas-Detection and Biosensing," *Sens. Actuators*, **4**(2), pp. 299–304.
- [14] Kharitonov, A. B., Wasserman, J., Katz, E., and Willner, I., 2001, "The Use of Impedance Spectroscopy for the Characterization of Protein-Modified ISFET Devices: Application of the Method for the Analysis of Biorecognition Processes," *J. Phys. Chem. B*, **105**(19), pp. 4205–4213.
- [15] Saum, A. G. E., Cumming, R. H., and Rowell, F. J., 1998, "Use of Substrate Coated Electrodes and AC Impedance Spectroscopy for the Detection of Enzyme Activity," *Biosens. Bioelectron.*, **13**(5), pp. 511–518.
- [16] Cui, Y., Wei, Q. Q., Park, H. K., and Lieber, C. M., 2001, "Nanowire Nanosensors for Highly Sensitive and Selective Detection of Biological and Chemical Species," *Science*, **293**(5533), pp. 1289–1292.
- [17] Saxton, M. J., 1997, "Single-Particle Tracking: The Distribution of Diffusion Coefficients," *Biophys. J.*, **72**(4), pp. 1744–1753.
- [18] Blair, D., and Dufresne, E., "The Matlab Particle Tracking Code Repository," <http://physics.georgetown.edu/matlab/>
- [19] Santiago, J. G., Wereley, S. T., Meinhart, C. D., Beebe, D. J., and Adrian, R. J., 1998, "A Particle Image Velocimetry System for Microfluidics," *Exp. Fluids*, **25**(4), pp. 316–319.
- [20] Olsen, M. G., and Adrian, R. J., 2000, "Brownian Motion and Correlation in Particle Image Velocimetry," *Opt. Laser Technol.*, **32**(7–8), pp. 621–627.
- [21] Hohreiter, V., Wereley, S. T., Olsen, M. G., and Chung, J. N., 2002, "Cross-Correlation Analysis for Temperature Measurement," *Meas. Sci. Technol.*,

- 13(7), pp. 1072–1078.
- [22] Ashkin, A., Dziedzic, J. M., Bjorkholm, J. E., and Chu, S., 1986, "Observation of a Single-Beam Gradient Force Optical Trap for Dielectric Particles," *Opt. Lett.*, **11**(5), pp. 288–290.
- [23] Felgner, H., Frank, R., and Schliwa, M., 1996, "Flexural Rigidity of Microtubules Measured With the Use of Optical Tweezers," *J. Cell. Sci.*, **109**, pp. 509–516.
- [24] Kurachi, M., Hoshi, M., and Tashiro, H., 1995, "Buckling of a Single Microtubule by Optical Trapping Forces: Direct Measurement of Microtubule Rigidity," *Cell Motil. Cytoskeleton*, **30**(3), pp. 221–228.
- [25] Henon, S., Lenormand, G., Richert, A., and Gallet, F., 1999, "A New Determination of the Shear Modulus of the Human Erythrocyte Membrane Using Optical Tweezers," *Biophys. J.*, **76**(2), pp. 1145–1151.
- [26] Suzuki, K., Sterba, R. E., and Sheetz, M. P., 2000, "Outer Membrane Monolayer Domains From Two-Dimensional Surface Scanning Resistance Measurements," *Biophys. J.*, **79**(1), pp. 448–459.
- [27] Ashkin, A., 1997, "Optical Trapping and Manipulation of Neutral Particles Using Lasers," *Proc. Natl. Acad. Sci. U.S.A.*, **94**(10), pp. 4853–4860.
- [28] Smith, S. P., Bhalotra, S. R., Brody, A. L., Brown, B. L., Boyda, E. K., and Prentiss, M., 1999, "Inexpensive Optical Tweezers for Undergraduate Laboratories," *Am. J. Phys.*, **67**(1), pp. 26–35.
- [29] Bechhoefer, J., and Wilson, S., 2002, "Faster, Cheaper, Safer Optical Tweezers for the Undergraduate Laboratory," *Am. J. Phys.*, **70**(4), pp. 393–400.
- [30] Buosciolo, A., Pesce, G., and Sasso, A., 2004, "New Calibration Method for Position Detector for Simultaneous Measurements of Force Constants and Local Viscosity in Optical Tweezers," *Opt. Commun.*, **230**(4–6), pp. 357–368.
- [31] Malagnino, N., Pesce, G., Sasso, A., and Arimondo, E., 2002, "Measurements of Trapping Efficiency and Stiffness in Optical Tweezers," *Opt. Commun.*, **214**(1–6), pp. 15–24.
- [32] Fields, B. N., Knipe, D. M., and Howley, P. M., 2007, *Fields' Virology*, 5th ed., Lippincott Williams and Wilkins, Philadelphia.
- [33] Lee, G. U., Metzger, S., Natesan, M., Yanavich, C., and Dufrene, Y. F., 2000, "Implementation of Force Differentiation in the Immunoassay," *Anal. Biochem.*, **287**(2), pp. 261–271.
- [34] Csaki, A., Kaplanek, P., Moller, R., and Fritzsche, W., 2003, "The Optical Detection of Individual DNA-Conjugated Gold Nanoparticle Labels After Metal Enhancement," *Nanotechnology*, **14**(12), pp. 1262–1268.
- [35] Crowther, J. R., 1995, *ELISA: Theory and Practice*, Humana, Totowa, NJ, p. 223.
- [36] Hagsater, S. M., Westergaard, C. H., Bruus, H., and Kutter, J. P., 2008, "Investigations on LED Illumination for Micro-PIV Including a Novel Front-Lit Configuration," *Exp. Fluids*, **44**, pp. 211–219.
- [37] Chamrathy, P., 2007, "Non-Intrusive Temperature Measurement Using Microscale Visualization Techniques," Ph.D. thesis Purdue University, West Lafayette.
- [38] Chandrasekhar, S., 1943, "Stochastic Problems in Physics and Astronomy," *Rev. Mod. Phys.*, **15**(1), pp. 1–89.
- [39] Lukic, B., Jeney, S., Tischer, C., Kulik, A. J., Forro, L., and Florin, E. L., 2005, "Direct Observation of Nondiffusive Motion of a Brownian Particle," *Phys. Rev. Lett.*, **95**(16), p. 160601.